

$$1M_1 \ 2M_2 \ 3M_3 \qquad \qquad 10\tilde{\chi}_1^0$$

HL/HE-LHC Physics Workshop Report

Higgs physics opportunities

Conveners: Maria Cepeda¹, Stefania Gori², Phil Ilten³, Marumi Kado⁴, Francesco Riva⁵

Contributors:

¹ CERN

² Institute 2

³ Laboratoire de l'Accélérateur Linéaire

⁴ Institute 4

⁵ Département de Physique Théorique, Université de Genève, 24 quai Ernest-Ansermet, 1211 Genève 4,
Switzerland

Abstract

This is an abstract

Contents

1	Introduction	4
1.1	Bibliography	5
2	Higgs boson precision measurements	6
2.1	Introduction	6
2.2	Theoretical predictions for the Higgs boson production at 14 and 27 TeV	6
2.2.1	PDF uncertainty expectations at the HE/HL-LHC	6
2.2.2	Progress on Higgs boson specific MC generators	10
2.3	Overview of experimental analysis for the Higgs boson measurement channels	10
2.3.1	Extrapolation assumptions	10
2.3.2	$H \rightarrow \gamma\gamma$	11
2.3.3	$H \rightarrow Z\gamma \rightarrow 2\ell\gamma$	12
2.3.4	$H \rightarrow ZZ^* \rightarrow 4\ell$	13
2.3.5	$H \rightarrow WW^* \rightarrow \ell\nu\ell\nu$	14
2.3.6	$H \rightarrow \tau\tau$	14
2.3.7	$H \rightarrow bb$	15
2.3.8	$H \rightarrow \mu\mu$	17
2.4	Fiducial and differential cross-section measurements	17
2.4.1	Measurements using $H \rightarrow \gamma\gamma$, $H \rightarrow ZZ^* \rightarrow 4\ell$, (boosted) $H \rightarrow b\bar{b}$ decay channels . .	17
2.4.2	Measurement of $p_T(H)$ spectrum in $t\bar{t}H$ production mode	18
2.5	Direct and indirect probing of top Yukawa coupling	19
2.5.1	Measurements in $t\bar{t}H$ and tH production modes	19
2.5.2	Constraints from differential measurements	23
2.6	Combination of Higgs boson measurement projections	24
2.6.1	Signal strength per-decay mode	25
2.6.2	Signal strength per-production mode	26
2.7	Kappa interpretation of the combined Higgs boson measurement projections	26
2.8	Kappa-formalism and the nonlinear EFT	30
2.9	Higgs couplings precision overview in the Kappa-framework and the nonlinear EFT	34
2.9.1	The fit to HL/HE-LHC Higgs precision data	35
2.9.2	Results	35
2.10	Projections of Higgs boson measurements to the HE-LHC	37
2.11	Probing of anomalous HVV interactions	37
2.11.1	Probes using differential distributions of CP sensitive observables	37
2.11.2	Experimental constraints on anomalous HVV couplings	43
2.12	Summary	43
3	Di-Higgs production and Higgs self couplings	44
3.1	NLO cross sections	44
3.1.1	SM Calculation	44
3.1.2	Di-Higgs production in the non-linear EFT with full m_t -dependence at NLO QCD . .	45
3.2	Double Higgs measurements and trilinear coupling	51

3.2.1	Measurements with the ATLAS experiment	51
3.2.2	Measurements with the CMS experiment	52
3.3	New ideas	54
3.3.1	Prospects for $hh \rightarrow (b\bar{b})(WW^*) \rightarrow (b\bar{b})(\ell^+\ell^-\nu_\ell\bar{\nu}_\ell)$	54
3.3.2	Prospects for $bb\gamma\gamma$: Bayesian optimization and BDT	57
3.4	HE prospects	61
3.4.1	Theory studies	61
3.4.2	ATLAS studies	68
3.5	Indirect probes	69
3.5.1	Indirect probes of the trilinear coupling through differential distributions measurements	69
3.5.2	Indirect probes through single Higgs boson production	69
3.5.3	Global fit	72
3.6	Implications	74
3.6.1	Implications for flavor models	74
3.6.2	Implications for theories of electroweak phase transition	77
4	High Energy Probes	78
4.1	$t\bar{t}$ differential measurements	78
4.2	WH/ZH at high energy/luminosity	78
4.3	Electroweak Precision Tests in High-Energy Diboson Processes	81
4.4	Novel measurements of anomalous triple gauge couplings for the HE and HL-LHC	86
4.4.1	Introduction	86
4.4.2	Solutions	88
4.4.3	Results	89
4.4.4	Higgs pair production in vector-boson fusion at the HL-LHC	90
4.5	Same-sign WW scattering at HL-LHC: a new strategy for the EFT-based analysis	94
4.6	Testing the universal Higgs nonlinearity	96
4.7	Same-sign WW scattering: A comparison of the HL- and HE-LHC reach for the selected Dim8 operators within the EFT approach	96
4.8	Dimension-6 EFT effects on Vector Boson Scattering at high energies	97
5	Higgs boson mass and width	100
5.1	Theory review	100
5.2	Measurement of the Higgs boson mass	104
5.3	Direct constraints from the Higgs boson lineshape	104
5.4	Direct constraints from the Higgs boson lifetime measurements	104
5.5	Width from the diphoton interference rate	104
5.6	Mass shift from the diphoton interference: constraints on the width	107
5.7	Width from Off-Shell higgs boson couplings	107

1 Introduction

Check

The main repository of the report material is Overleaf. If you are not registered with Overleaf as yet, you can do so. Use your cern.ch mail account, as this will give you, for free, the Professional license. This is needed if you want to access the full functionality, including the ability to grant editing rights to many people.

You can create the project for your section by just cloning this project. It's important that you do it using your professional Overleaf account (namely with your cern.ch email credentials), since the project inherits the functionalities available to its owner. After creating the project, make sure you set the proper administration rights, listing people who will have editing rights. You can do this clicking on the "share" button on top of the overleaf project page. You are given various options, such as making the project read/write accessible to anyone who has the url, or just readable to anyone who has a (different) url, or restricted to users selected in a list. The same button gives you the git repository url, to download the project locally. Notice that those you give rights to cannot further assign rights to others. Only the owner of the project can grant access rights. Of course section editors can clone a new version of the whole chapter, leave alone the other sections to focus on their own, and grant access to it to their co-editors. At the end they just put things back into the master project. I understood that it should be possible to grant rights to a CERN e-group, but I am not sure this is working already, I'm waiting for confirmation.

You can work directly on the Overleaf version, or you can download the whole package locally from the git repository. You can then use the standard git tools to commit updated versions. Working locally is almost essential at the beginning of the project, when you want to create a complete subfolder structure to contain the various sections of your report. Some scripts are available (see below) to facilitate this task.

This document can be compiled in its entirety, using the

```
> pdflatex report
```

command from the main directory. In alternative, you can compile individual sections, with the command

```
> pdflatex section
```

issued from the section subdirectory. This will generate the complete section, including its bibliography. I am not sure this is possible when working directly on the web with Overleaf. But this works in your local version, if you input the pdflatex commands yourself.

For this to work, you must preserve the template structure of the section.tex file in the directory of each section. You should also make sure that all style files contained in the main directory are present in the section directories. The simplest way to create a new section is to issue the command

```
> make newsection newfolder=new_folder_name
```

from the main directory. Here new_folder_name is the name of the directory you want to create to host the new section. A template section file will be created there, together with the img and bib directories (for figures and for the section.bib file, resp). All necessary style files are copied over. Now you just need to input the new_folder_name/section.tex file into the main driver file, report.tex, with the syntax:

```
\newpage
\subfile{\main/newdirectory/section}
```

When editing the new section.tex file, please pay attention to the header of the template. There are a few weird commands, and an apparently odd \begin{document} statement. These are required to be able to compile the section as a stand alone object. To this end, it is important that the command \providecommand{\main}{...} points \main to the directory containing the main driver file, report.tex. The file paths to figures (Fig. 1) must all include this absolute reference, as in

```
\includegraphics[width=0.45\textwidth]{\main/section1/img/hgg.pdf} .
```

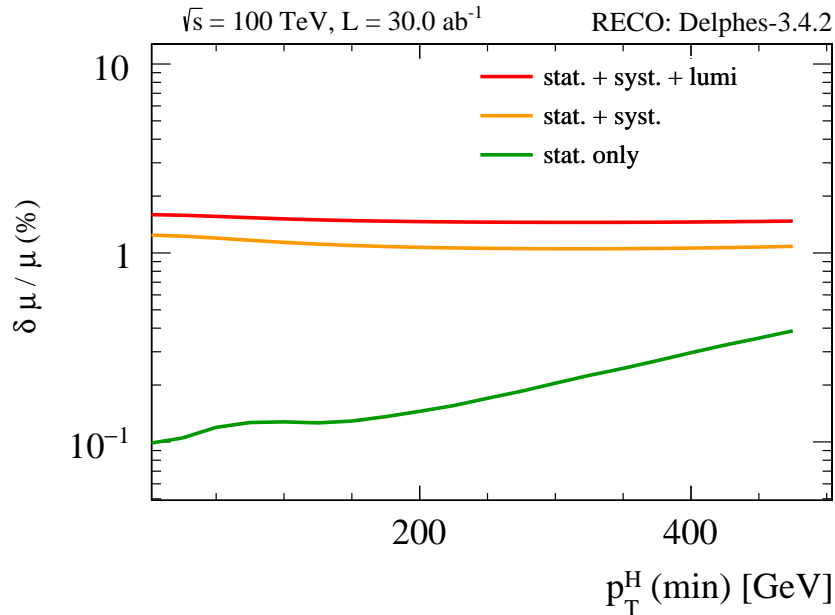


Fig. 1: Caption of the figure.

As for tables, please use the standard tabular environment, with the caption on top of the table. For cross referencing, try use labels such as `\label{eq: eqname}`, `\label{tab: tablename}` and `\label{fig: figname}`.

If you need subsections, you can include them here directly, or input them as files, which can live in their own subdirectory. If including a subsection from a file, import them with the command

```
\subfile{\main/section1/sub1/mysubsec}
```

where `mysubsec.tex` would start of course with the statement `\begin{subsection}`. In this case, make sure you define properly the path to figures and other files. This is crucial to guarantee compatibility of compilation of the whole Chapter and or the individual section. The fact that a Section compiles doesn't imply that the Chapter will compile, if paths are entered inaccurately. At this time I have not foreseen the ability to compile subsections standalone, I hope it is not necessary.

1.1 Bibliography

Keep each Section totally selfcontained, with its own folder(s) for figures, and its own file for bibliography [1]. Use bibtex format. Please get the bibtex from Inspire, other sources may generate conflicts with the bibliography style file. For internal notes of the LHC experiments, get the bibtex input from CDS (the CERN Document Service). Each section must have its own bib files. These are called `section.bib`, and should stay in the folder `\main/mysection/bib/section.bib`. When you create a new section, add the bib file to the string

```
\def\bibfiles{\main/bib/chapter,\main/section1/bib/section,\main/section2/bib/section}
```

that is included in the main driver, `report.tex`.

2 Higgs boson precision measurements

2.1 Introduction

To be written by: S. Alioli, M. Duehrssen, P. Milenovic

The large number of events expected in almost all Higgs boson measurement channels for the HL-LHC and HE-LHC will allow very precise measurements of Higgs boson cross section and coupling properties. In many channels, the expected overall statistical, experimental and theoretical uncertainties will be similar in size. Therefore, a close interaction between the experimental and theory communities will be needed in order to reach the best measurements.

Section 2.2 provides an overview of theoretical predictions for Higgs boson production at 14 and 27 TeV and of the uncertainties that are expected to be reached by the time of the final HL-LHC and HE-LHC measurements. These prediction are used as input to the studies of the sensitivity of ATLAS and CMS Higgs boson cross section and coupling measurements in individual channels that are summarized in Section 2.3 and for the expectations for differential cross section measurements presented in Section 2.4. Section 2.5 puts emphasis on all measurements related to the top Yukawa coupling, as this is the largest Yukawa couplings in the Standard Model with a value close to unity and hence of special interest in understanding the Higgs mechanism and its relation to fermions (TO EDIT: shall we expand this argument?). The combination of the expected measurements in ATLAS and CMS are presented in Section 2.6 together with an interpretation in the kappa-model [2, 3].

2.2 Theoretical predictions for the Higgs boson production at 14 and 27 TeV

To be written by: F. Caola, J. Campbell et al.

2.2.1 PDF uncertainty expectations at the HE/HL-LHC

Rabah Abdul Khalek, Shaun Bailey, Jun Gao, Lucian Harland-Lang, and Juan Rojo

PDFs in the HL-LHC era. The detailed understanding of the quark and gluon structure of the proton, quantified by the parton distribution functions (PDFs) [4–6], is an essential ingredient for the theoretical predictions at hadron colliders. PDF uncertainties represent one of the dominant theoretical systematic errors both for direct searches of new physics beyond the Standard Model (bSM) [7] as well as in the profiling of the Higgs boson sector [8]. Therefore, improving our knowledge of the proton structure is an essential task for the high-precision physics program to be carried out at future runs of the LHC, including the HL-LHC era.

Modern global PDF fits [9–12] include a wide range of LHC measurements in processes such as the production of jets, weak gauge bosons, and top quark pairs, among others. Recent breakthroughs in the calculation of NNLO QCD and NLO QED and electroweak corrections to most PDF-sensitive processes have been instrumental in allowing for the full exploitation of the information provided by the LHC measurements. The impact of high-precision LHC data combined with state-of-the art perturbative calculations has been quantified for many of the processes of interest, such as top-quark pair production [13, 14], the transverse momentum spectrum of Z bosons [15], direct photon production [?, 16], D meson production in the forward region [17–19], W production in association with charm quarks [?, 20, 21], and inclusive jet production [22, 23].

From the point of view of PDF determinations, the availability of the immense data samples at the HL-LHC will permit a significant extension of the kinematic coverage of PDF-sensitive measurements as well as a marked improvement in their statistical and systematic uncertainties. In this contribution, we summarise the main results of our PDF projections for the HL-LHC era presented in [24]. The main idea is to quantify the impact of the future HL-LHC measurements on the proton PDFs and their uncertainties,

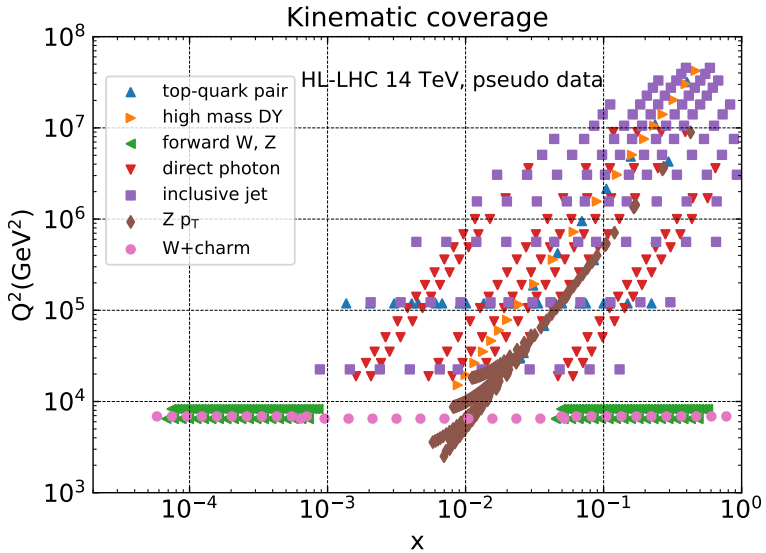


Fig. 2: The kinematical coverage in the (x, Q^2) plane of the HL–LHC pseudo-data.

with emphasis on their implications for Higgs physics. Specifically, we quantify the constraints of the HL–LHC pseudo-data on the PDF4LHC15 set [25–28] by means of the Hessian Profiling method [29] (see also [30]). We choose the PDF4LHC15 set since it broadly represents the state-of-the-art understanding of the proton structure.

In Fig. 2 we show the kinematical coverage in the (x, Q^2) plane of the HL–LHC pseudo-data included in this analysis. As indicated there, we have simulated pseudo-data for the following processes: top quark pair production, high-mass and forward Drell-Yan W, Z production, direct photon and inclusive jet production, the transverse momentum of Z bosons, and the production of W bosons in association with charm quarks. The HL–LHC pseudo-data therefore spans a wide region in the kinematic plane, namely $6 \times 10^{-5} < x < 0.7$ and $40 \text{ GeV} < Q < 7 \text{ TeV}$. In particular, one sees that the HL–LHC coverage of the large- x region, where current PDF fits exhibit large uncertainties, is markedly improved as compared to available LHC measurements.

Results. As an illustration of the impact of individual sets of HL–LHC pseudo-data, in Fig. 3 we show the comparison between the HL–LHC projected measurements and the theoretical predictions for the lepton rapidity distribution in forward $W + \text{charm}$ production and for the invariant mass $m_{t\bar{t}}$ distribution in top-quark pair production. These two particular datasets probe the poorly-known strange quark and the gluon at large- x , respectively. The theory calculations are shown both before (PDF4LHC15) and after profiling. In the bottom panel, we show the same results normalised to the central value of the original theory calculation. In both cases we see that the expected precision of the HL–LHC measurements is rather higher than the current PDF uncertainties, and therefore we observe a marked improvement once they are included in PDF4LHC15 via the Hessian profiling.

In this study we have considered three different scenarios for the experimental systematic uncertainties of the HL–LHC pseudo-data. These scenarios, ranging from more conservative to more optimistic, differ among them in the reduction factor applied to the systematic errors of the reference 8 TeV or 13 TeV measurements, see [24] for more details. In particular, in the optimistic scenario we assume a reduction of the systematic errors by a factor 2.5 (5) as compared to the reference 8 TeV (13 TeV) measurements, while for the conservative scenario we assume no reduction in systematic errors with respect to the 8 TeV reference. Reassuringly, we obtain that the main results of our study depend only mildly in the specific assumption for the values of this reduction factor.

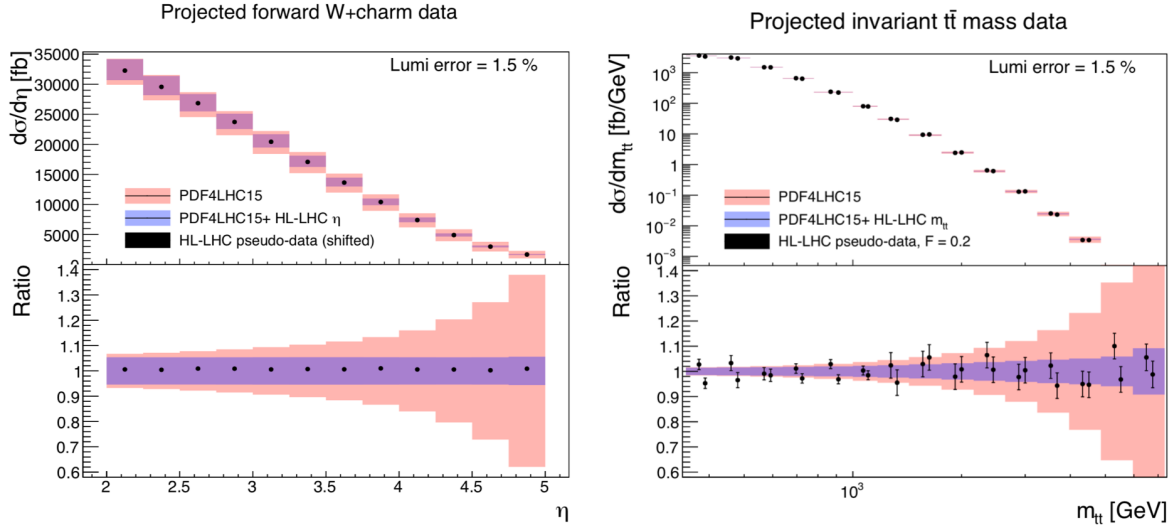


Fig. 3: Comparison between the HL–LHC pseudo-data and the theoretical predictions for forward W +charm production (left) and for the invariant mass $m_{t\bar{t}}$ distribution in top-quark pair production (right). The theory calculations are shown both before (PDF4LHC15) and after profiling.

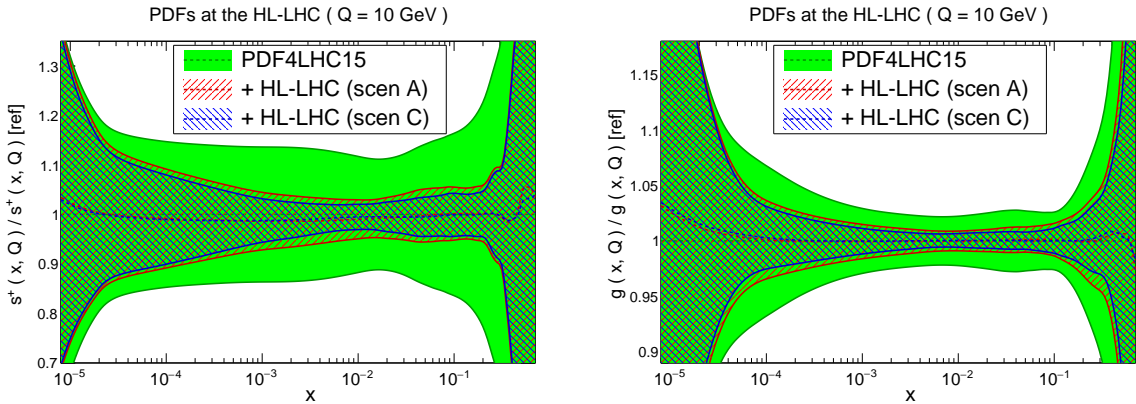


Fig. 4: Comparison of the PDF4LHC15 set with the profiled sets with HL–LHC pseudo-data. We show the strange (left) and gluon (right) PDFs normalized to the central value of the baseline.

In Fig. 4 we compare the PDF4LHC15 set with the strange quark and gluon PDFs obtained once the entire set of HL-LHC pseudo-data summarised in Fig. 2 has been included via profiling. We show results both in the conservative (A) and optimistic (C) scenarios for the projections of the experimental systematic uncertainties. We observe that the impact of the HL–LHC pseudo-data is reasonably similar in both scenarios. This is due to the fact that we have chosen those processes which will benefit from a significant improvement in statistics, independent of the specific assumption about the systematic errors. These then tend to lie in kinematic regions where the PDFs themselves are generally less well determined. We also observe a marked reduction of the PDF uncertainties in all cases. In the case of the gluon PDF, there is an improvement of uncertainties in the complete relevant range of momentum fraction x . This is a direct consequence of the fact that we have included several HL–LHC processes that have direct sensitivity to the gluon content of the proton, including jet, direct photon, and top quark pair production, as well as the transverse momentum of Z bosons. As we discuss next, this has direct implications for the phenomenology of Higgs boson production.

Ratio to baseline	$10 \text{ GeV} \leq M_X \leq 40 \text{ GeV}$	$40 \text{ GeV} \leq M_X \leq 1 \text{ TeV}$	$1 \text{ TeV} \leq M_X \leq 6 \text{ TeV}$
gluon-gluon	0.50 (0.60)	0.28 (0.40)	0.22 (0.34)
quark-quark	0.74 (0.79)	0.37 (0.46)	0.43 (0.59)
quark-antiquark	0.71 (0.76)	0.31 (0.40)	0.50 (0.60)

Table 1: The reduction of the PDF uncertainties as compared to the PDF4LHC15 baseline for different initial partonic combinations in the optimistic (conservative) scenario.

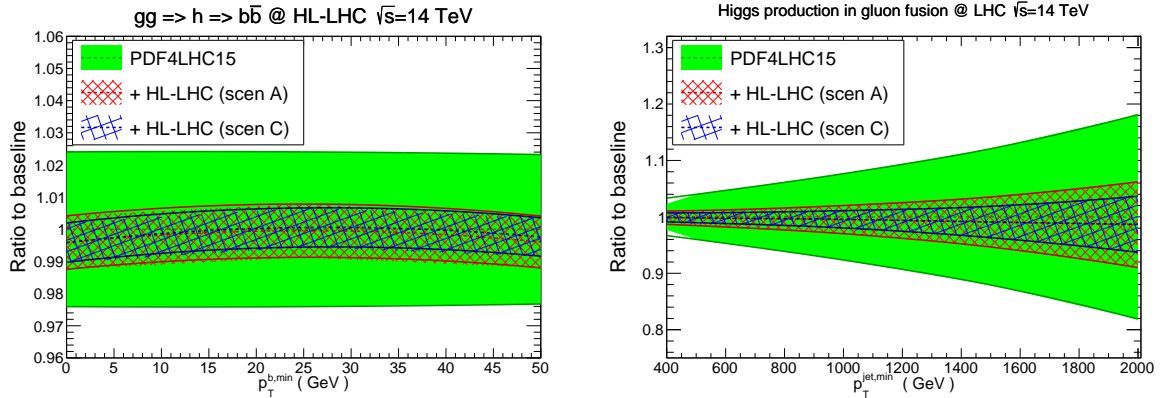


Fig. 5: Comparison of the predictions for SM Higgs production cross-sections at $\sqrt{s} = 14 \text{ TeV}$ between the PDF4LHC15 baseline and the profiled PDF sets with HL-LHC pseudo-data.

Implications for Higgs physics. In Table 1 we indicate the reduction of the PDF uncertainties in comparison to the PDF4LHC15 baseline for different initial partonic combinations (that is, a value of 1 corresponds to no improvement). Results are presented for three different bins of the invariant mass M_X of the produced system for the three initial states relevant for Higgs production: gluon-gluon (for $gg \rightarrow h$ and $t\bar{t}h$), quark-quark (for vector boson fusion) and quark-antiquark (for associated Wh and Zh production). The values shown outside (inside) the brackets correspond to the optimistic (conservative) scenario. We can see that for the M_X region relevant for the SM Higgs boson production, as well as for related bSM Higgs-like scalars, namely $40 \text{ GeV} \leq M_X \leq 1 \text{ TeV}$, the HL-LHC pseudo-data leads to a reduction by almost a factor four in the optimistic scenario in the gg channel, and around a factor three in the $q\bar{q}$ and qq channels. This implies that precision calculations of Higgs production at the HL-LHC should be possible with significantly reduced PDF uncertainties compared to current state-of-the-art predictions.

To illustrate this improvement, in Fig. 5 we present the comparison of the predictions for SM Higgs production at $\sqrt{s} = 14 \text{ TeV}$ between the PDF4LHC15 baseline and the profiled PDF sets. Specifically, we show Higgs boson production in gluon fusion with heavy top quark effective theory, both inclusive and decaying into $b\bar{b}$ as a function of $p_T^{b,\min}$ (left), and then in association with a hard jet as a function of its transverse momentum $p_T^{\text{jet},\min}$ (right). The calculations have been performed using MCFM8.2 with leading-order matrix elements. The marked reduction of PDF uncertainties is consistent with the values reported in Table 1.

Finally, there are two caveats to be added concerning this study. First we have only considered a subset of all possible measurements of relevance for PDF fits at HL-LHC. Second, possible data

incompatibility has not been accounted for fully. These may strengthen and weaken, respectively, the constraining powers of future LHC data on PDFs.

The results of this study are made publicly available in the LHAPDF6 format [31], for the three scenarios that have been considered, and can be downloaded from:

https://data.nnpdf.science/HLLHC_YR/PDF4LHC15_nnlo_hllhc_scen1.tgz
https://data.nnpdf.science/HLLHC_YR/PDF4LHC15_nnlo_hllhc_scen2.tgz
https://data.nnpdf.science/HLLHC_YR/PDF4LHC15_nnlo_hllhc_scen3.tgz

2.2.2 Progress on Higgs boson specific MC generators

To be written by: Simone Alioli, Stefan Höche, Fabio Maltoni and Stefan Prestel

Here goes the text

Monte Carlo's for Higgs Physics.

High-Lumi and High-energy

General purpose Monte Carlo's Total and differential cross section calculators Dedicated MC's

What are the improvements that are foreseen in the coming years that could change the field.
Where the most of the results can be expected? For what? NNLO+PS?

Collecting references for MINLO, Sherpa so that people can find where to look.

Table?

Instead of showing an actual plot, we show a mock-plot where the various features which are most important are summarized.

What can we say it would be needed and in the ball park of the feasible stuff. Examples for main channels.

- approx rapidity at N3LO for gluon-fusion
- N3LO VBF is available inclusive => exclusive?
- NNLO+NLL as the next revolution for ggH, VH, VBF,...
- top / bottom mass effects

Organise it in terms of methods and developments and then physics channels.

Fabio: Simone: StefanP: StefanH:

2.3 Overview of experimental analysis for the Higgs boson measurement channels

To be written by: M. Delmastro, P. Francavilla, A. de Wit

2.3.1 Extrapolation assumptions

The results presented in this Section are based on the extrapolation to an expected integrated luminosity of 3000 fb^{-1} at $\sqrt{s} = 14 \text{ TeV}$ of the corresponding ATLAS and CMS Run-2 results. For some of the Higgs decay final states (ATLAS: WW^* , $Z\gamma$, $t\bar{t}H$, $\tau\tau$; CMS: ...) the extrapolation is performed on results obtained with the 2015-2016 36 fb^{-1} datasets; the remaining final state analyses (ATLAS: $\gamma\gamma$, ZZ^* , $b\bar{b}$ and $\mu\mu$; CMS: ...) use the results based on the 2015+2016+2017 80 fb^{-1} data samples. The starting points of the extrapolated results are measurements based on datasets of size $\mathcal{O}(1\%)$ of the expected HL-LHC integrated luminosity. The extrapolations are in this respect very limited with respect to the potential reach of the real HL-LHC analyses, which large statistics will allow to probe corners of the phase space inaccessible at the LHC Run-2.

In addition to the increase in integrated luminosity, the extrapolations account for the increase of signal and background cross-sections from $\sqrt{s} = 13$ TeV to 14 TeV. The signal yields have been scaled according to the Higgs boson production cross sections values at 13 and 14 TeV, as reported in Ref. [8]. The background yields have been scaled according to the parton luminosity ratio between 13 and 14 TeV, as reported in Ref. [3], by taking into account whether the background process is predominantly quark pair or gluon pair initiated.

Object reconstruction efficiencies, resolutions and fake rates are assumed to be similar in the Run-2 and HL-LHC environments, based on the assumption that ATLAS and CMS upgraded detectors will compensate for the at HL-LHC higher pile-up environment. For the systematic uncertainties which include experimental, signal and background components, two scenarios have been considered. The first scenario (S1) assumes the same values as those used in the published Run-2 analyses. The second scenario (S2) implements a reduction of the systematic uncertainties according to the improvements expected to be reached at the end of HL-LHC program in twenty years from now: the correction factors follow the recommendations from Ref. [32]. Some systematics uncertainties are specifically treated in the individual analysis, and will be discussed in each dedicated section. In all analyses, the theory uncertainties for signal and background are generally halved, except where more precise extrapolated values have been provided. The uncertainty on the luminosity is set to 1%. The uncertainty related to Monte Carlo samples statistics is assumed to be negligible.

The extrapolated results are generally limited by systematic uncertainties. It is worth noting that, despite all efforts to design proper projections, the values of the systematic uncertainties of the Run-2 analyses cannot fully account for the HL-LHC conditions and process understanding. In this sense, they are to be considered an approximation. Future analyses will exploit and gain sensitivity from phase space regions that are not accessible yet, or use analysis techniques that reduce the impact of systematic uncertainties.

In the following, all analyses segment the selected events according to the objects campaigning the main Higgs decay products and their topology, in order to maximize the sensitivity to the main Higgs production modes ($ggH + b\bar{b}H$, VBF, $VH = qqZH + ggZH + WH$ and top = $t\bar{t}H + tH$) and to reduce the uncertainties on the respective cross sections. Details on how this segmentation is performed, and on the event selection and categorisation in the various analyses, are found in the Run-2 analysis references quoted in each section. $H \rightarrow WW^* \rightarrow e\nu\mu\nu$

2.3.2 $H \rightarrow \gamma\gamma$

The measurement of the Higgs boson properties in the $H \rightarrow \gamma\gamma$ channel is extrapolated from the most recent measurements by ATLAS with 80 fb^{-1} [33] and CMS with $XX\text{ fb}^{-1}$ [34]. Events are selected to contain two isolated photon candidates passing good quality requirements in the precision regions of the detectors. The Higgs production cross sections are measured for a Higgs boson absolute rapidity $|y_H|$ smaller than 2.5, and with further requirements on the objects campaigning the diphoton system (e.g. jet p_T). The $H \rightarrow \gamma\gamma$ signal is extracted by means of a combined signal-plus-background fit of the diphoton invariant mass spectra in the various event categories, where both the continuous background and the signal resonance are parameterized by analytical functions. The shape properties of the signal PDF are obtained by MC simulation, and constrained by performance studies of the photon energy scale and resolution. The background PDF is completely determined by the fit on data, with systematic uncertainties attributed to the specific choice of functional form following the procedure described in Ref. [34] or using the discrete profiling method [35].

The main systematic uncertainties affecting the results are the background modelling uncertainty, QCD scale uncertainties causing event migrations between the bins, photon isolation efficiencies and jet uncertainties. On top of the common assumptions mentioned in Section 2.3.1, the ATLAS $H \rightarrow \gamma\gamma$ results include a 10% increase of the background modeling systematic uncertainties, to account for the potentially worst knowledge of the background composition in each analysis category at HL-LHC: this

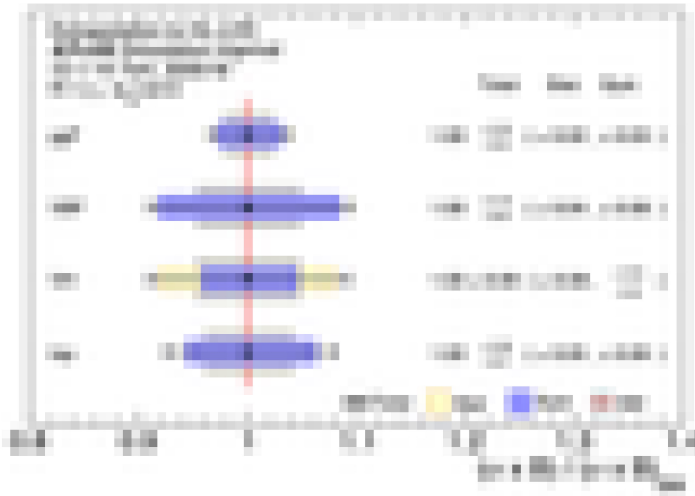


Fig. 6: Ratio of the cross-section times branching fraction measurements of the main four Higgs production modes in the $H \rightarrow \gamma\gamma$ decay channel to their respective theoretical SM predictions, as extrapolated at the HL-LHC for scenario S2 by ATLAS.

assumption has anyway negligible impact. In the Run-2 analyses, a conservative 100% uncertainty on the heavy flavour resonant background in top-sensitive categories is applied. Measurements by ATLAS and CMS of the heavy flavour content, or the b -jet multiplicity, are expected to better constrain these contributions: for the S2 scenario extrapolation, this uncertainty is therefore halved.

Figure 6 show the ratio of the extrapolated $H \rightarrow \gamma\gamma$ ATLAS measurements of the main four Higgs production modes to their respective theoretical SM predictions in the scenario S2. The reduction of the total uncertainty with respect to the 80 fb^{-1} results ranges from a factor of about 2(3) for the S1 (S2) scenario for the $ggH + b\bar{b}H$, VBF, top cross sections, to a factor of about 5(6) for the VH cross section.

2.3.3 $H \rightarrow Z\gamma \rightarrow 2\ell\gamma$

Due to the small branching fraction in the SM, the $H \rightarrow Z\gamma$ decay has not yet been observed at the LHC. The experimental observed limits at the 95% confidence level are currently 6.6 times the SM prediction for a Higgs boson mass of 125.09 GeV by ATLAS, based on the analysis of 36.1 fb^{-1} of pp collision at $\sqrt{s} = 13 \text{ TeV}$ [?], and XX times the SM prediction by CMS, based on ... []].

The analyses select event with an isolated photon candidate passing good quality requirements in the precision regions of the detectors, and a dilepton system with properties compatible with that of the decay of a Z boson. Events are separated according to lepton flavour, the event kinematical properties, and the present of jets compatible with the VBF production of the Higgs boson, in order to maximize the signal sensitivity. The signal is sought for by means of a combined signal-plus-background fit of the photon-dilepton invariant mass spectra in various event categories, where both the continuous background and the signal resonance are parameterized by analytical functions. The Run-2 analyses are strongly driven by statistical uncertainty, and the main systematic uncertainties are from the bias associated to the background modeling.

The extrapolations to HL-LHC are performed with a simple scaling approach, assuming the same signal and background modeling used in the Run-2 analyses. All experimental and systematic uncertainties are considered to remain the same, except the uncertainty associated to the background modeling, which is taken to be negligible.

The ATLAS expected significance to the SM Higgs boson decaying in $Z\gamma$ is 4.9σ with 3000 fb^{-1} . Assuming the SM Higgs production cross section and decay branching ratios, the signal strength is

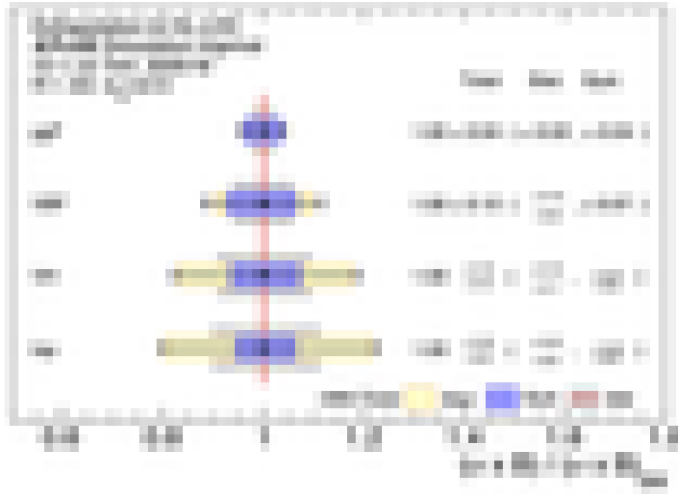


Fig. 7: Ratio of the cross-section times branching fraction measurements of the main four Higgs production modes in the $H \rightarrow ZZ^* \rightarrow 4\ell$ decay channel to their respective theoretical SM predictions, as extrapolated at the HL-LHC for scenario S2 by ATLAS.

expected to be measured with a ± 0.24 uncertainty. The cross section times branching ratio for the $pp \rightarrow H \rightarrow Z\gamma$ process is projected to be measured as 1.00 ± 0.23 times the SM prediction. Even at the HL-LHC scenario S1, the analysis sensitivity to $H \rightarrow Z\gamma$ will remain driven by the statistical uncertainty. The dominant source of systematic uncertainty in the extrapolation is that associated to the QCD scale variations.

2.3.4 $H \rightarrow ZZ^* \rightarrow 4\ell$

The measurement of the Higgs boson properties in the $H \rightarrow ZZ^* \rightarrow 4\ell$ is extrapolated from the most recent measurements by ATLAS with 80 fb^{-1} [36] and CMS with $XX\text{ fb}^{-1}$ [4]. Events are selected to contain at least two same-flavour opposite-sign dilepton pairs, chosen from isolated electrons and muons candidates passing good quality requirements in the precision regions of the detectors. Additional constraints on the kinematical properties of the pair associated with the decay the on-shell Z boson, and on the global topology of the event, helps to improve the signal to background ratio. The four-lepton invariant mass resolution is improved by correcting for the emission of final-state radiation photons by the leptons. The $H \rightarrow ZZ^* \rightarrow 4\ell$ signal is extracted from the four-lepton invariant mass spectra in the different event categories, after having evaluated the background components using simulation to constrain their shapes, and data control region to extrapolate their normalization in the signal regions.

The dominant systematic uncertainties affecting the extrapolation of the ggH cross section measurement are the lepton reconstruction and identification efficiencies and pile-up modeling uncertainties. The VBF and VH cross-sections are primarily affected by the uncertainty on the jet energy scale and resolution, and by the QCD scale uncertainties. The theory uncertainties related to QCD scale and parton shower modeling primarily affects the extrapolated top cross section.

The VBF, VH and top measurements in the $\tilde{\chi}_1^0$ decay channel remain largely dominated by statistical uncertainty when extrapolated to 3000 fb^{-1} while the $ggH + b\bar{b}H$ cross section is dominated by systematic uncertainties both in scenario S1 and S2. Figure 7 show the ratio of the extrapolated $H \rightarrow ZZ^* \rightarrow 4\ell$ ATLAS measurements of the main four Higgs production modes to their respective theoretical SM predictions in the scenario S2. The $H \rightarrow ZZ^* \rightarrow 4\ell$ HL-LHC measurements are expected to reach a level of precision comparable to the projected uncertainty on the corresponding theory predictions.

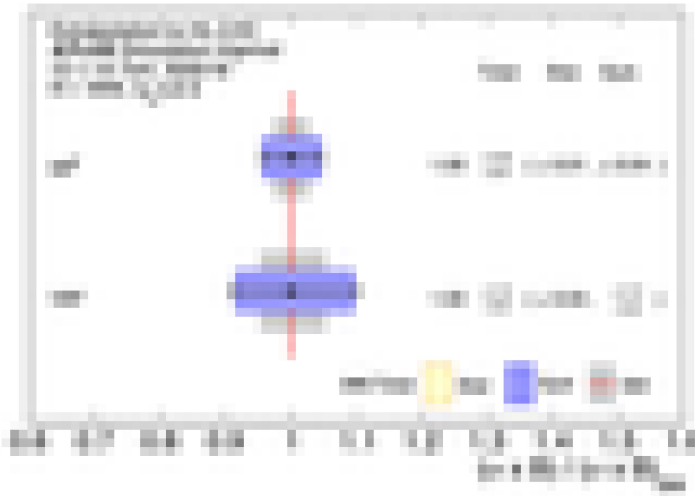


Fig. 8: Ratio of the cross-section times branching fraction measurements of the main four Higgs production modes in the $H \rightarrow WW^* \rightarrow e\nu\mu\nu$ decay channel to their respective theoretical SM predictions, as extrapolated at the HL-LHC for scenario S2 by ATLAS.

2.3.5 $H \rightarrow WW^* \rightarrow \ell\nu \ell\nu$

The measurement of the Higgs boson properties in the $H \rightarrow ZZ^* \rightarrow 4\ell$ is extrapolated from the most recent measurements by ATLAS in the $H \rightarrow WW^* \rightarrow e\nu\mu\nu$ channel using 80 fb^{-1} [37], and by CMS in the XX channel using $XX \text{ fb}^{-1}$ [38]. Events are selected to contain two opposite-charged isolated leptons passing good quality requirements in the precision region of the detectors and missing transverse momentum. Additional requirements on the event kinematical properties (e.g. on the dilepton transverse mass and invariant mass, on the azimuthal separation between the leptons) are applied to reduce the various background components. Events are categories as a function of the jet multiplicity, in order to extract the Higgs ggH and VBF production cross sections. The normalization of (non-resonant) WW , top ($t\bar{t}$ and Wt), and $Z \rightarrow \tau\tau$ backgrounds is set using dedicated control regions of the same jet multiplicity as the signal category to which the normalization is transferred.

The measurements are completely dominated by systematic uncertainties, and their extrapolation to the S2 scenario shows the expected reduction by a factor two. The measurement of the ggH cross section by branching fraction is dominated by theoretical PDF uncertainty, followed by experimental uncertainties affecting the signal acceptance, including uncertainties on the jet energy scale and flavour compositing, and lepton misidentification; the VBF result suffers of similar dominant uncertainties. Figure 8 shows the ratio of the extrapolated $H \rightarrow WW^* \rightarrow e\nu\mu\nu$ ATLAS measurements of the main four Higgs production modes to their respective theoretical SM predictions in scenario S2.

2.3.6 $H \rightarrow \tau\tau$

To be written by: P. Francavilla, ?

The studies presented here are performed based on a previous analysis, in which the ATLAS Collaboration analyzed the 2015/2016 proton-proton collision dataset collected at $\sqrt{s} = 13 \text{ TeV}$, which corresponds to an integrated luminosity of 36.1 fb^{-1} [39]. For the Higgs boson decay products all the leptonic (τ_{lep}) and hadronic (τ_{had}) decays of the τ 's are considered. The analysis is done by splitting events into three categories depending on the three tau final states of the decay products: (τ_{lep}, τ_{lep}) , (τ_{lep}, τ_{had}) and (τ_{had}, τ_{had}) .

2.3.7 $H \rightarrow bb$

To be written by: P. Francavilla, A. de Wit

TODO: Text currently reflects CMS studies only. Should be updated to reflect ATLAS and CMS studies. Differences for ATLAS: -> the analysis is the observation (78.9 fb⁻¹) -> tagger is named MVa, and we use a 70% WP -> mbb is improved with muon in jet correction and ptReco, + kinematic fit for 2 leptons -> add the mu for ATLAS -> Add the results from ATLAS

The ATLAS and CMS Collaborations have both reported the observation of the $H \rightarrow bb$ decay [38, 39]. The studies presented here are performed based on a previous analysis, in which the CMS Collaboration reported evidence for the $H \rightarrow bb$ decay in the VH production mode using the 2016 proton-proton collision dataset collected at $\sqrt{s} = 13$ TeV, which corresponds to an integrated luminosity of 35.9 fb^{-1} [40]. This analysis makes use of leptonic decays of the vector boson which is produced in association with the Higgs boson. The final states of the VH system covered in this analysis always contain two b-jets and either zero, one or two electrons or muons. Both leptons are required to have the same flavour in the two lepton selection. The b-jets are identified using a combined multivariate (CMVA) tagging algorithm. The inputs include track impact parameter and secondary vertex information from the jet. Three thresholds on the CMVA discriminant are used in the analysis, denoted tight, medium and loose, which have efficiencies for tagging b-jets ranging from 50–75% and for light quark or gluon jets from 0.15–3%.

Major backgrounds arising from SM production of vector boson plus heavy- or light-flavour jets, in addition to $t\bar{t}$ production, are controlled and constrained for each vector boson decay channel independently via dedicated control regions. Multivariate energy regression techniques are used to improve the b-jet energy resolution, and a boosted decision tree is used to improve the discrimination between signal and background. The distribution of this multivariate discriminator is used as the discriminating variable in the signal extraction fit. The signal strength observed in this analysis is $\mu_{VHbb} = 1.19^{+0.21}_{-0.20}\text{ (stat)}^{+0.34}_{-0.32}\text{ (syst)}$. Here the projected uncertainty on the signal strength up to 3000 fb^{-1} is reported, assuming $\mu_{VHbb} = 1$.

Figure 9 shows the uncertainty on μ_{VHbb} as a function of integrated luminosity, for scenario S1 (green points), scenario S2 (red points) and a scenario where all systematic uncertainties are ignored (blue points). In both scenarios S1 and S2 systematic uncertainties start to dominate very quickly, thus moving the projected uncertainty away from the statistical-only scaling curve.

Figure 10 shows the per-process and per-channel signal strength uncertainty, showing results for all three scenarios described above. The large improvement in the signal strength uncertainty for the 1-lepton channel, which is most sensitive to the WH production mode, is caused by the integrated luminosity scaling of an uncertainty in the modelling of the W boson p_T distribution. This uncertainty dominates this channel in scenario S1.

The contributions of different sources of uncertainty in scenarios S1 and S2 are shown in Table 2. Both in scenario S1 and S2 the largest component of the systematic uncertainty is theoretical. Moving from S1 to S2 the total signal theoretical uncertainty reduces to half its size. This is expected as in scenario S2 the input uncertainties are scaled down to half the current size. In the case of the background theory, where the input uncertainties are also scaled to half their original size when going from scenario S1 to scenario S2, the total uncertainty due to this component is not halved. This is because at 3000 fb^{-1} some of the theoretical uncertainties on the backgrounds can be constrained in the fit. The same is true for the experimental uncertainties, which in some cases are already moderately constrained in the current analysis.

Looking in more detail at the dominant signal theoretical uncertainties, the largest component in the uncertainty arises from the uncertainty in the gluon-induced ZH (ggZH) production cross section due to QCD scale variations. The ggZH process contributes a small fraction of the total ZH process. Despite this, the uncertainty in the production cross section for this process due to QCD scale variations

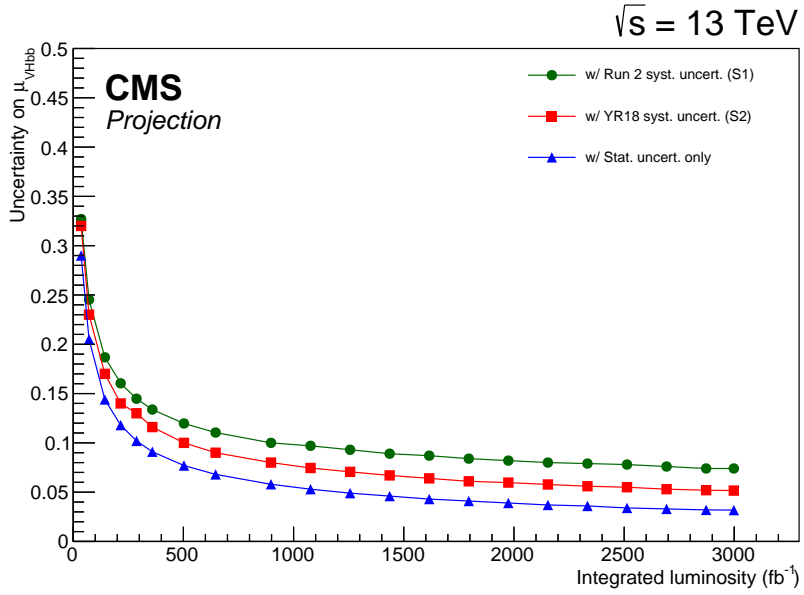


Fig. 9: Uncertainty on the signal strength μ_{VHbb} as a function of integrated luminosity for S1 (with Run 2 systematic uncertainties [40]) and S2 (with YR18 systematic uncertainties).

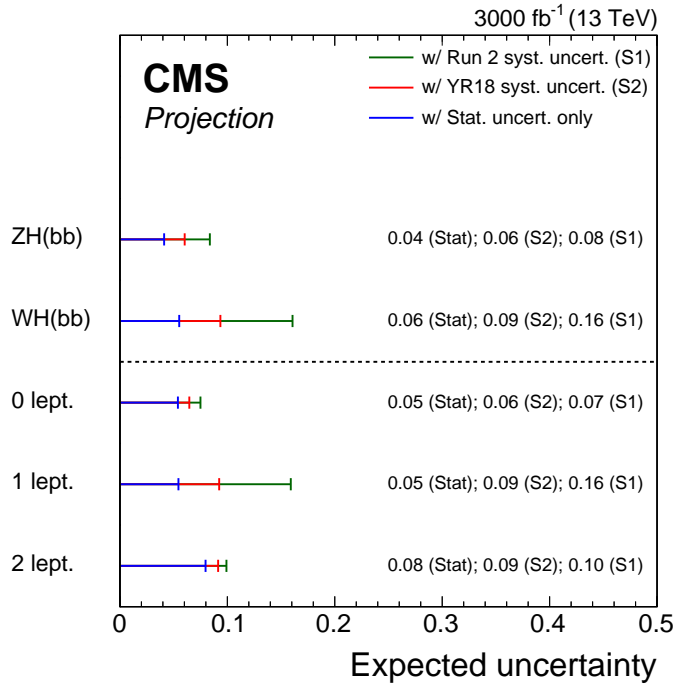


Fig. 10: Uncertainties in the per-process and per-channel signal strengths. Values are given for the S1 (with Run 2 systematic uncertainties [40]) and S2 (with YR18 systematic uncertainties) scenarios, as well as a scenario in which all systematic uncertainties are removed.

becomes dominant because it is very large: 25% for the ggZH process, compared to approximately 4% for the ZH process [8]. The next most important uncertainties are category-acceptance uncertainties in the dominant Z+bb and W+bb backgrounds due to QCD scale variations, as well as the uncertainty

in the ZH and WH production cross section due to QCD scale variations. In scenario S2 these four most important uncertainties contribute 1.6%, 1.5%, 1.3% and 1.2% (absolute) to the total uncertainty of 5.1%, respectively. To improve the precision of the measurement it is therefore important to improve these theoretical uncertainties.

Table 2: Contributions of particular groups of uncertainties in S1 (with Run 2 systematic uncertainties [40]) and S2 (with YR18 systematic uncertainties). The total uncertainty is decomposed into four components: signal theory, background theory, experimental and statistical. The signal theory uncertainty is further split into inclusive and acceptance parts, and the contributions of the b-tagging and JES/JER uncertainties to the experimental component are also given.

	S1	S2
Total uncertainty	0.073	0.051
Signal theory uncertainty	0.054	0.026
Inclusive	0.046	0.022
Acceptance	0.027	0.013
Background theory uncertainty	0.028	0.023
Experimental uncertainty	0.026	0.022
b-tagging	0.022	0.020
JES and JER	0.007	0.006
Statistical uncertainty	0.032	0.032

In the future, and at the HL-LHC in particular, the b-tagging efficiency may change. The conditions could worsen the efficiency, but at the same time new detectors and new techniques could also lead to an improvement in the b-tagging efficiency. The effect of changes in b-tagging efficiency on the overall signal strength uncertainty is evaluated. Changes in the b-tagging efficiency are emulated by scaling the rates of processes with a single b-tag by the change in b-tagging efficiency, and scaling the rates of processes with two b-tags by the change in b-tagging efficiency squared. The modifications are applied only to the efficiency to select genuine b-jets; the mistagging rates for light quark and gluon jets remain unchanged.

Figure 11 shows the results of the projection assuming various reductions and improvements in the b-tagging efficiency relative to the performance of the three CMVA working points used in the analysis. A 10% improvement in the b-tagging efficiency leads to a relative improvement in the signal strength uncertainty of up to 6%. The improvements on the signal strength precision are limited because the uncertainty is dominated by theoretical sources. When neglecting inclusive signal theory uncertainties this improvement becomes up to 8%. **TODO: Results at 300 fb⁻¹ will be removed from the plot.**

2.3.8 $H \rightarrow \mu\mu$

To be written by: P. Francavilla, ?

2.4 Fiducial and differential cross-section measurements

To be written by: M. Delmastro, T.Klijnsma

2.4.1 Measurements using $H \rightarrow \gamma\gamma$, $H \rightarrow ZZ^* \rightarrow 4\ell$, (boosted) $H \rightarrow b\bar{b}$ decay channels

Written by: T. Klijnsma

This section now closely follows FTR-18-011, and describes only CMS results.

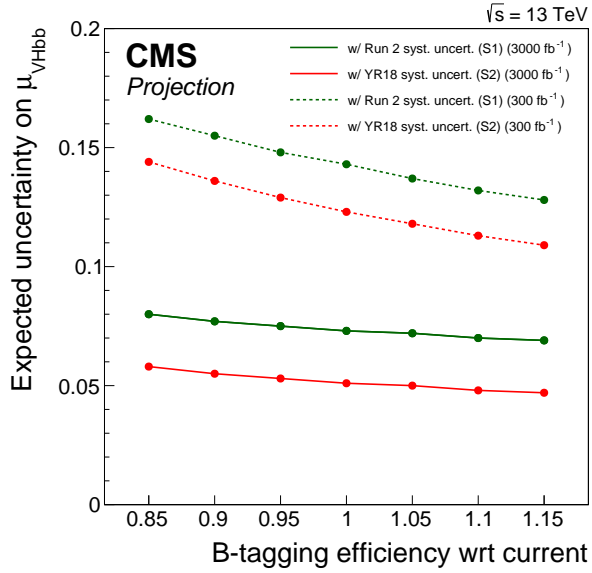


Fig. 11: Effect of varying the b-tagging efficiency on the uncertainty in the signal strength measurement when considering all systematic uncertainties.

In the context of Higgs boson property measurements, one of the main goals of HL-LHC, differential measurements provide a probe of various Higgs boson properties by looking at distortions of differential distributions. The p_T^H distribution is of particular interest, as potential new physics may reside in the tails of the distribution, which cannot be measured in inclusive measurements [41–43]. Differential Higgs boson production cross section measurements are available for a range of observables from both the ATLAS [44–49] and CMS [?, ?, 50–53] Collaborations at $\sqrt{s} = 8$ and 13 TeV. The most recent p_T^H spectra at $\sqrt{s} = 13$ TeV from both the ATLAS [49] and CMS [?] Collaborations are projected to an integrated luminosity of 3000 fb^{-1} . The projection of the p_T^H spectrum at 3000 fb^{-1} by the CMS Collaboration is shown in Fig. 12, for both S1 and S2. The corresponding relative uncertainties for both scenarios are given in Tables 3 and 4. With respect to the uncertainties at the current integrated luminosity of 35.9 fb^{-1} , the uncertainties at 3000 fb^{-1} in the higher p_T^H region are about a factor of ten smaller. This is expected, as the uncertainties in this region remain statistically dominated. The uncertainties in the lower p_T^H region are no longer statistically dominated however, as can be seen by comparing Table 3 with Table 4, where the reduced systematic uncertainties in S2 yield a reduction in the total uncertainty of up to 25% compared to S1.

p_T^H (GeV)	0-15	15-30	30-45	45-80	80-120	120-200	200-350	350-600	600- ∞
$H \rightarrow \gamma\gamma$	7.2%	6.8%	7.1%	6.9%	7.1%	6.7%	7.1%	9.9%	32.5%
$H \rightarrow ZZ$	6.2%	5.7%		5.0%		5.5%		9.6%	
$H \rightarrow bb$				<i>None</i>				38.2%	37.1%
Combination	4.7%	4.4%	5.0%	4.7%	4.8%	4.7%	5.2%	8.5%	25.4%

Table 3: Relative uncertainties on the projected p_T^H spectrum under S1 (with Run 2 systematic uncertainties [?]) at 3000 fb^{-1} .

2.4.2 Measurement of $p_T(H)$ spectrum in $t\bar{t}H$ production mode

To be written by: N. Wardle

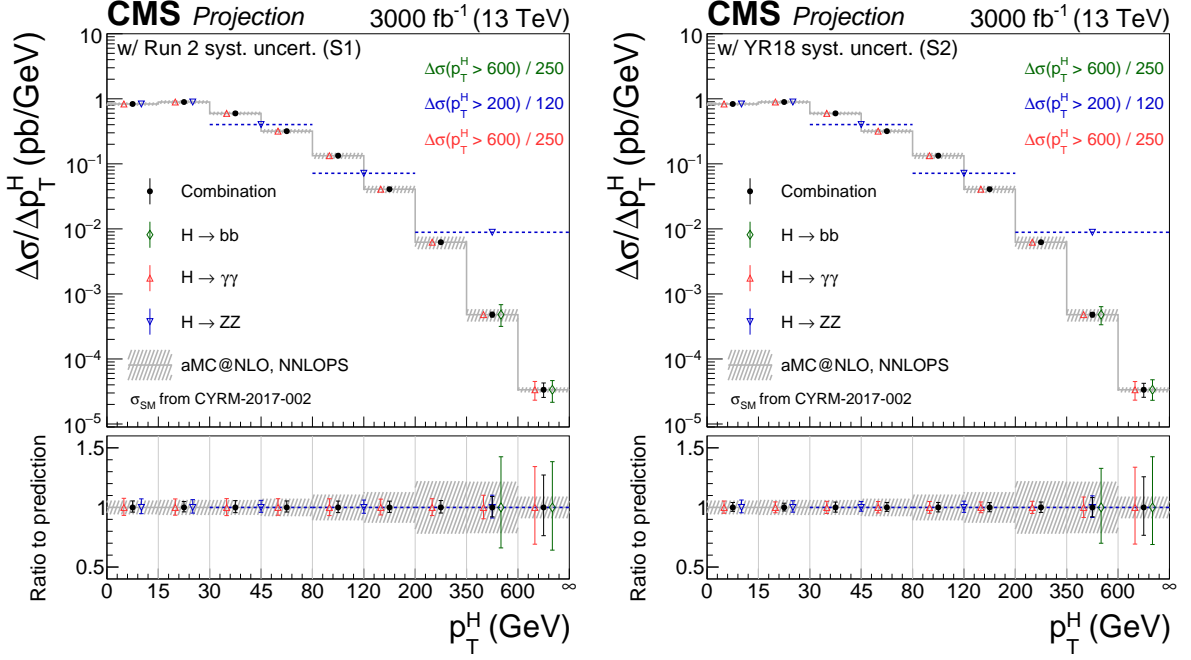


Fig. 12: Projected differential cross section for the p_T^H spectrum at an integrated luminosity of 3000 fb^{-1} , under S1 (upper, with Run 2 systematic uncertainties [?]) and S2 (lower, with YR18 systematic uncertainties).

p_T^H (GeV)	0-15	15-30	30-45	45-80	80-120	120-200	200-350	350-600	600- ∞
$H \rightarrow \gamma\gamma$	5.1%	4.6%	5.1%	4.8%	4.9%	4.5%	5.1%	8.6%	32.2%
$H \rightarrow ZZ$	5.4%	4.8%		4.1%		4.7%		9.1%	
$H \rightarrow bb$					<i>None</i>			31.4%	36.8%
Combination	3.7%	3.3%	4.2%	3.7%	4.0%	3.8%	4.4%	8.0%	24.5%

Table 4: Relative uncertainties on the projected p_T^H spectrum under S2 (with YR18 systematic uncertainties) at 3000 fb^{-1} .

2.5 Direct and indirect probing of top Yukawa coupling

2.5.1 Measurements in $t\bar{t}H$ and tH production modes

by A. Calandri, M. Schröder

One of the main targets of the High-Luminosity LHC (HL-LHC) upgrade is to achieve precision measurements of the Higgs boson properties. The Yukawa coupling of the Higgs boson to the top quark is expected to be of the order of unity and could be partially sensitive to effects beyond the Standard Model (SM). Therefore, a direct measurement of the coupling of the Higgs boson to top quarks is extremely important to access possible deviations in the top quark's Yukawa couplings due to couplings to new particles. Such a measurement can be performed by measuring the rate of the process where the Higgs boson is produced in association with a pair of top quarks ($t\bar{t}H$) or a single top quark (tH). Even though the $t\bar{t}H$ process is characterised by a small cross section compared to the dominant gluon fusion Higgs boson production (approximately two orders of magnitude smaller), the signature with top quarks in the final state can be exploited to reconstruct the event and gives access to many Higgs boson decay modes. The SM tH production cross-section is yet smaller by a factor five, but due to interference effects between diagrams with top-Higgs and W-boson-Higgs couplings, the process allows access to the sign

Table 5: Breakdown of the contributions to the expected uncertainties on the $t\bar{t}H$ signal-strength μ in the $H \rightarrow b\bar{b}$ channel at different luminosities for the scenarios S1 and S2 at CMS. The uncertainties are given in percent relative to $\mu = 1$. Results with 35.9 fb^{-1} are intended for comparison with the projections to higher luminosities and differ in parts from [?] for consistency with the projected results: uncertainties due to the limited number of Monte Carlo statistics have been omitted and the assumptions in S1/S2 on the theory uncertainties are applied.

Source	S1		S2	
	35.9 fb^{-1}	3000 fb^{-1}	35.9 fb^{-1}	3000 fb^{-1}
Total	48.7	11.1	46.1	7.3
Stat	26.7	2.9	26.7	2.9
SigTh	10.8	8.7	5.0	4.4
BkgTh	28.6	4.1	25.6	3.5
$t\bar{t} + \text{HF XS}$	14.6	0.8	16.5	0.7
Exp	17.4	4.2	16.6	2.6
Luminosity	1.6	1.8	0.5	0.8
B tagging	12.0	2.8	10.8	1.6
JES	10.9	1.6	11.3	1.6

of the top-Higgs Yukawa coupling. The ATLAS and CMS Collaborations have searched for the $t\bar{t}H$ and tH production with LHC Run 2 data of 2015, 2016, and 2017, and observed the Higgs boson production in association with a top-quark pair [54, 55]. The analyses are sensitive to a large variety of final-state event topologies, $H \rightarrow WW^*$, $H \rightarrow ZZ^*$, $H \rightarrow \tau^+\tau^-$, $H \rightarrow b\bar{b}$ and $H \rightarrow \gamma\gamma$. Dedicated multivariate analysis techniques, including boosted decision trees and deep neural networks, that combine the information of several discriminating variables, as well as classifiers based on a matrix element method are utilised to identify the signal against the background.

In this Section, projections based on dedicated analyses with 36 fb^{-1} of Run-II data of 2016 are presented, which target the $t\bar{t}H$, $H \rightarrow b\bar{b}$ channel with leptonic decays of the $t\bar{t}$ system [56, 57] and the $t\bar{t}H$ multi-lepton final state [58], where the Higgs boson decays into a pair of Z and W vector bosons or into τ leptons. Furthermore, results are presented for the projection of a search for tH production that considers all of the above decay channels.

2.5.1.1 Sensitivity to $t\bar{t}H$ production in the $b\bar{b}$ and multi-lepton final states

The $t\bar{t}H$ analyses in the $H \rightarrow b\bar{b}$ final state benefit from the large branching ratio. At the same time, the relatively poor b jet energy resolution, the large jet combinatorics, and the sizeable background of SM processes with large modelling uncertainties, in particular $t\bar{t} + \text{heavy-flavour jet}$ ($t\bar{t} + \text{HF}$) production, pose major challenges. The expected relative precision of the $t\bar{t}H$, $H \rightarrow b\bar{b}$ signal strength (μ) measurement for the ATLAS and CMS analyses [59, 60] reach the level of XX–XX% and 7–11% at 3000 fb^{-1} for ATLAS and CMS, respectively, depending on the scenario and the assumptions of the $t\bar{t} + \text{HF}$ background modelling, as detailed below.

Table 5 shows a breakdown of the contributing sources of uncertainty in the CMS analysis; their evolution with integrated luminosity is depicted in Fig. 13. Compared to the result at 35.9 fb^{-1} , the relative contribution of the experimental uncertainties, such as the b-tagging uncertainty, remains approximately the same, while the signal-theory uncertainty component increases and becomes the major uncertainty component, mostly driven by the inclusive cross-section uncertainty on the SM prediction entering μ . The statistical uncertainty becomes small compared to the systematic components. A similar behaviour is observed in the ATLAS analysis.

In both analyses, a rather sizeable reduction of the uncertainties related to the modelling of the

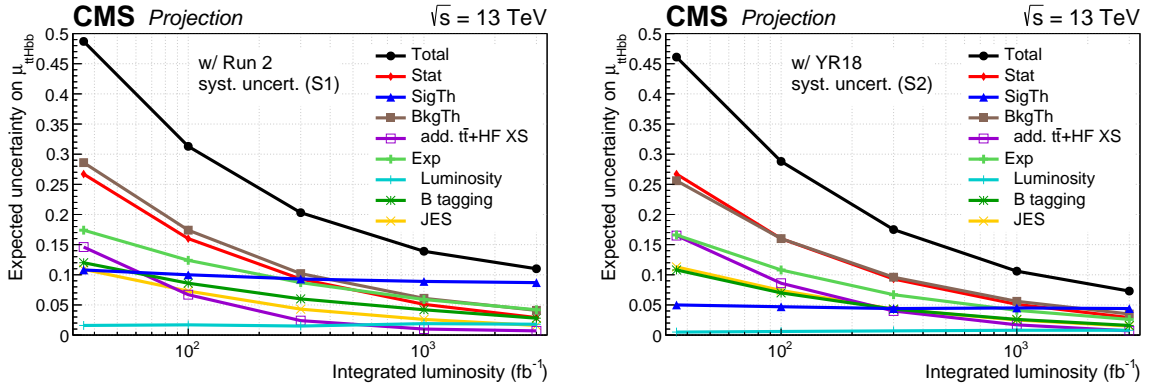


Fig. 13: Expected uncertainties on the $t\bar{t}H$ signal strength in the $H \rightarrow b\bar{b}$ channel as a function of the integrated luminosity under the S1 (left) and S2 (right) scenarios at CMS. Shown are the total uncertainty (black) and contributions of different groups of uncertainties. Results with 35.9 fb^{-1} are intended for comparison with the projections to higher luminosities and differ in parts from [?] for consistency with the projected results: uncertainties due to the limited number of MC events have been omitted and the assumptions in S1/S2 on the theory uncertainties are applied.

Fig. 14: Ranking of the ten most significant systematics uncertainties under S2 in the single lepton (a) and dilepton (b) final states at ATLAS listed in accordance to their post-fit impact on the $t\bar{t}H$ cross section.

$t\bar{t} + \text{HF}$ background, which relies on MC simulation, is observed. Relevant nuisance parameters are constrained to a few percent, such as the nuisance parameters describing the difference between four and five-flavour scheme calculations which is treated as a 2-point systematic uncertainty in the ATLAS analysis (Fig. 14) or the nuisance parameters describing the additional $t\bar{t} + \text{HF}$ cross-section uncertainties in the CMS analysis (Table 5 and Fig. 13). This is attributed to the increasing power of the profile likelihood fit to constrain the uncertainties.

The results illustrate that the background modelling, which has been designed to work well with 35.9 fb^{-1} of data, will need to be refined at 3000 fb^{-1} , requiring improved simulations or in-situ measurements of the $t\bar{t} + \text{HF}$ processes themselves. The observed constraints on the $t\bar{t} + \text{HF}$ background model systematics uncertainties shown in Fig. 14 demonstrate that there will be enough data at the HL-LHC to obtain further information about the background beyond the current modelling. The level at which the nuisance parameters are constrained at 3000 fb^{-1} , corresponding to a few percent cross-section uncertainty, demonstrate the level of sensitivity at which the data will be able to distinguish different models and sets a benchmark for the required precision. Monte Carlo prediction will thus need to improve sufficiently to match the data within the uncertainties expected at 3000 fb^{-1} .

Following the expected improvement in the theoretical uncertainties on the $t\bar{t} + \text{HF}$ cross-section calculation described in Section ??, ATLAS and CMS have also performed the $t\bar{t}H$, $H \rightarrow b\bar{b}$ extrapolation assuming that the reduction of the $t\bar{t} + \text{HF}$ modelling uncertainties is limited to factors of two (in scenario S1) and three (in scenario S2) relative to the uncertainty at 35.9 fb^{-1} . In this case, the obtained relative $t\bar{t} + \text{HF}$ modelling uncertainties are approximately 23% (S1) and 15% (S2) in the ATLAS analysis as reported in Table 7 and approximately 15% (S1) and 10% (S2) in the CMS analysis. These results enter the combined coupling measurement presented in Section ???. The impact of limiting the constraints of the $t\bar{t} + \text{HF}$ uncertainties on the total uncertainties on the extracted parameters is relatively small, e.g. the uncertainty on κ_t increases by approximately 10% and 15% in CMS and ATLAS, respectively.

In conclusion, $t\bar{t}H$ production in the $H \rightarrow b\bar{b}$ final state will provide a powerful channel to probe the top-Higgs Yukawa coupling at the HL-LHC. The control of the $t\bar{t} + \text{HF}$ background is crucial, and

Table 6: Breakdown of the contributions to the expected uncertainties on the $t\bar{t}H$ cross section in the $H \rightarrow b\bar{b}$ channel at different luminosities for the scenarios S1 and S2 at ATLAS. As discussed in the text, the extrapolation assumes the limitations on the reduction of the $t\bar{t} + \text{HF}$ modelling to a factor 2 and a factor 3 of the Run 2 prior uncertainties (Section ??). Therefore, the additional modelling uncertainty used for the extrapolation is 23% in S1 and 15% in S2. Uncertainties due to the limited number of Monte Carlo statistics have been omitted and the assumptions in S1/S2 on the theory uncertainties are applied.

Table 7: Breakdown of the contributions to the expected uncertainties on the $t\bar{t}H$ cross section in the multilepton channel at different luminosities for the scenarios S1 and S2 at ATLAS. Uncertainties due to the limited number of Monte Carlo statistics have been omitted and the assumptions in S1/S2 on the theory uncertainties are applied.

Fig. 15: Ranking of the ten most significant systematics uncertainties under S2 in the $t\bar{t}H$ final state with (a) and without (b) τ leptons in the ATLAS analysis listed in accordance to their post-fit impact on the $t\bar{t}H$ cross section.

it is expected to benefit from measuring relevant quantities from data, thus mitigating the impact of theoretical uncertainties.

ATLAS performs the extrapolation to HL-LHC also for the $t\bar{t}H$ multilepton final state [59] where the Higgs boson decays into a pair of Z and W vector bosons or into $\tau\tau$ s. Table ?? shows the results on the extrapolation to 3000 fb^{-1} under S1 and S2. As shown in the ranking plot in Figure 15, in the τ final state, the dominant uncertainty pertains to the object reconstruction for such a channel. It is also worth noting that the main theoretical systematics concerns the modelling of the $t\bar{t}+V$ background. Finally, fake lepton uncertainties are moderately constrained as well: this is due to the absence of reduction factor of prior uncertainties for such a source of systematics under S1 and S2.

2.5.1.2 Sensitivity to tH production

The sensitivity to the tH process at the HL-LHC is determined by extrapolating a combination of Run 2 analyses based on 35.9 fb^{-1} of data at $\sqrt{s} = 13 \text{ TeV}$ [61]. Two of these analyses are dedicated searches for tHq : one targets a multi-lepton final state [62] in which the Higgs boson decays to WW, ZZ or $\tau\tau$ pairs, and the other targets the $H \rightarrow bb$ decay [63]. In both analyses the presence of at least one central b tagged jet and an isolated lepton from the top quark decay is required. Furthermore, the presence of a light quark jet at high pseudorapidity, a unique feature of the tHq production mode, is exploited. Both analyses also rely heavily on multivariate techniques to discriminate the signal against the large $t\bar{t}+\text{jets}$ background. The \gg final state is also utilised, via a reinterpretation of the inclusive $H \rightarrow \gamma\gamma$ analysis [64]. In this analysis the tHq and tHW processes primarily contribute to the “ $t\bar{t}H$ leptonic” and “ $t\bar{t}H$ hadronic” event categories, and these are included in the combination.

In Figure 16 the variation of the expected upper limits on μ_{tH} is shown as a function of the integrated luminosity for the S1 and S2 scenarios. The limits are determined assuming a background-only hypothesis in which the tH process is considered as following the SM expectation ($\mu_{ttH} = 1$). In order to minimize further assumptions on the rate of tH production, μ_{ttH} is treated as a free parameter in the fit. In the S1 scenario the expected median upper limit on μ_{tH} at 3000 fb^{-1} is determined to be 2.35. The corresponding value in S2 is 1.51. With the 3000 fb^{-1} dataset and foreseen reduction in systematic uncertainties in S2, the expected upper limit on μ_{tH} improves by about a factor of eight with respect to the current exclusion.

The evolution of the expected uncertainty on the measurement of μ_{tH} , assuming the SM rate, is

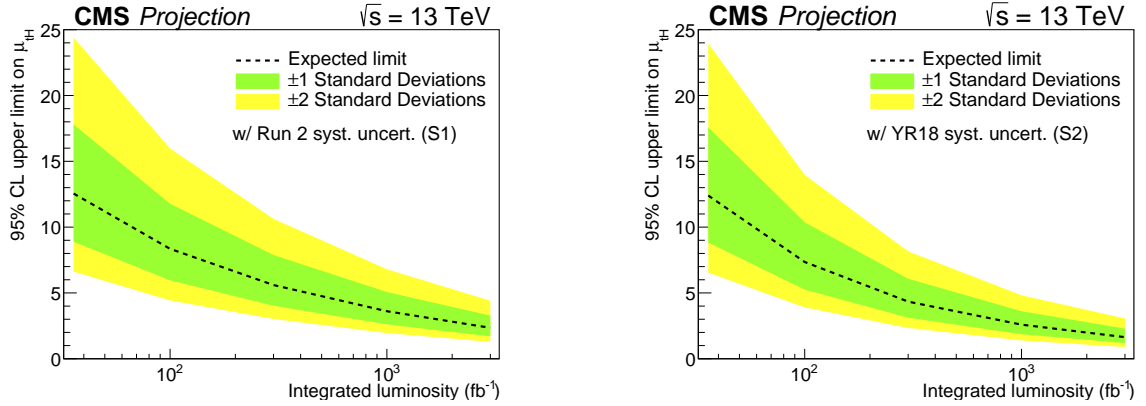


Fig. 16: The variation of expected upper limit on μ_{tH} with integrated luminosity for two projection scenarios S1 (with Run 2 systematic uncertainties [61]) and S2 (with YR18 systematic uncertainties).

given in Table 8. Values are given for two cases of background: one in which μ_{ttH} is unconstrained in the fit, and one in which it is fixed to the SM value of 1. In the latter case the uncertainties are reduced by around 10% at 3000 fb^{-1} , indicating that a precise simultaneous measurement of the $t\bar{t}H$ signal strength will be needed to obtain the optimal sensitivity to the tH channel. In both cases it is found that the reduced systematic uncertainties in S2 improve the precision by up to 30%.

Table 8: The $\pm 1\sigma$ uncertainties on expected $\mu_{tH}=1$ for scenarios S1 (with Run 2 systematic uncertainties [61]) and S2 (with YR18 systematic uncertainties) at all three luminosities, considering also the case when $\mu_{t\bar{t}H}$ is fixed at the SM value 1.

		μ_{ttH} floating	μ_{ttH} fixed
S1	35.9 fb^{-1}	+6.2	+5.8
	300 fb^{-1}	-5.8	-5.4
	3000 fb^{-1}	+2.9 -2.8 +1.2 -1.2	+2.5 -2.4 +1.1 -1.0
S2	35.9 fb^{-1}	+6.2	+5.8
	300 fb^{-1}	-5.8	-5.3
	3000 fb^{-1}	+2.2 -2.2 +0.9 -0.9	+2.0 -2.0 +0.8 -0.8

2.5.2 Constraints from differential measurements

Written by: T. Klijnsma

Higgs boson couplings can be constrained by fitting theoretical predictions for p_T^H [65–67] to data, exploiting not only the overall normalization (as is done in inclusive measurements [41–43]), but also the shape of the distribution. One of the first constraints on Higgs boson couplings using differential Higgs boson production cross sections was made in Ref. [65]. The limits $\kappa_c \in [-16, 18]$ at 95% CL were found, using data collected by the ATLAS Collaboration at $\sqrt{s} = 8 \text{ TeV}$ [68], corresponding to an integrated luminosity of 20.3 fb^{-1} . More recently, the CMS Collaboration performed a similar fit using data [?] collected at $\sqrt{s} = 13 \text{ TeV}$, corresponding to an integrated luminosity of 36.1 fb^{-1} . The limits on κ_b and κ_c are discussed in Section , whereas the interpretation in terms of κ_t and c_{ggh} , the anomalous direct coupling to the gluon field, is discussed here. The projected simultaneous limits on κ_t and c_{ggh} at 3000 fb^{-1} are shown in Fig. 18, assuming branching fractions that scale according to SM predictions. It

is expected to observe the loop in the gluon-fusion production process, which is clear from the fact that heavy top mass limit, given by the point ($\kappa_t = 0, c_{ggh} = \sim 1/12$), is excluded.

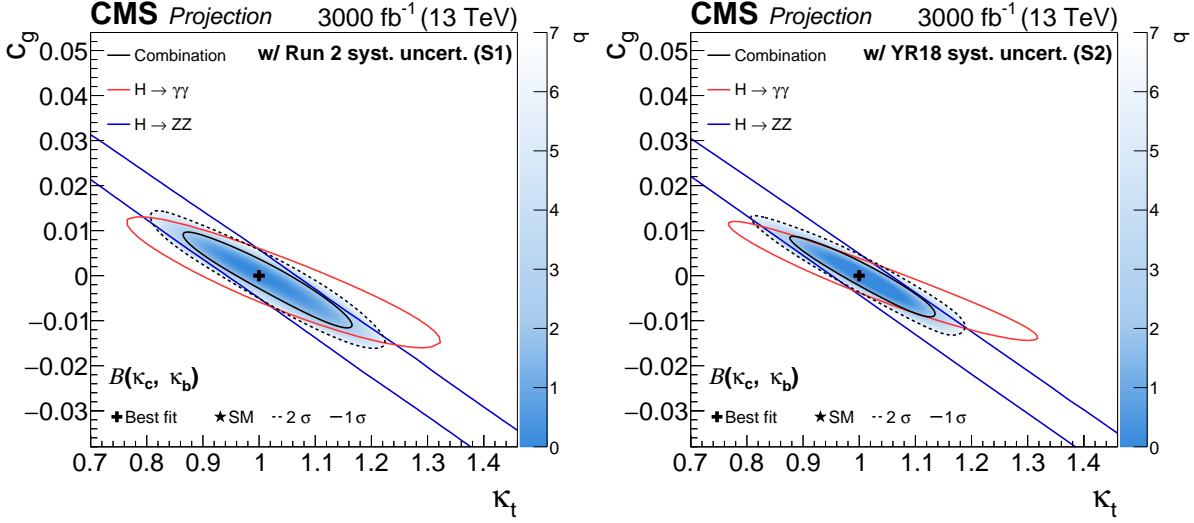


Fig. 17: Projected simultaneous fit for κ_t and c_{ggh} , assuming a coupling dependence of the branching fractions for Scenario 1 (left) and Scenario 2 (right). The one standard deviation contour is drawn for the combination ($H \rightarrow \gamma\gamma$, $H \rightarrow ZZ$, and $H \rightarrow bb$), the $H \rightarrow \gamma\gamma$ channel, and the $H \rightarrow ZZ$ channel in black, red, and blue, respectively. For the combination the two standard deviation contour is drawn as a black dashed line, and the shading indicates the negative log-likelihood, with the scale shown on the right hand side of the plots.

In order to determine solely the constraint obtained from the distribution (and not the overall normalization), the fit is repeated with the branching fractions implemented as nuisance parameters with no prior constraint, effectively profiling the overall normalization. With this parametrization, the sensitivity to the sign of κ_t coming from the $H \rightarrow \gamma\gamma$ branching fraction is lost. The fits obtained this way are shown in Fig. 18; although less significantly, the loop is still distinguished from the point-like coupling to the gluon field, using only the information in the shape of the distribution.

2.6 Combination of Higgs boson measurement projections

To be written by: R. Di Nardo, A. Gilbert, H. Yang

TODO: Text to be updated to reflect ATLAS+CMS combination.

The projections documented in this section are based on extrapolations of the following analyses:

- $H \rightarrow \gamma\gamma$, with ggH, VBF, VH and ttH production [64],
- $H \rightarrow ZZ^{(*)} \rightarrow 4\ell$, with ggH, VBF, VH and ttH production [69],
- $H \rightarrow WW^{(*)} \rightarrow \ell\nu\ell\nu$, with ggH, VBF and VH production [70],
- $H \rightarrow \tau\tau$, with ggH and VBF production [71],
- VH production with $H \rightarrow bb$ decay [40],
- Boosted H production with $H \rightarrow bb$ decay [72],
- ttH production with $H \rightarrow$ leptons [73],
- ttH production with $H \rightarrow bb$ [74, 75],
- $H \rightarrow \mu\mu$, with ggH and VBF production [76].

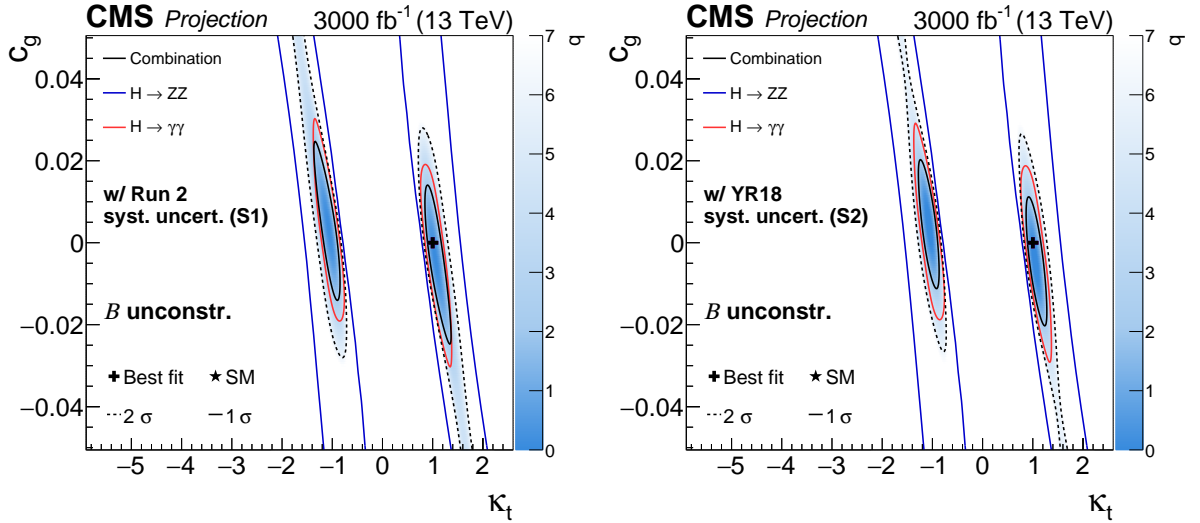


Fig. 18: Projected simultaneous fit for κ_t and c_{ggh} with the branching fractions implemented as nuisance parameters with no prior constraint for Scenario 1 (left) and Scenario 2 (right). The one standard deviation contour is drawn for the combination ($H \rightarrow \gamma\gamma$, $H \rightarrow ZZ$, and $H \rightarrow bb$), the $H \rightarrow \gamma\gamma$ channel, and the $H \rightarrow ZZ$ channel in black, red, and blue, respectively. For the combination the two standard deviation contour is drawn as a black dashed line, and the shading indicates the negative log-likelihood, with the scale shown on the right hand side of the plots.

The projected results given in this section are based on the combined measurement of these channels [77]. In the following results the signal model in the $H \rightarrow \mu\mu$ channel is modified to account for the improved dimuon mass resolution in the Phase-2 CMS tracker upgrade [78]. It is estimated that the reduced material budget and improved spatial resolution of the upgraded tracker will yield a 40% improvement in the relative di-muon mass resolution, for example a reduction from 1.1% to 0.65% for muons in the barrel region.

TODO: Switch to cross section and branching ratio results without inclusive theory uncertainties. Projections are given for two parametrisations of the signal, based on signal strength modifiers μ , defined as the ratio between the measured Higgs boson yield and its SM expectation. One set of parameters μ^f , where $f = ZZ, WW, \gg, \tau\tau, bb$ and $\mu\mu$, are introduced to scale the branching fractions of each decay mode independently, assuming the SM cross sections for the production modes. Another set, μ_i , where $i = ggH, VBF, WH, ZH$ and $t\bar{t}H$, scale each production cross section independently, assuming the SM values of the branching fractions.

2.6.1 Signal strength per-decay mode

The expected $\pm 1\sigma$ uncertainties on the per-decay-mode signal strength parameters in S1 and S2 are summarised in Figure 19 with numerical values given in Table 9. The table additionally gives the breakdown of the uncertainty into four components: statistical, signal theory, background theory and experimental. The S2 uncertainties range from 3–4%, with the exception of that on $\mu^{\mu\mu}$ at 10%. The S1 uncertainties are up to a factor of 1.5 larger than those in S2, reflecting the larger systematic component. The dominant uncertainty contribution is found to vary with the scenario and the integrated luminosity of the projection. The systematic uncertainties generally dominate in both S1 and S2. In S2 the signal theory uncertainty is the largest, or joint-largest, component for all parameters except $\mu^{\mu\mu}$, which remains limited by statistics due to the small $H \rightarrow \mu\mu$ branching fraction. The $\mu^{\mu\mu}$ uncertainty using the Run 2 dimuon mass

resolution instead of the Phase-2 expectation is 14%.

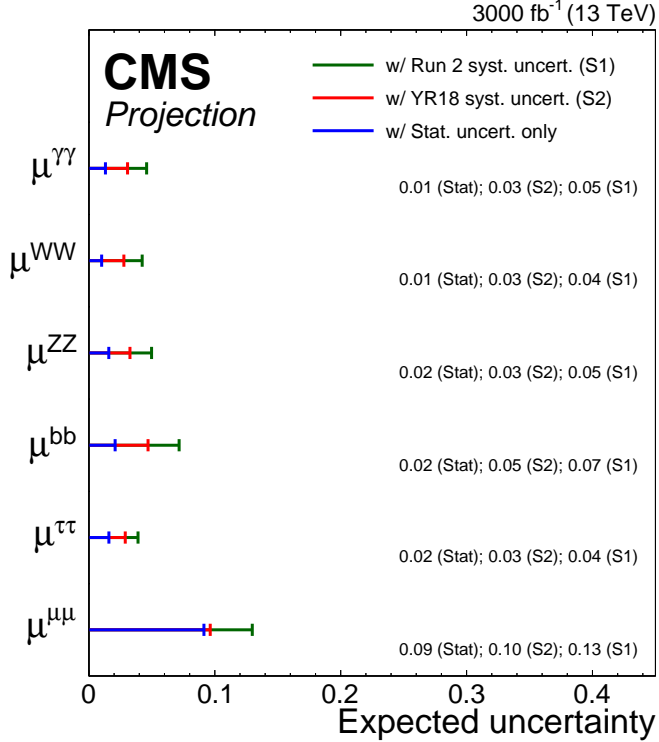


Fig. 19: Summary plot showing the total expected $\pm 1\sigma$ uncertainties in S1 (with Run 2 systematic uncertainties [77]) and S2 (with YR18 systematic uncertainties) on the per-decay-mode signal strength parameters. The statistical-only component of the uncertainty is also shown.

Another important aspect of the projected measurements is how the correlations between the measured parameters are expected to evolve. Correlations arise when analysis channels are sensitive to more than one production or decay mode and the chosen fit observables do not fully distinguish between these. In addition, correlations may arise when the same systematic uncertainties apply to multiple production or decay modes. Figure 20 shows the correlation coefficients between the signal strength parameters in S2. The correlations range up to +0.44, and are largest between modes where the sensitivity is dominated by gluon-fusion production. This reflects the impact of the theory uncertainties affecting the SM prediction of the gluon-fusion production rate.

2.6.2 Signal strength per-production mode

The expected $\pm 1\sigma$ uncertainties on the per-production-mode signal strength parameters in S1 and S2 are summarised in Figure 21 with numerical values given in Table 10. In S1 the signal theory is the main contribution for all modes except WH which remains limited by statistics. In S2 μ_{VBF} and μ_{WH} are also statistically limited.

Figure 22 shows the correlation coefficients between the signal strength parameters in S2. The correlations in this case are small compared to the per-decay measurements since production modes are generally well-isolated by independent analysis categories and the main theoretical uncertainties on the SM signal expectation are uncorrelated.

2.7 Kappa interpretation of the combined Higgs boson measurement projections

To be written by: R. Di Nardo, A. Gilbert, H. Yang

Table 9: The expected $\pm 1\sigma$ uncertainties, expressed as percentages, on the per-decay-mode signal strength parameters. Values are given for both S1 (with Run 2 systematic uncertainties [77]) and S2 (with YR18 systematic uncertainties). The total uncertainty is decomposed into four components: statistical (Stat), signal theory (SigTh), background theory (BkgTh) and experimental (Exp).

		3000 fb ⁻¹				
		Total	Stat	SigTh	BkgTh	Exp
$\mu^{\gamma\gamma}$	S1	4.6	1.3	3.5	0.3	2.6
	S2	3.1	1.3	2.1	0.3	1.7
μ^{WW}	S1	4.2	1.0	3.7	1.0	1.4
	S2	2.8	1.0	2.2	0.9	1.1
μ^{ZZ}	S1	5.0	1.6	3.5	1.9	2.5
	S2	3.3	1.6	2.1	0.7	1.7
μ^{bb}	S1	7.2	2.1	5.4	3.6	2.3
	S2	4.7	2.1	2.5	2.9	1.7
$\mu^{\tau\tau}$	S1	3.9	1.6	2.6	1.5	1.9
	S2	2.9	1.6	1.8	0.6	1.4
$\mu^{\mu\mu}$	S1	13.0	9.1	5.2	0.8	7.6
	S2	9.6	9.1	2.6	0.8	1.7

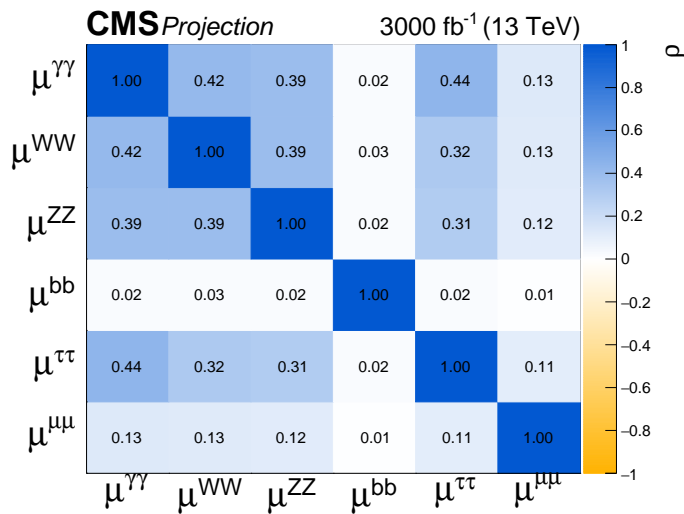


Fig. 20: Correlation coefficients (ρ) between parameters in the signal strength per-decay-mode parametrisation for S2 (with YR18 systematic uncertainties).

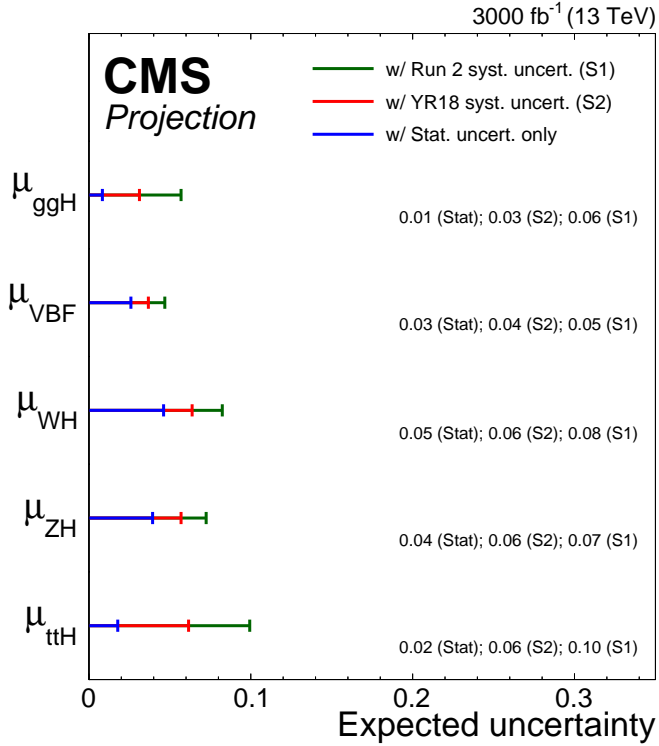


Fig. 21: Summary plot showing the total expected $\pm 1\sigma$ uncertainties in S1 (with Run 2 systematic uncertainties [77]) and S2 (with YR18 systematic uncertainties) on the per-production-mode signal strength parameters. The statistical-only component of the uncertainty is also shown.

Table 10: The expected $\pm 1\sigma$ uncertainties, expressed as percentages, on the per-production-mode signal strength parameters. Values are given for both S1 (with Run 2 systematic uncertainties [77]) and S2 (with YR18 systematic uncertainties). The total uncertainty is decomposed into four components: statistical (Stat), signal theory (SigTh), background theory (BkgTh) and experimental (Exp).

		3000 fb^{-1}				
		Total	Stat	SigTh	BkgTh	Exp
μ_{ggH}	S1	5.7	0.8	5.4	0.9	1.2
	S2	3.1	0.8	2.8	0.6	0.9
μ_{VBF}	S1	4.7	2.6	3.0	1.3	2.1
	S2	3.7	2.6	2.1	0.3	1.6
μ_{WH}	S1	8.2	4.6	2.9	3.3	5.2
	S2	6.4	4.6	1.4	2.7	3.2
μ_{ZH}	S1	7.2	3.9	5.1	2.5	2.1
	S2	5.7	3.9	3.0	2.3	1.7
μ_{ttH}	S1	9.9	1.8	8.3	4.1	3.1
	S2	6.2	1.8	4.2	3.4	2.4

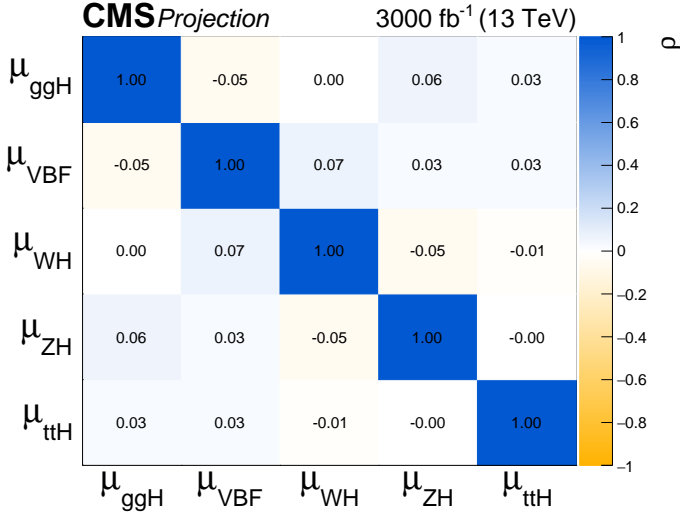


Fig. 22: Correlation coefficients (ρ) between parameters in the signal strength per-production-mode parametrisation for S2 (with YR18 systematic uncertainties) at 300 fb^{-1} (left) and 3000 fb^{-1} (right).

In this section combination results are given for a parametrisation based on the coupling modifier, or κ -framework [3]. A set of coupling modifiers, $\vec{\kappa}$, is introduced to parametrize potential deviations from the SM predictions of the Higgs boson couplings to SM bosons and fermions. For a given production process or decay mode j , a coupling modifier κ_j is defined such that,

$$\kappa_j^2 = \sigma_j / \sigma_j^{\text{SM}} \quad \text{or} \quad \kappa_j^2 = \Gamma_j / \Gamma_{\text{SM}}^j. \quad (1)$$

In the SM, all κ_j values are positive and equal to unity. Six coupling modifiers corresponding to the tree-level Higgs boson couplings are defined: κ_W , κ_Z , κ_t , κ_b , κ_τ and κ_μ . In addition, the effective coupling modifiers κ_g and κ_γ are introduced to describe ggH production and $H \rightarrow \gamma\gamma$ decay loop processes. The total width of the Higgs boson, relative to the SM prediction, varies with the coupling modifiers as $\Gamma_H / \Gamma_H^{\text{SM}} = \sum_j B_{\text{SM}}^j \kappa_j^2 / (1 - B_{\text{BSM}})$, where B_{SM}^j is the SM branching fraction for the $H \rightarrow jj$ channel and B_{BSM} is the Higgs boson branching fraction to BSM final states. In the results for the κ_j parameters presented here B_{BSM} is fixed to zero and only decays to SM particles are allowed. Projections are also given for the upper limit on B_{BSM} when this restriction is relaxed, in which an additional constraint that $|\kappa_V| < 1$ is imposed. A constraint on $\Gamma_H / \Gamma_H^{\text{SM}}$ is also obtained in this model by treating it as a free parameter in place of one of the other κ parameters.

The expected uncertainties for the coupling modifier parametrisation are summarised in Figure 23 with numerical values given in Table 11. The largest uncertainty component is generally the signal theory in S1, whereas in S2 all four components contribute at a similar level for κ_γ , κ_W , κ_Z and κ_τ . The signal theory remains the main component for κ_t and κ_g , and κ_μ is limited by statistics.

Table 11 also gives the expected uncertainties on B_{BSM} and $\Gamma_H / \Gamma_H^{\text{SM}}$ for the parametrisation with $B_{\text{BSM}} \geq 0$ and $|\kappa_V| \leq 1$. The 1σ uncertainty on B_{BSM} is 0.035 in S1 and 0.027 in S2, where in the latter case the statistical uncertainty is the largest component. The corresponding 95% CL expected upper limit is $B_{\text{BSM}} = 0.077(0.057)$ in S1 (S2). The uncertainty on $\Gamma_H / \Gamma_H^{\text{SM}}$ is 0.05 in S1 and 0.04 in S2, equivalent to 0.16 and 0.21 MeV respectively, assuming the SM width of 4.1 MeV. The main contribution is the statistical uncertainty, followed by the experimental one.

Figure 24 gives the correlation coefficients for the coupling modifiers for S2. In contrast to the per-decay signal strength correlations in Figure 20 the correlations here are larger, up to +0.74. One reason for this is that the normalisation of any signal process depends on the total width of the Higgs

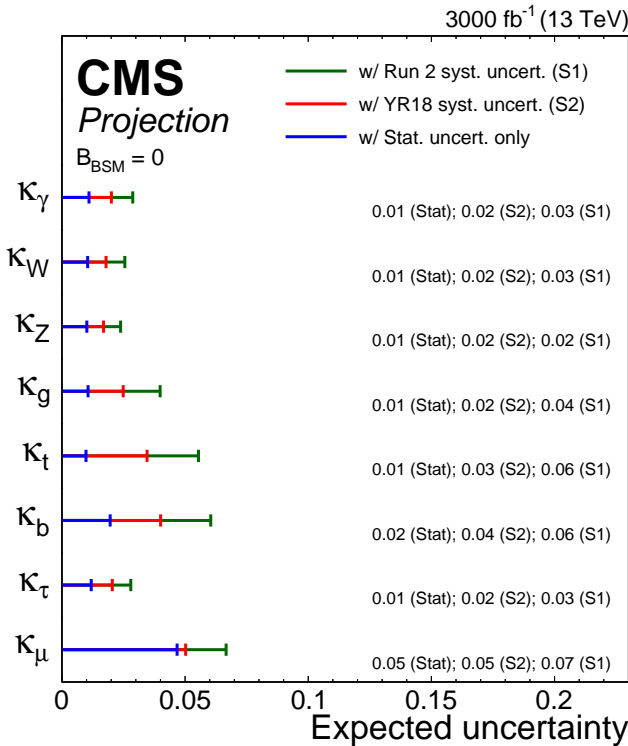


Fig. 23: Summary plot showing the total expected $\pm 1\sigma$ uncertainties in S1 (with Run 2 systematic uncertainties [77]) and S2 (with YR18 systematic uncertainties) on the coupling modifier parameters. The statistical-only component of the uncertainty is also shown.

boson, which in turn depends on the values of the other coupling modifiers. The largest correlations involve κ_b , as this gives the largest contribution to the total width in the SM. Therefore improving the measurement of the $H \rightarrow bb$ process will improve the sensitivity of many of the other coupling modifiers at the HL-LHC.

2.8 Kappa-formalism and the nonlinear EFT

by Claudio Krause and Oscar Catà

The κ -formalism was introduced in [2, 3] as an interim framework to report on the measurements of the Higgs-boson couplings and characterize the nature of the Higgs boson. The κ_i are defined as ratios of measured cross sections and decay widths with respect to their SM expectation, *i.e.*

$$\kappa_X^2 = \frac{\sigma(X_i \rightarrow h + X_f)}{\sigma(X_i \rightarrow h + X_f)_{\text{SM}}}, \quad \kappa_Y^2 = \frac{\Gamma(h \rightarrow Y)}{\Gamma(h \rightarrow Y)_{\text{SM}}}, \quad (2)$$

so that the SM is recovered for $\kappa_i = 1$.

The κ -framework, defined at the level of signal strengths, was appropriate for the observables under study at Run I, which tested deviations in event rates. For Run II and the analyses required at the HL-LHC, differential distributions are needed. In order to study event shapes the formalism, as defined by eq. (2), is clearly insufficient and has to be extended.

A closely related issue is how to relate the κ -framework to a QFT description. A naive interpretation of the κ factors as rescalings of SM Higgs couplings has been attempted, but this prescription is not necessarily consistent with QFT principles and has limitations that obstruct a successful implementation. More precisely, the following caveats apply:

Table 11: The expected $\pm 1\sigma$ uncertainties, expressed as percentages, on the coupling modifier parameters, as well as B_{BSM} and $\Gamma_H/\Gamma_H^{\text{SM}}$. Due to the constraint $B_{\text{BSM}} \geq 0$ the values for this parameter correspond to the $\pm 1\sigma$ uncertainties only. Values are given for both S1 (with Run 2 systematic uncertainties [77]) and S2 (with YR18 systematic uncertainties). The total uncertainty is decomposed into four components: statistical (Stat), signal theory (SigTh), background theory (BkgTh) and experimental (Exp).

3000 fb^{-1}						
	Total	Stat	SigTh	BkgTh	Exp	
$B_{\text{BSM}} = 0$						
κ_γ	S1	2.9	1.1	1.8	1.0	1.7
	S2	2.0	1.1	0.9	0.8	1.2
κ_W	S1	2.6	1.0	1.7	1.1	1.1
	S2	1.8	1.0	0.9	0.8	0.8
κ_Z	S1	2.4	1.0	1.7	0.9	0.9
	S2	1.7	1.0	0.9	0.7	0.7
κ_g	S1	4.0	1.1	3.4	1.3	1.2
	S2	2.5	1.1	1.7	1.1	1.0
κ_t	S1	5.5	1.0	4.4	2.7	1.6
	S2	3.5	1.0	2.2	2.1	1.2
κ_b	S1	6.0	2.0	4.3	2.9	2.3
	S2	4.0	2.0	2.0	2.2	1.8
κ_τ	S1	2.8	1.2	1.8	1.1	1.4
	S2	2.0	1.2	1.0	0.9	1.0
κ_μ	S1	6.7	4.7	2.5	1.0	3.9
	S2	5.0	4.7	1.3	0.8	1.1
$B_{\text{BSM}} \geq 0, \kappa_V \leq 1$						
$B_{\text{BSM}}^{(+1\sigma)}$	S1	3.8	1.9	2.4	1.5	1.7
	S2	2.7	1.9	1.0	1.2	1.3
$\Gamma/\Gamma_{\text{SM}}$	S1	5.8	2.7	3.6	2.4	2.7
	S2	4.3	2.7	1.9	1.8	2.1

1. In this prescription, only QCD corrections, which are factorizable, can be taken into account. Electroweak corrections cannot be implemented consistently.
2. Gauge invariance and unitarity are generically broken by ad-hoc variations of the SM couplings.
3. In processes that are loop-induced in the SM, such as $h \rightarrow \gamma\gamma$ or $gg \rightarrow h$, care has to be taken. A rescaled local coupling, for example for $h \rightarrow \gamma\gamma$, does not yield an overall κ_γ^2 factor, since the process is not mediated by the local interaction only. In these loop processes the interplay of different couplings, most prominently κ_t , has to be consistently included.

The way to circumvent the objections above is to work not at the level of rescaled couplings but at the level of Lagrangians, where locality, unitarity and gauge invariance are automatically implemented. In order to be as general as possible, an upgrade of the κ -formalism should be embedded in the language of EFTs.

Here we will discuss the interpretation of the κ factors within the electroweak chiral Lagrangian

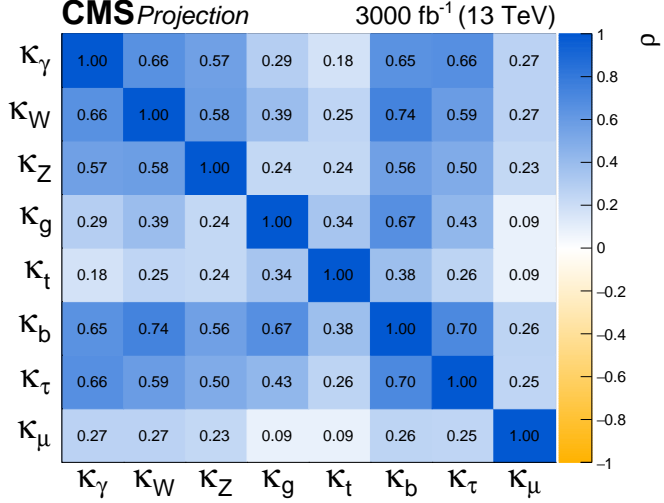


Fig. 24: Correlation coefficients (ρ) between parameters in the coupling modifier parametrisation for S2 (with YR18 systematic uncertainties).

(EWChL), also denoted as HEFT in the literature. Within this EFT, and only projecting out the leading contributions to processes with a single Higgs, one finds [79–81]

$$\begin{aligned} \mathcal{L}_{\text{fit}} = & 2c_V \left(m_W^2 W_\mu^+ W^{-\mu} + \frac{1}{2} m_Z^2 Z_\mu Z^\mu \right) \frac{h}{v} - \sum_{\psi} c_\psi m_\psi \bar{\psi} \psi \frac{h}{v} \\ & + \frac{e^2}{16\pi^2} c_\gamma F_{\mu\nu} F^{\mu\nu} \frac{h}{v} + \frac{e^2}{16\pi^2} c_{Z\gamma} Z_{\mu\nu} F^{\mu\nu} \frac{h}{v} + \frac{g_s^2}{16\pi^2} c_g \langle G_{\mu\nu} G^{\mu\nu} \rangle \frac{h}{v}, \end{aligned} \quad (3)$$

where m_i is the mass of particle i , $\psi \in \{t, b, c, \tau, \mu\}$, and the c_i describe the modifications of the Higgs couplings.

The previous Lagrangian differs from a naive rescaling of Higgs couplings, even though superficially it might seem to be equivalent. In particular, the Standard Model is consistently recovered in eq. (3) for

$$c_i^{\text{SM}} = \begin{cases} 1 & \text{for } i = V, t, b, c, \tau, \mu \\ 0 & \text{for } i = g, \gamma, Z\gamma. \end{cases} \quad (4)$$

which is not the case for a naive coupling rescaling. The crucial point is that the coupling modifiers in eq. (3) are not the full EFT, but just the relevant projection for the processes under study at non-trivial leading order in unitary gauge. Since the couplings differ from the SM ones, the previous Lagrangian, taken in isolation, would be non-renormalizable and break unitarity. These requirements are reinstated once eq. (3) is understood as part of the EWChL.

The EWChL [82–99] is a bottom-up effective field theory (EFT), constructed with the particle content and symmetries of the SM. These are the same requirements adopted in the construction of the SMEFT. The main difference between both EFTs concerns the Higgs particle. In the EWChL, the Higgs particle, h , is included as a scalar singlet, with couplings unrelated to the ones of the Goldstone bosons of EWSB. Therefore, h is not necessarily part of an SU(2) doublet and consequently the leading-order Lagrangian is non-renormalizable, i.e. loop divergences require the addition of new counterterms. The inclusion of the (finite) number of counterterms at each loop order makes the theory consistent. The procedure is analogous to the one employed in Chiral Perturbation Theory, whence the name EWChL. Counterterms needed for the 1-loop renormalization [100–102] are included as NLO operators [98] and are

therefore suppressed by a loop factor with respect to the leading order. The theory is thus renormalizable order by order in the loop expansion. The embedding of the EFT as a loop expansion can equivalently be expressed as an expansion in chiral dimensions [99], which allows to identify the counterterms in a straightforward way. Further details and justifications of the expansion are discussed in [80, 98, 99, 103].

Focussing on the leading effects of the measured processes only, the full EWChL reduces to the Lagrangian in eq. (3). Note that it includes only single-Higgs processes, as the κ -formalism also describes only single-Higgs processes. If needed, eq. (3) can also be extended to describe other processes, simply by projecting the relevant operators already present in the EWChL. For instance, for double-Higgs production from gluon fusion three more operators should be added, corresponding to the interactions $h^3, \bar{t}th^2, ggh^2$ [8, 104–106]. Double-Higgs production is discussed in more details in section 3.1.2.1. Since the observed processes are mediated by both tree level and one-loop amplitudes at the first non-vanishing order, operators of leading order in the EFT (first line of eq. (3)) and next-to-leading order in the EFT (second line of eq. (3)) have to be included [80]. Corrections beyond the leading ones, both strong and electroweak, can also be incorporated to arbitrary order in the description of Higgs processes. These corrections involve additional operators, not present in eq. (3), but contained in the EWChL.

Understood as corrections to the SM, the κ factors can also be generated with the SMEFT (see e.g. [107] and the discussion in [108]). The main differences between both EFT descriptions are the following: (i) in the EWChL, deviations from the SM appear at leading order, and $\mathcal{O}(1)$ corrections to the κ factors can be easily accommodated. In the SMEFT, the corrections to the SM appear at NLO, and therefore smaller effects, typically at the present level, are expected; (ii) In the SMEFT the Higgs is assumed to be a weak doublet. The EWChL instead describes a generic scalar and is therefore closer to the spirit of the κ formalism of testing the nature of the Higgs boson.

As stated above, the couplings in eq. (3) can receive a priori large contributions and have to be considered as $\mathcal{O}(1)$ numbers. This is the expectation if new physics contains strongly-coupled new interactions. In some of these scenarios, new-physics interactions can be progressively decoupled from the SM, and it is therefore useful to understand the Wilson coefficients in eq. (3) as functions of the parameter $\xi = v^2/f^2$, where $v \approx 246$ GeV is the electroweak vacuum expectation value, and f is the scale of new physics. The latter could correspond, for example, to the scale of global symmetry breaking in composite Higgs models. The SM is then recovered for $\xi = 0$. For $\xi \ll 1$, one can perform an expansion in ξ on top of the loop expansion in the EWChL. This yields a double expansion in ξ and $1/16\pi^2$ [109], in the spirit of the strongly-interacting light Higgs (SILH) [110]. The expected size of the Wilson coefficients is then

$$c_i = c_i^{\text{SM}} + \mathcal{O}(\xi). \quad (5)$$

The mapping of the Wilson coefficients c_i to the κ_i parameters is done using the relations of the signal strengths computed from the Lagrangian in eq. (3). The necessary formulas can be found in [79, 81]. These relations can be written as

$$\kappa_i = |f_i(c_j)| \equiv \frac{|\mathcal{A}_i(c_j)|}{|\mathcal{A}_i(c_j^{\text{SM}})|}, \quad (6)$$

where \mathcal{A} is the corresponding transition amplitude of each process. The absolute value on the right hand side is necessary, as the loop functions of the light fermions (b, τ, μ, \dots) for the κ_γ and κ_g are complex.

The inverse of eq. (6) is, however, not a well-defined function. We can still obtain an approximate inverse, to connect both formalisms in the opposite direction. This can be easily obtained if we assume that all the imaginary parts are negligible. While this is a good approximation for some of the coefficients in $f_i(c_j)$, for example for the coefficient of c_t , it is not the case for the coefficients of the light fermion loops, where real and imaginary parts are of similar size. Nevertheless, as long as the Wilson coefficients stay relatively close to the SM value, neglecting the imaginary parts completely is still a good approximation, because in κ_g (κ_γ) the real part of the top loop (top and W loops) contribution dominates over all the other terms.

With the assumption of vanishing imaginary parts, eq. (6) becomes

$$\begin{pmatrix} \kappa_V \\ \kappa_t \\ \kappa_b \\ \kappa_\ell \\ \kappa_g \\ \kappa_\gamma \end{pmatrix} = \begin{pmatrix} 1 & 0 & 0 & 0 & 0 & 0 \\ 0 & 1 & 0 & 0 & 0 & 0 \\ 0 & 0 & 1 & 0 & 0 & 0 \\ 0 & 0 & 0 & 1 & 0 & 0 \\ 0 & 1.055 & -0.055 & 0 & 1.3891 & 0 \\ 1.2611 & -0.2683 & 0.0036 & 0.0036 & 0 & -0.3039 \end{pmatrix} \cdot \begin{pmatrix} c_V \\ c_t \\ c_b \\ c_\tau \\ c_g \\ c_\gamma \end{pmatrix}. \quad (7)$$

These numbers also include the leading QCD corrections of the $h \rightarrow \gamma\gamma$ and $gg \rightarrow h$ amplitude. An explicit comparison of this approximation and the full formulas shows only negligible numerical differences. The inverse of eq. (7) is

$$\begin{pmatrix} c_V \\ c_t \\ c_b \\ c_\tau \\ c_g \\ c_\gamma \end{pmatrix} = \begin{pmatrix} 1 & 0 & 0 & 0 & 0 & 0 \\ 0 & 1 & 0 & 0 & 0 & 0 \\ 0 & 0 & 1 & 0 & 0 & 0 \\ 0 & 0 & 0 & 1 & 0 & 0 \\ 0 & -0.76 & 0.04 & 0 & 0.72 & 0 \\ 4.15 & -0.88 & 0.012 & 0.012 & 0 & -3.29 \end{pmatrix} \cdot \begin{pmatrix} \kappa_V \\ \kappa_t \\ \kappa_b \\ \kappa_\ell \\ \kappa_g \\ \kappa_\gamma \end{pmatrix}. \quad (8)$$

With these relations one can translate the results of a κ_i fit into the EWChL formalism and vice-versa. In order to do so, however, it is important to have all the relevant information about the fits. In particular, the median and errors of the parameters are not sufficient, since there may be also significant correlations between them.

2.9 Higgs couplings precision overview in the Kappa-framework and the nonlinear EFT

by Jorge de Blas, Otto Eberhardt, and Claudius Krause

After the discovery of the Higgs boson at the LHC, and the first exploration of the couplings of the new particle at the run 1 and 2, achieving an overall precision at the level of ten percent, one of the main goal of Higgs studies at the HL-LHC or HE-LHC will be to push such limits to a percent level. In this section we study the projected precision that would be possible at such high luminosity and high energy extensions of the LHC from a global fit to modifications of the different single Higgs couplings. Other important goals of the Higgs physics program at the HL/HE-LHC, such as extending/complementing the onshell studies with the study of differential distributions, or getting access to the Higgs trilinear coupling will be covered in other parts of this document.

Many explorations of deviation in Higgs couplings in the context of future proposed experiments are typically presented in the so called κ framework [2, 3]. In this phenomenological formalism one defines scaling factors, denoted κ_i , such that the production cross sections and decays of the Higgs boson involving the SM particle i , scale as κ_i^2 . This is indeed a helpful approach to quantify the precision in Higgs measurements. However, it lacks robustness from the theory point of view, as it cannot be extended at NLO and, in its more general form, misses correlations derived from well established symmetry principles. A more robust[/reliable] exploration of deformations in Higgs couplings can be performed within the formalism of effective field theories. In this section we consider the general parameterization provided by non-linear Higgs effective field theory. As explained, in section 2.8, as long as we restrict to the LO effective Lagrangian and one focuses only on deviations on Higgs couplings, it is possible to connect the results of this formalism to those from the κ framework. We refer the reader to section 2.8 for the introduction of the non-linear Higgs effective Lagrangian and its connection with the κ formalism. Throughout this section we will present the expected sensitivities to deviations on the Higgs couplings at the HL/HE-LHC, and compare with the recent results obtained using current data from [81]. A more general analysis going beyond pure modifications of Higgs couplings, allowing also for new physics

also in EW interactions, and combining the results of the Higgs fit with those from EW precision observables and diboson measurements will be presented in section ???. Such effect may become relevant once the precision on the Higgs measurements goes below the threshold were the sensitivity to other EW interactions is comparable to that from current EW precision tests.

In what follows we detail the fit procedure, the HL/HE-LHC projections used in our analysis, as well as the corresponding references for the analysis to current experimental data. We then present the results of the fit to the projected HL/HE-LHC uncertainties for the two formalisms mentioned above. We also translate the results from the fit to the HL/HE-LHC data in the EFT formalism in terms of composite Higgs scenarios. These are presented and discussed in section ??.

2.9.1 The fit to HL/HE-LHC Higgs precision data

The fits presented in this section have been performed using the `HEPfit` package [111, 112], and following a statistical Bayesian approach. The prior for the different model parameters both in the EFT and in the κ framework are taken as flat, centered around the SM solution, and restricting the ranges to avoid other solutions present due to the parametrization invariances of the different formalisms. Since no sensitivity to the $H \rightarrow c\bar{c}$ channel at the HL/HE-LHC has been reported yet we fix the corresponding parameters controlling the $Hc\bar{c}$ interactions to their SM values ($c_c, \kappa_c = 1$).¹

To assess the sensitivity to deviations from the SM, we assume the future measurements are SM-like and include them in the likelihood of the fit assuming Gaussian distributions with standard deviations given by the corresponding experimental uncertainty.

The analysis of current constraint has been taken directly from [81], it is based on the experimental data from [?, ?, ?, 41, 41, 47, 56–58, 58, 73, 73, 73, 75, 113–140]. For the HL-LHC fits we use [**We will use when available**] the corresponding ATLAS and CMS projections presented in section ?? of this document. For the systematics and theory uncertainties we use the 2 possible scenarios presented in section ??: S1, for which the systematics are kept as in current values, and S2, where experimental systematics are reduced with the luminosity and theory errors are reduced. Finally, we use our “naive” estimates for the HE-LHC uncertainties, derived from the detailed HL-LHC projection by scaling the statistical uncertainties according with the changes in the production cross section going from 14 TeV to 27 TeV, as well as the different luminosities (3 ab^{-1} for the HL-LHC and 15 ab^{-1} in the HE-LHC). Other experimental and theory uncertainties are kept as in the HL-LHC case, and we use the same S1 and S2 scenarios. To be conservative, no further scaling with the HE-LHC luminosity is applied in the scenario S2, i.e. it is kept as in the HL-LHC estimates.

2.9.2 Results

[PRELIMINARY: Based on preliminary CMS numbers from July + Our own guesstimates for HELHC (explained above). To be updated when the final experimental projections are available. Conclusions may therefore change.]

In Table 12 we show the results of the fit for the different scenarios discussed above for the non-linear Higgs effective Lagrangian. The numbers reported for the HE-LHC are obtained assuming the HL-LHC precision on the Higgs coupling is available at that time. No form of correlation between the HL-LHC and HE-LHC estimates is included, and therefore the results may be too optimistic. We also show the same results in Figure 25, where we also indicate the bound obtained at the HE-LHC alone. The analogous results for the fit using the κ formalism are presented in Table 26 and Figure 26. To make the comparison between the 2 approaches within the same theoretical grounds, we assume custodial symmetry as well as the absence of extra exotic decays of the Higgs in the κ fit. Focusing our attention

¹See [81] for a discussion of the multiplicities of the different solutions in the fit as well as the effect of letting the charm coupling float in the fits in absence of a significant direct constraint.

on the HL-LHC, and taking the conservative S1 scenario as the reference, we observe an improvement on the knowledge of Higgs coupling of at least a factor of 2-3 with respect to current experimental limits. The improvement is more notorious for channels that benefit from very high statistics, such as the $H \rightarrow \mu^+ \mu^-$ channel, with a precision almost 6 times better than in the current fit. Further progress is expected once we include the HE-LHC numbers, getting close to the 1% level of precision for the Higgs couplings to vector bosons and τ leptons, assuming theory and systematic uncertainties can be kept under control at the same level at the HL-LHC. One must be careful with the interpretation of these results though, since they implicitly assume only modifications in the Higgs couplings with respect to the SM or, in other words, that any other interaction entering on the relevant Higgs processes is known to be SM-like with infinite precision. At the level of precision we observe, close to the 1%, this may not be a justified assumption given current bounds on other electroweak interactions that could modify, e.g. VBF or VH associated production. This comment applies even more for the uncertainties obtained assuming the reduced theory and systematic uncertainties which, in particular, predict a subpercent precision for the Higgs coupling to vector bosons. We believe this to be too aggressive and that a realistic assessment of the HE-LHC uncertainties requires an equally realistic study of the experimental precisions at that machine, as well as the results of a full global fit combining Higgs data with other relevant observables of the EW sector. We refer to section ?? for more details in this regard.

	Current limits [81]	HL-LHC S1	HL-LHC S2	HE-LHC S1	HE-LHC S2
c_V	1.01 ± 0.06	± 0.021	± 0.015	± 0.013	± 0.008
c_t	$1.04^{+0.09}_{-0.1}$	± 0.049	± 0.028	± 0.031	± 0.016
c_b	0.95 ± 0.13	± 0.046	± 0.034	± 0.03	± 0.02
c_τ	1.02 ± 0.1	± 0.027	± 0.02	± 0.017	± 0.011
c_μ	$0.58^{+0.4}_{-0.38}$	± 0.069	± 0.052	± 0.035	± 0.02
c_g	$-0.01^{+0.08}_{-0.07}$	± 0.044	± 0.025	± 0.028	± 0.14
c_γ	0.05 ± 0.2	± 0.081	± 0.055	± 0.051	± 0.032

Table 12: Current and future constraints on c_i as shown in Figure 25.

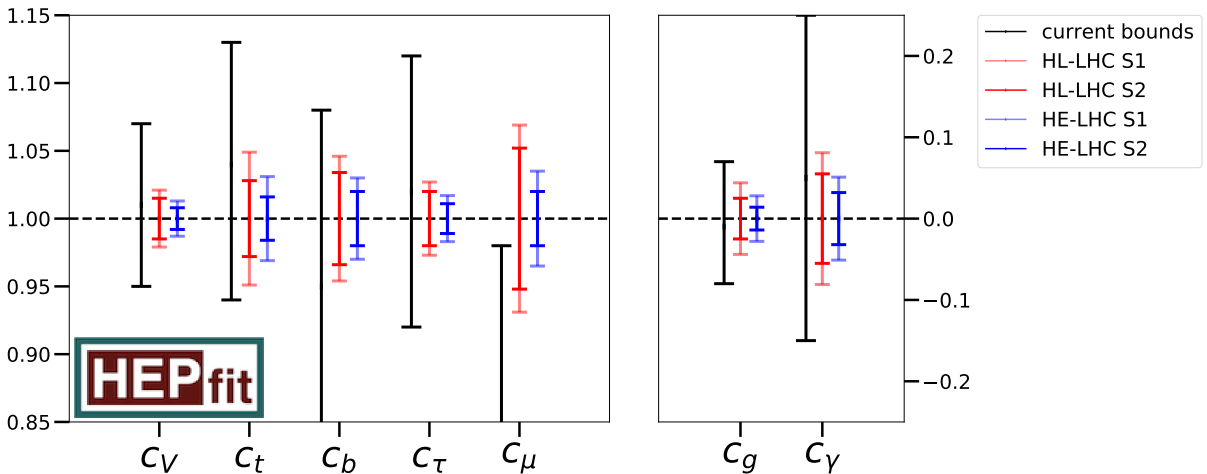


Fig. 25: Current and future constraints on c_i . The left line of each coupling is the current bound of [81]. The central line is the projection to the HL-LHC with scenario 1 in light red and scenario 2 in dark red. The right line is the projection to HE-LHC (including HL) with scenario 1 in light blue and scenario 2 in dark blue.

	Current limits [81]	HL-LHC S1	HL-LHC S2	HE-LHC S1	HE-LHC S2
κ_V	1.01 ± 0.06	± 0.021	± 0.015	± 0.013	± 0.008
κ_t	$1.04^{+0.09}_{-0.1}$	± 0.049	± 0.028	± 0.031	± 0.016
κ_b	0.94 ± 0.13	± 0.046	± 0.034	± 0.03	± 0.02
κ_τ	1.0 ± 0.1	± 0.027	± 0.02	± 0.017	± 0.011
κ_μ	$0.58^{+0.4}_{-0.38}$	± 0.069	± 0.052	± 0.035	± 0.02
κ_g	$1.02^{+0.08}_{-0.07}$	± 0.035	± 0.022	± 0.024	± 0.13
κ_γ	0.97 ± 0.07	± 0.028	± 0.02	± 0.017	± 0.011

Table 13: Current and future constraints on κ_i as shown in Figure 26.

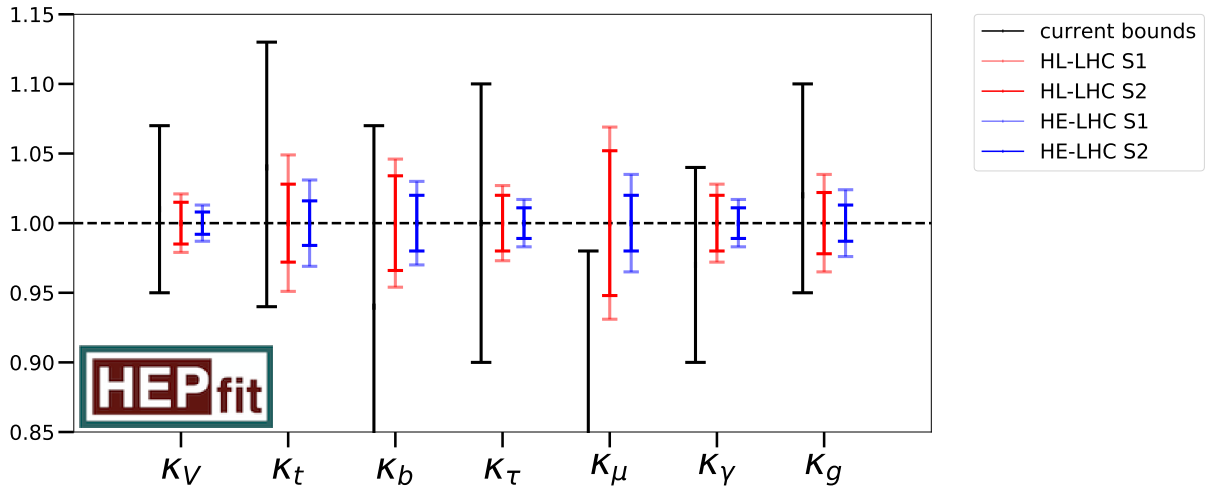


Fig. 26: Current and future constraints on κ_i . The left line of each κ is the current bound of [81]. The central line is the projection to the HL-LHC with scenario 1 in light red and scenario 2 in dark red. The right line is the projection to HE-LHC (including HL) with scenario 1 in light blue and scenario 2 in dark blue.

2.10 Projections of Higgs boson measurements to the HE-LHC

To be written by: J.Ellis, L.Silvestrini

2.11 Probing of anomalous HVV interactions

2.11.1 Probes using differential distributions of CP sensitive observables

To be written by: F. Piccinini, F. Yu, A. Shivaji, ???

By S. Boselli, C. M. Carloni Calame, G. Montagna, O. Nicrosini, F. Piccinini, A. Shivaji, F. Yu, Maria Moreno Llacer et al.

We present prospects for studies on CP -odd couplings in the couplings of the Higgs boson with the electroweak gauge bosons as well as in the Yukawa couplings of the Higgs boson with fermions, in particular with $\tau^+\tau^-$ pairs.

2.11.1.1 CP-odd VVH couplings

While a large number of studies assessing the impact of CP -even effective operators on Higgs physics is available in the literature (see for instance our analysis in Ref. [141] and the references therein),

Process	Combination	Theory	Systematic	Statistical
$H \rightarrow ZZ$	ggF	0.06	0.05	0.02
	VBF	0.17	0.10	0.10
	WH	0.16	0.06	0.13
	ZH	0.21	0.08	0.18
	$t\bar{t}H$	0.20	0.12	0.15

Table 14: Estimated relative uncertainties on the determination of single-Higgs production channels. The estimation of experimental uncertainties is for the high-luminosity LHC (14 TeV center of mass energy and 3 ab^{-1} integrated luminosity) [1]. The theoretical uncertainties are taken from [2].

the present analysis is focused on the impact of CP -odd effective operators on the interactions among the Higgs boson and the electroweak bosons. In the Higgs basis, the CP -violating sector of the BSM Lagrangian affecting VVH couplings is given by,

$$\mathcal{L}_{\text{CPV}} = \frac{H}{v} \left[\tilde{c}_{\gamma\gamma} \frac{e^2}{4} A_{\mu\nu} \tilde{A}^{\mu\nu} + \tilde{c}_{Z\gamma} \frac{e\sqrt{g_1^2 + g_2^2}}{2} Z_{\mu\nu} \tilde{A}^{\mu\nu} + \tilde{c}_{ZZ} \frac{g_1^2 + g_2^2}{4} Z_{\mu\nu} \tilde{Z}^{\mu\nu} + \tilde{c}_{WW} \frac{g_2^2}{2} W_{\mu\nu}^+ \tilde{W}^{-\mu\nu} \right] \quad (9)$$

where, g_1 and g_2 are the $U(1)_Y$ and $SU(2)_L$ gauge coupling constants. Out of the above four parameters only three of them are independent. In particular,

$$\tilde{c}_{WW} = \tilde{c}_{ZZ} + 2s_\theta^2 \tilde{c}_{Z\gamma} + s_\theta^4 \tilde{c}_{\gamma\gamma}. \quad (10)$$

The processes which are sensitive to CPV operators are the Higgstrahlung processes (WH and ZH), the vector boson fusion (VBF) and the Higgs decay into four charged leptons ($H \rightarrow 4\ell$). Here we focus on angular observables which are sensitive to CPV effects. Indeed, since the total cross-section is a CP -even quantity, the $1/\Lambda^2$ effects of CPV operators can affect the shape of some specific kinematic distributions only.

2.11.1.2 Global Fit

To study the sensitive on CP-violating parameters $\tilde{c}_{Z\gamma}$ and \tilde{c}_{ZZ} at HL and HE-LHC, we perform a χ^2 fit using the signal strength ($\mu_{i,f}$) as the observable. We can build a χ^2 as follows:

$$\chi^2(\tilde{c}_{Z\gamma}, \tilde{c}_{ZZ}) = \sum_{i,f} \frac{(\mu_{i,f} - \mu_{i,f}^{\text{obs.}})^2}{\Delta_{i,f}^2} \quad (11)$$

The signal strength, $\mu_{i,f}$ is function of the BSM parameters and it is defined as,

$$\mu_{i,f} = \mu_i \times \mu_f \quad (12)$$

$$= \frac{\sigma_i^{\text{BSM}}}{\sigma_i^{\text{SM}}} \times \frac{\text{BR}_f^{\text{BSM}}}{\text{BR}_f^{\text{SM}}}. \quad (13)$$

The uncertainty, $\Delta_{i,f}^2$ includes theoretical, experimental systematic and statistical uncertainties which are added in quadrature to obtain the total uncertainty. The one-sigma uncertainties for the high-luminosity (14 TeV center of mass energy and 3 ab^{-1} integrated luminosity) are given in table 14. Assuming same acceptance efficiency, we scale the statistical uncertainties at 14 TeV and 3 ab^{-1} luminosity appropriately to obtain the statistical uncertainties at 27 TeV and 15 ab^{-1} luminosity. The theoretical and systematic uncertainties are kept unchanged.

When considering kinematic distribution in the fit, we estimate the statistical uncertainty in each bin by scaling the overall statistical uncertainty by the fraction of number of events in each bin. On the other hand, the theoretical and systematic uncertainties are assumed to be the same in all the bins implying a very conservative scenario.

Since we are interested in the sensitivity on the CPV parameters that can be reached at HL and HE LHC for which we don't have any data, we take $\mu_{i,f}^{\text{obs.}} = 1$ implying that the future data would be consistent with the SM hypothesis. In the current analysis we consider all the production channels and Higgs decaying to four charged-lepton that is, $i = \text{ggF}, \text{VBF}, ZH, WH, t\bar{t}H$ and $f = 4\ell(2e2\mu, 4e, 4\mu)$. The projected uncertainties in these channels for HL-LHC are given in table 14. Note that only the $H \rightarrow 4\ell$ decay mode has a non-trivial kinematic distribution and therefore other decay modes in the present analysis have been ignored. All the results in the following sections are presented taking $M_H = 125$ GeV.

Production signal strengths : Inclusive

The first step is to calculate the signal strengths for the relevant production channels in presence of the CP-violating parameters $\tilde{c}_{Z\gamma}$ and \tilde{c}_{ZZ} . We use MG5 [] to obtain the inclusive cross sections in presence of these parameters. We have generated the required UFO model file for MG5 using the FeynRules package []. At 14 TeV, the production signal strengths are given by,

$$\mu_{ZH}^{14\text{TeV}} = 1.00 + 0.54 \tilde{c}_{Z\gamma}^2 + 2.80 \tilde{c}_{ZZ}^2 + 0.95 \tilde{c}_{Z\gamma}\tilde{c}_{ZZ} \quad (14)$$

$$\mu_{WH}^{14\text{TeV}} = 1.00 + 0.84 \tilde{c}_{Z\gamma}^2 + 3.87 \tilde{c}_{ZZ}^2 + 3.63 \tilde{c}_{Z\gamma}\tilde{c}_{ZZ} \quad (15)$$

$$\mu_{\text{VBF}}^{14\text{TeV}} = 1.00 + 0.25 \tilde{c}_{Z\gamma}^2 + 0.45 \tilde{c}_{ZZ}^2 + 0.45 \tilde{c}_{Z\gamma}\tilde{c}_{ZZ} \quad (16)$$

At 27 TeV, the corresponding signal strengths are given by,

$$\mu_{ZH}^{27\text{TeV}} = 1.00 + 0.63 \tilde{c}_{Z\gamma}^2 + 3.26 \tilde{c}_{ZZ}^2 + 1.11 \tilde{c}_{Z\gamma}\tilde{c}_{ZZ} \quad (17)$$

$$\mu_{WH}^{27\text{TeV}} = 1.00 + 0.98 \tilde{c}_{Z\gamma}^2 + 4.48 \tilde{c}_{ZZ}^2 + 4.16 \tilde{c}_{Z\gamma}\tilde{c}_{ZZ} \quad (18)$$

$$\mu_{\text{VBF}}^{27\text{TeV}} = 1.00 + 0.32 \tilde{c}_{Z\gamma}^2 + 0.67 \tilde{c}_{ZZ}^2 + 0.65 \tilde{c}_{Z\gamma}\tilde{c}_{ZZ} \quad (19)$$

The BSM predictions for VBF are derived using following cuts,

$$p_T(j) > 20 \text{ GeV}, |\eta(j)| < 5, \Delta\eta_{jj} > 3, m_{jj} > 130 \text{ GeV}.$$

The VH production modes are more sensitive to \tilde{c}_{ZZ} parameters. The ggF and $t\bar{t}H$ production channels are unaffected in presence of CP-violating VVH couplings. Therefore,

$$\mu_{\text{ggF}}^{14\text{TeV}} = \mu_{\text{ggF}}^{27\text{TeV}} = 1.00 \quad (20)$$

$$\mu_{t\bar{t}H}^{14\text{TeV}} = \mu_{t\bar{t}H}^{27\text{TeV}} = 1.00. \quad (21)$$

In the present analysis we do not consider any kinematic distribution in the production channels.

Decay signal strength : Inclusive

Now we turn to the calculation of signal strength for the decay channel $H \rightarrow 4\ell$. This decay channel receives contributions from $2e^+2e^-$ ($4e$), $2\mu^+2\mu^-$ (4μ) and $e^+e^-\mu^+\mu^-$ ($2e2\mu$) final states. We use the latest version of the Hto4l event generator [141] to obtain the partial decay widths in these

channels in presence of $\tilde{c}_{Z\gamma}$ and \tilde{c}_{ZZ} . Both the e and μ are treated massless. The ratio of the partial decay widths in BSM and in SM (R_Γ) for different channels are given by,

$$R_\Gamma(H \rightarrow 2e2\mu) = 1 + 1.174 \tilde{c}_{Z\gamma}^2 + 0.00291 \tilde{c}_{ZZ}^2 + (-0.00762) \tilde{c}_{Z\gamma} \tilde{c}_{ZZ} \quad (22)$$

$$\begin{aligned} R_\Gamma(H \rightarrow 4e) &= R_\Gamma(H \rightarrow 4\mu) \\ &= 1 + 1.106 \tilde{c}_{Z\gamma}^2 + 0.00241 \tilde{c}_{ZZ}^2 + (-0.00595) \tilde{c}_{Z\gamma} \tilde{c}_{ZZ}. \end{aligned} \quad (23)$$

The above expression for Higgs decay into $4e$ is obtained after applying a selection cut of 4 GeV on the leading and subleading lepton pairs of opposite sign.

In the present analysis, we also assume that total Higgs decay width remains unchanged in presence of BSM. In this case, the signal strength for decay is just the ratio of decay widths in BSM and in SM.

$$\begin{aligned} \mu_{4\ell} &= \frac{\Gamma_{4\ell}^{\text{BSM}}}{\Gamma_{4\ell}^{\text{SM}}} \\ &= 1 + 1.138 \tilde{c}_{Z\gamma}^2 + 0.00265 \tilde{c}_{ZZ}^2 + (-0.00674) \tilde{c}_{Z\gamma} \tilde{c}_{ZZ} \end{aligned} \quad (24)$$

We note that, the dependence of the 4ℓ decay signal strength on the parameter \tilde{c}_{ZZ} is very weak.

Decay signal strength : Differential

In our analysis, we are interested in assessing the role of kinematic distributions in $H \rightarrow 4\ell$ decay channel which are affected by CP-violating VVH couplings, in improving the sensitivity on $\tilde{c}_{Z\gamma}$ and \tilde{c}_{ZZ} at HL and HE-LHC. The Higgs rest frame angle ϕ between the decay planes of the two intermediate gauge bosons is one of the most sensitive kinematic observables to the CP-Violating VVH couplings. We have considered 50 bins of ϕ -distribution to perform the fit at differential level. For each bin, we calculate the signal strength ($\mu_{4\ell}^j, j = 1 \rightarrow 50$) corresponding to Eq. 24 which is also sensitive to linear terms in $\tilde{c}_{Z\gamma}$ and \tilde{c}_{ZZ} .

2.11.1.3 Result: HL and HE-LHC Analysis

The results of the χ^2 fit are displayed in Fig. 27 and Fig. 28. In these results, *incl.* refers to the fit obtained using the total partial decay width information in the $H \rightarrow 4\ell$ channel, while *diff.* refers to the fit obtained using ϕ -distribution in $H \rightarrow 4\ell$ decay. In Fig. 27, we show 1σ and 2σ bounds on $\tilde{c}_{Z\gamma}$ and \tilde{c}_{ZZ} in a one parameter (1P) analysis. At the inclusive level we gain better sensitivity on \tilde{c}_{ZZ} than on $\tilde{c}_{Z\gamma}$ when going from HL-LHC to HE-LHC. However, due to a stronger dependence of $\mu_{4\ell}$ on $\tilde{c}_{Z\gamma}$ the effect of using ϕ -distribution in the fit is larger for $\tilde{c}_{Z\gamma}$ than for \tilde{c}_{ZZ} .

In Fig. 28, we provide 1σ contour lines in the $\tilde{c}_{Z\gamma} - \tilde{c}_{ZZ}$ plane. We can see that the parameters $\tilde{c}_{Z\gamma}$ and \tilde{c}_{ZZ} are weakly correlated. Once again we find that using ϕ -distribution in the fit improves our sensitivity on CP-violating parameters significantly. The parameter \tilde{c}_{ZZ} is mainly constrained by the production channels VH and VBF . We have given a summary of 1σ bounds on $\tilde{c}_{Z\gamma}$ and \tilde{c}_{ZZ} obtained from our analysis for HL and HL-LHC in Table 15.

2.11.1.4 $h \rightarrow \tau^+ \tau^-$

The most promising direct probe of CP violation in fermionic Higgs decays is the $\tau^+ \tau^-$ decay channel, which benefits from a relatively large τ Yukawa giving a SM branching fraction of 6.3%. Measuring the CP violating phase in the tau Yukawa requires a measurement of the linear polarizations of both τ leptons and the azimuthal angle between them. This can be done by analyzing tau substructure, namely the angular distribution of the various components of the tau decay products.

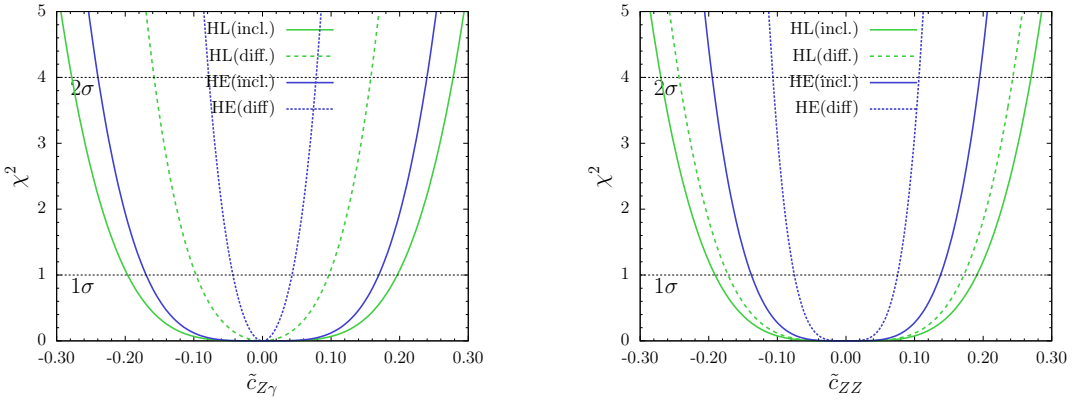


Fig. 27: χ^2 dependence on CP-violating parameters taking one parameter non-zero at a time at HL (3 ab^{-1}) and HE (15 ab^{-1}) LHC. Preliminary

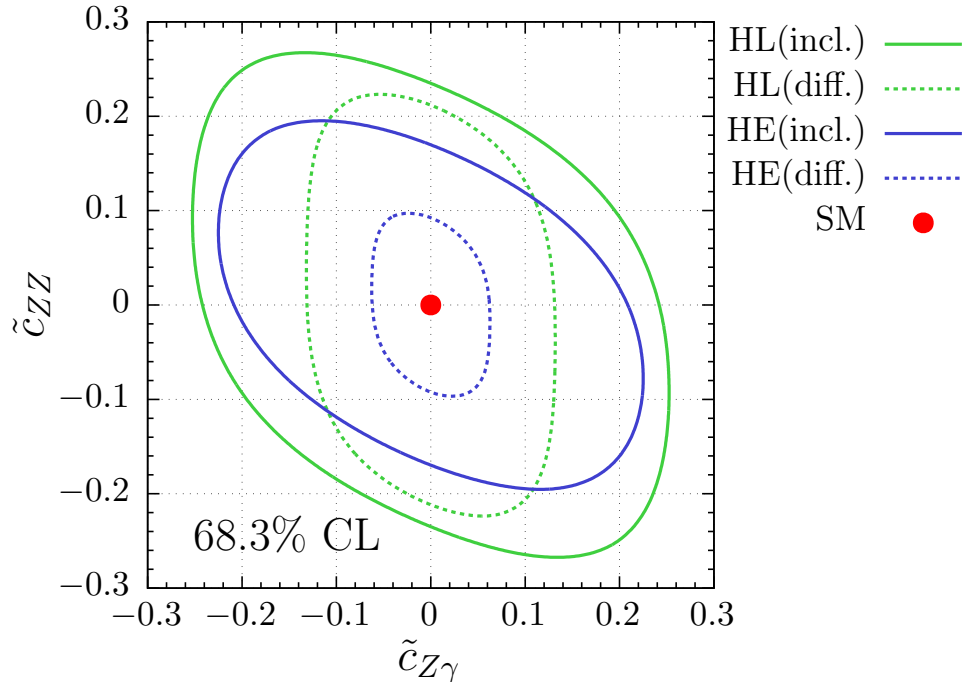


Fig. 28: 1σ reach on $\tilde{c}_{Z\gamma}$ and \tilde{c}_{ZZ} at HL (3 ab^{-1}) and HE (15 ab^{-1}) LHC. Preliminary

The main τ decay modes studied include $\tau^\pm \rightarrow \rho^\pm(770)\nu$, $\rho^\pm \rightarrow \pi^\pm\pi^0$ [142–147] and $\tau^\pm \rightarrow \pi^\pm\nu$ [148–150]. Assuming CPT symmetry, collider observables for CP violation must be built from differential distributions based on triple products of three-vectors. In the first case, $h \rightarrow \pi^\pm\pi^0\pi^\mp\pi^0\nu\nu$, angular distributions built only from the outgoing charged and neutral pions are used to determine the CP properties of the initial τ Yukawa coupling. In the second case, $h \rightarrow \pi^\pm\pi^\mp\nu\nu$, there are not enough reconstructible independent momenta to construct an observable sensitive to CP violation, requiring additional kinematic information such as the τ decay impact parameter.

In the kinematic limit when each outgoing neutrino is taken to be collinear with its corresponding reconstructed ρ^\pm meson, the acoplanarity angle, denoted Φ , between the two decay planes spanned by the $\rho^\pm \rightarrow \pi^\pm\pi^0$ decay products is exactly analogous to the familiar acoplanarity angle from $h \rightarrow 4\ell$ CP-property studies. Hence, by measuring the τ decay products in the single-prong final state, suppressing the irreducible $Z \rightarrow \tau^+\tau^-$ and reducible QCD backgrounds, and reconstructing the acoplanarity angle

Parameter Analysis	$\tilde{c}_{Z\gamma}$	\tilde{c}_{ZZ}	Case
HL-LHC (4ℓ , incl.)	[-0.20,0.20]	[-0.19,0.19]	1P
HL-LHC (4ℓ , incl.)	[-0.26,0.26]	[-0.26,0.26]	1P _{marg.}
HL-LHC (4ℓ , diff.)	[-0.10,0.10]	[-0.17,0.17]	1P
HL-LHC (4ℓ , diff.)	[-0.13,0.13]	[-0.22,0.22]	1P _{marg.}
HE-LHC (4ℓ , incl.)	[-0.17,0.17]	[-0.14,0.14]	1P
HE-LHC (4ℓ , incl.)	[-0.22,0.22]	[-0.20,0.20]	1P _{marg.}
HE-LHC (4ℓ , diff.)	[-0.04,0.04]	[-0.07,0.07]	1P
HE-LHC (4ℓ , diff.)	[-0.06,0.06]	[-0.10,0.10]	1P _{marg.}

Table 15: Summary of 1σ bounds on $\tilde{c}_{Z\gamma}$ and \tilde{c}_{ZZ} from various analysis considered here. 1P refers to the case where only one parameter is non-zero while 1P_{marg.} refers to the case in which one of the two parameters is marginalized. **Preliminary**

of ρ^+ vs. ρ^- , the differential distribution in Φ gives a sinusoidal shape whose maxima and minima correspond to the CP-phase in the τ Yukawa coupling.

An optimal observable using the colinear approximation was derived in [145]. Assuming 70% efficiency for tagging hadronic τ final states, and neglecting detector effects, the estimated sensitivity for the CP-violating phase of the τ Yukawa coupling using 3 ab^{-1} at the HL-LHC is 8.0° . A more sophisticated analysis [146] found that detector resolution effects on the missing transverse energy distribution degrade the expected sensitivity considerably, and as such, about 1 ab^{-1} is required to distinguish a pure scalar coupling (CP phase is zero) from a pure pseudoscalar coupling (CP phase is $\pi/2$).

At the HE-LHC, the increased signal cross section for Higgs production is counterbalanced by the increased background rates, and so the main expectation is that improvements in sensitivity will be driven by the increased luminosity and more optimized experimental methodology. Rescaling with the appropriate luminosity factors, the optimistic sensitivity to the τ Yukawa phase from acoplanarity studies is $4\text{-}5^\circ$, while the more conservative estimate is roughly an order of magnitude worse.

2.11.1.5 $t\bar{t}h$

CP violation in the top quark-Higgs coupling is strongly constrained by EDM measurements and Higgs rate measurements [151]. However, these constraints assume that the light quark Yukawa couplings and hWW couplings have their SM values. If this is not the case, the constraints the phase of the top Yukawa coupling relax.

Assuming the EDM and Higgs rate constraints can be avoided, the CP structure of the top quark Yukawa can be probed directly in $pp \rightarrow t\bar{t}h$. Many simple observables, such as $m_{t\bar{t}h}$ and $p_{T,h}$ are sensitive to the CP structure, but require reconstructing the top quarks and Higgs.

Some $t\bar{t}h$ observables have been proposed recently that access the CP structure without requiring full event reconstruction. These include the azimuthal angle between the two leptons in a fully leptonic $t/bart$ decay with the additional requirement that the $p_{T,h} > 200 \text{ GeV}$ [152], and the angle between the leptons (again in a fully leptonic t/\bar{t} system) projected onto the plane perpendicular to the h momentum [153]. These observables only require that the Higgs is reconstructed and are inspired by the sensitivity of $\Delta\phi_{\ell^+\ell^-}$ to top/anti-top spin correlations in $pp \rightarrow t\bar{t}$ [154]. The sensitivity of both of these observables improves at higher Higgs boost (and therefore higher energy), making them promising targets for the HE-LHC, though no dedicated studies have been carried out to date.

2.11.2 Experimental constraints on anomalous HVV couplings

To be written by: U. Sarica

2.12 Summary

To be written by: S. Alioli, M. Duehrssen, P. Milenovic

3 Di-Higgs production and Higgs self couplings

3.1 NLO cross sections

3.1.1 SM Calculation

3.1.1.1 HH production in subdominant channels

by Eleni Vryonidou

\sqrt{s} (TeV)	ZHH	WHH	VBF HH	$t\bar{t}HH$	$tjHH$
14	$0.359^{+1.9\%}_{-1.3\%} \pm 1.7\%$	$0.573^{+2.0\%}_{-1.4\%} \pm 1.9\%$	$1.95^{+1.1\%}_{-1.5\%} \pm 2.0\%$	$0.948^{+3.9\%}_{-13.5\%} \pm 3.2\%$	$0.0383^{+5.2\%}_{-3.3\%} \pm 4.7\%$
27	$0.963^{+2.1\%}_{-2.3\%} \pm 1.5\%$	$1.48^{+2.3\%}_{-2.5\%} \pm 1.7\%$	$8.21^{+1.1\%}_{-0.7\%} \pm 1.8\%$	$5.27^{+2.0\%}_{-3.7\%} \pm 2.5\%$	$0.254^{+3.8\%}_{-2.8\%} \pm 3.6\%$

Table 16: Signal cross section (in fb) for HH production at NLO QCD.

Results have been obtained within the MADGRAPH5_AMC@NLO [155] framework, as in Ref. [156]. The renormalisation and factorisation scale was set to $m_{HH}/2$ and varied up and down by a factor of two to obtain the scale uncertainties. The 5-flavour PDF4LHC NLO Monte Carlo PDF set was used to obtain the results (LHAPDF: 90500). The WHH results are the sum of the W^+ and W^- cross-sections. Similarly $tjHH$ involves both top and anti-top production.

3.1.1.2 Probing the Higgs boson self-coupling in di-Higgs production with full m_t -dependence at NLO QCD

by Gudrun Heinrich, Stephen Jones, Matthias Kerner, Gionata Luisoni, Ludovic Scyboz

While the couplings of the Higgs boson to vector bosons are very well measured meanwhile, and the couplings to third generation fermions also start to be well constrained and seem to confirm the Standard Model, the Higgs boson self-coupling could still reveal clear signs of New Physics. As it is not too far-fetched to have BSM scenarios in mind where the trilinear Higgs boson coupling λ is different from the SM value at the $\mathcal{O}(10\%)$ level, while the deviations in other Higgs boson couplings are at the percent level, we consider λ variations only in this section. In particular, we announce a version of the ggHH code [157–159] implemented in the POWHEG-BOX-V2 [160] where variations of λ are accessible to the user in a parton shower Monte Carlo program at full NLO.

3.1.1.3 Total cross sections at different values of the trilinear coupling

In Table 17 we list total cross sections at 14 TeV and 27 TeV for various values of the trilinear Higgs coupling λ . The results have been obtained using the parton distribution functions PDF4LHC15_nlo_100_pdfsas [?, 25, 161, 162], along with the corresponding value for α_s for both the NLO and the LO calculation. The masses have been set to $m_h = 125$ GeV, $m_t = 173$ GeV, and the top quark width has been set to zero. The scale uncertainties are the result of a 7-point scale variation around the central scale $\mu_0 = m_{hh}/2$, with $\mu_{R,F} = c_{R,F} \mu_0$, where $c_R, c_F \in \{2, 1, 0.5\}$, except that the extreme variations $(c_R, c_F) = (2, 0.5)$ and $(c_R, c_F) = (0.5, 2)$ are omitted.

Table 17 also shows that the K-factors do vary substantially as functions of the trilinear coupling. This fact is illustrated in Fig. 29, where it is demonstrated that the K-factor takes values between 1.57 and 2.16 if the trilinear coupling is varied between $-5 \leq c_{hhh} \leq 12$.

3.1.1.4 Differential cross sections at 14 TeV and 27 TeV

In Figs. 30 and 31 we show the m_{hh} distribution for various values of $c_{hhh} = \lambda_{\text{BSM}}/\lambda_{\text{SM}}$. The ratio plots show the differential K-factors.

$\lambda_{\text{BSM}}/\lambda_{\text{SM}}$	$\sigma_{\text{NLO}}@14\text{TeV} [\text{fb}]$	$\sigma_{\text{NLO}}@27\text{TeV} [\text{fb}]$	K-fac.@14TeV	K-fac.@27TeV
1	$32.88^{+13.5\%}_{-12.5\%}$	$127.7^{+11.5\%}_{-10.4\%}$	1.66	1.62
2	14.91	59.10		
2.4	xx	yy		
3	19.82	69.84		
5	98.42			
0	73.84	275.29		
-1	137.69			

Table 17: Total cross sections for Higgs boson pair production at full NLO. The given uncertainties are scale uncertainties. A statistical uncertainty of about 0.3% is not included in the quoted uncertainties.

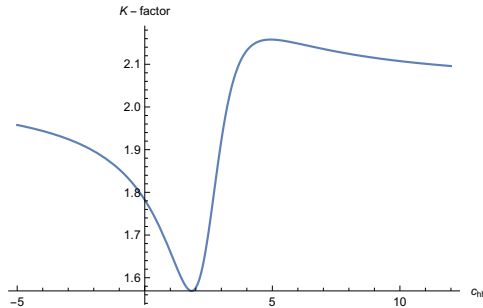
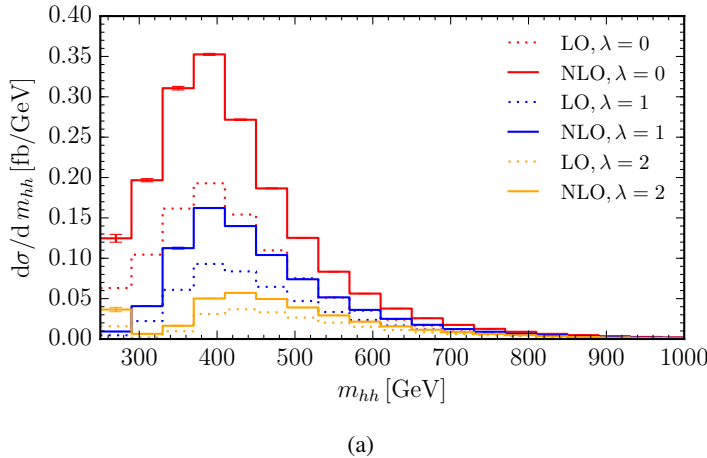


Fig. 29: Variation of the NLO K-factor with the trilinear coupling, $\sqrt{s} = 14 \text{ TeV}$.



(a)

Fig. 30: Higgs boson pair invariant mass distributions for various values of λ (relative to λ_{SM}) at 14 TeV.

... add 27TeV plots including ratio plots, to be completed

Fig. 32 shows the Higgs boson pair invariant mass distributions at NLO as a function of c_{hhh} as 3-dimensional heat maps. The other couplings are fixed to their SM values.

3.1.2 Di-Higgs production in the non-linear EFT with full m_t -dependence at NLO QCD

by Gerhard Buchalla, Alejandro Celis, Matteo Capozi, Gudrun Heinrich, Ludovic Scyboz

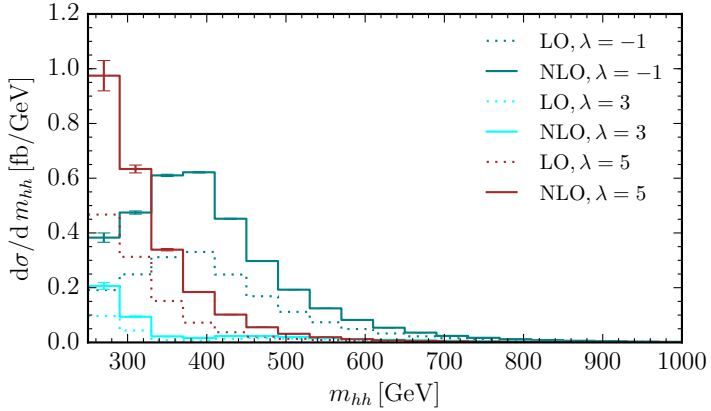


Fig. 31: Higgs boson pair invariant mass distributions for $\lambda/\lambda_{\text{SM}} = -1, 3, 5$ at 14 TeV.

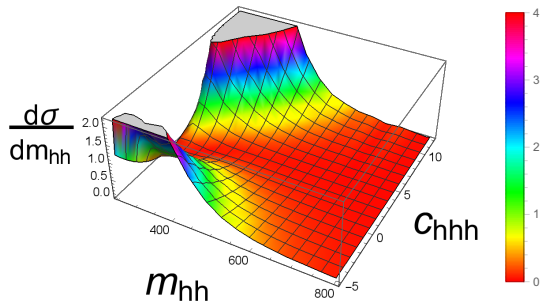


Fig. 32: 3-dimensional visualisation of the m_{hh} distribution at 14 TeV, as a function c_{hhh} .

3.1.2.1 The Higgs sector in the non-linear EFT framework

Below we will describe the potential impact of physics beyond the Standard Model through a non-linear Effective Field Theory (EFT), also called the electroweak chiral Lagrangian including a light Higgs boson [98, 99, 101]. This framework provides us with a consistent EFT for New Physics in the Higgs sector, where the Higgs field is an electroweak singlet h , independent of the Goldstone matrix $U = \exp(2i\varphi^a T^a/v)$. The latter transforms as $U \rightarrow g_L U g_Y^\dagger$ under the SM gauge group. The symmetry is non-linearly realised on the Goldstone fields φ^a , therefore the name non-linear EFT. More details about this framework already have been given in Section 2.8. Therefore we restrict ourselves to stating the part of the Lagrangian relevant for our study of anomalous Higgs couplings:

$$\mathcal{L} \supset -m_t \left(c_t \frac{h}{v} + c_{tt} \frac{h^2}{v^2} \right) \bar{t} t - c_{hhh} \frac{m_h^2}{2v} h^3 + \frac{\alpha_s}{8\pi} \left(c_{ggh} \frac{h}{v} + c_{gghh} \frac{h^2}{v^2} \right) G_{\mu\nu}^a G^{a,\mu\nu}. \quad (25)$$

To lowest order in the SM $c_t = c_{hh} = 1$ and $c_{tt} = c_{ggh} = c_{gghh} = 0$. In general, all couplings may have arbitrary values of $\mathcal{O}(1)$. Note that we have extracted a loop factor from the definition of the Higgs-gluon couplings.

The leading-order diagrams are shown in Fig. 33.

Examples for virtual diagrams at NLO are shown in Fig. 34. For further details we refer to Ref. [106].

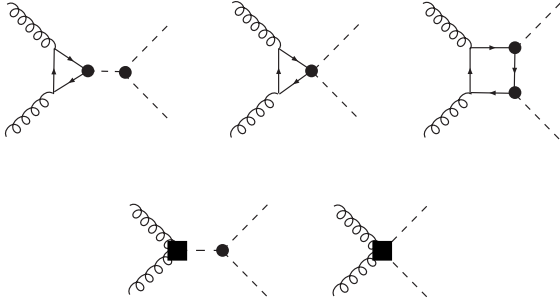


Fig. 33: Higgs-pair production in gluon fusion at leading order in the non-linear EFT Lagrangian.

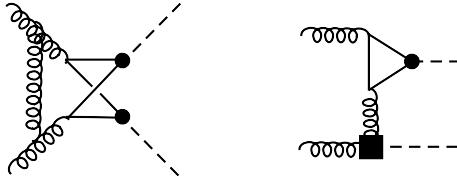


Fig. 34: Examples of virtual diagrams contributing at NLO QCD.

3.1.2.2 Total cross sections for 14 and 27 TeV at some benchmark points

In the following we will show results for some benchmark points, specified in Table 18, some of them having been first defined in Refs. [163]. The results at 14 TeV and 27 TeV are given in Table 19. Note that our conventions for c_{ggh} and c_{gghh} differ from the ones in Ref. [163, 164], the relations are $c_{ggh} = \frac{2}{3}c_g$ and $c_{gghh} = -\frac{1}{3}c_{2g}$, where c_g, c_{2g} are the couplings defined in Refs. [163, 164]. We also take into account recent constraints on c_{ggh} from Refs. [81, 165] and the limits on the Higgs boson pair production cross section from Refs [166, 167]. This is why we do not show results for the original benchmark point 5 anymore, as its value for c_{ggh} is outside the 2-sigma band of a combined fit of c_{ggh}, c_t from single Higgs production data [81, 165]. Benchmark point 6 is interesting because its value for c_{hh} is near the point where maximal destructive interference takes place between triangle-type and box-type contributions if the other couplings are SM-like, leading to a total cross section which is below the SM value.

Benchmark	c_{hh}	c_t	c_{tt}	c_{ggh}	c_{gghh}
5a	1	1	0	2/15	4/15
6	2.4	1	0	2/15	1/15
7	5	1	0	2/15	1/15
8a	1	1	1/2	4/15	0
SM	1	1	0	0	0

Table 18: Benchmark points used for the distributions shown below.

Table 19 shows that the total cross sections increase by a factor of 3.5-5 when increasing the centre-of-mass energy from 14 TeV to 27 TeV. The increase for B_{5a} is largest because of the large value of c_{gghh} , which yields a contribution growing linearly with energy.

3.1.2.3 HH invariant mass distributions at 14 and 27 TeV at some benchmark points

In Figs. 35 and 36 we show Higgs boson pair invariant mass distributions for the benchmark points 7 and 8a. For both of them the shape of the distribution is very different from the SM one, and the K-

Benchmark	σ_{NLO} [fb]	K-factor	scale uncert. [%]	stat. uncert. [%]	$\frac{\sigma_{NLO}}{\sigma_{NLO,SM}}$
B_{5a} [14 TeV]			$+x, -y$		
B_{5a} [27 TeV]			$+x, -y$		
B_6 [14 TeV]	24.69	1.89	$+2, -11$	2.1	0.75
B_6 [27 TeV]			$+x, -y$		
B_7 [14 TeV]	169.41	2.07	$+9, -12$	2.2	5.14
B_7 [27 TeV]	598.20	2.11	$+8, -10$	2.0	4.68
B_{8a} [14 TeV]	41.70	2.34	$+6, -9$	0.63	1.27
B_{8a} [27 TeV]	179.52	2.33	$+4, -7$	0.49	1.40
SM [14 TeV]	32.95	1.66	$+14, -13$	0.1	1
SM [27 TeV]	127.7	1.62	$+12, -10$	0.1	1

Table 19: Total cross sections at 14 and 27 TeV at NLO (2nd column), K-factor σ_{NLO}/σ_{LO} (3rd column), scale uncertainty (4th column), statistical uncertainty (5th column) and the ratio to the SM total cross section at NLO (6th column).

factor is non-homogeneous over the whole m_{hh} -range. Benchmark point 7 is characterised by a large enhancement of the low m_{hh} region, induced by the large value of c_{hhh} . The lower ratio plot shows the ratio of the two approximations “Born-improved HEFT” and “FT_{approx}” to the full NLO, where the former denotes the $m_t \rightarrow \infty$ limit rescaled by the m_t -dependent LO, while FT_{approx} includes the Born-improved $m_t \rightarrow \infty$ limit for the virtual part and the full m_t -dependence for the real radiation part. One can see from Fig. ?? that these approximations are off by about 20% even below the $2m_t$ threshold. Therefore one cannot claim that the $m_t \rightarrow \infty$ limit works well in the region below ~ 400 GeV. As the triangle-type contributions are dominating for $c_{hhh} = 5$, their full m_t -dependence plays a significant role.

Benchmark point 8a shows a characteristic dip near $m_{hh} = 2m_t$ and an enhancement in the tail compared to the SM. As the total cross section for B_{8a} is very similar to the SM one, both at 14 TeV and at 27 TeV, this is an example where the discriminating power of differential information is very important.

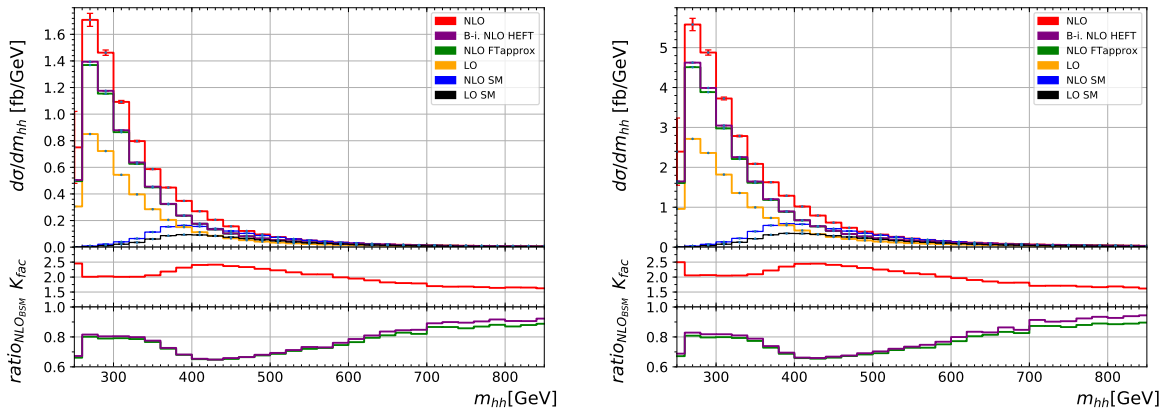


Fig. 35: Higgs boson pair invariant mass distributions for benchmark point 7, $c_{hhh} = 5$, $c_t = 1$, $c_{tt} = 0$, $c_{ggh} = 2/15$, $c_{gggh} = 1/15$, at 14 TeV (left) and 27 TeV (right).

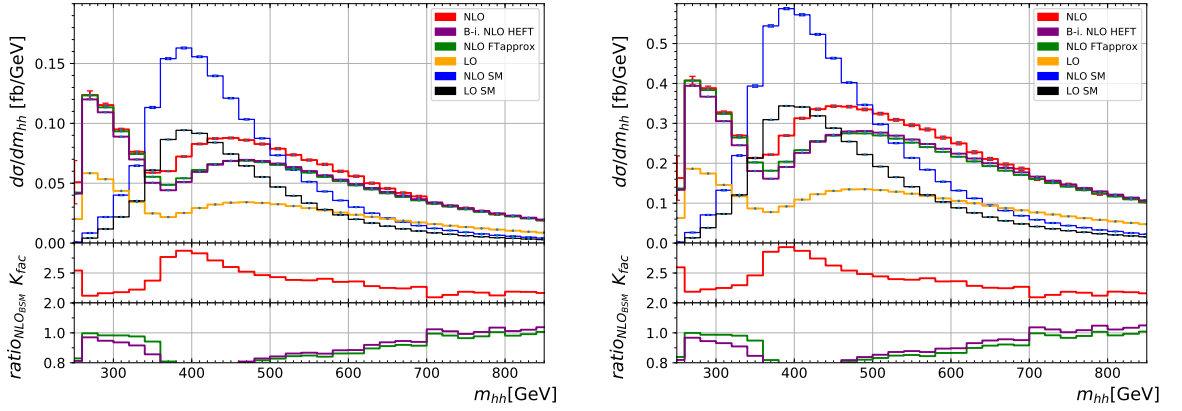


Fig. 36: Higgs boson pair invariant mass distributions for benchmark point 8a, $c_{hhh} = 1$, $c_t = 1$, $c_{tt} = 0.5$, $c_{ggh} = 4/15$, $c_{gghh} = 0$, at 14 TeV (left) and 27 TeV (right).

3.1.2.4 Characterising the BSM parameter space

The total cross section can be written in terms of the 15 coefficients A_1, \dots, A_{15} , at LO [163, 168] and in terms of 23 coefficients at NLO [106].

$$\begin{aligned} \sigma^{\text{NLO}} / \sigma_{SM}^{\text{NLO}} = & \\ & A_1 c_t^4 + A_2 c_{tt}^2 + A_3 c_t^2 c_{hhh} + A_4 c_{ggh}^2 c_{hhh} + A_5 c_{gghh}^2 + A_6 c_{tt} c_t^2 + A_7 c_t^3 c_{hhh} \\ & + A_8 c_{tt} c_t c_{hhh} + A_9 c_{tt} c_{ggh} c_{hhh} + A_{10} c_{tt} c_{gghh} + A_{11} c_t^2 c_{ggh} c_{hhh} + A_{12} c_t^2 c_{gghh} \\ & + A_{13} c_t c_{hhh}^2 c_{ggh} + A_{14} c_t c_{hhh} c_{gghh} + A_{15} c_{ggh} c_{hhh} c_{gghh} \\ & + A_{16} c_t^3 c_{ggh} + A_{17} c_t c_{tt} c_{ggh} + A_{18} c_t c_{ggh}^2 c_{hhh} + A_{19} c_t c_{ggh} c_{gghh} \\ & + A_{20} c_t^2 c_{ggh}^2 + A_{21} c_{tt} c_{ggh}^2 + A_{22} c_{ggh}^3 c_{hhh} + A_{23} c_{ggh}^2 c_{gghh}. \end{aligned} \quad (26)$$

Based on our results for A_1, \dots, A_{23} , we produce heat maps for the ratio σ/σ_{SM} , varying two of the five parameters, while for the fixed parameters the SM values are used, along with $\sigma_{SM}^{\text{LO}}[14 \text{ TeV}] = 19.85 \text{ fb}$, $\sigma_{SM}^{\text{NLO}}[14 \text{ TeV}] = 32.95 \text{ fb}$. The couplings are varied in a range which seems reasonable when taking into account the current constraints on the Higgs coupling measurements as well as recent limits on the di-Higgs production cross section [166, 167].

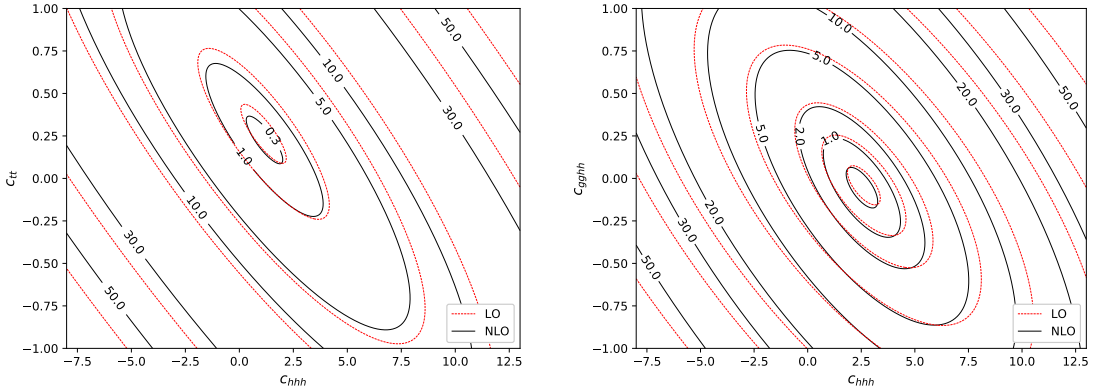


Fig. 37: Iso-contours of σ/σ_{SM} : (a) c_{hhh} versus c_{tt} and (b) c_{hhh} versus c_{gghh} at $\sqrt{s} = 14 \text{ TeV}$.

Fig. 37 shows variations of the triple Higgs coupling c_{hhh} in combination with c_{tt} and c_{gghh} at

$\sqrt{s} = 14$ TeV. We observe that the deviations from the SM cross section can be substantial. In Fig. 38

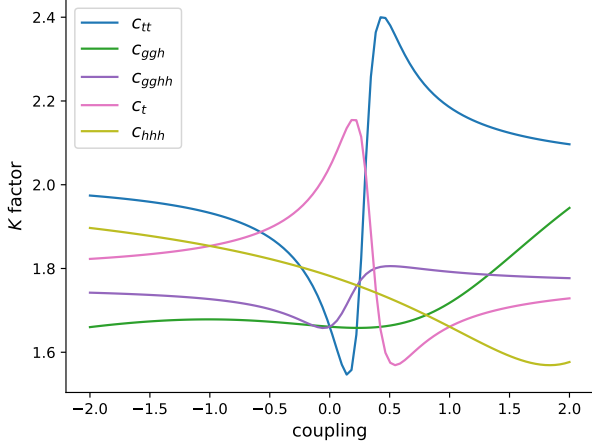


Fig. 38: K-factors for the total cross section at $\sqrt{s} = 14$ TeV as a function of the different couplings.

we show the K-factors as a function of the coupling parameters, with the others fixed to their SM values. It shows that the K-factors exhibit a much stronger dependence on the coupling parameters once the full top quark mass dependence is taken into account when compared to the results in the $m_t \rightarrow \infty$ limit [104, 169].

Fig. 39 shows the Higgs boson pair invariant mass distributions as a function of (a) c_{tt} and (b) c_{gggh} as 3-dimensional heat maps. In case (a) the other couplings are fixed to their SM values. We can see that large values of $|c_{tt}|$ lead to a substantial increase of the cross section, in particular at low m_{hh} values. In case (b) the other couplings are fixed to their SM values except for c_{hhh} , which is fixed to

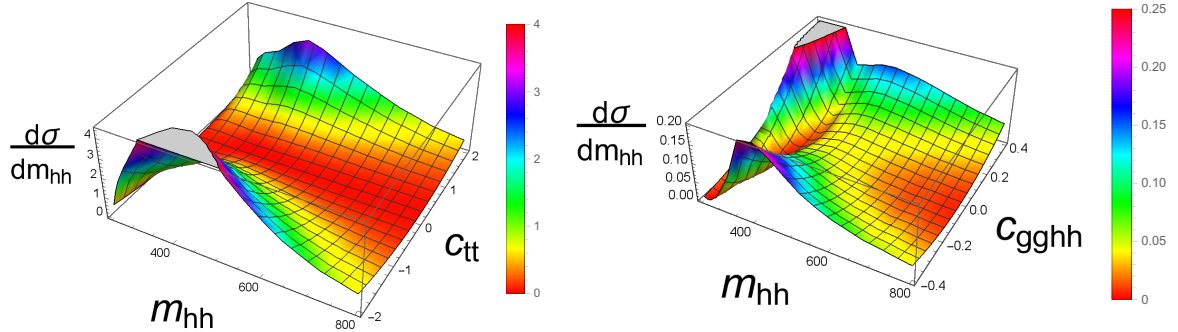


Fig. 39: 3-dimensional visualisation of the m_{hh} distribution (in units of fb/GeV) at 14 TeV as a function of (a) c_{tt} and (b) c_{gggh} . In case (a) all other couplings are fixed to their SM values, in case (b) $c_{hhh} = 2.4$.

$c_{hhh} = 2.4$ in order to demonstrate the following point: varying only c_{hhh} , the m_{hh} distribution shows a dip in the differential cross section just below $m_{hh} \sim 2m_t$ for $c_{hhh} \sim 2.4$, while the low m_{hh} region gets enhanced for larger values of c_{hhh} , see Section 3.1.1.2. However, this pattern can get destroyed by non-zero Higgs-gluon contact interactions. While c_{ggh} is increasingly well constrained meanwhile, c_{gggh} still could be relatively large. We can see from Fig. 39(b) that the dip is not present for very low (negative) c_{gggh} values and also gets very shallow for values of $c_{gggh} \sim 0.4$. Therefore it would be premature to conclude that a dip in the m_{hh} distribution points to a value of c_{hhh} close to 2.4.

We also point out that the LO and NLO A_i coefficients for both the total cross section and the m_{hh} distributions at both 14 TeV and 27 TeV are available as ancillary files, coming with the arXiv submission. These data files allow to reconstruct the full NLO result for any point in the 5-dimensional parameter space.

3.2 Double Higgs measurements and trilinear coupling

3.2.1 Measurements with the ATLAS experiment

by *N. Readioff, S. Olivares Pino, E. Petit, J. Stark, P. Bokan, D. Wardrope, M. Wielers*

A direct measurement of the Higgs boson trilinear self-coupling λ_{HHH} can be made via the study of Higgs boson pair production. Only the dominant production mechanism at hadron colliders, gluon fusion, is considered, with the other production mechanisms being more than an order magnitude smaller. The Feynman diagram which exhibits a λ_{HHH} dependence interferes destructively with the box diagram that is independent of λ_{HHH} , thus a small increase in the value of λ_{HHH} decreases the expected HH production cross section, and modifies the distributions of event kinematics.

The small SM non-resonant HH production cross section means that it is necessary to consider final states where at least one of the two Higgs bosons decays into a final state with a large branching ratio, ie $H \rightarrow b\bar{b}$. The most promising decays channels are $HH \rightarrow b\bar{b}b\bar{b}$, $HH \rightarrow b\bar{b}\tau\tau$ and $HH \rightarrow b\bar{b}\gamma\gamma$ with branching ratios of 33.9, 7.3 and 0.26% respectively.

3.2.1.1 The $HH \rightarrow b\bar{b}b\bar{b}$ channel

Projections for this channel were made by extrapolating from the ATLAS Run 2 analysis of 24.3 fb^{-1} of 13 TeV data, described in Ref. [170]. This extrapolation assumes similar detector performance to Run 2. The largest source of systematic uncertainty comes from the ability to model the QCD multi-jet background using control regions in data. The allowed range at 95% CL for κ_λ including (without) systematic uncertainties is $-4.1 - 8.7$ ($-1.2 - 8.0$).

3.2.1.2 The $HH \rightarrow b\bar{b}\tau\tau$ channel

Results [171] for this channel are computed by extrapolating from the Run 2 analysis of 36.1 fb^{-1} of 13 TeV data [172]. A multivariate analysis with a boosted decision tree (BDT) is performed on the leptonic/hadronic and hadronic/hadronic decay modes of the τ -lepton, and the BDT score is used as final discriminant. The largest systematic uncertainty of the Run 2 analysis, the simulation statistics, is neglected in the extrapolation. The expected significance of XX (XX) σ including (without) systematics uncertainties can be achieved. The allowed range at 95% CL for κ_λ including (without) systematic uncertainties is $XX - XX$ ($XX - XX$).

3.2.1.3 The $HH \rightarrow b\bar{b}\gamma\gamma$ channel

The analysis [171] is based on truth level particles convoluted with the detector resolution, efficiencies and fake rates computed for $\mu = 200$ which were extracted from fully simulated samples using the detector layout described in Ref. [170]. The selection is made using a multivariate analysis with a boosted decision tree. The diphoton invariant mass distribution, used to extract the signal through an analytical fit, is shown in Figure 40a. The number of signal, single Higgs and continuum background in a 123-127 GeV window is XX , XX and XX respectively, leading to a significance of XX (XX) σ including (without) systematics uncertainties. The allowed range at 95% CL for κ_λ including (without) systematic uncertainties is $XX - XX$ ($XX - XX$).

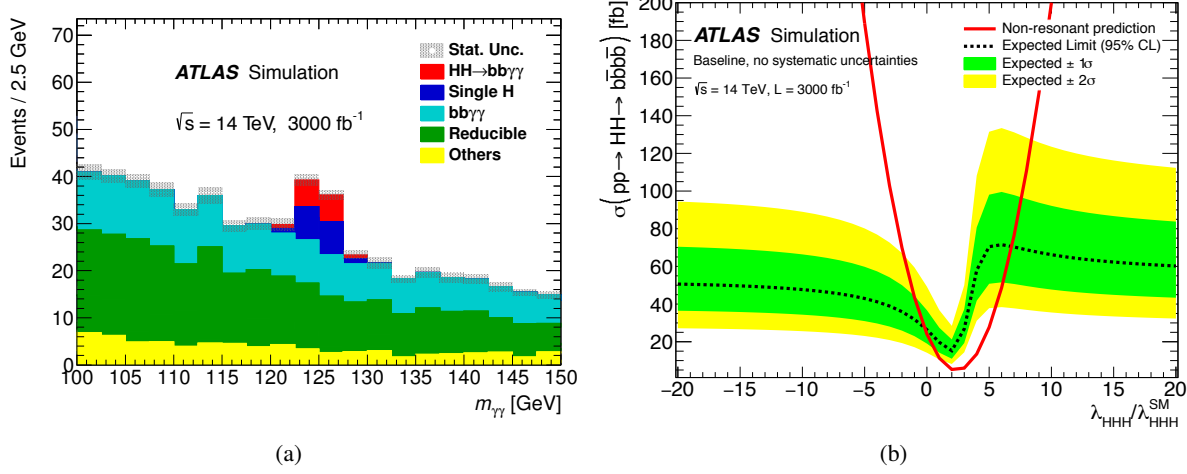


Fig. 40: (a) **PLACEHOLDER** Diphoton invariant mass distribution after selection, for the Standard Model HH signal and different background (plot from [170]). (b) **PLACEHOLDER** Expected 95% CL upper limit on the cross-section $\sigma(\text{HH})$ with 3000 fb^{-1} of data, as a function of the Higgs self-coupling constant modifier κ_λ . The non-resonant HH prediction shows the theoretical cross-section for di-Higgs production as function of κ_λ (plot from [170]).

3.2.1.4 Combined results

The combination of the three decay channels leads to an expected significance of $XX(XX)\sigma$ including (without) systematics uncertainties [171]. The 95% CL upper limit on the HH production cross-section is shown in Figure 40b. The allowed range at 95% CL for κ_λ including (without) systematic uncertainties is $XX - XX(XX - XX)$. A measurement of λ_{HHH} is also performed, improved by the use of the m_{HH} shape in the $HH \rightarrow b\bar{b}b\bar{b}$ and $HH \rightarrow b\bar{b}\gamma\gamma$ analyses. The trilinear coupling is measured to be:

$$1^{+XX}_{-XX} [{}^{+XX}_{-XX} (\text{stat}) {}^{+XX}_{-XX} (\text{syst})] \text{ at } 68\% \text{ CL}$$

$$1^{+XX}_{-XX} [{}^{+XX}_{-XX} (\text{stat}) {}^{+XX}_{-XX} (\text{syst})] \text{ at } 95\% \text{ CL}$$

3.2.2 Measurements with the CMS experiment

by N. De Filipis, M. Gouzevith, A. Carvalho

The estimations of the di-Higgs production in the HL-LHC is done by studying the possible analyses improvements based on Delphes [?] simulations. The Delphes framework was tuned to simulate the geometry of HL-LHC. Five channels are studied: $HH \rightarrow b\bar{b}b\bar{b}$, $HH \rightarrow b\bar{b}\tau\tau$ and $HH \rightarrow b\bar{b}\gamma\gamma$, $HH \rightarrow b\bar{b}l\bar{l}\nu\nu$, where one of the H decays as $H \rightarrow Z(l\bar{l})Z(\nu\nu)$ or $H \rightarrow W(l\nu)W(\nu)$, and $HH \rightarrow b\bar{b}ZZ(4l)$, the last two has a branching ratio of 2.1% ans XX% respectively.

3.2.2.1 The $HH \rightarrow b\bar{b}b\bar{b}$ channel

Two regimes are exploited on the $b\bar{b}b\bar{b}$ final state. The first consider a resolved situation, where four b-tagged jets are reconstructed as the H pair. The second considers the case where two fat jets are each one reconstructed as a boosted H .

In the resolved scenario events are pre-selected by requiring four jets with $p_T > 45 \text{ GeV}$ and $|\eta| < 3.5$ that satisfy the medium b-tagging working point. We assume the situation of 100% trigger, what is compatible with upgrades studies of the CMS trigger system, both at L1 and HLT, and the improvement and harmonization of online and offline b-tagging algorithms that are being considered [?]. Four b-tagged jets are selected and paired accordingly with proximity to the Higgs boson mass (the efficiency

of the pairing exceeds 95%), a selection around 40 GeV window around the Higgs boson mass on each di-jet pair is used to reduce background. As this is one of the analyses that most suffers with the huge size of its background, but it is also the region where most of the SM-like signal lives. To overcome this, multivariate variable (BDT) is used to best separate signal as signal extraction variable.

In the boosted scenario is typically a good handle to investigate other H couplings that not the trilinear coupling (see the comparison of the sensibility of this channel compared with the other channels on the combination of the 2016 HH analyses from CMs []). For that reason, for this specific channel we will show the prospected sensitivity on the shape benchmarks already described on section XXX. The two leading-p_T AK8 jets in the event, to be reconstructed each one as a Higgs boson, are required to have $p_T > 300$ GeV and lie within $|\eta| < 3.0$. The soft-drop [42, 43] jet grooming algorithm and n-subjetiness [XXXX] are used to remove soft and collinear components of the jet and retain the two subjets associated with the showering and hadronization of the two b quarks from the $H \rightarrow bb$ decay and background. The background estimation follows closely the approach in Ref. [46]. The background obtained from simulations is scaled by 0.7 based on comparisons with the LHC data at $\sqrt{s} = 13$ TeV. The main discriminating variable between the signal and the background is the invariant mass of the two selected jets and the M_{JJ} , which is correlated with the HH invariant mass. **FIXME: Explain better the signal extraction variables**

3.2.2.2 The $HH \rightarrow b\bar{b}\tau\tau$ channel

The $b\bar{b}\tau\tau$ final state is experimentally favourable thanks to its sizable branching fraction of 7.3% and the moderate background contamination. The decay of the Higgs boson to $\tau\tau$ gives rise to six possible combinations of decay channels for the signal: $e\tau_h$, $\mu\tau_h$, $\tau_h\tau_h$, $\mu\mu$, $e\mu$, and ee . For this investigation, we only consider the three most frequent final states, i.e. those involving at least one τ_h , that correspond to about 88% of the total decays of the $\tau\tau$ system and provide the largest sensitivity to the HH process. Events in all the three categories above are then required to contain at least two b-tagged jets with $p_T > 30$ GeV and $|\eta| < 2.4$. As for the case of resolved $b\bar{b}b\bar{b}$ analysis a multivariate variable is used for signal extraction. The final discriminant consists however of an ensemble of fully-connected deep neural networks (DNN), each consisting of three hidden layers of 100 neurons.

3.2.2.3 The $HH \rightarrow b\bar{b}\gamma\gamma$ channel

The $b\bar{b}\gamma\gamma$ channel was the most sensitive to a SM-like signal at CMS with data [?] and remains the most sensitive for the projections. The excellent resolution of the di-photon mass, clean trigger signature with 2 high p_T isolated photons, over-constrained and fully reconstructed final state is a strong asset to reduce the background contamination. The branching fraction is low compared to other channels, but still high enough to observe few 100-th of events after 3 ab^{-1} .

The two leading photons satisfying the loose working point $p_{T,1} > m_{\gamma\gamma}/3$ GeV and $p_{T,2} > m_{\gamma\gamma}/4$ GeV and $|\eta| < 2.5$ are selected and we constraint $100 < m_{\gamma\gamma} < 150$ GeV. Fiducial region between the barrel and endcap calorimeters is rejected. For this selection defined as is Run II [?] the trigger is expected to be fully efficient. The working point chosen for photon identification and isolation selects about 90% of photons within the required kinematic region.

The $H \rightarrow bb$ candidate is built from the two leading jets that satisfy $p_T > 25$ GeV and $|\eta| < 2.5$. The fiducial acceptance if this defined by Run II analysis. The Phase II tracker allows to extend the b-tagging region up to $|\eta| = 4$, but the impact on this analysis is very limited. The background from light flavour jets is suppressed by requiring both jets to satisfy a loose working point of the b tagging algorithm, corresponding to a 90% efficiency for a genuine b-jet (and 10% misidentification efficiency). The dijet invariant mass is required to be between 80 and 190 GeV. The main background to this analysis is coming from nonresonant production of $\gamma\gamma + 2$ jets. A contribution of $\approx 10\%$ of the events is expected, for the photon identification working point chosen in this analysis, from γ jet +2 jets where a jet is identified as

photon

A multivariate variable (BDT) is constructed to separate the HH signal from $t\bar{t}H \rightarrow \gamma\gamma$. This latter contribution is the dominant source of single $H \rightarrow \gamma\gamma$ background that have the same properties than HH production for the main discriminating variable $m_{\gamma\gamma}$. The BDT is trained to identify the presence of decay products from W bosons originating from top quark decays. The working point used allows to reject 75% of $t\bar{t}H \rightarrow \gamma\gamma$ events, while preserving 95% of the signal.

The signal extraction procedure is performed in purity categories obtained by training a classification BDT. This latter try to separate $\gamma\gamma + 2$ jets from the signal using kinematic (helicity angles, p_T and directions of the γ s and jets) and b-tagging variables. We define 2 categories, the high purity with the best ration signal over background and the medium purity one. The lowest purity events similar to $\gamma\gamma + 2$ jets are rejected.

We also define 3 categories in m_{HH} variable that is well approximated by $M_X = M_{\gamma\gamma bb} - M_{\gamma\gamma} - M_{bb} + 250$ GeV (see ??): $250 < M_X < 350$ GeV, $350 < M_X < 480$ GeV and $480 < M_X$ GeV. The first one have no impact on SM-like HH analysis but helps to constrain the Higgs self-coupling.

In each of the 3×2 categories the signal is extracted by a parametric maximum likelihood fit of the signal and background in 2 dimensions: $m_{\gamma\gamma} \times m_{\text{jet,jet}}$.

3.2.2.4 The $HH \rightarrow b\bar{b}ll\nu\nu$ channel

3.2.2.5 The $HH \rightarrow b\bar{b}ZZ(4l)$ channel

Up to now, the low signal rate leads to consider mostly final states with a sizable branching ratio. In view of HL-LHC, some rare but clean processes have been re-considered because of the increasing available statistics and the challenging conditions due to the enormous number of pile-up events.

Events are required to have at least four identified and isolated (isolation < 0.7) muons (electrons) with $p_T > 5(7)$ GeV and $|\eta| > 2.8$, where muons (electrons) are selected if passing the Loose (Medium) Working Point identification. Z boson candidates are formed from pairs of opposite-charge leptons (...) requiring a minimum angular separation between two leptons of 0.02. At least two di-lepton pairs are required. The Z candidate with the invariant mass closest to the nominal Z mass is denoted as Z1; then, among the other opposite-sign lepton pairs, the one with the highest $p_T >$ is labelled as Z2. In order to improve the sensitivity to the Higgs boson decay, Z candidates are required to have an invariant mass in the range [40, 120] GeV (Z1) and [12, 120] GeV (Z2), respectively. At least one lepton is required to have $p_T > 20$ GeV and a second is required to have $p_T > 10$ GeV. On figure 41 we show the resolution of the reconstructed $H \rightarrow ZZ \rightarrow 4l$ after baseline selections. The four leptons invariant mass is requested to be in the range [120,130] GeV. At least two (but not more than three) identified b-jets, reconstructed with the anti-kT algorithm inside a cone of radius $R = 0.4$, are required; a B-Tag Medium working point, exploiting the presence of the MIP Timing Detector (MTD) [], is assumed. The di-jet mass is required to be in the range [80, 160] GeV and the angular distance between the 2 b-jets has to be between 0.5 and 2.3. The signal is them extracted with a cut-and-count analysis.

Fig. 41: **PLACEHOLDER** Invariant mass distribution of the four leptons selected at the end of the CMS analysis for the $bb4l$ final state.

3.2.2.6 Combination

3.3 New ideas

3.3.1 Prospects for $hh \rightarrow (b\bar{b})(WW^*) \rightarrow (b\bar{b})(\ell^+\ell^-\nu_\ell\bar{\nu}_\ell)$

by Jeong Han Kim, Minho Kim, Kyoungchul Kong, Konstantin T. Matchev, Myeonghun Park

In this section, we discuss the discovery prospects for double Higgs production in the $hh \rightarrow (b\bar{b})(WW^*)$ channel. In order to increase sensitivity in the dilepton channel [173–175], we propose a novel kinematic method, which relies on two new kinematic functions, *Topness* and *Higgsness* [176]. They characterize features of the major ($t\bar{t}$) background and of hh events, respectively. The method also utilizes two less commonly used variables, the subsystem M_{T2} (or subsystem M_2) [177–179] for $t\bar{t}$ and the subsystem $\sqrt{\hat{s}}_{min}$ (or subsystem M_1) [179–181] for hh production. For any given event, Topness [176, 182] quantifies the degree of consistency to dilepton $t\bar{t}$ production, where there are 6 unknowns (the three-momenta of the two neutrinos, \vec{p}_ν and $\vec{p}_{\bar{\nu}}$) and four on-shell constraints, for m_t , $m_{\bar{t}}$, m_{W^+} and m_{W^-} , respectively. The neutrino momenta can be fixed by minimizing the quantity

$$\chi_{ij}^2 \equiv \min_{\vec{p}_T = \vec{p}_{\nu T} + \vec{p}_{\bar{\nu} T}} \left[\frac{(m_{b_i \ell^+ \nu}^2 - m_t^2)^2}{\sigma_t^4} + \frac{(m_{\ell^+ \nu}^2 - m_W^2)^2}{\sigma_W^4} + \frac{(m_{b_j \ell^- \bar{\nu}}^2 - m_t^2)^2}{\sigma_t^4} + \frac{(m_{\ell^- \bar{\nu}}^2 - m_W^2)^2}{\sigma_W^4} \right], \quad (27)$$

subject to the missing transverse momentum constraint, $\vec{p}_T = \vec{p}_{\nu T} + \vec{p}_{\bar{\nu} T}$. Since there is a twofold ambiguity in the paring of a b -quark and a lepton, we define *Topness* as the smaller of the two χ^2 s,

$$T \equiv \min(\chi_{12}^2, \chi_{21}^2). \quad (28)$$

In double Higgs production, the two b -quarks arise from a Higgs decay ($h \rightarrow b\bar{b}$), and therefore their invariant mass m_{bb} can be used as a first cut to enhance the signal sensitivity. For the decay of the other Higgs boson, $h \rightarrow WW^* \rightarrow \ell^+\ell^-\nu\bar{\nu}$, we define *Higgsness* [176] as follows:

$$H \equiv \min \left[\frac{(m_{\ell^+\ell^-\nu\bar{\nu}}^2 - m_h^2)^2}{\sigma_{h_\ell}^4} + \frac{(m_{\nu\bar{\nu}}^2 - m_{\nu\bar{\nu},peak}^2)^2}{\sigma_\nu^4} \right. \\ \left. + \min \left(\frac{(m_{\ell^+\nu}^2 - m_W^2)^2}{\sigma_W^4} + \frac{(m_{\ell^-\bar{\nu}}^2 - m_{W^*,peak}^2)^2}{\sigma_{W^*}^4}, \frac{(m_{\ell^-\bar{\nu}}^2 - m_W^2)^2}{\sigma_W^4} + \frac{(m_{\ell^+\nu}^2 - m_{W^*,peak}^2)^2}{\sigma_{W^*}^4} \right) \right], \quad (29)$$

where m_{W^*} is the invariant mass of the lepton-neutrino pair which resulted from the off-shell W . It satisfies $0 \leq m_{W^*} \leq m_h - m_W$ and $m_{W^*}^{peak} = \frac{1}{\sqrt{3}} \sqrt{2(m_h^2 + m_W^2) - \sqrt{m_h^4 + 14m_h^2m_W^2 + m_W^4}}$ is the peak in the m_{W^*} distribution. $m_{\nu\bar{\nu}}^{peak} = m_{\ell\ell}^{peak} \approx 30$ GeV is the location of the peak in the $\frac{d\sigma}{dm_{\nu\bar{\nu}}}$ or $\frac{d\sigma}{dm_{\ell\ell}}$ distribution [176, 183].

The σ values in Eqs. (27) and (29) result from the experimental uncertainties and intrinsic particle widths. In principle, they can be treated as free parameters and tuned using a neural network (NN), a boosted decision tree (BDT), etc. In our numerical study, we use $\sigma_t = 5$ GeV, $\sigma_W = 5$ GeV, $\sigma_{W^*} = 5$ GeV, $\sigma_{h_\ell} = 2$ GeV, and $\sigma_\nu = 10$ GeV. The main contribution in Eq. (29) comes from the on-shell conditions for the Higgs and the W , while the effects of the invariant mass of the two neutrinos and the off-shell W are minor.

Along with Higgsness and Topness, we adopt the subsystem $\hat{s}_{min}^{(\ell\ell)}$ for $h \rightarrow W^\pm W^{*\mp} \rightarrow \ell^+\ell^-\nu\bar{\nu}$ [180, 181] and the subsystem M_{T2} for the $b\bar{b}$ system ($M_{T2}^{(b)}$) and the lepton system ($M_{T2}^{(\ell)}$) [178]. The variable $\hat{s}_{min}^{(v)}$ is defined as $\hat{s}_{min}^{(v)} = m_v^2 + 2 \left(\sqrt{|\vec{P}_T^v|^2 + m_v^2 |\vec{p}_T|} - \vec{P}_T^v \cdot \vec{p}_T \right)$ [179–181], where (v) represents a set of visible particles under consideration, while m_v and \vec{P}_T^v are their invariant mass and transverse momentum, respectively. It provides the minimum value of the Mandelstam invariant mass \hat{s} which is consistent with the observed visible 4-momentum vector. The M_{T2} is defined as $M_{T2}(\tilde{m}) \equiv \min \{ \max [M_{TP_1}(\vec{p}_{\nu T}, \tilde{m}), M_{TP_2}(\vec{p}_{\bar{\nu} T}, \tilde{m})] \}$ where \tilde{m} is the test mass for the daughter particle and the

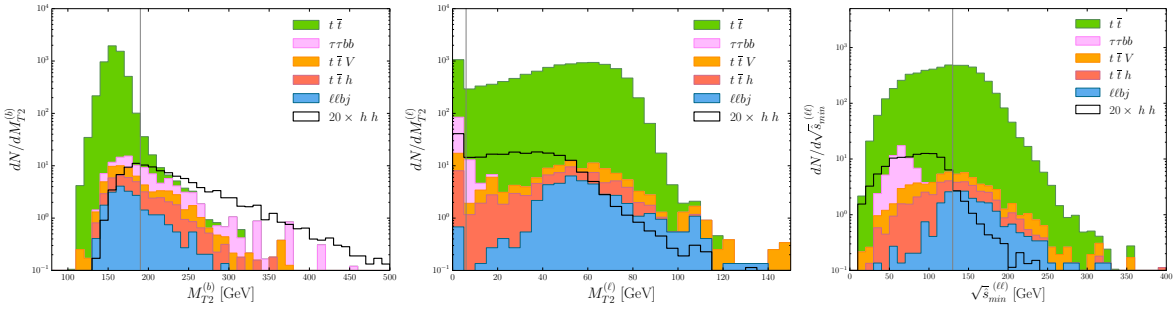


Fig. 42: Distributions for signal (hh) and all backgrounds ($t\bar{t}$, $t\bar{t}h$, $t\bar{t}V$, $\ell\ellbj$ and $\tau\taubb$) for $M_{T2}^{(b)}$, $M_{T2}^{(\ell)}$ and $\sqrt{\hat{s}}_{min}^{(\ell\ell)}$ after loose baseline selection cuts defined in Ref. [176]. The vertical lines at $M_{T2}^{(b)} = 190$ GeV, $M_{T2}^{(\ell)} = 6$ GeV and $\sqrt{\hat{s}}_{min}^{(\ell\ell)} = 130$ GeV mark the optimized cuts.

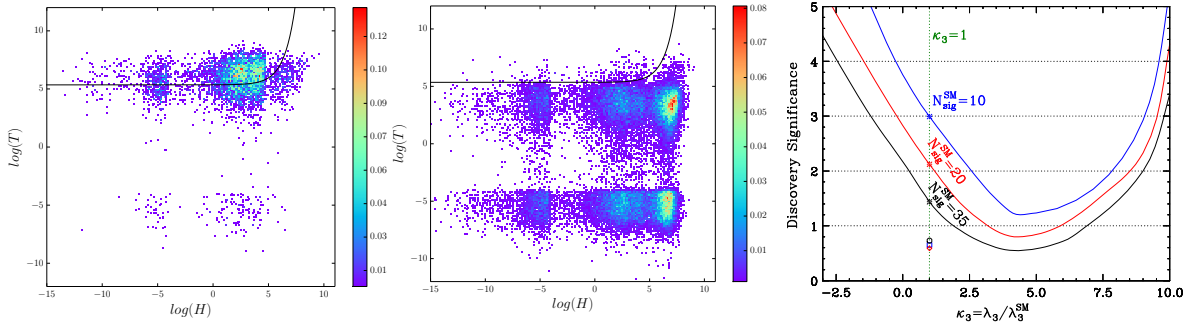


Fig. 43: Scatter distribution of $(\log H, \log T)$ for signal (hh in the left) and backgrounds ($t\bar{t}$, $t\bar{t}h$, $t\bar{t}V$, $\ell\ellbj$ and $\tau\taubb$ in the middle) after loose baseline selection cuts. The right panel shows the expected discovery significance at the 14 TeV LHC with 3 ab^{-1} as a function of the triple Higgs coupling κ_3 . We obtain each curve by applying the same set of cuts optimized for the SM point ($\kappa_3 = 1$) to non-SM points ($\kappa_3 \neq 1$) for $N_{sig}^{SM} = 35$ in black, $N_{sig}^{SM} = 20$ in red and $N_{sig}^{SM} = 10$ in blue. The curves in the left and middle panel are the optimized cuts for the $N_{sig}^{SM} = 20$ case. The three symbols \diamond , \circ and \square display the signal significance using CMS-NN [173], CMS-BDT [174] and BDT [175], respectively.

minimization over the transverse masses of the parent particles M_{TP_i} ($i = 1, 2$) is performed over the transverse neutrino momenta $\vec{p}_{\nu T}$ and $\vec{p}_{\bar{\nu} T}$ subject to the \vec{p}_T constraint [177–179, 184–187].

Events for the signal and all relevant background processes were simulated as described in Ref. [176]. After basic selection cuts, we use the kinematic information discussed above for further background suppression. Distributions of $M_{T2}^{(b)}$, $M_{T2}^{(\ell)}$ and $\sqrt{\hat{s}}_{min}^{(\ell\ell)}$ are shown in Fig. 42, while scatter distributions of Topness and Higgsness are displayed in Fig. 43. The right panel in Fig. 43 shows the expected signal significance at the HL-LHC as a function of the triple Higgs coupling κ_3 . We obtain each curve by applying the same set of cuts optimized for the SM point ($\kappa_3 = 1$) to non-SM points ($\kappa_3 \neq 1$) for $N_{sig}^{SM} = 35$ in black, $N_{sig}^{SM} = 20$ in red and $N_{sig}^{SM} = 10$ in blue. The three symbols \diamond , \circ and \square show the signal significance using CMS-NN [173], CMS-BDT [174] and BDT [175], respectively.

Finally Fig. 44 shows the significance for observing an anomalous Higgs self-coupling at the 14 TeV LHC with an integrated luminosity of 3 ab^{-1} and at 27 TeV with 15 ab^{-1} , respectively. For the HL-LHC, we follow the analysis presented in Ref. [176]. The red solid curves are obtained with nominal efficiencies for b (mis-)tagging ($\epsilon_{b \rightarrow b} = 0.7$, $\epsilon_{c \rightarrow b} = 0.2$ and $\epsilon_{j \rightarrow b} = 0.01$) [188]. The HL-LHC will rule out the Higgs self-coupling outside the range $(-0.5, 3.2)$. The four vertical dashed lines in the left panel represent the expected 95% CL exclusion of κ_3 in the $bbbb$ channel (black, from Ref. [189]), in

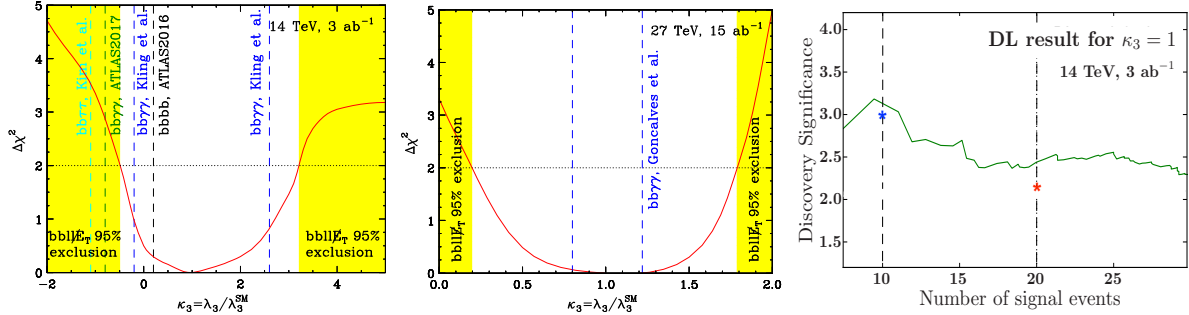


Fig. 44: Significance for observing an anomalous Higgs self-coupling at the 14 TeV LHC with an integrated luminosity of 3 ab^{-1} (left) and at 27 TeV with 15 ab^{-1} (middle). Right: the effect of using a Deep Learning algorithm to improve the discovery significance for $\kappa_3 = 1$ shown in the right panel of Fig. 43.

the $bb\gamma\gamma$ channel (blue, from Ref. [190] and green from Ref. [191]) and in the $bb\tau\tau$ channel (cyan, from Ref. [105]). We notice that the sensitivity in the $bbWW^*$ channel is comparable to the sensitivity in those other channels. For the 27 TeV study, we normalize our signal cross section to 139.9 fb [192], and use K factors of $K = 1.56$ for $t\bar{t}$ production [193], $K = 1.28$ for $t\bar{t}h$ [194], $K = 1.54$ for $t\bar{t}V$ and a conservative $K = 2$ for $\ell\bar{\ell}b\bar{b}$ and $\tau\bar{\tau}b\bar{b}$ [176]. Our result shows that the 27 TeV collider could observe double Higgs production at 5σ for a wide range of values for κ_3 and would be able to exclude κ_3 outside the range $(0.2, 1.8)$ (for a comparative study in the $bb\gamma\gamma$ channel, see Ref. [195] (vertical, dashed lines in the middle panel)).

In summary, we obtained a significant increase in the signal sensitivity for hh production in the dilepton channel compared to previous analyses [173–175]. The method can be easily incorporated into more advanced algorithms for further improvement. For example, using deep learning (convolutional neural network) slightly improves the discovery significance, see the right panel of Fig. 44. The discussed method is very general and can be easily applied to other processes such as the semi-leptonic final state, resonant hh production, non-resonant production with more than one Higgs boson, etc. It is straightforward to generalize the idea to different topologies in searches for other BSM particles as well.

3.3.2 Prospects for $bb\gamma\gamma$: Bayesian optimization and BDT

by Alexandre Alves, Tathagata Ghosh, and Kuver Sinha

Searches for double Higgs pair production in the $b\bar{b}\gamma\gamma$ channel are an important target for the future. In this section, we study this problem at the 14 TeV LHC in two steps, following [196]:

(i) We first propose a Bayesian optimization approach to select cuts on kinematic variables and study its performance compared to manual and random cuts, taking into account systematic uncertainties. We demonstrate our results with the Python algorithm Hyperopt .

(ii) We next perform a joint optimization of kinematic cuts and boosted decision trees (BDT) hyperparameters to further discriminate signal and background events. For our calculations, we use the XGBoost implementation of BDTs for Python.

3.3.2.1 Signal and Backgrounds

For the simulation of the signal, we use MadGraph5_aMC@NLO_v2.3.3 [?], to generate $pp \rightarrow hh$ process exclusively at the leading order (LO). The simulation of our signal include both the triangle and box diagrams. We scale our LO cross-section by the partial NNLO K-factor of 2.27 [197], calculated in the large quark mass limit and use the resulting production cross section of 36.8 fb.

The following backgrounds were taken into account in our study: (i) $b\bar{b}\gamma\gamma$; (ii) Zh with $Z \rightarrow bb$

and $h \rightarrow \gamma\gamma$; (iii) $b\bar{b}h$ with $h \rightarrow \gamma\gamma$; (iv) $t\bar{t}h \rightarrow b\bar{b} + \gamma\gamma + X$; (v) $jj\gamma\gamma$ where the light-jets jj are mistaken for a b -jet pair in the detector; (vi) $b\bar{b}jj$, where the light-jets jj are mistaken for a photon pair; (vii) $c\bar{c}\gamma\gamma$, where a c -jet is mistagged as a b -jet; (viii) $b\bar{b}\gamma j$, where one light-jet is mistaken for a photon; (ix) $c\bar{c}\gamma j$ where the c -jets are mistagged as bottom jets and the light-jet as a photon. We note that the $b\bar{b}\gamma j$, $c\bar{c}\gamma\gamma$, and $c\bar{c}\gamma j$ backgrounds were neglected in several early studies.

The cross section normalizations for the backgrounds from (i) - (v) are taken from ref. [168], which we consider reliable. In order to obtain the distributions of the kinematic variables of interest, we pass our simulated events to PYTHIA_v6.4 [?] for showering, hadronization and underlying event and finally to DELPHES_v3.3 [?] for detector simulation. For all further details of our signal and background simulation, we refer to our paper [196].

The following basic cuts were applied on both signal and background:

$$\begin{aligned} p_T(j) &> 20 \text{ GeV}, \quad p_T(\gamma) > 20 \text{ GeV}, \quad |\eta(j)| < 2.5, \quad |\eta(\gamma)| < 2.5 \\ 100 \text{ GeV} &< |M_{jj}| < 150 \text{ GeV}, \quad 100 \text{ GeV} < |M_{\gamma\gamma}| < 150 \text{ GeV}. \end{aligned} \quad (30)$$

The number of backgrounds events after imposing the basic cuts for 3 ab^{-1} of integrated luminosity is shown in Table 20.

signal	$b\bar{b}\gamma\gamma$	$c\bar{c}\gamma\gamma$	$jj\gamma\gamma$	$b\bar{b}\gamma j$	$t\bar{t}h$	$c\bar{c}\gamma j$	$b\bar{b}h$	Zh	total backgrounds
42.6	1594.5	447.7	160.3	137	101.1	38.2	2.4	1.8	2483

Table 20: The number of signal and the various types of backgrounds considered in this work after imposing the basic cuts of eq. (30) for 3 ab^{-1} of data. We found $b\bar{b}jj$ negligible after cuts and after estimating the probability of the jet pair faking a photon pair.

3.3.2.2 Bayesian Optimization

The $b\bar{b}\gamma\gamma$ channel has been studied by several groups using cut and count strategies. Once signal and background cross sections are normalized to the proper values, one finds that the analysis of any particular group does not radically outperform that of any other. For a detailed comparison, we refer to Table 2 of [196].

Bayesian optimization offers a systematic way to obtain the most optimal cuts on a set of kinematic variables. The algorithm we utilize is implemented in the Python library HyperOpt , based on the so-called sequential model-based optimization (SMBO) technique [198–200].

The kinematic variables used in our study are: (i) transverse momentum of b -jets and photons: $p_T(b)$ and $p_T(\gamma)$; (ii) $b\bar{b}$ and $\gamma\gamma$ invariant masses: M_{bb} and $M_{\gamma\gamma}$, where signal events exhibit resonance peaks at m_h ; (iii) transverse momentum of $b\bar{b}$ and $\gamma\gamma$: $p_T(bb)$ and $p_T(\gamma\gamma)$; (iv) invariant mass of two b -jets and two photons: $M_{bb\gamma\gamma}$; (v) distance between pairs of b -jets and photons: $\Delta R(bb)$, $\Delta R(\gamma\gamma)$ and $\Delta R(b\gamma)$, where $\Delta R = \sqrt{(\Delta\eta)^2 + (\Delta\phi)^2}$ in the pseudo-rapidity and azimuthal angle plane (η, ϕ) ; (vi) the fraction $E_T/M_{\gamma\gamma}$ for the two hardest photons in the event; these are variables used in experimental searches as in ref. [?, 201].

In Figure 45, we display the results obtained from the Bayesian optimization of cuts on the above kinematic variables. We see that after 100-200 trials, the signal significance does not change much and the optimized cuts achieved a significance of 2.81σ against 2.1σ of the manual search of ref. [168], a 34% improvement. If $b\bar{b}\gamma j$, $c\bar{c}\gamma\gamma$, and $c\bar{c}\gamma j$ backgrounds are incorporated, the Bayesian search reached 2.48σ against 1.85σ of the cuts of ref. [168], again roughly the same improvement. The performance of the Bayesian algorithm is also displayed in Figure 45.

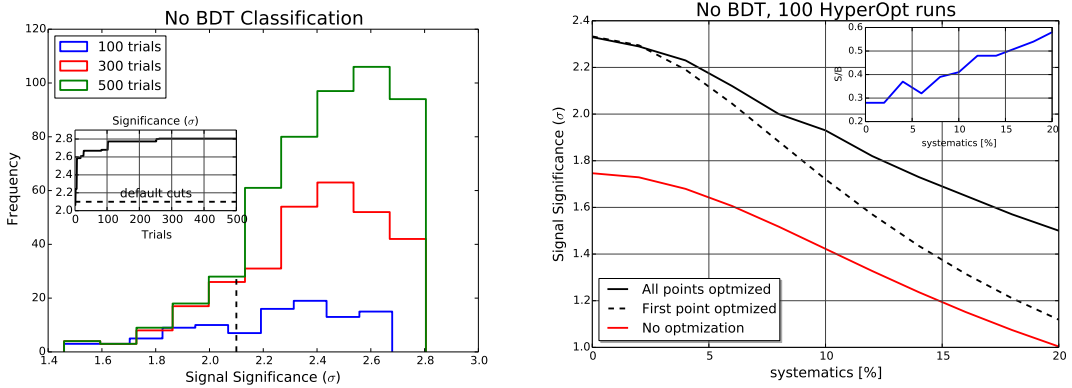


Fig. 45: Left panel: The left panel shows the optimized search with the TPE algorithm in HyperOpt with no systematic errors. The inset frame in the left plot shows the significance as a function of the number of trials. S/\sqrt{B} is used to compute the signal significance. The black dashed line represents the results obtained with the cuts of Azatov *et. al.*, ref. [168]. **Right panel:** The $S/\sqrt{B + (\varepsilon_B B)^2}$ significance metric as a function of ε_B , the systematic uncertainty in the total background rate. The red line represents the default cuts of Azatov *et. al.*, the black dashed assumes an optimized strategy just for the 0% systematics point, while for the solid upper line, the algorithm was solicited to learn the best cuts for each systematics level from 0 to 20%. In the inner plot we show the S/B ratio for the point-to-point optimization case.

3.3.2.3 BDT Analysis

We now turn to a discussion of the BDT analysis, for which we utilize the XGBoost implementation of BDTs for Python. XGBoost is chosen for its good discrimination performance, speed and capacity of parallelization. For our analysis we simulated ~ 880000 ; depending on the cuts, however, the total number of events usually drops to around 100000–300000 events which also turned out to be a sufficient number of samples to keep overfitting under control.

Using HyperOpt, we perform a joint optimization of the kinematic variables introduced previously in conjunction with the following BDT hyperparameters: the number of boosted trees, the learning rate, the maximum depth of the trees, and the minimum sum of instance weight needed in a child to continue the splitting process of the trees, `min_child_weight`. All the BDT results were obtained from a 5-fold cross validation by randomly splitting training and testing samples at the proportion of 2/3 and 1/3 of the total sample, respectively. We allowed for 300 trials in HyperOpt.

Hyperparameters like the number of boosted trees, maximum depth of the trees and the `min_child_weight` are directly related to the complexity of the algorithm by controlling the number, size and configuration of the trees. The learning rate, also known as shrinkage in this context, is a parameter that controls the weight new trees have to further model the data. A large value permits a larger effect from new added trees and might lead to more severe overfitting. There are other parameters which can be eventually used to prevent overfitting and loss of generalization power, but we found that tuning these parameters was sufficient to achieve a good performance.

A comparative result of a simple cut and count analysis and a sequential optimization of cuts and BDT hyperparameters are presented Table 21. We note that BDT outperforms simple cut and count, even when cutting is performed using Bayesian optimization. This is due to the better discrimination between the signal and background classes achieved by the machine learning algorithms as they find more profound correlations among the kinematic features and those classes. These correlations cannot be fully explored in simple/manual rectangular cut-and-count analyses.

However, there is a trade-off between the efficiency of the cuts and the ML performance which is

systematics (%)	Cut-and-count	BDT
0	2.34[1.76]	3.88
10	1.93 [1.43]	3.57
20	1.51[1.0]	3.10

Table 21: Signal significances for cut-and-count and BDT for 0, 10 and 20% systematics. We took all backgrounds into account for the computation of the AMS with optimized cuts and an integrated luminosity of 3 ab^{-1} at the 14 TeV LHC. The bold-face numbers represent the significances expected with the level of systematics anticipated by the experimental collaborations in refs. [?, ?, ?]. The numbers inside brackets are the significances computed with the default cuts of Azatov *et. al.*, ref. [168], which we took as baseline results.

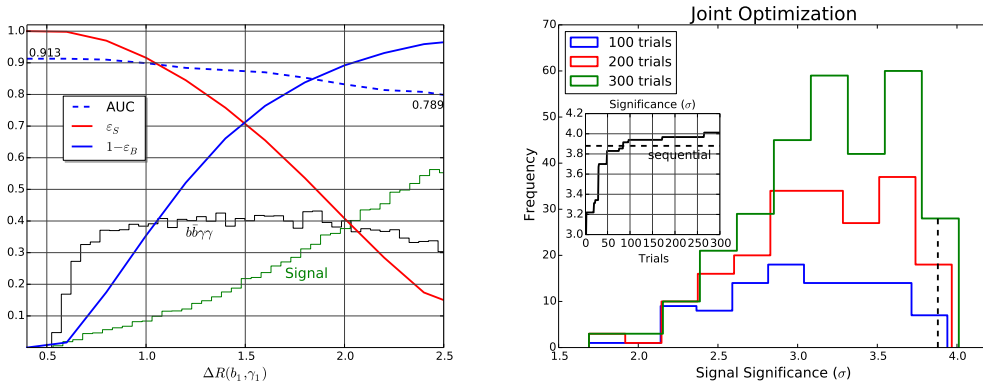


Fig. 46: **Left panel:** We show the results of the effects of imposing hard cuts on $\Delta R_{b_1\gamma_1}$ for the BDT performance, see [196] for further details. **Right panel:** The histogram of number of cut strategies producing a given significance interval in a BDT-aided classification analysis. The inset plot shows the significance as a function of the number of HyperOpt trials. No systematics are assumed, the backgrounds are those of ref. [168] and the S/\sqrt{B} used to compute the signal significances. The black dashed line represents the results obtained with the default cuts of Azatov *et. al.*, ref. [168].

usually neglected in phenomenological works where these tools are employed. The reasoning is simple: cutting harder cleans up more backgrounds but weakens the correlations between the kinematic variables and the event classes, thereby decreasing the ML performance. On the other hand, relaxing the cuts makes the correlations stronger helping to boost ML but the discrimination power gained might not be enough to get a good significance with a large number of surviving background events. Hence, a joint optimization of cuts and BDT hyperparameters improve the performance of our analysis further.

The maximum AMS significance is 4.0σ for a joint optimization analysis of cuts and BDT hyperparameters. The final selections of the kinematic variables and BDT hyperparameters are the following $p_T(1) > 72 \text{ GeV}$, $p_T(2) > 20 \text{ GeV}$; $\Delta R_{ij} > 0.15$, $\Delta R_{ii} < 3.6$; $M_{b\bar{b}\gamma\gamma} > 370 \text{ GeV}$, $p_{T_{ii}} > 145 \text{ GeV}$, $M_{b_1\gamma_1} > 100 \text{ GeV}$; $|M_{bb} - m_h| < 27 \text{ GeV}$, $|M_{\gamma\gamma} - m_h| < 11 \text{ GeV}$; number of trees = 157; learning rate = 0.101; maximum tree depth = 14; min_child_weight = 5. We have denoted $p_T(1)$ as the leading b -jet or photon, and $p_T(2)$ as the next-to-leading b -jet or photon.

The results are shown in Figure 46. The left panel shows the normalized $\Delta R_{b_1\gamma_1}$ histograms for the signal and the $b\bar{b}\gamma\gamma$ continuum background, the signal efficiency (background rejection) is the red (blue) line, and the area under the Receiver-Operator curve (ROC), AUC, is the dashed line. The bigger the AUC, the better the performance of a cut-and-count analysis based on that distribution. On the right panel, we show the histogram of number of cut strategies producing a given significance interval in a BDT-aided joint optimization analysis. Finding this optimal performance from the competition between

hard cuts and an ML algorithm is the core of the method presented in the section.

3.4 HE prospects

3.4.1 Theory studies

by Dorival Gonçalves, Tao Han, Felix Kling, Tilman Plehn and Michihisa Takeuchi

Higgs pair production $pp \rightarrow hh$ offers a direct path to pin down the Higgs self-coupling λ at a hadron collider [?, ?]. Theoretical studies as well as current analyses point to the $b\bar{b}\gamma\gamma$ decay as the most promising signature at the LHC [?]. For the high-luminosity LHC (HL-LHC), ATLAS and CMS projections indicate a very modest sensitivity to the Higgs self-coupling [?]. In the optimistic scenario that we can neglect systematic uncertainties, those studies indicate that the LHC will probe the coupling at 95% confidence level $-0.8 < \kappa_\lambda < 7.7$, where the SM value is $\kappa_\lambda = \lambda/\lambda_{SM} = 1$, falling short in precision in comparison to other Higgs property measurements at the LHC, and far from satisfactory in probing the Higgs potential. For example, $\mathcal{O}(1)$ determination of κ_λ would be required to test some of the EW Baryogenesis models [?].

Because of the rapidly growing gluon luminosity at higher energies, the hh production cross section increases by about a factor of 4 (40) at 27 (100) TeV. This means that at the HE-LHC with the anticipated integrated luminosity of 15 ab^{-1} the number of events in the $b\bar{b}\gamma\gamma$ channel increases by a factor $4 \times 5 = 20$ to around 5k events. A 100 TeV hadron collider with a projected integrated luminosity of 30 ab^{-1} features another increase by a factor $10 \times 2 = 20$, to around 100k expected Higgs pair events in the Standard Model. This estimate shows how the combination of increased energy and increased luminosity slowly turns Higgs pair production into a valid channel for precision measurements [?].

3.4.1.1 Information in Distributions

Previous studies have shown that multivariate analysis, taking into account kinematic distributions, gives a substantially better reach on the Higgs self coupling over the purely rate-based analysis [?, ?, ?, ?]. In the following, we therefore summarize which kinematic features include information about the Higgs self-coupling.

At leading order, Higgs pair production receives contributions both from a triangular loop diagram sensitive to the Higgs-self coupling and from a box or continuum diagram. The box contribution completely dominates the total rate over most of the phase space, making the Higgs coupling measurements a challenge. While we can define a number of kinematic observables describing the continuum backgrounds, the measurement of the Higgs self-coupling relies on a simple $2 \rightarrow 2$ process with two independent kinematic variables.

Three distinct phase space regions provide valuable information on a modified Higgs self-coupling, all from a large destructive interference between the triangle and box contributions. First, there is the threshold [?, ?] in the partonic center of mass energy $m_{hh} \approx 2m_h$. Based on the effective Higgs-gluon Lagrangian [?] we can therefore write the corresponding amplitude for Higgs pair production as

$$\frac{\alpha_s}{12\pi v} \left(\frac{\kappa_\lambda \lambda_{SM}}{s - m_h^2} - \frac{1}{v} \right) \rightarrow \frac{\alpha_s}{12\pi v^2} (\kappa_\lambda - 1) \stackrel{SM}{=} 0. \quad (31)$$

While the heavy-top approximation is known to give a poor description of the signal kinematics as a whole, it does describe the threshold dependence correctly [?]. This indicates that we can search for a deviation of the Higgs self-coupling by looking for an enhancement of the rate at threshold. Second, an enhanced sensitivity to the self-coupling appears as top mass effect. For large positive values of λ absorptive imaginary parts lead to a significant dip in the combined rate at the threshold $m_{hh} \approx 2m_t$ [?, ?]. The sharpest interference dip takes place near $\kappa_\lambda \approx 2$ while for negative values of κ_λ the interference becomes constructive. Finally, the triangular and box amplitudes have a generally different

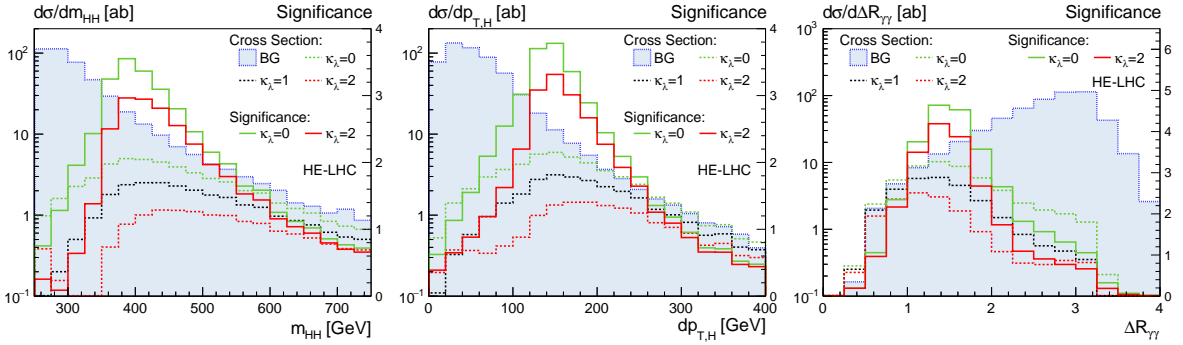


Fig. 47: Kinematic distributions (dashed lines with left vertical axes) and significance distribution (solid lines with right vertical axes) assuming a Higgs self-coupling with $\kappa_\lambda = 0, 1, 2$ for the HE-LHC. The significance describes the discrimination of an anomalous self-coupling $\kappa_\lambda \neq 1$ from the SM hypothesis $\kappa_\lambda = 1$.

scaling in the limit $m_{hh} \gg m_h, m_t$ [?, ?]. While the triangle amplitude features an explicit suppression of either m_h^2/m_{hh}^2 or m_t^2/m_{hh}^2 at high invariant mass, the box diagrams drops more slowly towards the high-energy regime. This explains why a rate based analysis focussing on the high di-Higgs mass region only has limited sensitivity. The impact of all three kinematic features can be quantified statistically and indicate that essentially the full information on the Higgs self-coupling can be extracted through a shape analysis of the m_{hh} distribution [?].

In Fig. 47 we present the signal and background distributions for three relevant kinematic variables: m_{hh} , $p_{T,h}$ and $\Delta R_{\gamma\gamma}$. Using the MADMAX approach [?], based on the Neyman Pearson Lemma we also estimate the maximum significance with which any multi-variate analysis will be able to extract an anomalous self-coupling $\kappa_\lambda \neq 1$. The corresponding differential distribution of maximum significance are shown as solid lines in Fig. 47. In addition to the signal features, the significance is limited by the rapidly dropping backgrounds, covering both of the above-mentioned regions with an enhanced dependence on the triangle diagram. In the absence of background, the significance indeed peaks between the production threshold and the top-mass threshold [?]. The drop towards large values of m_{hh} is a combination of the dominance of the box diagram in the signal and the limited number of expected signal events. The significance with which we can extract modified self-couplings either smaller ($\kappa_\lambda = 0$) or larger ($\kappa_\lambda = 2$) than in the Standard Model shows a similar phase space dependence. The only difference is a slightly harder significance distributions for $\kappa_\lambda = 2$, an effect of the dip at $m_{hh} \approx 2m_t$.

3.4.1.2 Detector-Level Analysis

Based on our findings above, we now design a detailed analysis strategy to extract the Higgs self-coupling with a focus on the shape of the m_{hh} distribution [?]. Our signal is $pp \rightarrow hh + X \rightarrow b\bar{b} \gamma\gamma + X$. The signal and background samples are generated with MADGRAPH5+PYTHIA8 [?, ?], including one extra jet using the MLM scheme [?].

In the final state we demand two b -tagged jets and two isolated photons with the minimal acceptance and trigger cuts

$$p_{T,j} > 30 \text{ GeV}, \quad |\eta_j| < 2.5, \quad p_{T,\gamma} > 30 \text{ GeV}, \quad |\eta_\gamma| < 2.5, \quad \Delta R_{\gamma\gamma, jj, jj} > 0.4 . \quad (32)$$

The background to our $b\bar{b} \gamma\gamma$ signal consists of other Higgs production modes ($t\bar{t}h, Zh$) with $h \rightarrow \gamma\gamma$, continuum $b\bar{b}\gamma\gamma$ production, and of multi-jet events with light-flavor jets faking either photons or b -jets ($jj\gamma\gamma, b\bar{b}\gamma j$) [?].

The proper simulation of efficiencies and fake rates are a key ingredient for a realistic background

estimate in this analysis. For the HE-LHC and the future 100 TeV collider we follow the ATLAS projections [?]. The efficiency for a tight photon identification can be well parametrized by

$$\epsilon_{\gamma \rightarrow \gamma} = 0.863 - 1.07 \cdot e^{-p_{T,\gamma}/34.8 \text{ GeV}}, \quad (33)$$

and a jet-to-photon mis-identification rate by

$$\epsilon_{j \rightarrow \gamma} = \begin{cases} 5.30 \cdot 10^{-4} \exp(-6.5(p_{T,j}/(60.4 \text{ GeV}) - 1)^2) & \text{for } p_{T,j} < 65 \text{ GeV}, \\ 0.88 \cdot 10^{-4} [\exp(-(p_{T,j}/(943 \text{ GeV}) + 248 \text{ GeV}/p_{T,j})] & \text{for } p_{T,j} > 65 \text{ GeV}. \end{cases} \quad (34)$$

This leads to a photon efficiency of about 40% at $p_{T,\gamma} = 30 \text{ GeV}$, saturating around 85% for $p_{T,\gamma} > 150 \text{ GeV}$. Note that the Higgs decay products tend to be soft, $p_{T,\gamma} \sim m_h/2$. For b -tagging, we adopt an efficiency with $\epsilon_b = 0.7$ associated with mis-tag rates of 15% for charm quarks and 0.3% for light flavors. These flat rates present a conservative estimate from the two dimensional distribution on $(p_{T,j}, \eta_j)$ shown in the HL-LHC projections [?]. Encouragingly, the small light flavor fake rate projections result in a strong suppression for the initially dominant $jj\gamma\gamma$ background.

To control the continuum backgrounds, we require two Higgs mass windows,

$$|m_{bb} - m_h| < 25 \text{ GeV}, \quad |m_{\gamma\gamma} - m_h| < 1 \text{ GeV}. \quad (35)$$

An obvious way to enhance the Higgs pair signal is to improve the resolution on the reconstructed photons and b -jets from the Higgs decays. We adopt the rather conservative resolution for m_{bb} as in Eq. (35). Any improvement on it in experiments would be greatly helpful for the signal identification and background separation.

To take the information in the differential distribution m_{hh} into account, we employ a binned log-likelihood analysis based on the CL_s method, using the full m_{hh} distribution to extract κ_λ [?]. As a starting point, we show the 5σ determination on the Higgs pair signal strength for the SM hypothesis $\kappa_\lambda = 1$ as a function of the luminosity in the left panel of Fig. 48. Here we require two b -tagged jets among the two or three leading jets. We decompose the latter case in two sub-samples (bb, bbj) and (jbb, bjb). We see how exploring the extra-jet emission significantly improves the significance as compared to the standard procedure adopted in the literature. The 5σ measurement for HE-LHC is pushed from 2.8 ab^{-1} to below 2.3 ab^{-1} .

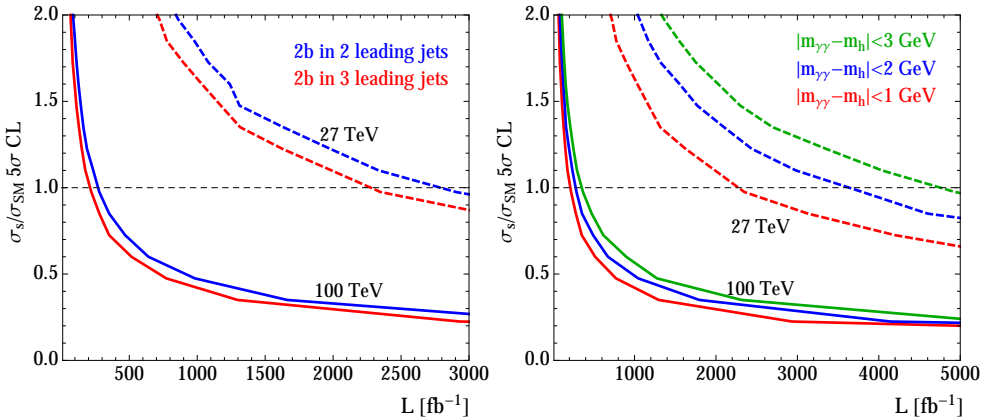


Fig. 48: Luminosity required for a 5σ discover of Higgs pair production for the HE-LHC (dashed) and a 100 TeV collider (full). Left: sensitivity in terms of the total rate, demanding two b -tags among the two or three leading jets and assuming $|m_{\gamma\gamma} - m_h| < 1 \text{ GeV}$. Right: sensitivity for three mass windows $|m_{\gamma\gamma} - m_h| < 1, 2, 3 \text{ GeV}$. We assume the SM hypothesis with $\kappa_\lambda = 1$ and use a binned log-likelihood analysis of the m_{hh} distribution.

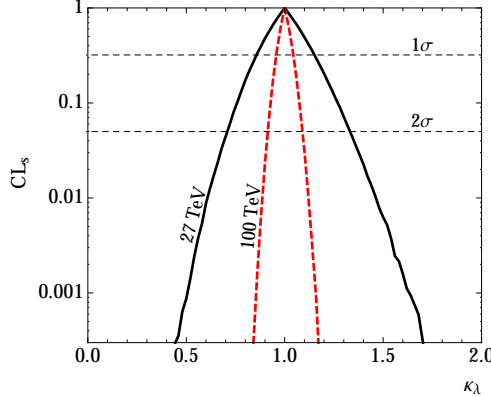


Fig. 49: Confidence level for separating an anomalous Higgs self-coupling hypothesis from the Standard Model $\kappa_\lambda = 1$.

In the right panel of Fig. 48 we show the discovery reach for the Higgs pair signal at HE-LHC and a 100 TeV collider for three di-photon invariant mass resolutions described by a Gaussian width of 0.75, 1.5, 2.25 GeV and corresponding Higgs mass windows $|m_{\gamma\gamma} - m_h| < 1, 2, 3$ GeV. As resolution of 1.5 GeV has already been achieved at the LHC [202]. Higgs pair production will be discovered at the HE-LHC with approximately $2.5 \dots 5 \text{ ab}^{-1}$ and at the 100 TeV collider with $0.2 \dots 0.3 \text{ ab}^{-1}$ of data, in both cases well below the design luminosity.

As commented in the introduction, there exist physics scenarios in which the Higgs self-coupling could be modified at the level of order one deviation from the SM value. The accurate measurement of the Higgs self-coupling via Higgs pair production at future colliders has the best promise to uncover the new physics associated with the Higgs sector. In Fig. 49, we show the accuracy on this measurement. We find that the Higgs self-coupling can be measured with a precision

$$\begin{aligned} \kappa_\lambda \approx 1 \pm 15\% \text{ at } 68\% \text{ CL} \quad &\text{and} \quad \kappa_\lambda \approx 1 \pm 30\% \text{ at } 95\% \text{ CL} && (\text{HE-LHC, 27 TeV, } 15 \text{ ab}^{-1}), \\ \kappa_\lambda \approx 1 \pm 5\% \text{ at } 68\% \text{ CL} \quad &\text{and} \quad \kappa_\lambda \approx 1 \pm 10\% \text{ at } 95\% \text{ CL} && (100 \text{ TeV, } 30 \text{ ab}^{-1}). \end{aligned} \quad (36)$$

While our conclusions on the determination of Higgs-self-interaction at future hadron colliders are robust and important, there is still room to improve. Although the final state $b\bar{b}\gamma\gamma$ is believed to be the most sensitive channel because of the background suppression and signal reconstruction, there exist complementary channels such as $gg \rightarrow hh \rightarrow b\bar{b}\tau^+\tau^-$, $b\bar{b}W^+W^-$, $b\bar{b}b\bar{b}$, etc. The kinematics-based measurement and the all features related to QCD radiation at higher energies should be equally applicable to all of them.

by Samuel Homiller and Patrick Meade

The Higgs self-coupling plays a central role in the spontaneous breaking of electroweak symmetry, and governs a pure elementary scalar interaction – one that has never been observed in nature. Unfortunately, due to the small rate of hh production, measuring the Higgs self-coupling at a 14 TeV appears exceedingly difficult unless it deviates substantially from the Standard Model value [191, 203]. A precision measurement of the Higgs self-coupling is thus one of the primary goals of any higher energy collider. In this section we use the convention

$$V_{\text{int}} = \lambda_3 \frac{m_h^2}{2v} h^3 + \lambda_4 \frac{m_h^2}{8v^2} h^4 \quad (37)$$

such that in the SM $\lambda_3 = 1$.

While the prospects of a 100 TeV collider in measuring the self-coupling have been well studied [204], relatively less attention has been paid to intermediate energy colliders such as HE-LHC. Previous studies indicate that the $hh \rightarrow b\bar{b}\gamma\gamma$ channel has the most promising signature at hadron colliders, and this is expected to be true at 27 TeV as well. However, the $b\bar{b}\gamma\gamma$ channel still suffers from significant backgrounds from particle misidentification in the detector, making a dedicated detector study including these effects essential. Finally, as discussed below, single-Higgs production – including through gluon-fusion – is a significant background that must be properly understood to accurately project the capabilities of HE-LHC. In what follows, we present a projection of the capabilities of a HE-LHC to measure the self-coupling with these intricacies carefully considered.

3.4.1.3 Signal and Background Simulations

The signal and background samples generated for this study are summarized in Table 22. We also show the cross sections of 14 TeV samples generated for validation with previous projections.

The details of the signal and background simulations mimic those in Ref. [205]. The $pp \rightarrow hh \rightarrow b\bar{b}\gamma\gamma$ signal is simulated at leading order using MADGRAPH5_AMC@NLO [155, 206] using the NNPDF2.3LO PDF set [207] including all finite top mass effects. The MADSPIN package [208] was used for the Higgs boson decays and PYTHIA 8 [209] for the showering and hadronization of events. The LO signal is normalized to match the state of the art NNLO/NNLL calculation with finite top mass effects included at NLO in QCD [192]. Additional samples with the self-coupling modified to values between -1 and 10 times the SM value were also generated. Representative kinematic distributions of the signal at parton level are shown in Fig. 50.

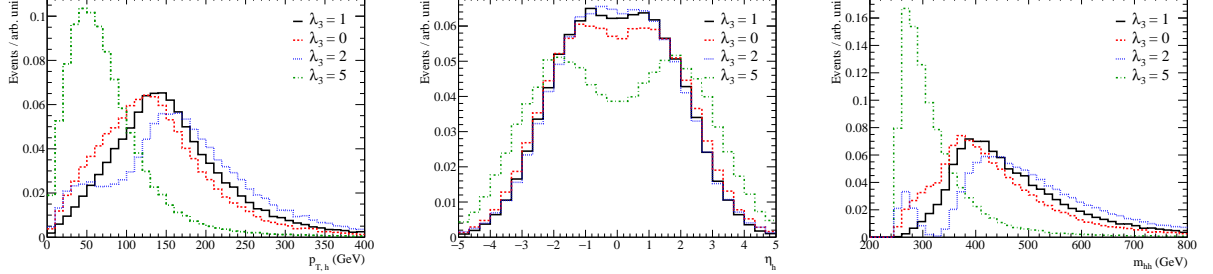


Fig. 50: (Left:) The transverse-momentum distribution of the true Higgs bosons generated in our 27 TeV samples, prior to showering and detector smearing, for several different values of λ_3 . (Center:) The same, but for the Higgs pseudorapidity. Right: The same, but for the distribution of the true Higgs pair invariant mass.

Backgrounds to the $b\bar{b}\gamma\gamma$ decay channel include single Higgs production modes, non-resonant QCD backgrounds, as well as $Z(b\bar{b})\gamma\gamma$ and $t\bar{t}(\gamma)$ production. We include all backgrounds where up to two additional photons or b -jets can arise from either misidentified light jets or electrons misidentified as photons.

The background from single Higgs production via gluon fusion ($ggF(\gamma\gamma)$) was generated in MADGRAPH with up to two extra partons allowed in the matrix element, with no additional k -factor due to the already present real emissions. Events from other single Higgs production modes were generated directly in PYTHIA 8 at LO and normalized based on the recommendations in Ref. [8]. The remaining backgrounds were generated in MADGRAPH interfaced with PYTHIA 8 for showering and hadronization, with one additional jet allowed in the matrix element with MLM matching [210, 211] to the parton shower.

Process	Generator	$\sigma \cdot BR$ [fb]		Order QCD	Expected Events (27 TeV, 15 ab $^{-1}$)
		14 TeV	27 TeV		
$h(b\bar{b})h(\gamma\gamma)$	MADGRAPH/PYTHIA 8	0.11	0.41	NNLO/NNLL	209.6 \pm 0.2
$tth(\gamma\gamma)$	PYTHIA 8	1.40	6.54	NLO	286.8 \pm 1.6
$Zh(\gamma\gamma)$	PYTHIA 8	2.24	5.58	NLO	67.1 \pm 0.7
$ggF(\gamma\gamma)$	MADGRAPH/PYTHIA 8	83.2	335.1	N^3LO	349.7 \pm 9.5
$b\bar{b}\gamma\gamma$	MADGRAPH/PYTHIA 8	3.4×10^2	9.5×10^2	LO	414.6 \pm 10.3
$c\bar{c}\gamma\gamma$	MADGRAPH/PYTHIA 8	4.4×10^2	1.5×10^3	LO	185.7 \pm 4.2
$jj\gamma\gamma$	MADGRAPH/PYTHIA 8	5.9×10^3	1.4×10^4	LO	63.3 \pm 3.8
$b\bar{b}j\gamma$	MADGRAPH/PYTHIA 8	1.1×10^6	3.4×10^6	LO	199.6 \pm 9.4
$c\bar{c}j\gamma$	MADGRAPH/PYTHIA 8	4.8×10^5	1.6×10^6	LO	25.3 \pm 3.0
$b\bar{b}jj$	MADGRAPH/PYTHIA 8	3.7×10^8	1.5×10^9	LO	155.4 \pm 8.2
$Z(b\bar{b})\gamma\gamma$	MADGRAPH/PYTHIA 8	2.61	5.23	LO	21.5 \pm 0.4
$t\bar{t}$	MADGRAPH/PYTHIA 8	6.7×10^5	2.9×10^6	NNLO	11.6 \pm 3.3
$t\bar{t}\gamma$	MADGRAPH/PYTHIA 8	1.7×10^3	7.9×10^3	NLO	145.0 \pm 10.3
Total Background					1925.8 \pm 22.7
Significance (S/\sqrt{B})					4.77 \pm 0.14

Table 22: List of signal and background processes, the event generator used to simulate the matrix element and parton shower, and the cross section of each process along with the corresponding order in QCD at which the cross section is normalized. In the right-most column we show the expected number of events after all the event selection criteria have been applied.

3.4.1.4 Detector Simulation

To approximate the effects of detector resolution and reconstruction efficiencies, we use DELPHES 3 with a dedicated card developed to approximate the performance of ATLAS and CMS at HL-LHC. We take this as a reasonable benchmark for the expected performance after the HE-LHC upgrade.

With respect to the DELPHES setup used in [205], the card here has an improved E-Cal resolution and assumes a higher photon identification efficiency, but a somewhat degraded dijet mass resolution. Aside from resolution and efficiency effects, particle misidentification in the detector is also an important source of backgrounds to $hh \rightarrow b\bar{b}\gamma\gamma$. To avoid issues with MC statistics, we implement b -tagging and jet mistagging rates at analysis level using a reweighting scheme, with probabilities taken as functions of the jet p_T as in Ref. [205]. These probabilities correspond to roughly $p_{b \rightarrow b} \approx 70\%$, $p_{c \rightarrow b} \approx 20\%$ and $p_{j \rightarrow b} \lesssim 1\%$. The probability for a light jet to fake a photon in the detector is also included via reweighting at analysis level as a function of p_T (see [205]) which peaks at 5×10^{-4} for $p_{T,j} \sim 60$ GeV before falling exponentially to $\sim 1 \times 10^{-4}$.

3.4.1.5 Results and Limits on the Self-Coupling

To isolate the $hh \rightarrow b\bar{b}\gamma\gamma$ signal, we implement selection cuts as follows:

- At least 2 isolated photons and b-tagged jets with leading $p_T > 60$ GeV and sub-leading $p_T > 35$ GeV, all with $|\eta_{\gamma,b}| < 2.5$.
- $p_{T,\gamma\gamma}, p_{T,b\bar{b}} > 125$ GeV.
- $\Delta R_{b\bar{b}}, \Delta R_{\gamma\gamma} < 3.5$.
- $|m_{\gamma\gamma} - 125.0$ GeV| < 4.0 GeV.
- $|m_{b\bar{b}} - 125.0$ GeV| < 25 GeV.
- $n_{\text{jets}} < 6$ for jets with $p_T > 30$ GeV, $|\eta| < 2.5$.
- No isolated leptons with $p_T > 25$ GeV.
- $|\cos \theta_{hh}| < 0.8$.

where $\cos \theta_{hh}$ is the decay angle of the Higgs boson pair evaluated in the lab frame (see Fig. 51).

Note that cuts on the p_T and Δ_R of the $\gamma\gamma$ and $b\bar{b}$ pair are tightly correlated with the invariant mass of the hh system. As seen in Fig. 51 the photon pair p_T has strong discriminating power for the

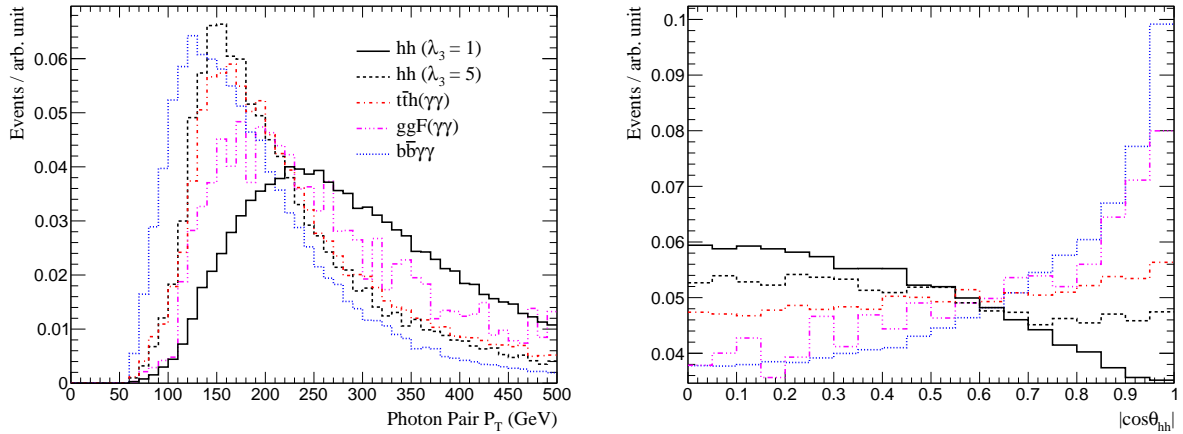


Fig. 51: Normalized distributions of (Left:) the p_T of the reconstructed $h \rightarrow \gamma\gamma$ and (Right:) the magnitude of $\cos\theta_{hh}$, the Higgs decay angle defined in the text. We show the distributions for the signal with $\lambda_3 = 1$ and 5 as well as several representative backgrounds.

SM hh signal, but for non-SM values of λ_3 , the signal and background become more degenerate.

The final selection efficiency is 3.4%, and the expected number of events from each signal/background channel after applying all the cuts and detector effects is given in Table 22 assuming 15 ab^{-1} integrated luminosity at HE-LHC. The uncertainty for each sample is estimated by partitioning the full event sample in to subsamples and computing the standard deviation of the results from each subsample.

The largest backgrounds are from continuum $b\bar{b}\gamma\gamma$ and single Higgs production and decay to $\gamma\gamma$. Particularly, we see that the ggF induced mode contributes an $\mathcal{O}(1)$ background, despite being neglected in previous studies. The accurate modeling of the extra jets that arise in the hadron collision is a necessity for properly understanding this contribution. Other large backgrounds arise from processes where a jet is reconstructed as a photon – even when two fake photons are needed. Finally, we see that $t\bar{t}$ and $t\bar{t}\gamma$ are not insignificant backgrounds with the set of cuts we've applied. Several of these backgrounds might be mitigated by exploring the additional kinematic information in events with multiple jets, but the single-Higgs production backgrounds are difficult to reduce in light of the true $h \rightarrow \gamma\gamma$ present.

To understand the attainable precision on λ_3 , we assume a hypothetical observation of $S+B$ events after all selection cuts with S and B as in Table 22. This allows us to derive 68 and 95% confidence intervals on the expected number of signal events using a likelihood scan, including only the MC and statistical uncertainties. The expected number of signal events with 15 ab^{-1} integrated luminosity is plotted in Fig. 52 along with the 1σ (2σ) regions in green (yellow).

We can also compute the expected number of events at 15 ab^{-1} as a function of λ_3 , taking into account both the varying σ_{hh} cross section and the modified acceptance due to changes in the signal kinematics. The resulting curve is shown in red in Fig. 52. The intersection of this curve with the 1 and 2σ regions indicate the expected precision on λ_3 in the absence of systematic uncertainties. We find

$$\lambda_3 \in [0.58, 1.45] \quad \text{at 68\% C.L.} \quad (38)$$

Note that, as a result of the destructive interference between the triangle and box diagrams leading to hh production, there is a degeneracy in the expected number of events around $\lambda_3 \sim 5$. However, the kinematic structure of the hh signal is very different at large values of λ_3 , and such values could be easily rejected using differential measurements (e.g., with $m_{hh} = m_{b\bar{b}\gamma\gamma}$ or $p_{T,hh}$), so the degeneracy can be safely ignored for the purposes of this work.

In conclusion, we find that with a full account of the detector effects and backgrounds to $hh \rightarrow$

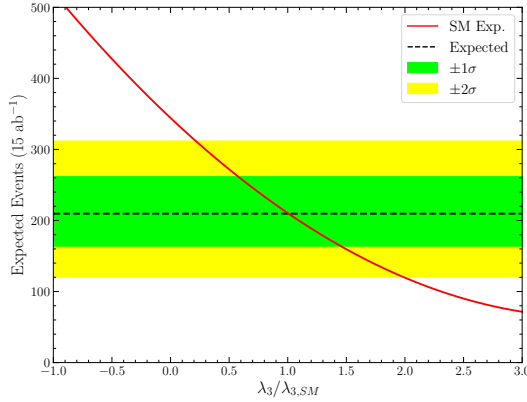


Fig. 52: The expected number of signal events in a hypothetical experiment assuming the signal and background rates computed in Table 22 at $L = 15 \text{ ab}^{-1}$ for HE-LHC with the regular detector performance assumption. The black dashed line indicates the expected number of events from signal while the green (yellow) regions show the 1σ (2σ) uncertainty regions arising from a likelihood scan with the statistical and MC uncertainties on the signal and background counts. The red curve shows the expected number of events from signal in a background free measurement as a function of λ_3 , accounting for the changes in the signal acceptance due to kinematic differences at different λ_3

$b\bar{b}\gamma\gamma$, a cut based analysis leads to an expected significance of $4.77 \pm 0.14\sigma$, corresponding to a 45% measurement of the Higgs self-coupling at 27 TeV with 15 ab^{-1} . Future improvements can be made both by considering other decay channels (e.g., $hh \rightarrow b\bar{b}b\bar{b}, b\bar{b}\tau\tau$, and $b\bar{b}WW$) and by exploiting the additional information present in the hh invariant mass distribution, as discussed elsewhere in this report.

3.4.2 ATLAS studies

by P. Bokan, E. Petit, M. Wielers

The results presented in Section 3.2.1 were extended to provide estimates of the prospects at the HE-LHC, assuming a centre of mass collision energy of 27 TeV and 15 ab^{-1} of data.

The assumption is made that the detector performance will be the same as of the HL-LHC ATLAS detector. Comparisons between simulation at centre of mass energy of 14 and 27 TeV show that the kinematic of the Higgs boson decay particles, as well as the m_{HH} distribution are similar. However the pseudorapidity of the particle tends to point more frequently in the forward region, which would decrease the acceptance by around 10%. This effect is not taken into account and the impact is expected to be small.

The event yields for the various background processes are scaled by the luminosity increase and the cross-section ratio between the two centre of mass energies. For the signal the cross-section of 139.9 fb is used.

Without including systematic uncertainties a significance of XX and XX standard deviations is expected for the $b\bar{b}\gamma\gamma$ and $b\bar{b}\tau\tau$ channels respectively. The hypothesis of no Higgs self-coupling can be excluded with a significance of XX and XX standard deviations respectively. Finally the κ_{lambda} parameter is expected to be measured with a precision of XX% and XX% respectively.

3.5 Indirect probes

3.5.1 *Indirect probes of the trilinear coupling through differential distributions measurements*

3.5.2 *Indirect probes through single Higgs boson production*

Bizon, Gorbahn, Haisch, Maltoni, Pagani, Shivaji, Zanderighi, Zhao

In this section we discuss the possibility of indirectly extracting information on the trilinear self interactions of the Higgs boson via precise measurements of single-Higgs production [212–220] at the HL-LHC and HE-LHC. This strategy is complementary to the direct measurement via double-Higgs production (see section ??), which already at leading order, i.e. at one loop in the case of $gg \rightarrow HH$, depends on the trilinear Higgs self interaction. In the case of single-Higgs production, on the contrary, the Higgs self interactions enter only via one-loop corrections, i.e., at the two-loop level for the gluon-fusion (ggF) production mode. The effects of modified Higgs self interactions are therefore generically much smaller, but for single-Higgs production processes the precision of the experimental measurements is and will be much better than for double-Higgs production. This, and the fact that for single-Higgs production many different final states and both inclusive as well as differential measurements are possible will lead to competitive indirect determinations of the trilinear Higgs self coupling. In [221, 222] also electroweak (EW) precision observables have been considered to this purpose.

In the following subsection, we will briefly recall the calculation framework introduced in [213, 214]. We also provide numerical results for the effects due to a modified trilinear Higgs coupling in the most important inclusive and differential single-Higgs production cross sections as well as the Higgs branching ratios. Based on these results, we will analyse in section ?? the sensitivity of the HL-LHC and HE-LHC in constraining the trilinear Higgs self interactions.

3.5.2.1 *Theoretical framework*

The effects of anomalous Higgs interactions can be extracted from experimental data via the signal strength parameters μ_i^f , which are defined for any specific combination of production and decay channel $i \rightarrow H \rightarrow f$ as follows

$$\mu_i^f \equiv \mu_i \times \mu^f = \frac{\sigma(i)}{\sigma^{\text{SM}}(i)} \times \frac{\text{BR}(f)}{\text{BR}^{\text{SM}}(f)}. \quad (39)$$

Here the quantities μ_i and μ^f are the production cross sections $\sigma(i)$ ($i = ggF, \text{VBF}, WH, ZH, t\bar{t}H, tHj$) and the branching ratios $\text{BR}(f)$ ($f = \gamma\gamma, ZZ, WW, b\bar{b}, \tau\tau$) normalised to their SM values, respectively. Assuming on-shell production, the product $\mu_i \times \mu^f$ therefore corresponds to the rate for the $i \rightarrow H \rightarrow f$ process normalised to the corresponding SM prediction.

The quantities μ_i and μ^f that enter the definition of μ_i^f in (39) can be expressed as

$$\mu_i = 1 + \delta\sigma_{\lambda_3}(i), \quad \mu^f = 1 + \delta\text{BR}_{\lambda_3}(f), \quad (40)$$

where $\delta\sigma_{\lambda_3}(i)$ and $\delta\text{BR}_{\lambda_3}(f)$ are the deviations induced by an anomalous trilinear Higgs self interaction to the production cross sections and branching ratios, respectively. This definition can be straightforwardly extended to the differential level and one has $\mu_i^f = \mu_i = \mu^f = 1$ in the SM.

In single-Higgs production, the trilinear Higgs self interactions start to enter only at the one-loop level in the case of vector boson fusion (VBF), $WH, ZH, t\bar{t}H, tHj$ production, while in the case of ggF production and the decays $H \rightarrow gg, \gamma\gamma$ one has to calculate two-loop EW corrections. The appearance of the quadrilinear Higgs self coupling in single-Higgs processes is further delayed by one loop order.

For the strategy discussed here, the anomalous trilinear Higgs self interactions can be equivalently parameterised either via an anomalous trilinear coupling

$$\lambda_3 \equiv \kappa_3 \lambda_3^{\text{SM}} \quad (41)$$

where $\lambda_3^{\text{SM}} = m_H^2/(2v^2)$ with $v = (\sqrt{2}G_F)^{-1/2} \simeq 246$ GeV the EW vacuum expectation value, or via the corresponding dimension-six operator

$$\mathcal{O}_6 = -\frac{\lambda_3^{\text{SM}} c_6}{v^2} |\Phi|^6, \quad (42)$$

with Φ denoting the usual SM Higgs doublet. In the normalisation adopted in (42), the simple relation

$$\kappa_3 = 1 + c_6, \quad (43)$$

is obtained and allows to translate constraints on the coupling modifier κ_3 into bounds on the Wilson coefficient c_6 and vice versa.

In the presence of modified trilinear Higgs self interactions, all single-Higgs production and decay channels receive two types of contributions [213, 214]: firstly, a process and kinematic dependent one, denoted as C_1 hereafter, which is linear in c_6 or κ_3 and second, a universal one proportional to the Higgs wave function renormalisation constant Z_H , which is proportional to κ_3^2 and therefore contains both a linear and quadratic piece in c_6 . The quantity $\delta\sigma_{\lambda_3}(i)$ introduced in (40) as well as any differential distribution related to it can thus be written as²

$$\delta\sigma_{\lambda_3}(i) = (\kappa_3 - 1) C_1^\sigma + (\kappa_3^2 - 1) \delta Z_H = c_6 C_1^\sigma + (2c_6 + c_6^2) \delta Z_H, \quad (44)$$

where δZ_H denotes the one-loop correction to the Higgs wave function renormalisation constant associated to modifications of the trilinear Higgs self coupling. In the case of the decays, the effects due to Higgs wave function renormalisation cancel in the branching ratios, and as a result the quantities $\delta\text{BR}_{\lambda_3}(f)$ defined in (40) take the following form

$$\delta\text{BR}_{\lambda_3}(f) = (\kappa_3 - 1) (C_1^\Gamma - C_1^{\Gamma_{\text{tot}}}) = c_6 (C_1^\Gamma - C_1^{\Gamma_{\text{tot}}}). \quad (45)$$

Here $C_1^{\Gamma_{\text{tot}}}$ is an effective term that describes the process dependent corrections to the total decay width of the Higgs boson.

In the following we provide the values of the C_1 coefficients that are used in the numerical analyses presented in section ???. The given values correspond to the input

$$\begin{aligned} G_F &= 1.1663787 \times 10^{-5} \text{ GeV}^{-2}, & m_W &= 80.385 \text{ GeV}, \\ m_Z &= 91.1876 \text{ GeV}, & m_H &= 125 \text{ GeV}, & m_t &= 172.5 \text{ GeV}. \end{aligned} \quad (46)$$

For these parameters one finds numerically [214]

$$\delta Z_H = -1.536 \times 10^{-3}, \quad C_1^{\Gamma_{\text{tot}}} = 2.3 \times 10^{-3}. \quad (47)$$

In the calculations of production cross sections and distributions, the renormalisation and factorisation scales are taken to be $\mu_R = \mu_F = \frac{1}{2} \sum_f m_f$ with m_f the masses of the particles in the final state and PDF4LHC2015 [25] parton distribution functions are used. On the other hand, the dependence of the C_1 coefficients on μ_R , μ_F and the PDF set is negligible.

In table 23 we list the values of C_1^σ for the various production modes at different centre of mass (CM) energies. One first notices that WH , ZH and especially $t\bar{t}H$ production depend stronger on the anomalous trilinear Higgs self coupling than the ggF , the VBF and the tHj channel. Furthermore, in the case of WH , ZH and $t\bar{t}H$ production the loop corrections contributing to C_1^σ feature a Sommerfeld enhancement, which results in an increased sensitivity to anomalous trilinear Higgs self interactions at low energies [214, 215, 218]. This feature is illustrated in tables 24 and 25 where we give the

²This equation is in reality a linearised version of the complete formula that is used for extracting the results in Section ... and involves the Higgs wave function resummation [214, 218]. Also (45) is a linear expansion.

$C_1^\sigma [\%]$	ggF	VBF	WH	ZH	tH	tHj
13 TeV	0.66	0.64	1.03	1.19	3.51	0.91
14 TeV	0.66	0.64	1.03	1.18	3.47	0.89
27 TeV	0.66	0.62	1.01	1.16	3.20	0.79

Table 23: C_1^σ coefficients for inclusive single-Higgs production cross sections at different CM energies.

$p_T(H)$ [GeV]	[0, 25]	[25, 50]	[50, 100]	[100, 200]	[200, 500]	> 500
VBF	0.97	0.88	0.73	0.58	0.45	0.29
ZH	2.00	1.75	1.21	0.51	0.01	-0.10
WH	1.70	1.49	1.04	0.44	0.01	-0.09
tH	5.31	5.07	4.38	3.00	1.27	0.17
tHj	1.23	1.18	1.02	0.74	0.33	-0.06

Table 24: C_1^σ coefficients for single-Higgs production processes at 13 TeV in different $p_T(H)$ bins.

$p_T(H)$ [GeV]	[0, 25]	[25, 50]	[50, 100]	[100, 200]	[200, 500]	> 500
VBF	0.65	0.65	0.65	0.62	0.52	0.29
ZH	2.00	1.74	1.21	0.50	0.00	-0.10
WH	1.70	1.49	1.04	0.44	0.01	-0.09
tH	5.00	4.78	4.14	2.86	1.23	0.22
tHj	1.06	1.03	0.91	0.69	0.33	0.02

Table 25: Same as table 24 but for a CM energy of 27 TeV.

$C_1^\Gamma [\%]$	$\gamma\gamma$	ZZ	WW	gg
on-shell H	0.49	0.83	0.73	0.66

Table 26: C_1^Γ coefficients for the phenomenologically relevant decay modes of the Higgs boson.

values of C_1^σ in bins of the Higgs transverse momentum $p_T(H)$ for pp collisions at 13 TeV and 27 TeV, respectively.³ Table 26 finally provides the values of the C_1^Γ coefficients for the decay modes of the Higgs boson that are relevant in our numerical study.

Notice that all the formulas and numbers presented in this subsection take into account only effects associated to an anomalous trilinear Higgs self coupling. The extension to more general and physically motivated scenarios that include also other new-physics effects is simple and has been worked out in [216, 218]. It consists in adding to (44) and (45) the effects of other anomalous interactions such as a modified top Yukawa coupling or altered/new gauge-Higgs vertices. In the next subsection, we perform a global analyses of the constraints on λ_3 that the HL-LHC and the HE-LHC should be able to set. We thereby follow the lines of the study [216], using the results for the coefficients C_1 provided above.

As discussed in refs. [216, 218], the constraints that can be set on c_6 critically depend on the interplay between the following aspects:

- The number of additional parameters related other anomalous interactions.

³Results for a different binning or different observables can be easily obtained with the code presented in [218].

- The number of independent measurements considered in the analysis.
- The inclusion of differential information.
- The assumptions on the theoretical and experimental (statistical and systematic) errors.

In the next section we explore this interplay for the cases of the HL- and HE-LHC following the lines of the study presented in refs. [216] augmented with the new results provided in this section. Independent analyses performed by the ATLAS and CMS collaborations with a full-fledged treatment of all the correlations among experimental uncertainties are desirable. It is worth noting that, when other anomalous interactions are also considered, the effects of Z_H^{BSM} are degenerate with those in general affecting the Higgs wave-function normalisation, typically parameterised via the Wilson coefficient \mathcal{C}_H . Thus, the coefficients C_1^σ and therefore the differential distributions have a primary role in the extraction of the information on κ_3 from measurements of single Higgs production.

We also recall that limits on κ_3 or equivalently c_6 obtained with this strategy are sensible only when $|\kappa_3| < 20$; as discussed in refs. [214] this limit guarantees that the perturbative loop expansion is converging and that the leading missing higher orders depending on $\kappa_3 - 1 = c_6$ are below 10% level. On the contrary, as discussed in refs. [220, 223], when the information from double Higgs production is considered a more cautious limit $|\kappa_3| < 6$ should be adopted in order to achieve both perturbative unitarity and the convergence of the loop expansion.

3.5.3 Global fit

Stefano Di Vita, Gauthier Durieux, Jiayin Gu, Zhen Liu, Giuliano Panico, Marc Riembau, Thibaud Vantalon

In the previous chapter (cite) it has been shown that assuming the trilinear is the only coupling deviating from its SM value that single Higgs observable can give competitive bound with double Higgs production, see also Refs. [213–215, 218, 221], electroweak process where the Higgs trilinear enter at the two loop level have also been studied in [222]. Nevertheless, departures of the Higgs self-coupling from its SM prediction signal the existence of new dynamics that, in general, would leave an imprint on other Higgs couplings as well which have a strong impact on the bound as shown by Ref. [216]. The importance of a global fit is therefore two-fold, namely to assess the robustness of the studies that take into account deformations exclusively in the Higgs trilinear, and to single out the sensitivity on the single-Higgs couplings that is required to minimize the impact of the possible correlations.

To include the effect of the different deformations away from the SM, we use the EFT framework described in Ref. [216], where 9 parameters describe the deviations of the single-Higgs couplings. In particular, we consider three⁴ parameters for the Yukawa interactions (δy_t , δy_b , δy_τ), two for the contact interactions with gluons and photons (c_{gg} , $c_{\gamma\gamma}$), rescalings of the SM hZZ and hWW interactions (parametrized by one coefficient, δc_z , if custodial symmetry is unbroken), and three coefficients (c_{zz} , $c_{z\square}$, $c_{z\gamma}$) parametrizing interactions of the Higgs with the electroweak bosons that have non-SM tensor structures. Note that two combinations of the last three parameters are constrained by diboson data, showing an interesting interplay between the gauge and the Higgs sectors. A global fit on the Higgs self-coupling, parametrized by $\delta\kappa_\lambda$ (which is zero in the SM) using only inclusive single Higgs observables, and taking into account the additional 9 EFT deviations described above, suffers from a flat direction. To lift it, it is necessary to include data from differential measurements of those processes, since the single-Higgs deformations and $\delta\kappa_\lambda$ tend to affect the distributions in complementary ways.

The global fit for the HL-LHC is summarized in Fig. 53. In the left plot, we show in green the $\Delta\chi^2$ including only single-Higgs data, both in an exclusive study (dotted), and after profiling over all the

⁴If other fermionic decay channels can be observed, further parameters can be included, with no effect on the number of degrees of freedom.

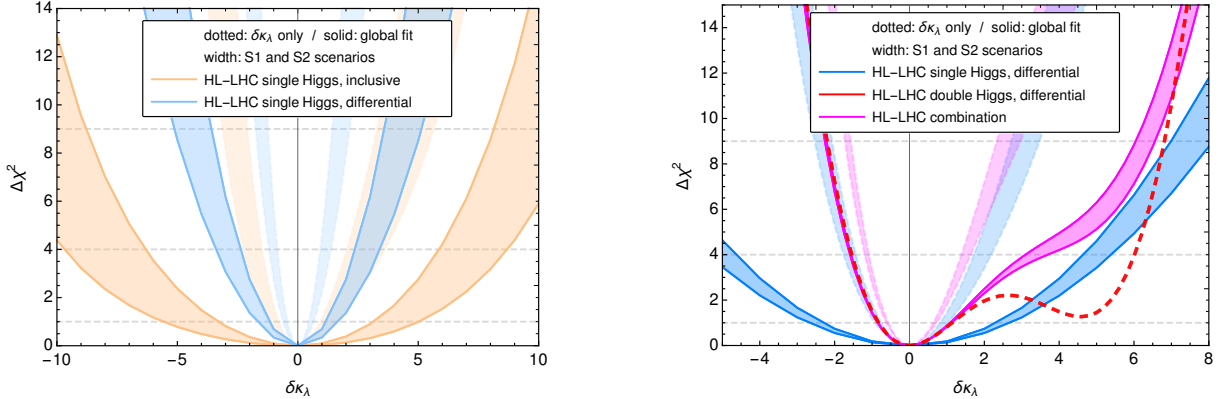


Fig. 53: χ^2 analysis of the Higgs self-coupling $\delta\kappa_\lambda$ using single- and double-Higgs processes for the HL-LHC at 13 TeV and 3 ab^{-1} . **Left:** Comparison of the constraints obtained using differential single-Higgs processes (green), with the ones using differential double-Higgs data together with inclusive single-Higgs measurements (blue). **Right:** Comparison of the constraints from differential single- and double-Higgs (orange), with those from differential double-Higgs data together with inclusive single-Higgs measurements (blue).

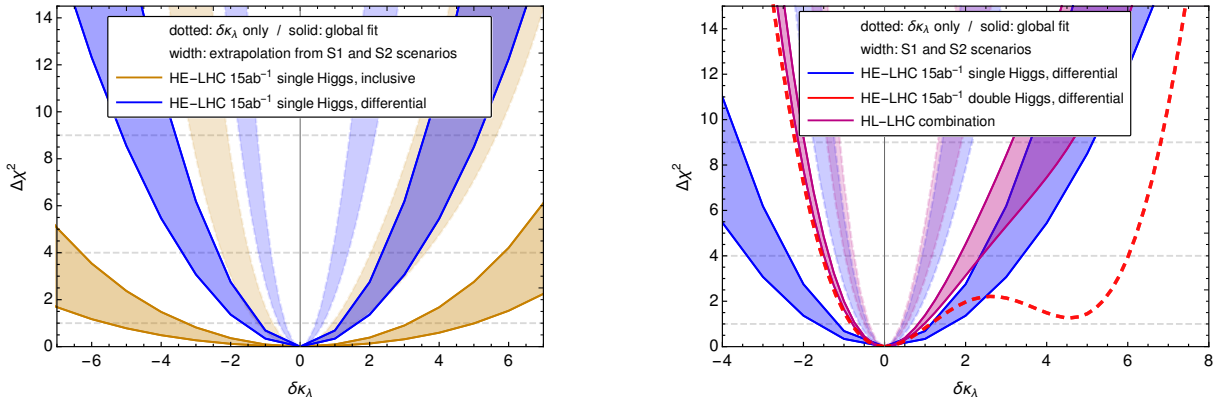


Fig. 54: χ^2 analysis of the Higgs self-coupling $\delta\kappa_\lambda$ using single-Higgs processes for the HE-LHC at 27 TeV and 15 ab^{-1} . **Left:** Comparison of the constraints using inclusive single-Higgs processes at HE-LHC (pink) with the global fit of HL-LHC (green) and its combination (Orange). **Right:** Comparison of the constraints using differential single-Higgs processes at HE-LHC (blue) with the global fit of HL-LHC (green) and its combination (red).

other parameters (solid). The width of the lines corresponds to different assumptions on the extrapolation of the projected experimental sensitivities on the inclusive signal strengths, to differential ones. We can see that, in a global fit, the constraint on the trilinear is worsened due to correlations (mainly with the top yukawa δy_t and the contact interaction with gluons c_{gg} , and, to a lesser degree, between δy_b and δc_z refer to fig4 if we include it). The fit to differential double-Higgs data and inclusive single-Higgs measurements, taken from the study in Ref. [168], is depicted in blue. In the right plot we can see that, while double-Higgs is clearly driving the bound, differential single-Higgs data is nonetheless relevant as it can help lift the degenerate minima around $\delta\kappa_\lambda \sim 5$.

We now discuss projections for the HE-LHC at 27 TeV with 15 ab^{-1} of integrated luminosity. For the uncertainties we perform a simple extrapolation where the theory and systematic uncertainties are kept the same as in the HL-LHC projections, while the statistical uncertainty is rescaled accordingly [195]. We show the results in Fig. 54. In the left plot, in pink, we present the χ^2 analysis using the

projections for the single-Higgs channels at HE-LHC at the inclusive level. Inclusive measurements are able to lift the flat direction due to the measurement of the $t\bar{t} + j$ production and the $z\gamma$ decay. The combination with the full HL-LHC analysis closes the flat direction and the second minimum can be excluded at $\sim 95\%$ CL. In the right plot the fit using differential observables in single-Higgs production at HE-LHC is shown in blue. The differential information is enough to lift the flat directions and the single-Higgs data is more constraining than the full HL-LHC combination, even in the global fit. Combination with HL-LHC gives a constraint of about $|\delta\kappa_\lambda| \lesssim 2$ at 95% CL. Moreover, the combination (in red) reduces the impact of the correlations.

Since it is expected that the theory and systematic uncertainties will change over time, in Fig. 55 we explore how our findings are affected if both uncertainties are rescaled by a common factor. Getting more than a factor two improvement on those uncertainties, which is a rather reasonable benchmark, does not significantly improve the constraints, and we conclude that the precision is limited by statistics.

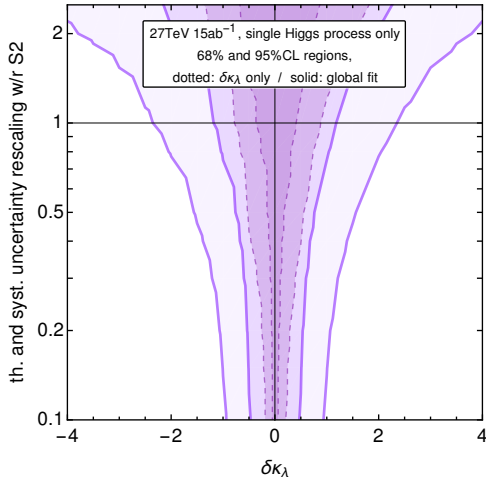


Fig. 55: $\Delta\chi^2 = 1$ and $\Delta\chi^2 = 3.85$ contour regions on the anomalous Higgs self-coupling $\delta\kappa_\lambda$ for the HE-LHC projections, as a function of the common rescaling factor of both the theory and systematic uncertainties with respect to the HL-LHC projections. The dashed lines indicate the constraints for an exclusive fit to $\delta\kappa_\lambda$, while the solid lines indicate the constraints after profiling over the remaining parameters.

3.6 Implications

3.6.1 Implications for flavor models

by Martin Bauer, Marcela Carena and Adrián Carmona

In 2HDMs, the term $H_1 H_2 \equiv H_1^T (i\sigma_2) H_2$ is a SM singlet which can however be charged under an additional $U(1)$ flavor symmetry. This is an interesting possibility that allows to generate the different fermion masses with a Froggatt-Nielsen (FN) mechanism where the flavon is replaced by the $H_1 H_2$ operator. In this way, the new physics scale Λ where the higher dimensional FN operators are generated is tied to the electroweak scale, leading to much stronger phenomenological consequences. Let us assume for concreteness a type-I like 2DHM with the following Yukawa Lagrangian

$$\mathcal{L}_Y \supset y_{ij}^u \left(\frac{H_1 H_2}{\Lambda^2} \right)^{n_{u_{ij}}} \bar{q}_L^i H_1 u_R^j + y_{ij}^d \left(\frac{H_1^\dagger H_2^\dagger}{\Lambda^2} \right)^{n_{d_{ij}}} \bar{q}_L^i \tilde{H}_1 d_R^j + y_{ij}^\ell \left(\frac{H_1^\dagger H_2^\dagger}{\Lambda^2} \right)^{n_{e_{ij}}} \bar{\ell}_L^i \tilde{H}_1 e_R^j + \text{h.c.}, \quad (48)$$

where $\tilde{H}_1 \equiv i\sigma_2 H_1^*$ as usual and the charges $n_{u,d,e}$ are a combination of the $U(1)$ charges of H_1 , $(H_1 H_2)$ and the different SM fermion fields. For simplicity, we set the flavor charges of $(H_1 H_2)$ and H_2 to 1 and 0, respectively, such that

$$n_{u_{ij}} = a_{q_i} - a_{u_j}, \quad n_{d_{ij}} = a_{q_i} - a_{d_j}, \quad n_{e_{ij}} = a_{\ell_i} - a_{e_j}, \quad (49)$$

if we denote by a_{q_i}, a_{u_i}, \dots , the $U(1)$ charges of the SM fermions. In general, the fermion masses are given by

$$m_\psi = y_\psi \varepsilon^{n_\psi} \frac{v}{\sqrt{2}} \quad \varepsilon = \frac{v_1 v_2}{2\Lambda^2} = \frac{t_\beta}{1 + t_\beta^2} \frac{v^2}{2\Lambda^2}, \quad (50)$$

with the vacuum expectation values $\langle H_{1,2} \rangle = v_{1,2}$ and $t_\beta \equiv v_1/v_2$. Besides being able to accommodate the observed hierarchy of SM fermion masses and mixing angles for the right assignment of flavor charges [], this framework can lead to enhanced diagonal Yukawa couplings between the Higgs and the SM fermions while having suppressed FCNCs. If we denote by h and H the two neutral scalar mass eigenstates, with h being the observed 125 GeV Higgs, the couplings between the scalars $\varphi = h, H$ and SM fermions $\psi_{L_i, R_i} = P_{L,R} \psi_i$ in the mass eigenbasis read

$$\mathcal{L} = g_{\varphi \psi_{L_i} \psi_{R_j}} \varphi \bar{\psi}_{L_i} \psi_{R_j} + \text{h.c.} \quad (51)$$

with i , such that $u_i = u, c, t$, $d_i = d, s, b$ and $e_i = e, \mu, \tau$. This induces flavor-diagonal couplings

$$g_{\varphi \psi_{L_i} \psi_{R_i}} = \kappa_{\psi_i}^\varphi \frac{m_{\psi_i}}{v} = \left(g_{\psi_i}^\varphi(\alpha, \beta) + n_{\psi_i} f^\varphi(\alpha, \beta) \right) \frac{m_{\psi_i}}{v}, \quad (52)$$

as well as flavor off-diagonal couplings

$$g_{\varphi \psi_{L_i} \psi_{R_j}} = f^\varphi(\alpha, \beta) \left(\mathcal{A}_{ij} \frac{m_{\psi_j}}{v} - \frac{m_{\psi_i}}{v} \mathcal{B}_{ij} \right). \quad (53)$$

The flavor universal functions in (52) and (53) read

$$g_{\psi_i}^h = \frac{c_{\beta-\alpha}}{t_\beta} + s_{\beta-\alpha}, \quad g_{\psi_i}^H = c_{\beta-\alpha} - \frac{s_{\beta-\alpha}}{t_\beta}, \quad (54)$$

and

$$f^h(\alpha, \beta) = c_{\beta-\alpha} \left(\frac{1}{t_\beta} - t_\beta \right) + 2s_{\beta-\alpha}, \quad f^H(\alpha, \beta) = -s_{\beta-\alpha} \left(\frac{1}{t_\beta} - t_\beta \right) + 2c_{\beta-\alpha}, \quad (55)$$

where $c_x \equiv \cos x$, $s_x \equiv \sin x$. One can see that, unless all flavor charges for a given type of fermions are equal, the off-diagonal elements in matrices \mathcal{A} and \mathcal{B} lead to FCNCs which are chirally suppressed by powers of the ratio ε , see [224] for more details.

The scalar couplings to the different gauge bosons are the same as in a normal type-I 2HDM while the scalar coupling between the heavy Higgs H and two SM Higgs scalars h , as well as the triple Higgs coupling can be expressed as [225, 226]

$$g_{Hhh} = \frac{c_{\beta-\alpha}}{v} \left[(1 - f^h(\alpha, \beta) s_{\beta-\alpha}) (3M_A^2 - 2m_h^2 - M_H^2) - M_A^2 \right], \quad (56)$$

$$g_{hhh} = -\frac{3}{v} \left[f^h(\alpha, \beta) c_{\beta-\alpha}^2 (m_h^2 - M_A^2) + m_h^2 s_{\beta-\alpha} \right], \quad (57)$$

where M_A is the pseudoscalar mass. The $U(1)$ flavor symmetry restricts the number of allowed terms in the scalar potential forbidding e.g. terms proportional to $H_1 H_2$. The interesting feature is that one can rewrite such self scalar interactions with the help of the function $f^h(\alpha, \beta)$, since it is somehow related

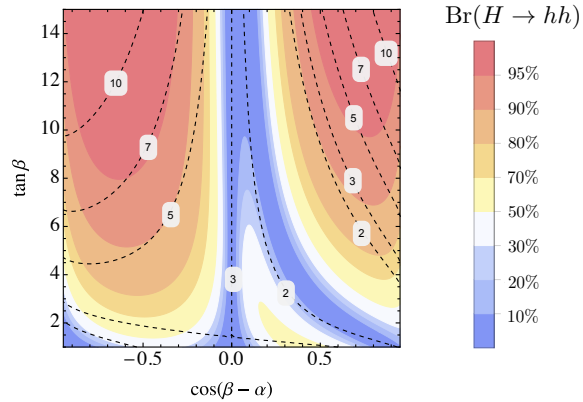


Fig. 56: $\text{Br}(H \rightarrow hh)$ as a function of $\cos(\beta - \alpha)$ and $\tan \beta$ for $M_H = M_{H^\pm} = 550$ GeV and $M_A = 450$ GeV. The dashed contours correspond to constant values $|\kappa_\psi^h|$ for $n_\psi = 1$.

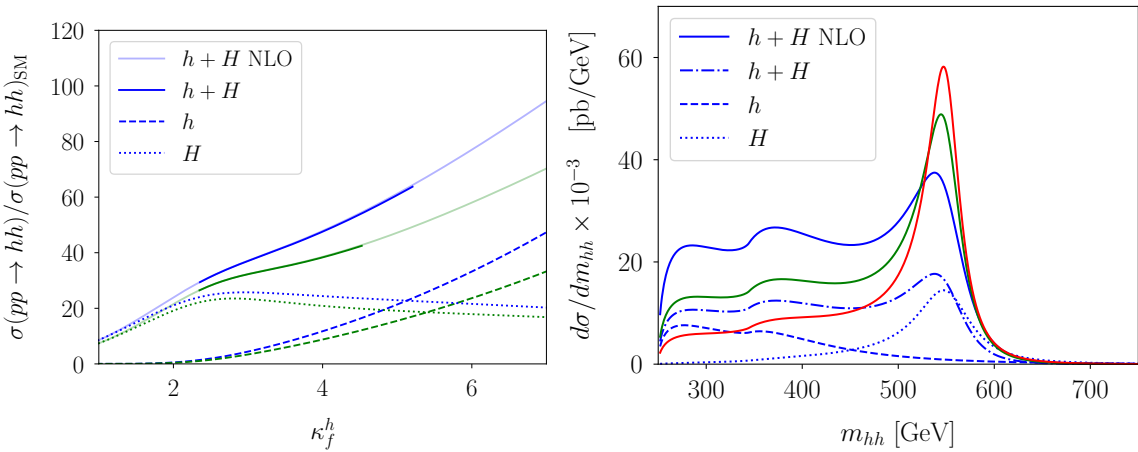


Fig. 57: Left: Cross section for Higgs pair production in units of the SM prediction as a function of κ_ψ^h for $c_{\beta-\alpha} = -0.45$ (-0.4) and $M_A = 450$ GeV, $M_H = M_{H^\pm} = 550$ GeV in blue (green) at $\sqrt{s} = 27$ TeV. Right: Invariant mass distribution for the different contributions to the signal with $c_{\beta-\alpha} = -0.45$ and $\kappa_\psi^h = 5$ (blue), $\kappa_\psi^h = 4$ (green) and $\kappa_\psi^h = 3$ (red) at $\sqrt{s} = 27$ TeV, respectively.

to the combination $H_1 H_2^\dagger$ appearing in both the scalar potential and the higher dimensional operators generating the different Yukawa couplings. Therefore, the parameter space for which $f^h(\alpha, \beta) \gg 1$ and $c_{\beta-\alpha} \neq 0$ leads to maximally enhanced diagonal couplings of the SM Higgs to fermions (52) as well as to an enhancement of the trilinear couplings (56) and (57). For maximally enhanced Yukawa couplings, the mass of the heavy Higgs H cannot be taken arbitrarily large and resonant Higgs pair production has to be present. This correlation between the enhancement of the Higgs Yukawa couplings κ_ψ^h and $\text{Br}(H \rightarrow hh)$ is illustrated for $M_H = M_A = M_{H^\pm} = 500$ GeV in Fig. 56 where we plot the dependence of $\text{Br}(H \rightarrow hh)$ on $c_{\beta-\alpha}$ and t_β . The dashed contours correspond to constant values of $|\kappa_\psi^h|$ for $n_\psi = 1$. This correlation does not depend on the factor n_ψ , although $n_\psi > 1$ leads to a larger enhancement. The two exceptions for which this correlation breaks down are the limits $c_{\beta-\alpha} \approx 0$ and $c_{\beta-\alpha} \approx \pm 1$. Whereas the second case is strongly disfavoured by SM Higgs couplings strength measurements, the first one (which corresponds to the decoupling limit) is at odds with the flavor model, for it requires large values of the spurion $\mu_3 \propto M_A$ which softly breaks the $U(1)$ flavor symmetry.

The enhancement in $\text{Br}(H \rightarrow hh)$ shown in Figure 56 is partially cancelled in the production cross section $\sigma(gg \rightarrow H)$ for large values of t_β due to the fact that $\sigma(gg \rightarrow H) \propto 1 + 1/t_\beta^2 - (\kappa_t^h)^2$,

with $\kappa_t^h \approx 1$. However, the cross-section $\sigma(gg \rightarrow h \rightarrow hh)$ is not suppressed for such values of t_β and the combination of both contributions leads to a continuous enhancement in the di-Higgs cross-section. There is therefore a non-trivial interplay between resonant and non-resonant contributions, which we illustrate in the left panel of Fig. 57, where we plot both contributions assuming as a function of κ_ψ^h for fixed values of $c_{\beta-\alpha}$ (which is a monotonic function of t_β). We assume a center-of-mass energy of $\sqrt{s} = 27$ TeV and set $M_A = 450$ GeV and $M_H = M_{H^\pm} = 550$ GeV, while choosing two different values of $c_{\beta-\alpha} = -0.45$ and -0.4 . Dashed (dotted) lines correspond to the non-resonant (resonant) contributions, whereas the solid lines represent the full $\sigma(gg \rightarrow hh)$ in the 2HDM in units of the SM prediction, both at LO and NLO. Solid lines show the NLO results, while the solid shaded lines mark the values of κ_ψ excluded by perturbativity and unitarity constraints [227]. More details about the calculation of the signal and plots for $\sqrt{s} = 13$ TeV can be found in Ref. [224]. The values of κ_ψ^h in Fig. 57 correspond to $n_\psi = 1$ but values of $\mathcal{O}(10)$ and larger are obtained for $n_\psi > 1$. We also show in the right panel of Fig. 57 the invariant mass distribution for the different contributions to the di-Higgs signal for $c_{\beta-\alpha} = -0.45$ and three different values of $\kappa_\psi^h = 3, 4$ and 5 . The interesting feature is that, when the enhancement in the Higgs Yukawa couplings is large enough, the interference between both non-resonant and resonant contributions turns the broad peak into a shoulder in the $d\sigma/dm_{hh}$ distribution for the total cross section, as shown for the case $\kappa_\psi^h = 5$ by the blue line in the right panel of Fig. 57. Resolving such shape in the invariant mass distribution can be quite challenging. We encourage a dedicated analysis considering the corresponding $d\sigma/dm_{hh}$ templates to maximize the sensitivity to features in the di-Higgs invariant mass distribution from the simultaneous enhancement of g_{hhh} , g_{Hhh} and κ_ψ^h .

3.6.2 Implications for theories of electroweak phase transition

4 High Energy Probes

4.1 tt differential measurements

4.2 WH/ZH at high energy/luminosity

Shankha Banerjee^a, Rick S. Gupta^a, Christoph Englert^b and Michael Spannowsky^a

^a*Institute of Particle Physics Phenomenology, Durham University, Durham DH1 3LE, UK*

^bSUPA, School of Physics and Astronomy, University of Glasgow, Glasgow G12 8QQ, UK

Introduction and EFT analysis

In this note we perform a collider study of the Higgs-strahlung process, $pp \rightarrow Z(\ell^+\ell^-)h(b\bar{b})$ in the Standard Model Effective Field Theory (SMEFT) framework. We will see that the leading high energy contribution to the $pp \rightarrow Zh$ process comes from the four contact interactions $hZ_\mu \bar{u}_{L,R} \gamma^\mu u_{L,R}$ and $hZ_\mu \bar{d}_{L,R} \gamma^\mu d_{L,R}$ that appear in the dimension-6 Lagrangian. These are the same four EFT directions, the so called “high energy primaries” that control high energy Wh , WW and WZ production (see Ref. [228]). The (pseudo-)observables involved in these diboson processes (anomalous TGCs and Z -pole observables) have already been constrained at LEP. We show in this note that because of the higher energies accessible at the LHC one can obtain bounds on these observables that are at least an order of magnitude stronger than those obtained at LEP.

The vertices in the dimension 6 Lagrangian that contribute to the $ff \rightarrow Vh$ (where $V = W, Z$) process in unitary gauge are as follows,

$$\begin{aligned} \Delta\mathcal{L}_6 \supset & \sum_f \delta g_f^Z Z_\mu \bar{f} \gamma^\mu f + \delta g_{ud}^W (W_\mu^+ \bar{u}_L \gamma^\mu d_L + h.c.) + g_{VV}^h h \left[W^{+\mu} W_\mu^- + \frac{1}{2c_{\theta_W}^2} Z^\mu Z_\mu \right] \\ & + \delta g_{ZZ}^h h \frac{Z^\mu Z_\mu}{2c_{\theta_W}^2} + \sum_f g_{Zf}^h \frac{h}{v} Z_\mu \bar{f} \gamma^\mu f + g_{Wud}^h \frac{h}{v} (W_\mu^+ \bar{u}_L \gamma^\mu d_L + h.c.) + \kappa_{Z\gamma} \frac{h}{v} A^{\mu\nu} Z_{\mu\nu} \\ & + \kappa_{WW} \frac{h}{v} W^{+\mu\nu} W_{\mu\nu}^- + \kappa_{ZZ} \frac{h}{2v} Z^{\mu\nu} Z_{\mu\nu}. \end{aligned} \quad (58)$$

Here we have used the Lagrangian presented in Ref. [229, 230], where α_{em} , m_Z and m_W have been used as input parameters and any corrections to the SM vector boson propagators have been traded in favor of the vertex corrections. After summing over all V -polarizations, the leading piece in the high energy cross-section deviation for $ff \rightarrow Vh$, is proportional to the four contact interactions: g_{Zf}^h , with $f = u_L, u_R, d_L$ and d_R .⁵ Table 27, shows the linear combinations of Wilson coefficients contributing to the four g_{Zf}^h couplings in different EFT bases. The aforementioned directions are shown in the BSM Primary basis of Ref. [229], where the Wilson coefficients are already constrained pseudo-observables. In this basis we see that these can be written in terms of already constrained LEP (pseudo)observables.

Given the inability to control the polarization of the initial state partons in a hadron collider, the process, in reality, only probes two of the above four directions. Taking only the interference term, we find these directions to be

$$g_{\mathbf{u}}^Z = g_{Zu_L}^h + \frac{g_{u_R}^Z}{g_u^Z} g_{Zu_R}^h, \quad g_{\mathbf{d}}^Z = g_{Zd_L}^h + \frac{g_{d_R}^Z}{g_{d_L}^Z} g_{Zd_R}^h. \quad (59)$$

⁵There exists a basis independent constraint at the dimension-6 level, $\sqrt{2} g_{Wud}^h = (g_{Zd_L}^h - g_{zu_L}^h)$.

	EFT directions probed by high energy $ff \rightarrow Vh$ production
Warsaw Basis [231]	$-\frac{2g}{c_{\theta_W}} \frac{v^2}{\Lambda^2} (T_3^f c_L^1 - T_3^f c_L^3 + (1/2 - T_3^f) c_f)$
BSM Primaries [229]	$\frac{2g}{c_{\theta_W}} Y_f t_{\theta_W}^2 \delta \kappa_\gamma + 2 \delta g_f^Z - \frac{2g}{c_{\theta_W}} (T_3^f c_{\theta_W}^2 + Y_f s_{\theta_W}^2) \delta g_1^Z$
SILH Lagrangian [110]	$\frac{g}{c_{\theta_W}} \frac{m_W^2}{\Lambda} (2 T_3^f \hat{c}_W - 2t_{\theta_W}^2 Y_f \hat{c}_B)$
Universal observables	$\frac{2g}{c_{\theta_W}} Y_f t_{\theta_W}^2 (\delta \kappa_\gamma - \hat{S} + Y) - \frac{2g}{c_{\theta_W}} (T_3^f c_{\theta_W}^2 + Y_f s_{\theta_W}^2) \delta g_1^Z - \frac{2g}{c_{\theta_W}} T_3^f W$
High Energy Primaries [228]	$- \frac{2m_W^2}{gc_{\theta_W}} (T_3^f a_q^{(1)} - T_3^f a_q^{(3)} + (1/2 - T_3^f) a_f)$

Table 27: The linear combinations of Wilson coefficients contributing to the contact interaction couplings g_{Zf}^h where $f = u_L, d_L, u_R, d_R$. the direction for a given f can be read off from this table by substituting the corresponding value of the $SU(2)_L$ and $U(1)_Y$ quantum numbers T_3^f and Y_f . Here $\hat{c}_W = c_W + c_{HW} - c_{2W}$ and $\hat{c}_B = c_B + c_{HB} - c_{2B}$. For the nomenclature of the operators, their corresponding Wilson coefficients and observables see for eg. Ref. [228].

At a given energy, a linear combination of the up-type and down-type coupling deviations, enters the interference term for the $pp \rightarrow Z h$ process, $g_{\mathbf{p}}^Z = g_{\mathbf{u}}^Z + \frac{\mathcal{L}_d(\hat{s})}{\mathcal{L}_u(\hat{s})} g_{\mathbf{d}}^Z$, where $\mathcal{L}_{u,d}$ is the $u\bar{u}$, $d\bar{d}$ luminosity at a given partonic centre of mass energy. The luminosity ratio changes very little with energy: between 0.65 and 0.59 as $\sqrt{\hat{s}}$ is varied from 1 to 2 TeV. Thus, to a good approximation, $pp \rightarrow Z h$ probes the single direction,

$$g_{\mathbf{p}}^Z = g_{Zu_L}^h - 0.76 g_{Zd_L}^h - 0.45 g_{Zu_R}^h + 0.14 g_{Zd_R}^h. \quad (60)$$

using $\hat{s} = (1.5 \text{ TeV})^2$. Using Tab. 27, one can now write this in terms of the LEP-constrained pseudo-observables,

$$\begin{aligned} g_{Z\mathbf{p}}^h &= 2 \delta g_{Zu_L}^h - 1.52 \delta g_{Zd_L}^h - 0.90 \delta g_{Zu_R}^h + 0.28 \delta g_{Zd_R}^h \\ &\quad - 0.14 \delta \kappa_\gamma - 0.89 \delta g_1^Z \\ g_{Z\mathbf{p}}^h &= -0.14 (\delta \kappa_\gamma - \hat{S} + Y) - 0.89 \delta g_1^Z - 1.3 W \end{aligned} \quad (61)$$

where the first and second lines apply respectively to the general and universal case (third and fourth row of Table 27).

To estimate the cut-off for our EFT, note that the g_{Vf}^h couplings arise from current-current operators that can be generated, for instance, by integrating out at tree-level a heavy $SU(2)_L$ triplet (singlet) vector W'^a (Z') that couples to SM fermion currents, $\bar{f} \sigma^a \gamma_\mu f$ ($\bar{f} \gamma_\mu f$) with a coupling g_f and to the Higgs current $iH^\dagger \sigma^a \overset{\leftrightarrow}{D}_\mu H$ ($iH^\dagger \overset{\leftrightarrow}{D}_\mu H$) with a coupling g_H . This gives $g_{Zf}^h \sim g_H g g_f v^2 / \Lambda^2$, where Λ is the mass of the massive vector and thus the cut-off for our EFT description. A universal coupling to the SM fermions can arise via kinetic mixing of the heavy vector with the SM gauge bosons; this would give $g_f = g/2$ ($g_f = g' Y$), such that,

$$g_{Zu_L, d_L}^h \sim \frac{g_H g^2 v^2}{2\Lambda^2}, \quad g_{Zu_R, d_R}^h \sim \frac{g_H g g' Y_{u_R, d_R} v^2}{\Lambda^2}. \quad (62)$$

For a given set of couplings $\{g_{Zu_L}^h, g_{Zd_L}^h, g_{Zu_R}^h, g_{Zd_R}^h\}$, the cut-off is evaluated using Eq. 62 with $g_H = 1$ (note that this is somewhat larger than the value corresponding to the SM hZZ coupling) and taking the smallest of the four values.

Collider Analysis

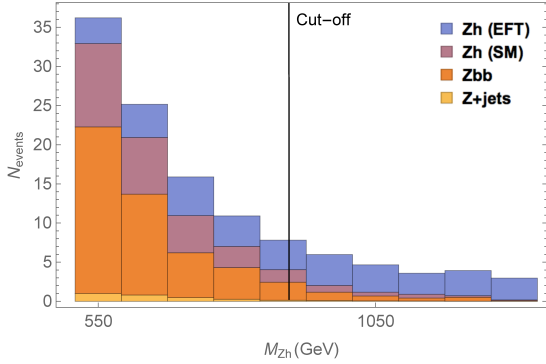


Fig. 58: The differential distribution of events at an integrated luminosity of 300 fb^{-1} with respect to M_{Zh} for the EFT signal as well as the different backgrounds. The EFT signal corresponds to the point $\{g_{Zu_L}^h, g_{Zd_L}^h, g_{Zu_R}^h, g_{Zd_R}^h\} = \{-0.005, 0.0001, -0.010, 0.005\}$ which is allowed by LEP bounds. The vertical line shows the cut-off evaluated using Eq. 62

For our collider analysis, we consider $Z(\ell^+\ell^-)h$ production from a pair of quarks as well as from a pair of gluons. For the decay of the Higgs boson, we find that at an integrated luminosity of 300 fb^{-1} , the diphoton mode is not feasible as it yields less than 5 events at high energies ($p_{T,Z} > 150 \text{ GeV}$). We thus focus on the decay $h \rightarrow b\bar{b}$ to obtain large statistics. The dominant backgrounds are then $Zb\bar{b}$ and the irreducible Zh production in SM. Reducible contributions also arise from $Z + \text{jets}$ production (where we include c -quarks but do not require that they are explicitly tagged). We employ the BDRS approach [232] and demand a fat jet with a cone radius of $R = 1.2$. More details of the Monte-Carlo analysis, the QCD corrections, the detailed cut-based and multivariate analyses (MVA) can be found in Ref. [233]. Finally, we find a cut-based (MVA) SM Zh to $Zb\bar{b}$ ratio of ~ 0.26 (0.50).

To discriminate between the EFT signal and the irreducible SM $Zh(b\bar{b})$ background we study the growth of the EFT cross-section at high energies. This can be seen in Fig. 58 where we show the differential distribution with respect to M_{Zh} , the invariant mass of the leptons and the fat jet, for the EFT signal as well as for the different backgrounds. The EFT signal corresponds to a point that can be excluded in our analysis but is allowed by the LEP constraint. To fully utilise the shape deviation of the EFT signal with respect to the background, we perform a binned log likelihood analysis assuming a 5% systematic error taking only events below the cut-off (evaluated as explained below Eq. 62). To obtain the 95% CL exclusion curve, we assume that the observed number of events would agree with the SM.

Discussion and Conclusions

Taking into account only the SM-BSM interference term, we find the following per-mille level bounds for 300 (3000) fb^{-1} ,

$$g_{Zp}^h \in [-0.004, 0.004] \quad ([-0.001, 0.001]) \quad (63)$$

The above bounds translate to a lower bound on the scale of new physics given by 2.4 TeV (4.4 TeV) at 300 fb^{-1} (3000 fb^{-1}) using Eq. 62. To compare the above projections with existing LEP bounds, one can now extract bounds on the LEP observables contributing to g_{Zp}^h in Eq. 61 by turning them on one by one. We show the results in Tab. 28. For the TGCs δg_1^Z and $\delta \kappa_\gamma$, our projections are much stronger than the LEP bounds and in the case of the Z -pole observables δg_f^Z , that parametrize the deviations of the Z coupling to quarks, they are comparable.

For the universal case, we perform a more detailed analysis. The results are shown in the $\delta \kappa_\gamma - \hat{S}$ vs. δg_1^Z plane in Fig. 59 for the interesting class of models where $W = Y = 0$ [228]. The direction related to the $pp \rightarrow Zh$ interference term, *i.e.*, $g_{Zp}^h = 0$ (see Eq. 60 and the second line of Eq. 61) is

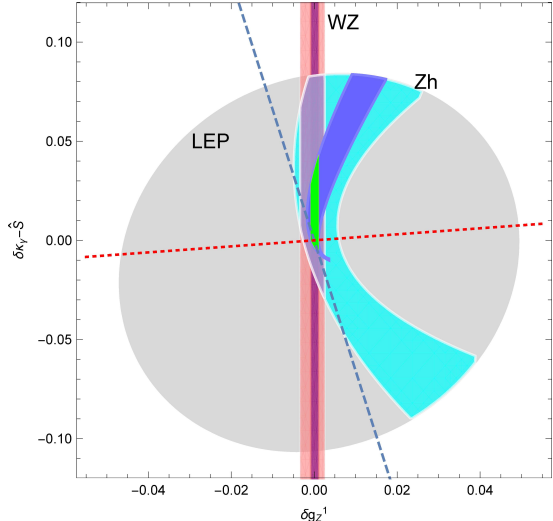


Fig. 59: The light blue (dark blue) region above shows the projection for the allowed region with 300 fb^{-1} (3 ab^{-1}) data from the $pp \rightarrow Zh$ process in the $\delta\kappa_\gamma - \hat{S}$ vs δg_1^Z plane for universal models. We show in grey the allowed region after LEP bounds (taking the TGC $\lambda_\gamma = 0$, a conservative choice) are imposed. In pink (dark pink) we show the region that corresponds to the projection from the WZ process with 300 fb^{-1} (3 ab^{-1}) data derived in Ref. [228] and the purple (green) region shows the region that survives from a combination of the Zh and WZ projections with 300 fb^{-1} (3 ab^{-1}) data.

shown by the dashed blue line, whereas the direction orthogonal to it is shown by the dotted red line. Once the LEP II bounds [234] from the $e^+e^- \rightarrow W^+W^-$ process are imposed, the allowed region that remains is shown by the grey shaded area. We show the results of this work in blue (light (dark) blue for results at 300 (3000) fb^{-1}). The shape of the allowed region arises due to the fact that the interference term vanishes along the dashed blue line and the squared term increases in magnitude as we move away from the origin. This curves the allowed region away from the dashed line as we move away from the origin. The accidental cancellation of the interference term means that our bounds are susceptible to dimension-8 effects along this direction. On the other hand our bounds are more robust and not susceptible to such effects in the orthogonal direction shown by the red dotted line.

As VV production constrains the same set of operators as the Vh production in Fig. 59, we also show the projected bound from the WZ process at 300 fb^{-1} obtained in Ref. [228]. Only the purple region remains when both these bounds are combined at 300 fb^{-1} . This shrinks further to the green region at 3000 fb^{-1} . A drastic reduction in the allowed LEP region is thus possible by considering the $pp \rightarrow Zh$ at high energies.

4.3 Electroweak Precision Tests in High-Energy Diboson Processes

Roberto Franceschini^a, Giuliano Panico^b, Alex Pomarol^{b,c},
Francesco Riva^d and Andrea Wulzer^{d,e,f}

^a*Dipartimento di Matematica e Fisica, Università di Roma Tre and INFN, 00146 Rome*

^b*IFAE and BIST, Universitat Autònoma de Barcelona, 08193 Bellaterra, Barcelona*

^c*Dept. de Física, Universitat Autònoma de Barcelona, 08193 Bellaterra, Barcelona*

^d*Theoretical Physics Department, CERN, Geneva, Switzerland*

^e*Institut de Théorie des Phénomènes Physiques, EPFL, Lausanne, Switzerland*

^f*Dipartimento di Fisica e Astronomia, Università di Padova and INFN Padova, Italy*

	Our Projection	LEP Bound
$\delta g_{u_L}^Z$	$\pm 0.002 (\pm 0.0007)$	-0.0026 ± 0.0016
$\delta g_{d_L}^Z$	$\pm 0.003 (\pm 0.001)$	0.0023 ± 0.001
$\delta g_{u_R}^Z$	$\pm 0.005 (\pm 0.001)$	-0.0036 ± 0.0035
$\delta g_{d_R}^Z$	$\pm 0.016 (\pm 0.005)$	0.0016 ± 0.0052
δg_1^Z	$\pm 0.005 (\pm 0.001)$	$0.009^{+0.043}_{-0.042}$
$\delta \kappa_\gamma$	$\pm 0.032 (\pm 0.009)$	$0.016^{+0.085}_{-0.096}$
\hat{S}	$\pm 0.032 (\pm 0.009)$	0.0004 ± 0.0007
W	$\pm 0.003 (\pm 0.001)$	0.0000 ± 0.0006
Y	$\pm 0.032 (\pm 0.009)$	0.0003 ± 0.0006

Table 28: Comparison of the bounds obtained in this work with existing LEP bounds obtained by turning on the LEP observables in Eq. 61 one by one and using Eq. 63. The LEP bounds on the Z coupling to quarks has been obtained from Ref. [235], the bound on the TGCs from Ref. [234], the bound on \hat{S} from Ref. [236] and finally the bounds on W, Y have been obtained from Ref. [237]. Except for the case of the bounds on δg_f^Z , all of the bounds in the last column were derived by turning on only the given parameter and putting all other parameters to zero. The numbers outside (inside) brackets, in the second column, denote our bounds with $\mathcal{L} = 300$ (3000) fb^{-1} .

High-Energy Primary Effects in Diboson Production

Diboson production processes provide a very good sensitivity to a large set of new-physics effects and can be effectively used to test interesting classes of BSM theories. In this section we classify the leading new-physics effects that can be tested in these channels, showing that they can be encapsulated in four real “high-energy primary” (HEP) parameters [238]. We also assess the reach on these parameters at the HL-LHC and at future hadronic colliders, focusing in particular on the fully leptonic WZ channel that appears particularly promising.

We are interested in processes which fulfill two conditions. First, their amplitudes must receive BSM contributions that grow with E^2 at the leading order (i.e., $d = 6$) in the EFT operator expansion. Second, the SM amplitudes must be constant and sizable at high energy, in such a way that, at the linear order in the EFT Wilson coefficient, the E^2 -growth of the BSM amplitudes results into a E^2 -growth of the differential cross-sections thanks to the SM-BSM interference. As explained in detail in Ref. [238], only $pp \rightarrow V_L V_L$ and $pp \rightarrow V_L h$ production processes enjoy quadratic energy growth at the interference level; we thus focus on these in the rest of the section.⁶ The study of longitudinally-polarized dibosons production in the high-energy limit $E \gg m_W$ is greatly simplified by using the Equivalence Theorem [241, 242]. In this formalism, external longitudinally-polarized vector states are represented in Feynman diagrams as the corresponding scalar Goldstone bosons, up to corrections of order m_W/E from diagrams with gauge external lines. In order to assess the leading energy behavior, it is sufficient to study the amplitude in the unbroken phase, where the EW bosons are massless and the $G_{\text{SM}} = \text{SU}(2)_L \times \text{U}(1)_Y$ symmetry is exact. Given that the Goldstone bosons live in the Higgs doublet H , together with the Higgs particle, G_{SM} implies that the high-energy behavior of the former ones are connected with the latter. This is the reason why $V_L V_L$ and $V_L h$ production processes, collectively denoted as $\Phi \Phi'$ in what follows, should be considered together.

Focusing our interest to the production of $\Phi \Phi'$ out of a quark q' with helicity λ' and an anti-quark \bar{q} with helicity λ we can restrict the form of the BSM amplitudes that interfere with SM one. At order E^2/M^2 in the EFT expansion the relevant BSM effects can be parametrized as corrections to the $J = 1$

⁶Notice however that promising strategies to circumvent the non-interference problem have been recently proposed [239, 240], which allow for instance to “resurrect” interference effects in transverse vector bosons production.

Amplitude	High-energy primaries	Low-energy primaries
$\bar{u}_L d_L \rightarrow W_L Z_L, W_L h$	$\sqrt{2} a_q^{(3)}$	$\sqrt{2} \frac{g^2}{m_W^2} \left[c_{\theta_W} (\delta g_{uL}^Z - \delta g_{dL}^Z) / g - c_{\theta_W}^2 \delta g_1^Z \right]$
$\bar{u}_L u_L \rightarrow W_L W_L$ $\bar{d}_L d_L \rightarrow Z_L h$	$a_q^{(1)} + a_q^{(3)}$	$-\frac{2g^2}{m_W^2} \left[Y_L t_{\theta_W}^2 \delta \kappa_\gamma + T_Z^{u_L} \delta g_1^Z + c_{\theta_W} \delta g_{dL}^Z / g \right]$
$\bar{d}_L d_L \rightarrow W_L W_L$ $\bar{u}_L u_L \rightarrow Z_L h$	$a_q^{(1)} - a_q^{(3)}$	$-\frac{2g^2}{m_W^2} \left[Y_L t_{\theta_W}^2 \delta \kappa_\gamma + T_Z^{d_L} \delta g_1^Z + c_{\theta_W} \delta g_{uL}^Z / g \right]$
$\bar{f}_R f_R \rightarrow W_L W_L, Z_L h$	a_f	$-\frac{2g^2}{m_W^2} \left[Y_{f_R} t_{\theta_W}^2 \delta \kappa_\gamma + T_Z^{f_R} \delta g_1^Z + c_{\theta_W} \delta g_{fR}^Z / g \right]$

Table 29: Parameter combinations (in the high- and in the low-energy primary bases) that control E^2 -enhanced effects in each polarized longitudinal diboson production process. Here, $T_Z^f = T_3^f - Q_f s_{\theta_W}^2$ and Y_{L,f_R} is the hypercharge of the left-handed and right-handed quark (e.g., $Y_L = 1/6$).

partial wave amplitudes [238], namely

$$\delta \mathcal{A}(q'_\pm \bar{q}_\mp \rightarrow \Phi \Phi') = f_{q'_\pm \bar{q}_\mp}^{\Phi \Phi'}(s) \sin \theta = \frac{1}{4} A_{q'_\pm \bar{q}_\mp}^{\Phi \Phi'} E^2 \sin \theta^*, \quad (64)$$

where θ^* is the scattering angle in the $\Phi \Phi'$ center of mass, and $E = \sqrt{s}$ is the center of mass energy.

Eq. (64) shows that at the leading order in the SM EFT expansion each diboson process is sensitive at high energy to a single constant new-physics parameter $A_{q'_\pm \bar{q}_\mp}^{\Phi \Phi'}$ for every combination of initial or final states. This can be taken real since its imaginary part does not interfere with the SM. In addition, the SM symmetry group, which is restored in the high-energy limit, as previously explained, implies several relations among these parameters [238]. As a consequence, only 4 HEP parameters are enough to parametrize the BSM effects we are interested in. This is very non-trivial from an EFT perspective, since a total of 6 anomalous couplings coming from $d = 6$ effective operators contribute to longitudinal diboson processes. These couplings can be identified as δg_{uL}^Z , δg_{uR}^Z , δg_{dL}^Z , δg_{dR}^Z , δg_1^Z and $\delta \kappa_\gamma$ in the notation of Ref. [229].

The relations between the HEP parameters and the 4 combinations of the low-energy primaries that produce growing-with-energy effects are reported in the third column of table 29.

The relations between the HEP and the Wilson coefficients in the SILH basis [110] are given by

$$a_q^{(3)} = \frac{g^2}{M^2} (c_W + c_{HW} - c_{2W}), \quad a_q^{(1)} = \frac{g'^2}{3M^2} (c_B + c_{HB} - c_{2B}), \quad (65)$$

and

$$a_u = -2a_d = 4a_q^{(1)}. \quad (66)$$

These relations can also be written using the \hat{S} , \hat{T} , W and Y parameters (we follow the notation of Ref. [237]) in addition to the two anomalous triple gauge couplings (aTGC), δg_1^Z and $\delta \kappa_\gamma$. We have

$$a_q^{(3)} = -\frac{g^2}{m_W^2} \left(c_{\theta_W}^2 \delta g_1^Z + W \right), \quad a_q^{(1)} = \frac{g'^2}{3m_W^2} \left(\hat{S} - \delta \kappa_\gamma + c_{\theta_W}^2 \delta g_1^Z - Y \right), \quad (67)$$

which can be useful in order to compare HEP analyses from LHC with other experiments, such as LEP.

In the Warsaw basis [231], the HEP are transparently identified with contact interactions between quarks and scalars⁷

$$a_u = 4 \frac{c_R^u}{M^2}, \quad a_d = 4 \frac{c_R^d}{M^2}, \quad a_q^{(1)} = 4 \frac{c_L^{(1)}}{M^2}, \quad a_q^{(3)} = 4 \frac{c_L^{(3)}}{M^2}. \quad (68)$$

LHC Primaries Sensitivity: The WZ Channel

To illustrate the HE-LHC reach on the high-energy primaries we focus on WZ production. This channel gives access to the $a_q^{(3)}$ primary and has a very high sensitivity to new physics [238]. We consider the fully leptonic final state

$$pp \rightarrow W^\pm Z + \text{jets} \rightarrow \ell\nu\ell'\bar{\ell}' + \text{jets}, \quad \text{with } l, l' = e, \mu,$$

which is likely to be measured with good accuracy and can benefit from a straightforward reconstruction of the final-state leptons and a very low reducible background [243]. At the experimental level the situation might not be too much different from the neutral Drell-Yan process, in which a measurement with 2% relative systematic uncertainty of the differential cross-section was performed, with run-1 LHC data, up to TeV energies [244]. A systematic uncertainty of 5% might be considered as a realistic goal for the differential cross-section measurement in the leptonic WZ channel.

The main obstacle to obtain sensitivity to new physics is the potentially large contribution of the other polarizations, which for our purposes constitute a background, since they are insensitive to the new physics parameter $a_q^{(3)}$. In the WZ channel these effects are automatically under control in the high- p_T region and they can be further reduced by suitable selection criteria, as we will discuss later.

Due to the symmetry structure, the emission of transversely polarized W and Z bosons in the central rapidity region is disfavored [238]. No suppression is instead expected for longitudinally polarized gauge bosons, therefore it is advantageous to concentrate our analysis on central scattering region, $|\cos\theta^*| \sim 0$, or, equivalently, at large $p_{T,V}$ ($p_{T,V} > 1$ TeV). We stress that other diboson processes, e.g. $pp \rightarrow WW$, do not enjoy this suppression of transverse vector boson emission, therefore are expected to be less sensitive probes of the high energy primaries. The interested reader can find estimates of the results achievable with the other diboson channels in Ref. [238].

Analysis

We now estimate the reach on $a_q^{(3)}$ based on a full NLO simulation of the $pp \rightarrow 3\ell\nu$ process. We report the analysis of Ref. [238] to which we refer for more details. We consider generation-level leptons momenta, but we include an overall detector efficiency for reconstructing the three leptons that we estimate around 50% [245]. We furthermore apply standard acceptance cuts on the leptons (see Table 30). The same-flavor and opposite-charge lepton pair with invariant mass closer to the Z boson mass is taken as the Z candidate and the remaining lepton is taken to be the decay product of the W boson. The missing transverse energy vector of the event (\cancel{E}_T) is estimated from the generation-level transverse neutrino momentum, to which we apply a Gaussian smearing with standard deviation $\sigma_{\cancel{E}_{T,i}}^2 = (0.5)^2 \cdot \sum_f |p_i| \cdot \text{GeV}$.

In order to highlight the production of longitudinally polarized vector bosons in the central rapidity region is useful to eliminate events with hard real radiation, which tend to be more abundant for our background of transverse polarized gauge bosons. To tame real radiation events in a controlled way we employ a selection on the transverse momentum of the WZ system, denoted by $p_{T,VV} = |\vec{p}_{T,W} + \vec{p}_{T,Z}|$.⁸

⁷These relations, as well as those in eq. (65), are obtained by computing the diboson helicity amplitudes in the presence of the EFT operators, and matching with the results of the low energy primaries. See Ref. [238] for details.

⁸Alternatively, a jet veto might be considered, which however could lead to lower accuracy because of the experimental and theoretical uncertainties in jets reconstruction. See also Ref. [246] for a different approach.

acceptance cuts	$p_{T,\ell} > 30 \text{ GeV}, \quad \eta_\ell < 2.4$
analysis cuts	$p_{T,VV}/p_{T,V} < 0.5$ $ \cos \theta^* \leq 0.5$

Table 30: List of acceptance and analysis cuts.

We require $p_{T,VV}$ to be smaller than 50% of the transverse momentum of the gauge bosons in the event, $p_{T,V} = \min(p_{T,W}, p_{T,Z})$. We also impose a cut on the scattering angle in the WZ center of mass frame $|\cos \theta^*| \leq 0.5$. The cuts are summarized in Table 30.

The kinematical variables described so far allow us to determine $p_{T,Z}$ and $p_{T,W}$, and in turn $p_{T,V}$ and $p_{T,VV}$, used to construct the binned distribution and for the selection cuts. In order to extract $|\cos \theta^*|$ the neutrino rapidity is reconstructed by the standard technique of imposing the invariant mass of the neutrino plus lepton system to be as close as possible to the physical W boson mass. A twofold ambiguity in the reconstruction is resolved by imposing the $|\cos \theta^*|$ cut on both solutions, i.e. by retaining for the analysis only events such that both the possible neutrino configurations satisfy the selection criteria.

We study the 3 collider energy options that correspond to the LHC (14 TeV), to the High-Energy LHC (HE-LHC, 27 TeV) and to the FCC-hh (100 TeV). In each case we consider suitably designed $p_{T,V}$ bins, namely

$$\begin{aligned} \text{LHC: } p_{T,V} &\in \{100, 150, 220, 300, 500, 750, 1200\}, \\ \text{HE-LHC: } p_{T,V} &\in \{150, 220, 300, 500, 750, 1200, 1800\}, \\ \text{FCC: } p_{T,V} &\in \{220, 300, 500, 750, 1200, 1800, 2400\}. \end{aligned} \quad (69)$$

The binning is chosen such as to cover the kinematical regime that is accessible at each collider and it is taken as fine as possible in order to maximize the BSM sensitivity. On the other hand, a minimum bins size $\Delta p_{T,V}/p_{T,V} \gtrsim 30\%$ is required in order to avoid a degradation of the accuracy due to the $p_{T,V}$ resolution.

The predicted cross-sections are used to construct the χ^2 , under the assumption that observations agree with the SM, and are eventually used to derive 95% CL bounds on $a_q^{(3)}$. The uncertainties in each bin are the sum in quadrature of the statistical error, obtained from the SM expected events yield, and of a systematical component (uncorrelated across bins) which we take as a fixed fraction (δ_{syst}) of the SM expectations. With this procedure we obtain, for different collider energies and luminosities and for $\delta_{\text{syst}} = 5\%$

$$\begin{aligned} \text{HL-LHC, } 3 \text{ ab}^{-1}: \quad a_q^{(3)} &\in [-4.9, 3.9] 10^{-2} \text{ TeV}^{-2} \\ \text{HE-LHC, } 10 \text{ ab}^{-1}: \quad a_q^{(3)} &\in [-1.6, 1.3] 10^{-2} \text{ TeV}^{-2} \\ \text{FCC-hh, } 20 \text{ ab}^{-1}: \quad a_q^{(3)} &\in [-7.3, 5.7] 10^{-3} \text{ TeV}^{-2} \end{aligned} \quad (70)$$

We see that the HE-LHC will improve the HL-LHC reach by a factor of 3, while a gain of nearly one order of magnitude would be possible with the FCC-hh collider. The FCC-hh reach is comparable with the one of CLIC, as extracted from the analysis in Ref. [247].

The results of eq. (70) rely on BSM cross-section predictions obtained by integrating up to very high center of mass energies, formally up to the collider threshold. Therefore these limits assume that the description of the underlying BSM model offered by the EFT is trustable in the whole relevant kinematical regime, i.e. that the cutoff M of the BSM EFT is high enough. We quantify how large M concretely needs to be for our results to hold by studying [248–250] how the limit deteriorates if only events with low WZ invariant mass, $m_{WZ} < m_{WZ}^{\max}$ are employed. This obviously ensures that the limit is consistently set within the range of validity of the EFT provided the EFT cutoff M is below m_{WZ}^{\max} .

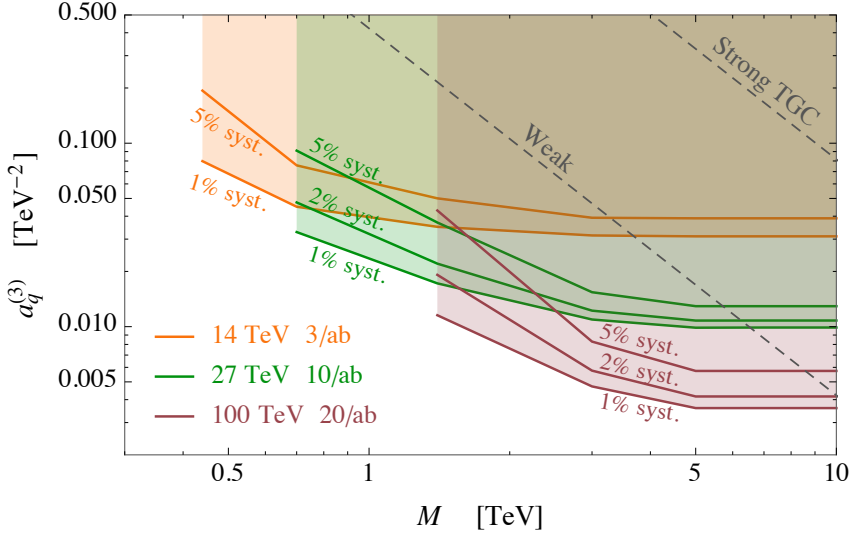


Fig. 60: Expected 95% CL bounds from fully leptonic WZ on the high-energy primary parameter $a_q^{(3)}$ as a function of the new physics scale M . The plots reports the results for the HL-LHC (orange lines), HE-LHC (green lines) and FCC-hh (brown lines) for different values of the systematic uncertainties.

The results are reported in figure 60. Since the 95% CL interval is nearly symmetric around the origin only the upper limit is reported in the figure for shortness.

Several conclusions can be drawn from figure 60. First of all we see that the reach saturates for m_{WZ}^{\max} below around 1.5 TeV at the HL-LHC if the systematic uncertainties are low, meaning that the limits obtained without m_{WZ} cut apply to theories with cutoff M above that threshold. The threshold grows to around 3 and 4 TeV at the HE-LHC and at the FCC-hh, respectively. The figures show that $\delta_{\text{syst}} = 5\%$ is sufficient to probe ‘‘Weak’’ theories in all cases, but it also shows that the impact of larger or smaller uncertainties on the reach can be significant. Systematic errors at the $\delta_{\text{syst}} = 5\%$ level already make an appreciable difference with respect to $\delta_{\text{syst}} = 1\%$. This is due to the fact that the low- $p_{T,V}$ bins have small statistical error and the reach in those bins benefits from lower systematics. The effect is even more pronounced at the HE-LHC and at the FCC-hh, where even with $\delta_{\text{syst}} = 2\%$ the reach deteriorates significantly with respect the ideal case $\delta_{\text{syst}} = 1\%$. The fact that more accurate measurements would improve the reach of future colliders is an element that should be taken into account in the design of the corresponding detectors.

4.4 Novel measurements of anomalous triple gauge couplings for the HE and HL-LHC

A. Azatov, D. Barducci, J. Elias-Miró and Elena Venturini

SISSA and INFN sezione di Trieste, Via Bonomea 265; I-34137 Trieste, Italy

4.4.1 Introduction

In this work we are interested in the measurement of the Standard Model (SM) Triple Gauge Couplings (TGCs). This is a classic test of the SM and a possible measurement of deviations from its expectations would signify an invaluable piece of information for the theory beyond the SM. A consistent way to parametrize such possible deviations is through the SM Effective Field Theory (EFT) approach. We are

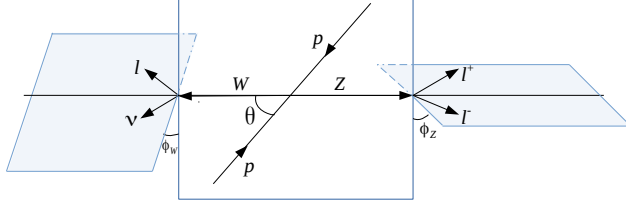


Fig. 61: Angles for $2 \rightarrow 4$ scattering.

going to consider the SM EFT as defined in [240], in particular we are going to focus on the measurement of the EFT operator

$$\mathcal{O}_{3W} = \frac{g}{3!} \epsilon^{abc} W^{a,\mu\nu} W_{\nu\rho}^b W_{\mu}^{c,\rho}, \quad (71)$$

which is associated to the the anomalous triple gauge coupling (aTGC) λ_z .

A precise determination of the TGC stems from the measurement of the $2 \rightarrow 2$ cross section $\sigma(q\bar{q} \rightarrow VV)$ [243, 251]. Naive dimensional analysis and standard EFT reasoning predicts that the energy scaling of such cross-section is given by

$$\sigma(q\bar{q} \rightarrow VV) \sim \frac{g_{\text{SM}}^4}{E^2} \left[1 + \overbrace{c_i \frac{E^2}{\Lambda^2}}^{\text{BSM}_6 \times \text{SM}} + \overbrace{c_i^2 \frac{E^4}{\Lambda^4}}^{\text{BSM}_6^2} + \dots \right], \quad (72)$$

where the first factor g_{SM}^4/E^2 accounts for the energy flux of the initial quarks, c_i are the relevant Wilson coefficients, and we have omitted numerical factors. In (72) we have explicitly indicated dimension six squared (BSM_6^2) and SM-dimension six interference terms ($\text{BSM}_6 \times \text{SM}$).⁹ The ellipses in (72) are due to corrections from operators of dimension ≥ 8 , which we will neglect. The leading such term is an interference term of the type $\text{BSM}_8 \times \text{SM}$ and it is of order $O(E^4/\Lambda^4)$.

A closer inspection however reveals that the $2 \rightarrow 2$ diboson production through the dimension six operator \mathcal{O}_{3W} has an interference piece with a suppressed energy scaling. Indeed, the energy scaling of such process is

$$\sigma(q\bar{q} \rightarrow VV) \sim \frac{g_{\text{SM}}^4}{E^2} \left[1 + C_{3W} \frac{m_V^2}{\Lambda^2} + C_{3W}^2 \frac{E^4}{\Lambda^4} + O(E^4/\Lambda^4) \right]. \quad (73)$$

This is a consequence of the helicity selection rules, see [239, 240, 252, 253]. The suppressed energy scaling can be problematic for the correct EFT interpretation of the $\sigma(q\bar{q} \rightarrow VV)$ measurement. Namely, in view of (73), the sensitivity on C_{3W} is largely dominated by the quadratic piece BSM_6^2 , which is $O(E^4/\Lambda^4)$. Furthermore, in this case, the measurements become insensitive to the sign of the Wilson coefficient. The main objective of the present work is to improve the sensitivity to the linear piece $\text{BSM}_6 \times \text{SM}$. We will present two classes of solutions to achieve this goal. Firstly, in section 4.4.2 we will show that the differential angular cross-section of the process $q\bar{q} \rightarrow VV \rightarrow 4\psi$ has a large sensitivity on $\text{BSM}_6 \times \text{SM}$ compared to the inclusive cross-section. Secondly, in section 4.4.2 we will show that accounting for extra radiation $q\bar{q} \rightarrow VV + j$ also results in an improved sensitivity on the leading piece $\text{BSM}_6 \times \text{SM}$. These measurements are specially interesting in a HL/HE phase of the LHC, for which we show the prospects in section 4.4.3.

4.4.2 Solutions

Next we will present two ways to improve the sensitivity to the aTGC λ_z by restoring the energy growth $g_{\text{SM}}^4/E^2 \left[1 + c_i E^2/\Lambda^2 + \dots \right]$ of the interference piece $\text{BSM}_6 \times \text{SM}$ of the \mathcal{O}_{3W} operator.

Interference resurrection via angular distributions

The first way of enhancing the interference term is by noting that in a collider experiment instead of the $2 \rightarrow 2$ process we actually measure a $2 \rightarrow 4$ scattering, i.e. vector bosons decay into fermions $q\bar{q} \rightarrow V_1 V_2 \rightarrow 4\psi$.

Let us start by considering the differential cross section for the production of the polarized particles $W_{T+} Z_T \rightarrow W_{T+} l_+ \bar{l}_-^{10}$

$$\frac{d\sigma(q\bar{q} \rightarrow W_{T+} l_- \bar{l}_+)}{d\text{LIPS}} = \frac{1}{2s} \frac{\left| \sum_i (\mathcal{M}_{q\bar{q} \rightarrow W_{T+} Z_i}^{\text{SM}} + \mathcal{M}_{q\bar{q} \rightarrow W_{T+} Z_i}^{\text{BSM}}) \mathcal{M}_{Z_i \rightarrow l_- \bar{l}_+} \right|^2}{(k_Z^2 - m_Z^2)^2 + m_Z^2 \Gamma_Z^2}, \quad (74)$$

where sum runs over intermediate Z polarizations and $d\text{LIPS} \equiv (2\pi)^4 \delta^4(\sum p_i - p_f) \prod_i d^3 p_i / (2E_i (2\pi)^3)$ is the Lorentz Invariant differential Phase Space. Then in the narrow width approximation the leading contribution to the interference, i.e. the cross term $\text{SM} \times \text{BSM}_6$ in 74, is given by $d\sigma_{\text{int}}(q\bar{q} \rightarrow W_{T+} l_- \bar{l}_+)/d\phi_Z \propto E^2/\Lambda^2 \cos(2\phi_Z)$, where ϕ_Z is the azimuthal angle between the plane defined by the decaying leptons and the plane defined by the collision and WZ momenta, see Fig. 61. Note that $d\sigma_{\text{int}}(q\bar{q} \rightarrow W_{T+} l_- \bar{l}_+)/d\phi_Z$ has the energy growth expected from naive dimensional analysis, see Eq. 72. An analogous derivation goes through if we also consider the decay of the W gauge boson. The differential interference term for the process $q\bar{q} \rightarrow WZ \rightarrow 4\psi$ is unsuppressed and modulated as

$$\frac{d\sigma_{\text{int}}(q\bar{q} \rightarrow WZ \rightarrow 4\psi)}{d\phi_Z d\phi_W} \propto \frac{E^2}{\Lambda^2} (\cos(2\phi_Z) + \cos(2\phi_W)), \quad (75)$$

where $\phi_{W,Z}$ are the corresponding azimuthal angles. Integrating 75 over the fermion phase space the interference term vanishes as expected from the discussion in section 4.4.1. Since the dependence on the two azimuthal angles is additive, integrating over ϕ_W leads to a differential cross-section that is modulated by $\cos(2\phi_Z)$ and that features E^2/Λ^2 energy growth. We will use the result in Eq. 75 to prove the aTGC λ_Z , with an increased overall sensitivity to both the magnitude and sign of the Wilson coefficient.

Angle ambiguities [239]

Let us make a few remarks on the experimental measurement of $\phi_{Z,W}$ in Eq. 75. The angle ϕ_Z can be determined up to an ambiguity $\phi_Z \leftrightarrow \phi_Z \pm \pi$, since experimentally we can only measure the charges but not the helicities of the leptons from Z decay. The reconstruction of the W azimuthal angle ϕ_W in the $l\nu$ final state suffers from an ambiguity $\phi_W \leftrightarrow \pi - \phi_W$ due to the twofold ambiguity in the determination of the neutrino momentum. Interestingly, none of these ambiguities affects Eq. 75.

Interference resurrection via jet emission

A second way to resurrect the expected energy growth of the interference term is based on the observation that the helicity selection rule holds only at tree-level [240]. So the next-to-leading-order (NLO) effects will necessarily lead to the enhancement of the interference. Virtual effects are expected to be suppressed

⁹Note that operators of dimension 7 necessarily violate either baryon or lepton number. We assume the scale of such symmetry violation to be very large and therefore irrelevant for diboson physics at the LHC.

¹⁰We ignore the longitudinal Z polarization which is subdominant at the LHC [254].

by a factor $\mathcal{O}(\alpha_s/4\pi)$ with respect to the contributions coming from azimuthal modulation discussed in the previous section. Alternatively we will consider processes with an extra hard jet emission, which will improve on the signal over the background ratio. In this case, since we are dealing with the hard $2 \rightarrow 3$ process, the same polarization configuration $q\bar{q} \rightarrow V_\pm V_\pm g_\mp$ is allowed both in SM and in the BSM five point amplitude with the \mathcal{O}_{3W} insertion. Therefore the interference is not suppressed and the leading quadratic energy scaling is restored by requiring an extra (hard) QCD radiation.

4.4.3 Results

HL-LHC

In order to test the sensitivity of the High-Luminosity (HL) phase of the LHC on the \mathcal{O}_{3W} with the proposed solution to the non-interference behaviour we proceed in the following way. We generate with MadGraph5 aMC@NLO [155] parton level events for $pp \rightarrow W^\pm Z$ decaying into a four leptons (electron and muon) final state together with events for the same process where we allow for a jet emission in the initial state. We perform two different analyses (see [240] for more details): an inclusive one where we restrict to events up to $p_T^j < 100$ GeV and do not bin on the ϕ_Z variable and an exclusive one where we bin both on the jet transverse momentum and on ϕ_Z , where for the latter we define two bins with the threshold $|\cos(\phi_Z)| = 1/\sqrt{2}$. All together the results for the bound on the C_{3W} Wilson coefficient are reported in Fig. 62 as a function of the maximum transverse mass of the WZ system, which allows to have an estimate of the validity of the EFT computation, see again [240] for a detailed discussion¹¹.

One might wonder if a simulation beyond the parton level accuracy might spoil these results. To this end we have performed a more detailed simulation by showering the events through PYTHIA 8 [155] and simulating the detector response via Delphes 3 [255]. By analysing the density of events in the two azimuthal bins we found that with respect to the parton level case the relative difference is of at most a few %, thus making our parton level analysis solid, see ref. [?].

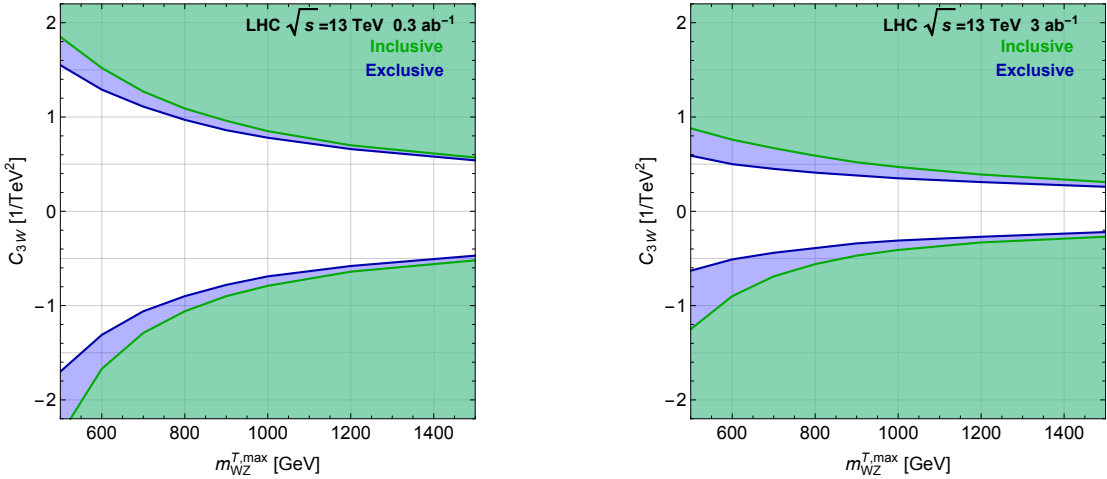


Fig. 62: Bounds on the C_{3W} Wilson coefficient for the inclusive and exclusive categories at the LHC 13 for 300 fb^{-1} (left) and 3000 fb^{-1} (right) of integrated luminosity.

HE-LHC

We now estimate the reach of a future HE phase of the LHC with $\sqrt{s} = 27$ TeV. For these preliminary results we adopt the same binning, both in ϕ_Z and in jet transverse momentum, of the previous section. We show the results in Fig. 63. We found a slight increase of order 30% on the reach on C_{3W} . We

¹¹These results are obtained by keeping both the linear and the quadratic terms in the cross section determination.

expect that a dedicated HE analysis will lead to a further improvement of these bounds; this can be done by exploiting in a more efficient way the high energy tails of the differential distributions.

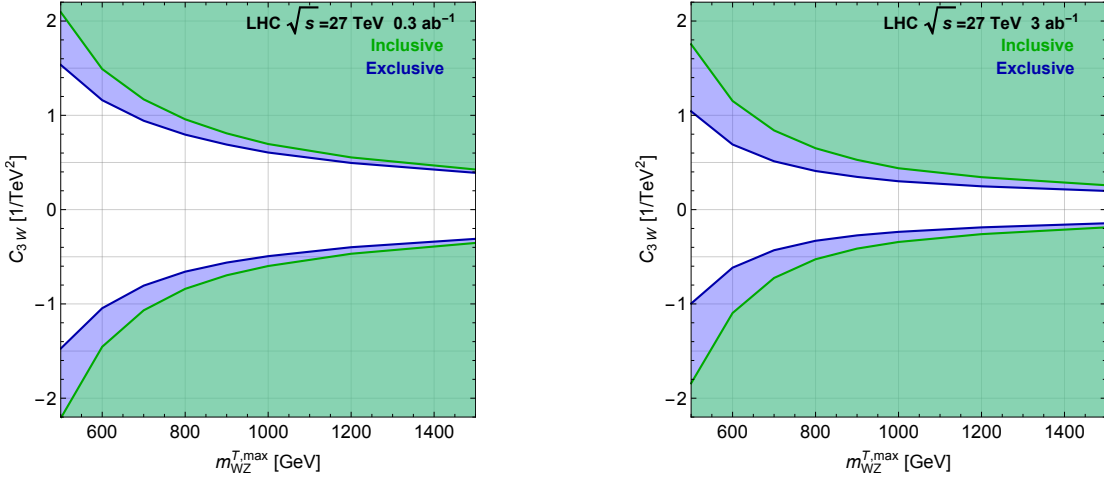


Fig. 63: Bounds on the C_{3W} Wilson coefficient for the inclusive and exclusive categories at the LHC 27 for 300 fb^{-1} (left) and 3000 fb^{-1} (right) of integrated luminosity.

4.4.4 Higgs pair production in vector-boson fusion at the HL-LHC

by Fady Bishara, Roberto Contino, and Juan Rojo

4.4.4.1 Introduction

While the dominant production channel of Higgs boson pairs at hadron colliders is the gluon-fusion mechanism, other channels are also of phenomenological relevance. In particular, Higgs pair production in weak vector-boson fusion [256] is interesting since it probes the strength of the Higgs non-linear interactions with vector bosons at high energies. This process can therefore provide unique information to test the nature of the Higgs boson, whether it is a composite or elementary state, and whether or not it emerges as a Nambu-Goldstone boson (NGB) of some new dynamics at the TeV scale [110, 257, 258].

The production of Higgs pairs in the VBF channel [110, 257, 259–262] proceeds via the soft emission of two vector bosons from the incoming protons followed by the hard $VV \rightarrow hh$ scattering, with $V = W, Z$. In the SM, the VBF inclusive cross section at 14 TeV is around 2 fb, more than one order of magnitude smaller than in gluon fusion. Higher order QCD corrections are moderate ($\sim 10\%$) as expected for an electroweak process. Despite the small rate, Higgs pair production via VBF is relevant since even small modifications of the SM couplings induce a striking increase of the cross section as a function of the di-Higgs mass, for instance in models where the Higgs is a composite pseudo-NGB (pNGB) of new strong dynamics at the TeV scale [263]. In these theories, the Higgs anomalous couplings imply a growth of the $VV \rightarrow hh$ cross section with the partonic center-of-mass energy, $\hat{\sigma} \propto \hat{s}/f^4$, where f is the pNGB decay constant [110]. This enhanced sensitivity to the underlying strength of the Higgs interactions makes double Higgs production via VBF a key process to test the nature of the electroweak symmetry breaking dynamics and to constrain the $hhVV$ quartic coupling in a model-independent way.

Here we review the feasibility of measuring and interpreting the VBF Higgs pair production at the HL-LHC in the $hh \rightarrow b\bar{b}b\bar{b}$ final state. While QCD multi-jet backgrounds are huge, this final state turns out to be within the reach of the HL-LHC thanks to the unique VBF topology, characterized by two forward jets well separated in rapidity and with a large invariant mass and a reduced hadronic activity in the central region. In addition, the di-Higgs system will acquire a substantial boost in the presence of

BSM dynamics, and jet substructure techniques [264–266] make possible to fully exploit the high-energy limit and optimize the signal significance.

Here the theoretical description of di-Higgs VBF production follows [257], where general parametrization of the couplings of a light Higgs-like scalar h to the SM vector bosons and fermions was introduced. In this formalism, assuming that the couplings of the Higgs boson to SM fermions scale with their masses and do not violate flavor, the resulting effective Lagrangian in [257] is given by

$$\begin{aligned} \mathcal{L} \supset & \frac{1}{2}(\partial_\mu h)^2 - V(h) + \frac{v^2}{4} \text{Tr}\left(D_\mu \Sigma^\dagger D^\mu \Sigma\right) \left[1 + 2c_V \frac{h}{v} + c_{2V} \frac{h^2}{v^2} + \dots\right] \\ & - m_i \bar{\psi}_{Li} \Sigma \left(1 + c_\psi \frac{h}{v} + \dots\right) \psi_{Ri} + \text{h.c.}, \end{aligned} \quad (76)$$

where $V(h)$ denotes the Higgs potential,

$$V(h) = \frac{1}{2}m_h^2 h^2 + c_3 \frac{1}{6} \left(\frac{3m_h^2}{v}\right) h^3 + c_4 \frac{1}{24} \left(\frac{3m_h^2}{v^2}\right) h^4 + \dots \quad (77)$$

The parameters c_V , c_{2V} , c_ψ , c_3 , and c_4 are in general arbitrary coefficients, normalized so that they equal 1 in the SM. In this contribution we focus on the determination of c_{2V} by means of di-Higgs VBF production in the $b\bar{b}b\bar{b}$ final state.

4.4.4.2 Analysis strategy

Signal and background events are simulated at leading-order (LO) by means of matrix-element generators and then processed through a parton shower (PS). The dominant background is given by QCD multijet production, while other backgrounds, such as top-quark pair production and Higgs pair production via gluon-fusion, turn out to much smaller. After the parton shower, events are clustered with FASTJET v3.0.1 [267] using the anti- k_t algorithm [268] with a jet radius $R = 0.4$. The resulting jets are then processed through a b -tagging algorithm, where a jet is tagged as b -jet with probability $\varepsilon(b\text{-tag})$ if it contains a b -quark with $p_T^b > 15$ GeV. In order to account for b -jet misidentification (fakes), jets which do not meet this requirement are also tagged as b -jets with probability $\varepsilon(c\text{-mistag})$ or $\varepsilon(q, g\text{-mistag})$ depending on whether they contain a c -quark or not. Only events with four or more jets, of which at least two must be b -tagged, are retained at this stage.

Subsequently to b -tagging, events are classified through a scale-invariant tagging procedure [265, 266]. This step is crucial to efficiently reconstruct the Higgs boson candidates and suppress the otherwise overwhelming QCD backgrounds while at the same time taking into account all the relevant final-state topologies. The basic idea of this method is to robustly merge three event topologies – boosted, intermediate and resolved – into a common analysis. This is particularly relevant for our study given that the degree of boost of the di-Higgs system strongly depends on the deviations of c_{2V} from its SM value.

Acceptance cuts to match detector coverage are applied to signal and background events. We require the p_T of both the light and b -tagged jets to be larger than 25 GeV, while the pseudo-rapidities of light and b -tagged jets, η_j and η_b , are limited by the coverage of the forward calorimeters and by the tracking region where b -tagging can be applied respectively. We also impose a set of selection cuts tailored to the VBF topology which is characterized by two forward and very energetic jets with little hadronic activity between them. In particular, we cut on the rapidity separation $\Delta y_{jj} \equiv |\eta_j^{\text{lead}} - \eta_j^{\text{sublead}}|$ and the invariant mass m_{jj} of the two VBF-tagging jets, and impose a central jet veto (CJV) on the hardest non-VBF light jet in the central region. The VBF tagging jets are defined as the pair of light jets satisfying the acceptance cuts of with the largest invariant mass m_{jj} . Moreover, a CJV cut is imposed in VBF analyses to veto light jets, with pseudo-rapidity η_{j_3} , lying between those of the VBF-tagging jets, $\eta_j^{\text{max}} > \eta_{j_3} > \eta_j^{\text{min}}$, above a given p_T threshold.

Figure 64 (right) shows the m_{hh} distribution after all analysis cuts for both for the signal (SM and $c_{2V} = 0.8$) and the total background. For $c_{2V} = 0.8$, the crossover between the resolved and boosted categories takes place at $m_{hh} \simeq 1.5$ TeV, although this specific value depends on the choice of the jet radius R [265]. Unsurprisingly, we find that background events are always dominated by the resolved topology. The decomposition of the total background in terms of individual processes as a function of m_{hh} is shown in Fig. 64 (left), where each component is stacked on top of each other. We see how the $4b$ background dominates for large m_{hh} while the $2b2j$ one is instead the most important for small m_{hh} .

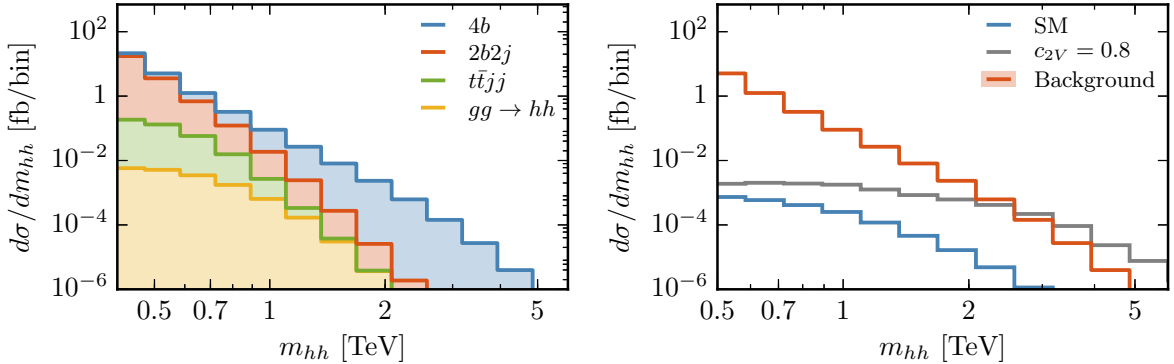


Fig. 64: Left: Decomposition of the total background into individual processes as a function of m_{hh} after all analysis cuts have been imposed. Right: the di-Higgs invariant mass distribution after all analysis cuts for the signal (SM and $c_{2V} = 0.8$) and the total background.

Cross-sections (fb)					
	Acceptance	VBF	Higgs reco.	m_{hh} cut	
Signal SM	0.011	0.0061	0.0039	0.0020	
14 TeV	Signal $c_{2V} = 0.8$	0.035	0.020	0.017	0.011
	Bkgd (total)	1.3×10^5	4.9×10^3	569	47

Table 31: Cross sections, in fb, after the successive application of the acceptance, VBF cuts, and Higgs reconstruction cuts for signal events (SM and $c_{2V} = 0.8$) and for the total background.

In Table 31 we show the cross-sections after the successive application of the acceptance, VBF cuts, and Higgs reconstruction cuts for signal events (SM and $c_{2V} = 0.8$) and for the total background. We find that the VBF di-Higgs signal in the SM is rather small already after the basic acceptance cuts. On the other hand, the signal event yield is substantially increased for $c_{2V} \neq 1$ as illustrated by the benchmark value of $c_{2V} = 0.8$ leading to more than a factor 3(5) enhancement compared to the SM after the acceptance (all analysis) cuts. The fact that this cross-section enhancement for the $c_{2V} = 0.8$ scenario is more marked at the end of the analysis is not a coincidence: our selection cuts have been designed so as to improve the sensitivity to c_{2V} by increasing the signal significance in the large- m_{hh} region. Note however that even after all analysis cuts the background is still much larger than the signal (either SM or $c_{2V} = 0.8$) at the level of inclusive rates. It is only by exploiting the large- m_{hh} region that the former can be made small enough to achieve high signal significances.

4.4.4.3 Projections for the HL-LHC

Following the analysis strategy outlined in the previous section, we can now estimate the expected precision on the determination of the c_{2V} coupling at the HL-LHC. In the left panel of Fig. 65 we show

the posterior probabilities for c_{2V} at 14 TeV, from where we can assess the expected precision its measurement at the HL-LHC assuming SM couplings. The corresponding 68% probability intervals for the determination of c_{2V} at the HL-LHC are listed in Table 32 for two different scenarios for the background cross section.

	68% probability interval on $\delta_{c_{2V}}$	
	$1 \times \sigma_{\text{bkg}}$	$3 \times \sigma_{\text{bkg}}$
LHC ₁₄	[-0.37, 0.45]	[-0.43, 0.48]
HL-LHC	[-0.15, 0.19]	[-0.18, 0.20]

Table 32: Expected precision (at 68% probability level) for the measurement of $\delta_{c_{2V}}$ at the HL-LHC for SM values of the Higgs couplings, for two scenarios for the background cross section.

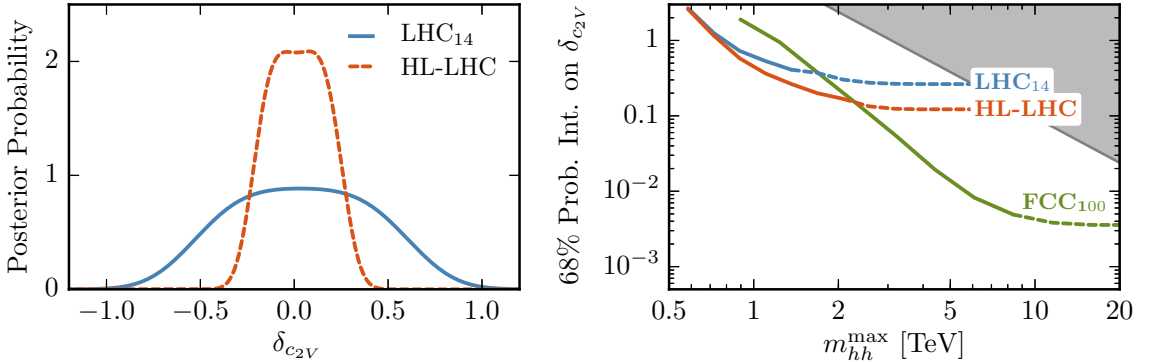


Fig. 65: Left: the posterior probability densities for $\delta_{c_{2V}}$ at the HL-LHC. Right: the expected precision for a measurement of $\delta_{c_{2V}}$ at the 68% CL as a function of m_{hh}^{max} , where the gray area indicates the region where $\delta_{c_{2V}} > \delta_{c_{2V}}^{\text{max}}$.

From Table 32, we find that the c_{2V} coupling, for which there are currently no direct experimental constraints, can be measured with a precision of around $^{+19\%}_{-15\%}$ at the HL-LHC. It is interesting to compare these results with the experimental precision expected on the fiducial VBF di-Higgs cross section after all analysis cuts, expressed in terms of μ , the signal strength parameter normalized to the SM result. We find that the 95% CL upper limits on μ for the nominal background cross section is $\mu \leq 109$ with 300 fb⁻¹, and $\mu \leq 49$ at the HL-LHC. This result highlights that the high precision expected on c_{2V} can be obtained despite the loose constraints expected on the VBF di-Higgs cross section itself.

The results of Table 32 have been obtained by making full use of the information contained on the di-Higgs invariant mass distribution m_{hh} . However, the EFT expansion might break down at large enough values of m_{hh} , corresponding to large partonic center-of-mass energies, and some assessment on the validity of our procedure is thus required. In particular, results can be consistently derived within the EFT framework only if the new physics scale Λ is smaller than the largest value of m_{hh} included in the analysis. Indeed, constraining Λ requires making assumptions on the structure of the UV dynamics extending the SM [269]. For example, for the case where the new physics is characterized by a single coupling strength g_* and mass scale Λ [110], one expects $\delta_{c_{2V}} \approx g_*^2 v^2 / \Lambda^2$, so that for maximally strongly-coupled UV completions (with $g_* \simeq 4\pi$) it is possible to derive the upper limit $\delta_{c_{2V}}^{\text{max}} \approx 16\pi^2 v^2 / \Lambda^2$ which connects $\delta_{c_{2V}}$ with the new physics scale Λ . The validity of the EFT can thus be monitored by introducing a restriction $m_{hh} \leq m_{hh}^{\text{max}}$, and then determining how the sensitivity on $\delta_{c_{2V}}$ varies as a function of m_{hh}^{max} [269]. The precision on $\delta_{c_{2V}}$ is shown in Fig. 65 as a function of

m_{hh}^{\max} , where the gray area indicates the region where $\delta_{c_{2V}} > \delta_{c_{2V}}^{\max}$. As expected, increasing m_{hh}^{\max} leads to stronger constraints. We therefore find that in the kinematic region accessible at the HL-LHC the EFT description of the di-Higgs VBF process should be valid.

4.5 Same-sign WW scattering at HL-LHC: a new strategy for the EFT-based analysis

J. Kalinowski,^a P. Kozów,^a S. Pokorski,^a J. Rosiek,^a M. Szleper^b and S. Tkaczyk^c

^a Faculty of Physics, University of Warsaw, Warsaw, Poland,

^b National Center for Nuclear Research, Warsaw, Poland,

^c Fermi National Accelerator Laboratory, Batavia, IL 60510, USA.

Although any statistically significant deviation in data from the Standard Model(SM) predictions would be a manifestation of a BSM physics, the question is what we can learn about its scale and its strength before discovering new particles. The appropriate tool for answering this question is the Effective Field Theory(EFT) approach: the information about the scale Λ and the strength C of new physics is encoded in the Wilson coefficients of the higher dimension operators, $f_i = C^m/\Lambda^n$. The usefulness of any EFT analysis of a given process relies on the assumption that only a few higher-dimension terms in the expansion $\mathcal{L} = \mathcal{L}_{SM} + \sum_i f_i^{(6)} \mathcal{O}_i^{(6)} + \sum_i f_i^{(8)} \mathcal{O}_i^{(8)} + \dots$ provide adequate approximation to an unknown UV completion. This assumption introduces a strong model-dependent aspect and therefore it is convenient to introduce the concept of EFT "models" defined by the choice of operators and the values of their Wilson coefficients $(\mathcal{O}_i^{(d)}, f_i^{(d)})$. Our focus is on the proper use of the EFT "models" in their range of validity for the WW scattering in purely leptonic W decay channels where the WW invariant mass cannot be determined experimentally [270].

Following a common practice we take one operator at a time setting others to zero, which effectively defines the EFT "model", and consider the process $pp \rightarrow 2jW^+W^+ \rightarrow 2jl^+\nu l^+\nu'$. The EFT "model" can be maximally valid up to the invariant mass M of the W^+W^+ system $M < \Lambda \leq M^U$, where $M^U = M^U(f)$ is the perturbative partial wave unitarity bound in the chosen EFT "model". If the kinematic range M_{max} at the LHC is greater than Λ , there is necessarily a contribution to observables from the region $\Lambda < M < M_{max}$. Two questions arise: 1) what is the discovery region in the space (Λ, f) for the chosen EFT "model", 2) if a deviation from the SM predictions is indeed observed, how to verify the chosen EFT "model" by fitting it to a set of experimental distributions D and in what range of Λ, f_i such a fit is really meaningful?

For a given EFT "model" the unitarity bound is very different for different helicity amplitudes. As M^U we take the *lowest* value, universally for all helicity amplitudes. The BSM signal S of the EFT "model" $(\mathcal{O}_i^{(d)}, f_i^{(d)})$ can be defined as the deviation of some observable D from the SM prediction $S = D^{model} - D^{SM}$. A quantitative estimate of the signal can be written as

$$D^{model} = \int_{2M_W}^{\Lambda} \frac{d\sigma}{dM} \Big|_{model} dM + \int_{\Lambda}^{M_{max}} \frac{d\sigma}{dM} \Big|_{SM} dM, \quad (78)$$

which comes uniquely from the operator that defines the "model" in its range of validity and assumes only the SM contribution in the region $M > \Lambda$. BSM contribution from the region above Λ may enhance the signal, but it may also preclude proper description of the data in the EFT "model", which makes sense *if and only if* this additional contribution is small enough compared to the contribution from the validity region. For a quantitative estimate of this contribution we define a second estimate in which all the helicity amplitudes above Λ are assumed to remain constant at their respective values they reach at Λ

$$D^{model} = \int_{2M_W}^{\Lambda} \frac{d\sigma}{dM} \Big|_{model} dM + \int_{\Lambda}^{M_{max}} \frac{d\sigma}{dM} \Big|_{A=const} dM. \quad (79)$$

For $\Lambda = \Lambda_{max}$ this prescription regularizes the helicity amplitudes that violate unitarity at M^U . We adopt the criterion that the EFT "model" is tested for values of $(\Lambda \leq M^U, f_i)$ when the signals computed from Eq.(78) are statistically consistent within 2σ with the signals computed with Eq.(79).

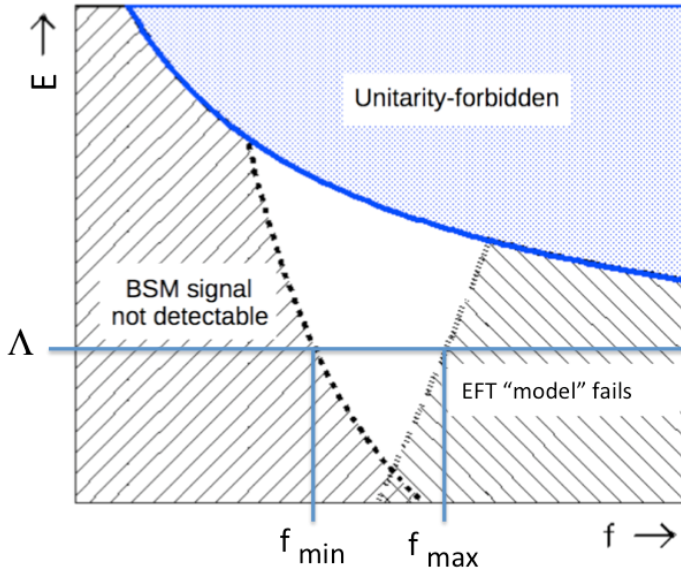


Fig. 66: Cartoon plot showing the regions in f_i and Λ in terms of BSM signal observability and applicability of the EFT "model" for the same-sign WW process with purely leptonic decays. The white triangle shows the region where the BSM physics can be studied within the chosen EFT "model".

The observability of the EFT "model" predictions imposes some minimum value of f_{min} , while the description within the EFT "model" imposes some maximum value of f_{max} such that signal estimates computed from Eqs.(78) and (79) remain statistically consistent. For $\Lambda = M^U$ a finite interval of f_i values is possible, while for $\Lambda < M^U$ the respective limits on f_i depend on the actual value of Λ . It is illustrated in a cartoon plot in Fig. 66, where the white "triangle" is bounded from above by the unitarity bound $M^U(f_i)$, from the left by the signal significance criterion and from the right by the consistency criterion. The EFT "model" could be the right framework to describe the BSM signal as long as the "triangle" shown in our cartoon plot is not empty.

Our preferred strategy for data analysis is as follows:

- Measure distributions D that offer the highest sensitivity to the studied EFT "model",
- if deviations from the SM are observed, fit the values of $(\Lambda \leq M^U, f_i)$ according to Eq.(79),
- using the fitted values of f_i and Λ recalculate D templates according to Eq.(78),
- check statistical consistency between estimates based on Eqs.(78) and (79).

Physics conclusions from the obtained (Λ, f_i) values can only be drawn if such a consistency is found. Stability of the result against alternative regularization methods would provide a measure of uncertainty of the procedure - too much sensitivity to the region above Λ means the procedure is destined to fail and that data cannot be described within the chosen EFT "model".

To demonstrate our strategy we considered EFT "models" defined by one-at-a-time dimension-8 operator that affects $WWWW$ couplings. Details of the simulation of events for the process $pp \rightarrow jj\mu^+\mu^+\nu\nu$ (at 14 TeV with 3/ab integrated luminosity) and their processing according to our strategy can be found in [270]. Assuming Λ equal to the respective unitarity bounds, the lower and upper limits for the values of f for each dimension-8 operator, for positive and negative f values, as well as the applicability "triangles" in the (Λ, f_i) plane for each operator have been calculated. These limits define the (continuous) sets of testable EFT "models" based on the choice of single dimension-8 operators. The "triangles" turned to be rather narrow, but in most cases non-empty.

To summarize: we have introduced the concept of EFT “models” defined by the choice of higher dimension operators and values of the Wilson coefficients and analyzed “models” based on single dimension-8 operators at a time. We argue that usage of EFT “models” in the analysis of purely leptonic W decay channels requires bounding the possible contribution from the region $M_{WW} > \Lambda$, no longer described by the “model”, and ensuring it does not significantly distort the measured distributions compared to what they would have looked from the region of EFT validity alone and propose a data analysis strategy to satisfy the above requirements. We find that, with a possible exception of \mathcal{O}_{S1} , all dimension-8 operators which affect the $WWWW$ quartic coupling have regions where a 5σ BSM signal can be observed at HL-LHC with 3 ab^{-1} of data, while data could be satisfactorily described using the EFT approach.

Acknowledgments: Work partially supported by the National Science Centre (Poland) grants DEC-2015/18/M/ST2/00054, DEC-2016/23/G/ST2/04301 (SP), DEC-2015/19/B/ST2/02848 (JR) and HARMONIA project UMO-2015/18/M/ST2/00518 (JK). ST is supported by Fermi Research Alliance, LLC under Contract No. De-AC02-07CH11359 with the US DoE.

4.6 Testing the universal Higgs nonlinearity

D. Liu,^a I. Low,^{a,b} Z. Yin,^b

^a High Energy Physics Division, Argonne National Laboratory, Argonne, IL 60439, USA

^b Department of Physics and Astronomy, Northwestern University, Evanston, IL 60208, USA.

We initiate a phenomenological study of “universal relations” in composite Higgs models, which are dictated by nonlinear shift symmetries acting on the 125 GeV Higgs boson. These are relations among one Higgs couplings with two electroweak gauge bosons (HV), two Higgses couplings with two electroweak gauge bosons (HHV), one Higgs couplings with three electroweak gauge bosons (HVVV), as well as triple gauge boson couplings (TGC), which are all controlled by a single input parameter: the decay constant f of the pseudo-Nambu-Goldstone Higgs boson. Assuming custodial invariance in strong sector, the relation is independent of the symmetry breaking pattern in the UV, for an arbitrary symmetric coset G/H . The complete list of corrections to HV, HHV, HVV and TGC couplings in composite Higgs models is presented to all orders in $1/f$, and up to four-derivative level, without referring to a particular G/H . We then present several examples of universal relations in ratios of coefficients which could be extracted experimentally. Measuring the universal relation requires a precision sensitive to effects of dimension-8 operators in the effective Lagrangian and highlights the importance of verifying the tensor structure of HHV interactions in the standard model, which remains untested to date.

Acknowledgments: This work is supported in part by the U.S. Department of Energy under contracts No. DE-AC02-06CH11357 and No. DE-SC0010143.

4.7 Same-sign WW scattering: A comparison of the HL- and HE-LHC reach for the selected Dim8 operators within the EFT approach

G. Chaudhary,^a J. Kalinowski,^b M. Kaur,^a P. Kozów,^b K. Sandeep,^a M. Szleper^c and S. Tkaczyk^d

^a University of Panjab, Chandigarh, India,

^b Faculty of Physics, University of Warsaw, Warsaw, Poland,

^c National Center for Nuclear Research, Warsaw, Poland,

^d Fermi National Accelerator Laboratory, Batavia, IL 60510, USA.

In Sect.4.5 a new strategy for the EFT-based analysis of the same-sign WW scattering in the purely leptonic W decay channels at the LHC has been proposed. Since in this process the scale of the WW scattering cannot be reconstructed experimentally, the main idea of the proposed strategy is to require that the dominant contribution to the observed signal should come from the EFT controlled region of the phase space. As a result, for the given EFT scale Λ one expects a finite interval of the Wilson coefficient, from f_{min} to f_{max} , where the BSM signal is observable and the EFT description can be trusted. Together

THIS IMAGE NEEDS TO BE REPLACED

Fig. 67: Regions in f_{M6} and Λ in terms of BSM signal observability for the EFT “model” based on M6 operator at the HL- and HE-LHC.

with the unitarity bound the f_{min} and f_{max} eventually will form a “trangle”, as shown in the cartoon plot Fig.66, where the BSM physics can be studied within the chosen EFT “model”.

Following the above strategy we have compared the expected reach the expected reach for the dim-8 operator O_{M6} at the HL- and HE-LHC assuming the integrated luminosities $3/ab$ and $?/ab$, respectively. Fig.67 shows the respective “triangles”.

4.8 Dimension-6 EFT effects on Vector Boson Scattering at high energies

Roberto Covarelli^a and Raquel Gomez-Ambrosio^b

^a*Università di Torino and INFN sezione di Torino, Via Pietro Giuria 1, 10125, Turin, Italy*

^b*Institute of Particle Physics Phenomenology, Durham University, Durham DH1 3LE, UK*

Introduction

In this note we assess the sensitivity of vector boson scattering (VBS) processes to different dimension-6 ($\text{dim} = 6$) operators. We focus here on the ZZ final state, decaying to 4 charged leptons. This experimental channel, currently statistically limited at the LHC [271], will become more interesting at the HL-LHC because of the attainable selection purity. The full reconstruction of the final states also gives access to cleaner observables with respect to final states involving W bosons, where neutrino 4-momenta must be inferred using approximated methods. This analysis can nevertheless be repeated analogously to other VBS final states.

In [272] we studied the purely electroweak component of the $pp \rightarrow ZZjj$ process, referred to as VBS(ZZ). Sensitivity to several $\text{dim} = 6$ operators has been demonstrated, as well as the impact of such EFT contribution on the VBS cross-section and triple and quartic gauge couplings (TGCs and QGCs).

Here we update predictions for the HL-LHC setup and show the kinematic distributions for a handful of relevant operators. For the $\text{dim} = 6$ parametrisations we use the *Warsaw basis* from [231], following the notation and classification from [273]. Other technical details can be found in the original publication [272].

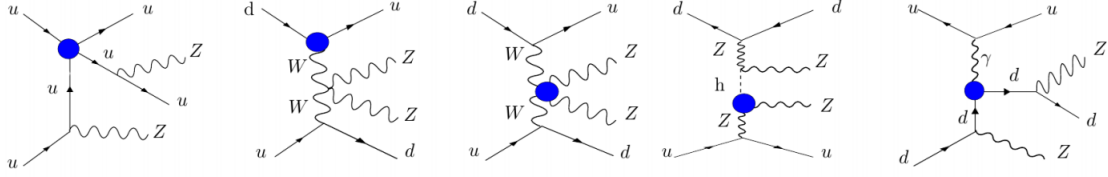


Fig. 68: Examples of some EFT diagrams for the VBS(ZZ) signal. The blobs represent $\text{dim} = 6$ insertions.

Effective Field Theory parametrization

We consider a standard SMEFT parametrisation:

$$\mathcal{L}_{\text{SMEFT}} = \mathcal{L}_{\text{SM}} + \sum_i \frac{c_i}{\Lambda^2} \mathcal{O}_i^{(6)} + \dots \quad (80)$$

where the $\mathcal{O}_i^{(6)}$ represent a basis of $\text{dim} = 6$ operators built from SM fields and respecting the known gauge symmetries¹², and c_i are the Wilson coefficients of the theory. Further, the SMEFT amplitudes and cross sections can be parametrised as

$$\mathcal{A}_{\text{EFT}} = \mathcal{A}_{\text{SM}} + \frac{g'}{\Lambda^2} \mathcal{A}_6 + \frac{g'^2}{\Lambda^4} \mathcal{A}_8 + \dots \quad (81)$$

$$\sigma_{\text{EFT}} \sim |\mathcal{A}_{\text{SM}}|^2 + 2 \frac{g'}{\Lambda^2} \mathcal{A}_{\text{SM}} \mathcal{A}_6 + \frac{g'^2}{\Lambda^4} (2 \mathcal{A}_{\text{SM}} \mathcal{A}_8 + |\mathcal{A}_6|^2) + \dots \quad (82)$$

Here, we assume the linear contribution (red) of the EFT effects to be leading. Analysis of the $\text{dim} = 6$ quadratic terms and the $\text{dim} = 8$ interference terms (both in blue) will be subject of further studies. In particular, $\text{dim} = 8$ are commonly associated with quartic gauge couplings and such contribution, albeit subleading, would represent some added value to the linear $\text{dim} = 6$ prediction.

Definition of the fiducial region

The VBS(ZZ) process has a very peculiar experimental signature, with two energetic forward jets and 4 identifiable charged leptons ($\ell, \ell' = \mu$ or e). The electroweak component of the process $pp \rightarrow ZZjj \rightarrow \ell\bar{\ell}\ell'\bar{\ell}'jj$ is defined and isolated through some experimental cuts. The ones used in the CMS analysis (in the measurement of the fiducial cross-section) can be found in [271]. Here we define a similarly VBS-enriched region, with a relaxed m_{jj} selection: **Editors, I'd like to have this in 2 columns but I don't want to mess up anything.... use package multicol didn't work unfortunately**

- $p_T(j) > 30 \text{ GeV}$
- $\Delta\eta(j_1 j_2) > 2.4$
- $m_{jj} > 100 \text{ GeV}$
- *on-shell* Z_1, Z_2

¹²In particular, we assume CP symmetry, neglecting the CP-odd operators since their impact on VBS cross-sections and differential distributions is negligible. However it is well known that certain variables of these processes (namely spin correlations and polarizations) can be sensible to CP-violation.

EFT analysis

In tables 33 and 34 we show the sensitivities to different dim = 6 operators of the VBS(ZZ) process, as well as of its main background at LHC: the diboson production channel from quark-antiquark annihilation associated to gluon radiation (studied in depth by CMS for LHC runs I and II in [274], QCD(ZZ)).

Further, in figure 69 we show differential distributions for a subset of the previous operators. In particular we chose the three operators that directly affect triple and quartic gauge couplings: [this as well](#)

- $\mathcal{O}_W = \epsilon^{ijk} W_\mu^{i\nu} W_\nu^{j\rho} W_\rho^{k\mu}$
- $\mathcal{O}_{HW} = H^\dagger H W_{\mu\nu}^I W^{\mu\nu I}$
- $\mathcal{O}_{HWB} = H^\dagger \tau^I H W_{\mu\nu}^I B^{\mu\nu}$

However, as reported in tables 33 and 34, there are other relevant operators for the VBS process, for example $\mathcal{O}_{\ell\ell}$, the 4-lepton operator that affects G_F , or \mathcal{O}_{HB} that enters the Z boson propagator. More details can be found for example in [107].

Figure 69 should be interpreted as follows: we select one paradigmatic operator (for example \mathcal{O}_W), and see how much does its interference term affect the VBS and diboson signals (2.5% in this case). As the VBS(ZZ) cross section is still mostly unconstrained experimentally, while the QCD(ZZ) has a 21% uncertainty in the 2-jet bin [274], we know the bounds within which we can vary this coefficient. If we assume for example a 10% positive interference with the total cross-section, we observe that such a small contribution to the total cross-section can represent a large modification in certain bins of the differential distributions. This advantage is twofold: with this procedure we can select the optimal bin(s) for the study and fit of each EFT operator; and, by applying unitarity considerations, we can constrain the values of the Wilson coefficients further. In our example, a contribution of 10% in \mathcal{O}_W , still allowed for the total rate, has a large impact on the high energy bins of the $p_T(Z_1)$ distribution.

Conclusions

The VBS(ZZ) and QCD(ZZ) final states, still largely unexplored at the LHC, will be an important source of constraints on dim = 6 EFT operators at the HL-LHC. We have shown the impact that values of Wilson coefficients still experimentally allowed have on differential distributions that are easily accessible experimentally in this channel.

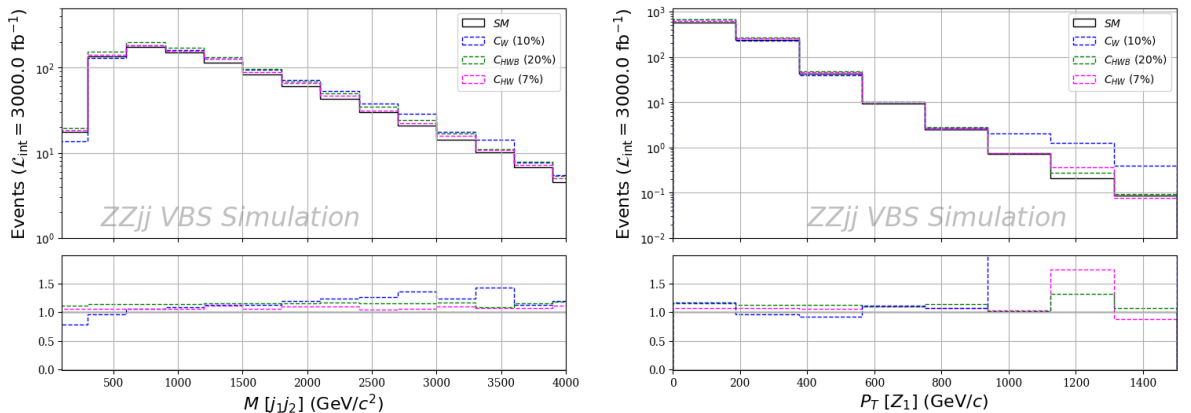


Fig. 69: Two generic simulations showing the EFT effects on key differential distributions: invariant mass of the di-jet system (left) and transverse momentum of the leading Z boson (right). We selected arbitrary values for the Wilson coefficients $\{c_W, c_{HW}, c_{HWB}\}$

VBS Signal	Signal strengths (Linear EFT)
Class 1:	$\mathcal{O}_W = c_W \cdot 2.5\%$
Class 3:	$\mathcal{O}_{HD} = c_{HD} \cdot 6.0\%$
Class 4:	$\mathcal{O}_{HW} = c_{HW} \cdot 5\%, \mathcal{O}_{CHB} = c_{HB} \cdot 0.2\%, \mathcal{O}_{HWB} = c_{HWB} \cdot 14\%$
Class 7:	$\mathcal{O}_{Hl^{(3)}} = c_{Hl^{(3)}} \cdot 48\%, \mathcal{O}_{Hq^{(1)}} = c_{Hq^{(1)}} \cdot 2\%,$ $\mathcal{O}_{Hq^{(3)}} = c_{Hq^{(3)}} \cdot 46\%, \mathcal{O}_{Hu} = c_{Hu} \cdot 0.8\%$
Class 8a: $(L\bar{L})(L\bar{L})$	$(G_F \rightarrow) \mathcal{O}_{\ell\ell} = c_{\ell\ell} \cdot 24\%, \mathcal{O}_{qq^{(1)}} = c_{qq^{(1)}} \cdot 12\%,$ $\mathcal{O}_{qq^{(11)}} = c_{qq^{(11)}} \cdot 14\%, \mathcal{O}_{qq^{(33)}} = c_{qq^{(33)}} \cdot 100\%, \mathcal{O}_{qq^{(31)}} = c_{qq^{(31)}} \cdot 75\%$

Table 33: Different sensitivities to each of the Warsaw basis operators. The operators that are not listed do not intervene in the process, or do it in a negligible way. Each sensitivity ϵ_i is calculated as $\epsilon_i = |\frac{\sigma_{EFT} - \sigma_{SM}}{\sigma_{SM}}|$, and they include a standard EFT prefactor $\frac{v^2}{\Lambda^2}|_{\Lambda=1TeV}$ which needs to be taken into account if substituting values for the c_i in the table. NB: we quote the absolute value for the sensitivities ϵ .

ZZ Diboson	Sensitivities (Linear EFT)
Class 1:	$\mathcal{O}_G = 2.5\%, \mathcal{O}_W = 2.5\%$
Class 3:	$\mathcal{O}_{HD} = 6.0\%$
Class 4:	$\mathcal{O}_{CHW} = 0.2\%, \mathcal{O}_{CHG} = 8\%, \mathcal{O}_{CHB} = 0\%, \mathcal{O}_{CHWB} = 12\%$
Class 7:	$\mathcal{O}_{Hl^{(3)}} = c_{Hl^{(3)}} \cdot 25\%, \mathcal{O}_{Hq^{(1)}} = c_{Hq^{(1)}} \cdot 3\%,$ $\mathcal{O}_{Hq^{(3)}} = c_{Hq^{(3)}} \cdot 31\%, \mathcal{O}_{Hu} = c_{Hu} \cdot 1.1\%$
Class 8a: $(L\bar{L})(L\bar{L})$	$(G_F \rightarrow) \mathcal{O}_{\ell\ell} = c_{\ell\ell} \cdot 12\%, \mathcal{O}_{qq^{(1)}} = c_{qq^{(1)}} \cdot 1.0\%,$ $\mathcal{O}_{qq^{(11)}} = c_{qq^{(11)}} \cdot 1.3\%, \mathcal{O}_{qq^{(33)}} = c_{qq^{(33)}} \cdot 8.4\%, \mathcal{O}_{qq^{(31)}} = c_{qq^{(31)}} \cdot 8.0\%$

Table 34: Sensitivities to the different dim = 6 operators in the diboson production channel, main background for the VBS(ZZ) at LHC. A large sensitivity does not necessarily mean that a large EFT effect is expected, since the corresponding Wilson coefficient might as well be very small.

5 Higgs boson mass and width

5.1 Theory review

F. Caola, R. Röntsch

The total decay width is an important property of the Higgs boson, as it contains information about the interactions of the Higgs with all other fundamental particles, and is predictable both in the Standard Model and its extensions. Therefore, measuring this property is an important part of Higgs studies. Direct measurements of the Higgs width are very challenging at hadron colliders, as these require a scan of the invariant mass profile of the Higgs decay products. This is limited by detector resolution to roughly ~ 1 GeV, which is three orders of magnitude larger than the SM prediction of $\Gamma_H \sim 4$ MeV. Current LHC measurements have already attained this level of precision, and no significant improvement is anticipated.¹³

Given this situation, there has been considerable interest in devising indirect probes of the Higgs width. In general, a standard Higgs analysis in the $H \rightarrow X$ decay channel measures the production cross section times branching ratio, $\sigma \sim \sigma_{\text{prod}} \times \Gamma_{H \rightarrow X}/\Gamma_H$, and is thus only sensitive to a combination of the coupling and the width. Schematically,

$$\sigma \sim \frac{g_{\text{prod}}^2 \times g_{\text{dec}}^2}{\Gamma_H}, \quad (83)$$

¹³Lower bounds on the Higgs width can be obtained from lifetime measurements, see Sec. 5.4 for details.

where g_{prod} and g_{dec} are the couplings that enter the Higgs production and decay channels, respectively. An independent measurement of the couplings and the decay width is therefore not possible from such analyses. The idea behind all indirect determinations of Γ_H is to find an observable whose dependence on g_i and Γ_H is different from Eq. (83), which allows one to lift the coupling/width degeneracy. Indirect determinations can be broadly separated in two classes: *on-shell* methods, which rely on delicate interference effects on the Higgs resonant peak, and *off-shell* methods, which combine on-peak and off-peak information. In the following, we provide a quick overview of these methods, emphasizing their strengths and weaknesses.

The starting point of the *on-shell* methods [275–278] is the observation that measurements in the $H \rightarrow X$ decay channel receive a contribution both from the signal $pp \rightarrow H \rightarrow X$ process and from the continuum background $pp \rightarrow X$, and the two interfere. Schematically, the amplitude for the process can be written as

$$\mathcal{A}_{pp \rightarrow X} = \frac{Sm_H^2}{s - m_H^2 + im_H\Gamma_H} + B, \quad (84)$$

where $S \propto g_{\text{prod}} \times g_{\text{dec}}$ is the signal part and B is the background contribution. This leads to

$$|\mathcal{A}_{pp \rightarrow X}|^2 = \frac{m_H^4}{(s - m_H^2)^2 + m_H^2\Gamma_H^2} \times \left[|S|^2 + \frac{(s - m_H^2)}{m_H^2} 2\text{Re}(SB^*) + \frac{\Gamma_H}{m_H} 2\text{Im}(SB^*) \right] + |B|^2. \quad (85)$$

Here, $|S|^2 \propto g_{\text{prop}}^2 \times g_{\text{dec}}^2$, but $SB^* \propto g_{\text{prop}} \times g_{\text{dec}}$, so a combined determination of the signal $|S|^2$ and interference SB^* contributions can lift the coupling/width degeneracy of Eq. (83), thus giving access to Γ_H . For this method to be effective, one needs to consider channels where the interference is large. The best candidate is then the $gg \rightarrow H \rightarrow \gamma\gamma$ channel: indeed, in this case both the $gg \rightarrow H$ production and the $H \rightarrow \gamma\gamma$ are loop induced, as is the continuum contribution $gg \rightarrow \gamma\gamma$. This implies that at least naively there is a loop enhancement factor in the interference w.r.t. the pure signal, thus making the former noticeable.

The *real part of the interference* in Eq. (85) is antisymmetric around the Higgs peak, so it does not affect the total rate. However, it leads to a distortion in the shape of the $m_{\gamma\gamma}$ distribution around the Higgs peak, which in turns translates into a slight shift in the reconstructed Higgs mass [276]. The size of this mass shift is proportional to the interference contribution, whose dependence on couplings and width is different from Eq. (83). A measurement of the mass shift then allows for a determination of Γ_H . This can be done for example by comparing the mass extracted in the $\gamma\gamma$ channel with that determined in the $4l$ channel, where these interference effects are negligible. However, even if the $4l$ channels lead to a very good mass determination once high enough statistics have been accumulated, extracting the mass shift from a $\gamma\gamma$ vs $4l$ comparison introduces additional systematics. Because of this, it is preferable to consider only the $\gamma\gamma$ decay mode and to compare different kinematic regions. This is possible since the interference is strongly dependent on the transverse momentum of the Higgs [277]. In particular, hard radiation tends to lessen this effect somewhat. Another candidate for a reference mass could be obtained from studying Higgs production in association with two hard jets. Indeed, in this case there are cancellations between the ggF and VBF contributions and the net result for the interference is very small [279]. Theoretical predictions for the mass shift are under good control, with the interference being known to NLO in QCD [277, 280, 281] and matched to parton shower [282, 283]. It turns out that radiative corrections deplete the interference contribution somewhat. Although it is well known that higher order corrections are important for Higgs physics, for this analysis the main limitation comes from experimental systematics, namely the detector response, which must be properly modeled to extract the interference contribution from the measured mass shift. In the SM, the mass shift at the LHC is rather small, $\Delta m_{\gamma\gamma} \sim \mathcal{O}(50 - 100)$ MeV. This implies that at the HL-LHC this method could lead to bounds on Γ_H of the order $\Gamma_H \sim \mathcal{O}(10 - 50) \times \Gamma_{H,\text{SM}}$. Detailed projections can be found in Sec. 5.6.

The *imaginary part of the interference* [277, 278] in Eq. (85) is symmetric around the Higgs peak,

so it leads to a change in the rate. Unfortunately, because of helicity conservation this imaginary part is highly suppressed at LO. Higher order corrections provide a new mechanism to generate an imaginary part, lifting this suppression [277]. However, because the bulk of the interference effectively enters at NLO, the anticipated loop enhancement factor in the interference relative to the pure signal (mentioned above) is not present, and the actual size of the effect is quite small. In the SM, it reduces the total rate by about 2%, which makes it challenging to observe, and the effect is further diluted by additional radiation [278]. Thus this technique requires very good control on the total rate, both experimental and theoretical. To reduce the former, it is profitable to consider cross-section ratios; for example, the $\gamma\gamma$ to $4l$ ratio is projected to be measured at the few percent level. However, this introduces additional experimental and theoretical systematics, including theoretical model dependence since one would need to make assumptions about the structure of Higgs couplings. For this reason, it is again preferable to perform the interference effect extraction in the $\gamma\gamma$ channel alone, by considering different kinematic regions. As with the real part of the interference, this effect is also quite sensitive to the transverse momentum of the Higgs, with the bulk of the interference effect confined to the small p_t region, as shown in an NLO analysis in Ref. [278]. However, since the interference is essentially an NLO effect, as discussed above, the residual theoretical uncertainty at this order is still quite sizable. Moreover, a fine-grained comparison of the low and high Higgs p_t regions requires very good theoretical control. For the former, this is notoriously complicated as several different effects are at play, see e.g. [284] and references therein for a recent discussion of this point. Because of this, assuming a few percent experimental accuracy, the width extraction from this method would be limited by theoretical uncertainties. Although computing higher order corrections for this effect is well beyond our current ability, it is reasonable to assume that the situation will improve on the HL/HE-LHC timescale, along the lines described in Section 2.2. Currently, it is expected that this technique would lead to bounds of the order $\Gamma_H \sim \mathcal{O}(10) \times \Gamma_{H,\text{SM}}$, see section 5.5 for details.

The main advantage of the on-shell width determinations discussed above is that – although being indirect measurements – they require minimal theoretical assumptions on potential BSM effects. This is because couplings are extracted at the same energy scale, ideally from the same process. Unfortunately, since interference effects scale like $g_{\text{prod}} \times g_{\text{dec}}$ at the first power, the constraints on the width are quite mild. Indeed, if one assumes that the on-shell rates are kept fixed, a linear dependence on the coupling translates into a square root dependence on the width.

Another option to constrain the width is off-shell methods [285–288], which are based on the following observation. Schematically, the cross section can be written as

$$\sigma \sim \frac{g_{\text{prod}}^2 \times g_{\text{dec}}^2}{(s - m_H^2)^2 + m_H^2 \Gamma_H^2}. \quad (86)$$

On the resonant peak, this leads to the usual relation Eq. (83). Typically, most of the cross section is concentrated there. In the VV decay channel though there is a sizable contribution from the off-shell $s \gg m_H^2$ region [285]: indeed, Higgs decay to vector bosons is strongly enhanced at high energy. In the far off-shell region, Eq. (86) reduces to $\sigma \sim (g_{\text{prod}}^2 \times g_{\text{dec}}^2)/s^4$. Assuming that the on-peak rates are kept fixed, this quadratic dependence on the couplings translates into a linear dependence on Γ_H , allowing this quantity to be constrained by a comparison of on- and off-shell rates.

However, it is important to stress that to extract Γ_H from off-shell measurements one has to assume that on-shell and off-shell couplings are the same. Since the two are evaluated at very different energy scales, this introduces a theoretical model dependence. Indeed, there are several new physics scenarios where BSM effects decorrelate on- and off- shell couplings, see e.g. [289–291]. These include for example new light degrees of freedom coupled to the Higgs, additional Higgs states, or anomalous HVV couplings. Therefore, to constrain the width using an off-shell analysis, it is important to perform complementary measurements to control potential BSM effects. This was studied in detail for the case of HVV anomalous couplings in [292]. Projections at the HL-LHC will be presented in section 5.7.

In general, off-shell measurements offer the opportunity to investigate Higgs interactions at high energy scale, thus leading to interesting information that is not limited to the width extraction. For example, in combination with measurements of boosted Higgs, HH and $t\bar{t}H$, an off-shell analysis can help lifting the degeneracy between ggH and $t\bar{t}H$ couplings [293]. The off-shell program will clearly benefit from the increased statistics and energy of the HL/HE upgrade. For example, this would allow for off-shell studies in the VBF production mode [294]. Although the rate here is very small, by looking at same-sign vector boson final states one can significantly reduce backgrounds. Although it is estimated that HL-LHC measurements in this channel would lead to constraints at the same level of current ones in the ggF channel [294], the completely different production mechanism makes them complementary to the ggF constraints, thus allowing for a less model dependent interpretation. Aside from these considerations, it is interesting to study the potential of future LHC upgrades to constrain Γ_H under the assumption that no large decorrelations between on- and off-shell couplings occur. Because of the linear dependence on the width discussed above, such constraints are quite powerful. Indeed, assuming a reasonable reduction in the theoretical uncertainty in the HL-LHC timescale, it will be possible to probe values close to the SM value $\Gamma_H \sim 4$ MeV. Projections under different assumptions for the theoretical uncertainty are reported in section 5.7.

A reliable theoretical description of the off-shell region is non trivial. First, there is a large $q\bar{q} \rightarrow VV$ background, which needs to be properly subtracted to access the signal yield. More important, there is an irreducible $gg \rightarrow VV$ continuum background that interferes with the signal process $gg \rightarrow H \rightarrow VV$. The interference effect is sizable and destructive, which is a consequence of the Higgs mechanism ensuring unitarity in the SM. Because of the large interference, it is necessary to have good theoretical control not only on the signal process but also on the continuum background amplitude. This is non trivial, since the $gg \rightarrow VV$ process is loop induced, so higher order corrections – expected to be large given the gg initial state – involve multi-loop amplitudes. Moreover, at large invariant masses, the contribution of virtual top quarks to the amplitude becomes dominant. Its proper description would then require multi-loop amplitudes involving internal massive states, which are extremely challenging to compute. For this reason, exact predictions for the background amplitude are only known to LO in the off-shell region. NLO corrections are known below the top threshold, and only in an approximate form above [295–301]. Nevertheless, recent developments in numerical techniques [159] make NLO computations for the background feasible in the near future. One subtle point in this discussion is the role of quark-initiated reactions. On the one hand, they appear naturally in the computation of NLO corrections to $gg \rightarrow VV$ from initial state splitting. On the other hand this kind of contribution – although separately finite and gauge invariant – only forms a small subset of the whole $qg \rightarrow VVq$ process at $\mathcal{O}(\alpha_s^3)$, which are part of the genuine N³LO corrections to the quark-initiated $q\bar{q} \rightarrow VV$ process. Therefore, only including the contribution coming from initial state splitting in the $gg \rightarrow VV$ process, although formally possible, may not entirely capture the correct physics. In general, this problem is not particularly relevant because the gluon channel provides the bulk of the contribution. This is however no longer the case if strong requirements on extra jet activities (typical e.g. for WW analysis) are imposed. Understanding this issue is an interesting theoretical problem, and the high statistics available at the HL/HE-LHC motivates its detailed investigation. Another issue that should be investigated is the impact of electroweak corrections, which can be sizable at high energy. Once again, although they are currently unknown, it is natural to expect progress in this direction within the HL-LHC timescale.

The modeling of the $gg \rightarrow H \rightarrow VV$ process is under better control than the background one. Still, since in the far off-shell region the top loop cannot be approximated by a contact interaction, computations are still much harder than in the on-shell region, where such an approximation is justified. As a consequence, exact results are only known to NLO. A full computation of NNLO corrections would require significant advances on current technology, which are however likely to occur in the HL-LHC timescale. It is reasonable to expect [8] that the K -factor for the exact theory is rather similar to that obtained from calculations in which the top loop is integrated out. In the absence of an exact calculation,

one can use this approximation to estimate rates at the HL/HE LHC.

The HL/HE-LHC upgrade will improve off-shell analysis in several ways. On the one hand, the larger statistics will allow for a better discrimination of the $q\bar{q} \rightarrow VV$ vs $gg \rightarrow VV$ background and – crucially – interference. Currently, this is done by using the different kinematic behavior of these contributions. Clearly, a higher statistical sample would allow for more powerful discrimination. Furthermore, increasing the collider energy would lead to a larger fraction of gluon initiated events w.r.t. quark initiated events. For example, the $(gg \rightarrow H \rightarrow VV)/(q\bar{q} \rightarrow VV)$ ratio increases by a factor of roughly 1.5 in the off-shell region when the center-of-mass energy is increased from 14 TeV to 27 TeV. Furthermore, the increase in the total rate at the HE-LHC will lead to a significant number of off-shell events in the few-TeV region. This would allow for precise investigations of the Higgs sector in the high-energy region, which could shed light on the unitarity structure of the SM.

5.2 Measurement of the Higgs boson mass

5.3 Direct constraints from the Higgs boson lineshape

5.4 Direct constraints from the Higgs boson lifetime measurements

5.5 Width from the diphoton interference rate

¹⁴ ¹⁵

The SM Higgs total decay width can be constrained from the change in on-shell Higgs rates due to interference effects between the Higgs signal and the QCD background [278]. This change in rates requires the existence of a so-called strong phase in the amplitudes, that can be present both in the Higgs signal and in the continuum background, as is the case in the SM. We shall demonstrate that, the different scaling behavior between the strong phase induced interference and the Breit-Wigner parts of the on-shell Higgs rate may allow the placement of bounds on, or even measurements of, the Higgs boson total width. Both theoretical and experimental uncertainties are the leading limiting factors in this program. On the other hand, without the strong phase induced interference effects, fits to on-shell Higgs rates can only place bounds on the total width by making definite theoretical assumptions [2, 302, 303].

It is useful to write the amplitude for $gg \rightarrow h \rightarrow \gamma\gamma$ in a form which explicitly factors out the loop-induced couplings to gluons (F_{gg}) and photons ($F_{\gamma\gamma}$),

$$A_h \equiv A_{gg \rightarrow h \rightarrow \gamma\gamma} \propto \frac{\hat{s}}{\hat{s} - m_h^2 + i\Gamma_h m_h} F_{gg} F_{\gamma\gamma}. \quad (87)$$

Both the Higgs couplings F_{gg} and $F_{\gamma\gamma}$ as well as the background amplitude A_{bkg} receive absorptive contributions that arise from loops of particles that are sufficiently light to be on shell. The resulting induced phases are usually dubbed ‘strong phases’ in the flavor literature and we will adopt this terminology here.¹⁶ In the presence of a strong phase we can write the interference term as

$$\begin{aligned} |\mathcal{M}_h|_{\text{int}}^2 &\equiv 2\Re[A_h A_{\text{bkg}}^*] = \frac{2|A_{\text{bkg}}||F_{gg}||F_{\gamma\gamma}|}{(\hat{s} - m_h^2)^2 + \Gamma_h^2 m_h^2} \\ &\times \left[(\hat{s} - m_h^2) \cos(\delta_{\text{bkg}} - \delta_h) + m_h \Gamma_h \sin(\delta_{\text{bkg}} - \delta_h) \right], \end{aligned} \quad (88)$$

¹⁴ Authors: John Campbell^a, Marcela Carena^{a,b,c}, Roni Harnik^a and Zhen Liu^{a,d}

^a Theoretical Physics Department, Fermilab, Batavia, IL 60510, USA

^b Enrico Fermi Institute, University of Chicago, Chicago, IL 60637

^c Kavli Institute for Cosmological Physics, University of Chicago, Chicago, IL 60637

^d Maryland Center for Fundamental Physics, Department of Physics, University of Maryland, College Park, MD 20742

¹⁵ This manuscript has been authored by Fermi Research Alliance, LLC under Contract No. DE-AC02-07CH11359 with the U.S. Department of Energy, Office of Science, Office of High Energy Physics.

¹⁶ Strong phases, which are CP even, get their name because they often arise in flavor physics from QCD dynamics. This is in contrast with CP odd weak phases, e.g., the relative size of the Higgs couplings to $F\tilde{F}$ versus FF

where we have taken $\delta_h = \arg[F_{gg}] + \arg[F_{\gamma\gamma}]$ and $\delta_{\text{bkg}} = \arg[A_{\text{bkg}}]$ as the signal and background strong phases, respectively. The first term in the square bracket is the contribution to the interference term that does not modify the overall rate upon integration over \hat{s} . The second term is the subject of this work and leads to a modified rate in the presence of a strong phase. For convenience, we define $|\mathcal{M}_h|_{\text{int}}^2 = \mathcal{R}_h^{\text{int}} + \mathcal{I}_h^{\text{int}}$ and $\delta_s = \delta_{\text{bkg}} - \delta_h$ such that

$$\begin{aligned}\mathcal{R}_h^{\text{int}} &\equiv \frac{2|A_{\text{bkg}}||F_{gg}||F_{\gamma\gamma}|}{(\hat{s} - m_h^2)^2 + \Gamma_h^2 m_h^2} (\hat{s} - m_h^2) \cos \delta_s \\ \mathcal{I}_h^{\text{int}} &\equiv \frac{2|A_{\text{bkg}}||F_{gg}||F_{\gamma\gamma}|}{(\hat{s} - m_h^2)^2 + \Gamma_h^2 m_h^2} m_h \Gamma_h \sin \delta_s.\end{aligned}\quad (89)$$

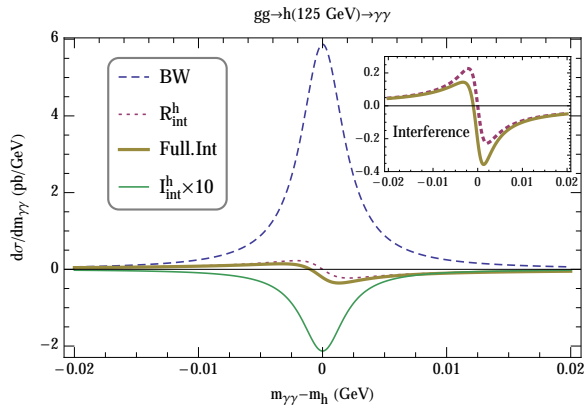


Fig. 70: The lineshape induced by various contributions to the cross-section for $gg \rightarrow h \rightarrow \gamma\gamma$ in the SM. The Breit-Wigner line-shape, with no interference, is shown in blue (dashed) while the effect of $\mathcal{R}_h^{\text{int}}$ and $\mathcal{I}_h^{\text{int}}$ (multiplied by a factor of 10) are shown in red (dotted) and green (solid), respectively. The overall effect of the interference in the full NLO calculation is given by the brown (solid) line. The insert in the top right is a magnification of the corresponding interference lineshapes.

In the SM the dominant contribution to $\mathcal{I}_h^{\text{int}}$ comes from the phase of the background amplitude at two loops [275, 304]. The signal amplitude also contains a strong phase, mainly due to bottom quark loops. We have performed a calculation of the interference effect that accounts for absorptive effects from both signal and background. In Fig. 70 we illustrate the features of the interference effects. The line shape, the differential cross-section as a function of \hat{s} , is shown for the pure Breit-Wigner (only $|A_h|^2$), and for the interference contributions $\mathcal{I}_h^{\text{int}}$ and $\mathcal{R}_h^{\text{int}}$ as well as for the sum of both. For visualization, the interference contribution $\mathcal{I}_h^{\text{int}}$ has been magnified by a factor of 10. In this figure we show the lineshapes obtained including NLO effects with virtual corrections only. After summing over different interfering helicity amplitudes, we obtain averaged strong phases $\delta_h = (\pi + 0.036)$ and $\delta_{\text{bkg}} = -0.205$ for the signal and background, respectively.

As a concrete example that demonstrates the potential of this novel effect, without loss of generality we can consider excursions in the flat direction corresponding to,

$$\frac{|F_{gg}|^2 |F_{\gamma\gamma}|^2}{|F_{gg}^{\text{SM}}|^2 |F_{\gamma\gamma}^{\text{SM}}|^2} = \frac{\Gamma_h}{\Gamma_h^{\text{SM}}}.\quad (90)$$

The total Higgs cross section can then be written as,

$$\sigma = \sigma_{\text{BW}}^{\text{SM}} \left(1 + \frac{\sigma_{\text{int}}^{\text{SM}}}{\sigma_{\text{BW}}^{\text{SM}}} \sqrt{\frac{\Gamma_h}{\Gamma_h^{\text{SM}}}} \right) \simeq \sigma_{\text{BW}}^{\text{SM}} \left(1 - 2\% \sqrt{\frac{\Gamma_h}{\Gamma_h^{\text{SM}}}} \right).\quad (91)$$

The result of a full NLO calculation of the interference effect are presented in Fig. 71, that shows the relative size of the interference effect as a function of the total width, normalized to its SM value, for parameter excursions defined by Eq. (90).¹⁷ The variation of the interference effect with the total width is shown imposing a 20 GeV p_T^h -veto, with and without LHC cuts on the final state photons. Since the interference effect is largest at small scattering angles, the photon cuts reduce the expected interference. This small consideration in the SM leads to much bigger differences for $\Gamma_h \gg \Gamma_h^{\text{SM}}$. Observe that in the SM the interference contribution is destructive. However, if the sign of $F_{gg}F_{\gamma\gamma}$ were flipped, ($\delta_s \rightarrow \pi + \delta_s$), the interference effect would lead to an enhancement of the diphoton rate rather than a suppression. The theoretical scale uncertainty is shown in the bottom panel of Fig. 71 and amounts to about $^{+50\%}_{-30\%}$. For example, the interference effect is $-(2.20^{+1.06}_{-0.55})\%$ without photon cuts for SM Higgs. Although a measurement at the 2% level may be challenging at the LHC, this shows that a precise

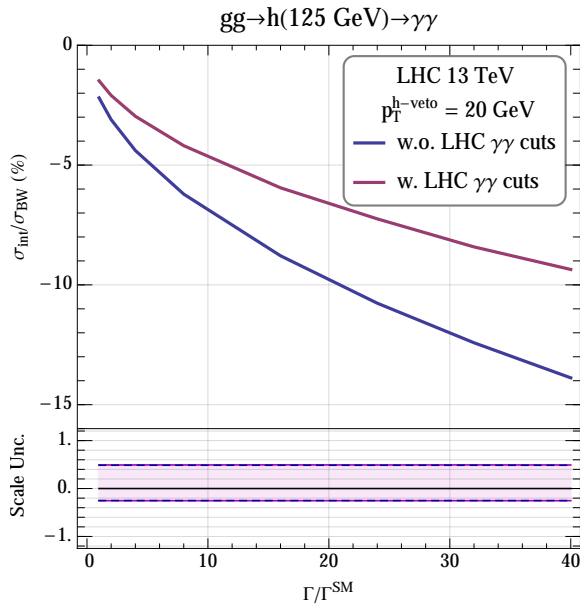


Fig. 71: The total signal rate change due to the interference effect as a function of the Higgs total width normalized to its SM value, while keeping the Breit-Wigner cross section identical to that of the SM Higgs. The magenta and blue (solid) lines represent the cases with and without LHC cuts on the final state photons, respectively. The lower panel shows the scale variation uncertainties for these interference terms as bands delimited by the blue (dashed) and magenta (solid) lines. The curves are obtained with a veto on the Higgs boson p_T at 20 GeV.

measurement of the $gg \rightarrow h \rightarrow \gamma\gamma$ rate can place a limit on the width of the Higgs boson. In this respect a measurement of the ratio of the $\gamma\gamma$ rate to the 4ℓ rate is a promising route to reduce many of the systematic and theoretical, e.g. PDF and other parametric, uncertainties.

The best measured channels at the LHC, $gg \rightarrow h \rightarrow \gamma\gamma$ and $gg \rightarrow h \rightarrow 4\ell$, provide the most accurate cross section ratio, projected to be measurable at the 4% level [316]. In contrast to single cross section measurements, the precision on this ratio is statistically limited. Keeping the current theoretical uncertainty band in mind, the projected sensitivity of 4% on the ratio of $\gamma\gamma$ to 4ℓ yields can be translated into an upper limit of 22, 14, and 8 on $\Gamma_h/\Gamma_h^{\text{SM}}$ at 1- σ level, for low, central and high theoretical expectations on this interference effect, respectively.¹⁸ This assumes that the couplings to photons and Z bosons maintain their SM ratio and the photon and gluon couplings respect Eq. (90). The Higgs cross

¹⁷For details of the NLO calculation , see the supplemental material with Refs [10, 280, 305–315].

¹⁸This limit is worse by one order of magnitude than the off-shell Higgs measurement that constrains the Higgs total width [285–287]. However, unlike the off-shell Higgs measurement, our effect is independent from the assumptions on the

section precisions are anticipated to improve by a factor of three or so from statistical improvement at the HE-LHC with 27 TeV center of mass energy and 15 fb^{-1} of integrated luminosity. This can be naively translated into lower and upper limits on the Higgs total width of $\Gamma_h/\Gamma_h^{\text{SM}} < 5$ at 1σ level using the central value from our NLO theory calculation.

In summary, we discuss the change in the $gg \rightarrow h \rightarrow \gamma\gamma$ on-shell rate, due to interference between the Higgs signal and the QCD background amplitudes, as a way to provide a novel handle to constrain - or even measure - the Higgs boson total width. We perform a full NLO calculation at order α_s^3 of the interference effect and find that in the standard model it leads to a reduction of the on-shell rate by $\sim 2\%$. The proposed method for gaining sensitivity to the Higgs boson width is complementary to other methods that have been discussed in the literature. Altogether our study aims at motivating a more thorough examination of Higgs precision physics taking into account the strong phase induced interference effect in different Higgs boson observables.

5.6 Mass shift from the diphoton interference: constraints on the width

5.7 Width from Off-Shell higgs boson couplings

References

- [1] M. Mangano, *Physics at the FCC-hh, a 100 TeV pp collider*. CERN Yellow Reports: Monographs. CERN, Geneva, 2017. <https://cds.cern.ch/record/2270978>.
- [2] LHC Higgs Cross Section Working Group Collaboration, A. David, A. Denner, M. Duehrssen, M. Grazzini, C. Grojean, G. Passarino, M. Schumacher, M. Spira, G. Weiglein, and M. Zanetti, *LHC HXSWG interim recommendations to explore the coupling structure of a Higgs-like particle*, arXiv:1209.0040 [hep-ph].
- [3] LHC Higgs Cross Section Working Group Collaboration, J. R. Andersen et al., *Handbook of LHC Higgs Cross Sections: 3. Higgs Properties*, arXiv:1307.1347 [hep-ph].
- [4] J. Gao, L. Harland-Lang, and J. Rojo, *The Structure of the Proton in the LHC Precision Era*, Phys. Rept. **742** (2018) 1–121, arXiv:1709.04922 [hep-ph].
- [5] J. Rojo et al., *The PDF4LHC report on PDFs and LHC data: Results from Run I and preparation for Run II*, J. Phys. **G42** (2015) 103103, arXiv:1507.00556 [hep-ph].
- [6] S. Forte and G. Watt, *Progress in the Determination of the Partonic Structure of the Proton*, Ann. Rev. Nucl. Part. Sci. **63** (2013) 291–328, arXiv:1301.6754 [hep-ph].
- [7] W. Beenakker, C. Borschensky, M. Kramer, A. Kulesza, E. Laenen, S. Marzani, and J. Rojo, *NLO+NLL squark and gluino production cross-sections with threshold-improved parton distributions*, Eur. Phys. J. **C76** (2016) no. 2, 53, arXiv:1510.00375 [hep-ph].
- [8] LHC Higgs Cross Section Working Group Collaboration, D. de Florian et al., *Handbook of LHC Higgs Cross Sections: 4. Deciphering the Nature of the Higgs Sector*, arXiv:1610.07922 [hep-ph]. FERMILAB-FN-1025-T.
- [9] NNPDF Collaboration, R. D. Ball et al., *Parton distributions from high-precision collider data*, Eur. Phys. J. **C77** (2017) no. 10, 663, arXiv:1706.00428 [hep-ph].
- [10] S. Dulat, T.-J. Hou, J. Gao, M. Guzzi, J. Huston, P. Nadolsky, J. Pumplin, C. Schmidt, D. Stump, and C. P. Yuan, *New parton distribution functions from a global analysis of quantum chromodynamics*, Phys. Rev. **D93** (2016) no. 3, 033006, arXiv:1506.07443 [hep-ph].
- [11] L. A. Harland-Lang, A. D. Martin, P. Motylinski, and R. S. Thorne, *Parton distributions in the LHC era: MMHT 2014 PDFs*, Eur. Phys. J. **C75** (2015) no. 5, 204, arXiv:1412.3989 [hep-ph].

high-energy behavior of the Higgs boson and the absence of new physics contribution in the off-shell region. For more detailed discussion, see e.g., chapter I.8 of the Higgs Yellow Report [8] and Refs. [289, 290].

- [12] S. Alekhin, J. Blümlein, S. Moch, and R. Placakyte, *Parton distribution functions, α_s , and heavy-quark masses for LHC Run II*, Phys. Rev. **D96** (2017) no. 1, 014011, arXiv:1701.05838 [hep-ph].
- [13] M. Czakon, N. P. Hartland, A. Mitov, E. R. Nocera, and J. Rojo, *Pinning down the large- x gluon with NNLO top-quark pair differential distributions*, JHEP **04** (2017) 044, arXiv:1611.08609 [hep-ph].
- [14] M. Guzzi, K. Lipka, and S.-O. Moch, *Top-quark pair production at hadron colliders: differential cross section and phenomenological applications with DiffTop*, JHEP **01** (2015) 082, arXiv:1406.0386 [hep-ph].
- [15] R. Boughezal, A. Guffanti, F. Petriello, and M. Ubiali, *The impact of the LHC Z-boson transverse momentum data on PDF determinations*, JHEP **07** (2017) 130, arXiv:1705.00343 [hep-ph].
- [16] J. M. Campbell, J. Rojo, E. Slade, and C. Williams, *Direct photon production and PDF fits reloaded*, Eur. Phys. J. **C78** (2018) no. 6, 470, arXiv:1802.03021 [hep-ph].
- [17] R. Gauld, J. Rojo, L. Rottoli, and J. Talbert, *Charm production in the forward region: constraints on the small- x gluon and backgrounds for neutrino astronomy*, JHEP **11** (2015) 009, arXiv:1506.08025 [hep-ph].
- [18] PROSA Collaboration, O. Zenaiev et al., *Impact of heavy-flavour production cross sections measured by the LHCb experiment on parton distribution functions at low x* , Eur. Phys. J. **C75** (2015) no. 8, 396, arXiv:1503.04581 [hep-ph].
- [19] R. Gauld and J. Rojo, *Precision determination of the small- x gluon from charm production at LHCb*, Phys. Rev. Lett. **118** (2017) no. 7, 072001, arXiv:1610.09373 [hep-ph].
- [20] ATLAS Collaboration, G. Aad et al., *Measurement of the production of a W boson in association with a charm quark in pp collisions at $\sqrt{s} = 7$ TeV with the ATLAS detector*, JHEP **05** (2014) 068, arXiv:1402.6263 [hep-ex].
- [21] CMS Collaboration, S. Chatrchyan et al., *Measurement of the muon charge asymmetry in inclusive $pp \rightarrow W + X$ production at $\sqrt{s} = 7$ TeV and an improved determination of light parton distribution functions*, Phys. Rev. **D90** (2014) no. 3, 032004, arXiv:1312.6283 [hep-ex].
- [22] J. Currie, E. W. N. Glover, and J. Pires, *Next-to-Next-to Leading Order QCD Predictions for Single Jet Inclusive Production at the LHC*, Phys. Rev. Lett. **118** (2017) no. 7, 072002, arXiv:1611.01460 [hep-ph].
- [23] J. Rojo, *Constraints on parton distributions and the strong coupling from LHC jet data*, Int. J. Mod. Phys. **A30** (2015) 1546005, arXiv:1410.7728 [hep-ph].
- [24] R. A. Khalek, S. Bailey, J. Gao, L. Harland-Lang, and J. Rojo, *Towards Ultimate Parton Distributions at the High-Luminosity LHC*, arXiv:1810.03639 [hep-ph].
- [25] J. Butterworth et al., *PDF4LHC recommendations for LHC Run II*, J. Phys. **G43** (2016) 023001, arXiv:1510.03865 [hep-ph].
- [26] J. Gao and P. Nadolsky, *A meta-analysis of parton distribution functions*, JHEP **07** (2014) 035, arXiv:1401.0013 [hep-ph].
- [27] S. Carrazza, J. I. Latorre, J. Rojo, and G. Watt, *A compression algorithm for the combination of PDF sets*, Eur. Phys. J. **C75** (2015) 474, arXiv:1504.06469 [hep-ph].
- [28] S. Carrazza, S. Forte, Z. Kassabov, J. I. Latorre, and J. Rojo, *An Unbiased Hessian Representation for Monte Carlo PDFs*, Eur. Phys. J. **C75** (2015) no. 8, 369, arXiv:1505.06736 [hep-ph].
- [29] H. Paukkunen and P. Zurita, *PDF reweighting in the Hessian matrix approach*, JHEP **12** (2014) 100, arXiv:1402.6623 [hep-ph].
- [30] C. Schmidt, J. Pumplin, C. P. Yuan, and P. Yuan, *Updating and Optimizing Error PDFs in the Hessian Approach*, Phys. Rev. **D98** (2018) no. 9, 094005, arXiv:1806.07950 [hep-ph].

- [31] A. Buckley, J. Ferrando, S. Lloyd, K. Nordstr  m, B. Page, M. R  ijfenacht, M. Sch  nherr, and G. Watt, *LHAPDF6: parton density access in the LHC precision era*, Eur. Phys. J. **C75** (2015) 132, arXiv:1412.7420 [hep-ph].
- [32] *Recommendations for Systematic Uncertainties at HL-LHC*,
<https://twiki.cern.ch/twiki/bin/view/LHCPhysics/HLHELHCCCommonSystematics>. Currently collected in a Twiki page, numbers will go either in a YR Appendix or in a standalone note.
- [33] ATLAS Collaboration, T. A. collaboration, *Measurements of Higgs boson properties in the diphoton decay channel using 80 fb^{-1} of pp collision data at $\sqrt{s} = 13\text{ TeV}$ with the ATLAS detector*, .
- [34] ATLAS Collaboration, G. Aad et al., *Observation of a new particle in the search for the Standard Model Higgs boson with the ATLAS detector at the LHC*, Phys. Lett. **B716** (2012) 1–29, arXiv:1207.7214 [hep-ex].
- [35] P. D. Dauncey, M. Kenzie, N. Wardle, and G. J. Davies, *Handling uncertainties in background shapes*, JINST **10** (2015) no. 04, P04015, arXiv:1408.6865 [physics.data-an].
- [36] ATLAS Collaboration, The ATLAS Collaboration, *Measurements of the Higgs boson production, fiducial and differential cross sections in the 4ℓ decay channel at $\sqrt{s} = 13\text{ TeV}$ with the ATLAS detector*, .
- [37] The ATLAS Collaboration, *Measurements of gluon-gluon fusion and vector-boson fusion Higgs boson production cross-sections in the $H \rightarrow WW^* \rightarrow e\nu\mu\nu$ decay channel in pp collisions at $\sqrt{s} = 13\text{ TeV}$ with the ATLAS detector*, arXiv:1808.09054 [hep-ex].
- [38] ATLAS Collaboration, M. Aaboud et al., *Observation of $H \rightarrow b\bar{b}$ decays and VH production with the ATLAS detector*, Phys. Lett. **B786** (2018) 59–86, arXiv:1808.08238 [hep-ex].
- [39] CMS Collaboration, A. M. Sirunyan et al., *Observation of Higgs boson decay to bottom quarks*, Phys. Rev. Lett. **121** (2018) no. 12, 121801, arXiv:1808.08242 [hep-ex].
- [40] CMS Collaboration, *Evidence for the Higgs boson decay to a bottom quark-antiquark pair*, Phys. Lett. B **780** (2018) 501, arXiv:1709.07497 [hep-ex].
- [41] ATLAS, CMS Collaboration, G. Aad et al., *Measurements of the Higgs boson production and decay rates and constraints on its couplings from a combined ATLAS and CMS analysis of the LHC pp collision data at $\sqrt{s} = 7$ and 8 TeV* , JHEP **08** (2016) 045, arXiv:1606.02266 [hep-ex].
- [42] ATLAS, CMS Collaboration, G. Aad et al., *Combined Measurement of the Higgs Boson Mass in pp Collisions at $\sqrt{s} = 7$ and 8 TeV with the ATLAS and CMS Experiments*, Phys. Rev. Lett. **114** (2015) 191803, arXiv:1503.07589 [hep-ex].
- [43] CMS Collaboration, C. Collaboration, *Combined measurements of the Higgs boson's couplings at $\sqrt{s} = 13\text{ TeV}$* , .
- [44] ATLAS Collaboration, G. Aad et al., *Measurements of fiducial and differential cross sections for Higgs boson production in the diphoton decay channel at $\sqrt{s} = 8\text{ TeV}$ with ATLAS*, JHEP **09** (2014) 112, arXiv:1407.4222 [hep-ex].
- [45] ATLAS Collaboration, G. Aad et al., *Fiducial and differential cross sections of Higgs boson production measured in the four-lepton decay channel in pp collisions at $\sqrt{s}=8\text{ TeV}$ with the ATLAS detector*, Phys. Lett. **B738** (2014) 234–253, arXiv:1408.3226 [hep-ex].
- [46] ATLAS Collaboration, G. Aad et al., *Measurement of fiducial differential cross sections of gluon-fusion production of Higgs bosons decaying to $WW \rightarrow E\bar{E}^{\prime\prime} l^+l^-l^+l^-$ with the ATLAS detector at $\sqrt{s} = 8\text{ TeV}$* , JHEP **08** (2016) 104, arXiv:1604.02997 [hep-ex].
- [47] ATLAS Collaboration, M. Aaboud et al., *Measurements of Higgs boson properties in the diphoton decay channel with 36 fb^{-1} of pp collision data at $\sqrt{s} = 13\text{ TeV}$ with the ATLAS detector*, Phys. Rev. **D98** (2018) 052005, arXiv:1802.04146 [hep-ex].

- [48] ATLAS Collaboration, M. Aaboud et al., *Measurement of inclusive and differential cross sections in the $H \rightarrow ZZ^* \rightarrow 4\ell$ decay channel in pp collisions at $\sqrt{s} = 13$ TeV with the ATLAS detector*, JHEP **10** (2017) 132, arXiv:1708.02810 [hep-ex].
- [49] ATLAS Collaboration, M. Aaboud et al., *Combined measurement of differential and total cross sections in the $H \rightarrow \gamma\gamma$ and the $H \rightarrow ZZ^* \rightarrow 4\ell$ decay channels at $\sqrt{s} = 13$ TeV with the ATLAS detector*, Phys. Lett. **B786** (2018) 114, arXiv:1805.10197 [hep-ex].
- [50] CMS Collaboration, V. Khachatryan et al., *Measurement of differential cross sections for Higgs boson production in the diphoton decay channel in pp collisions at $\sqrt{s} = 8$ TeV*, Eur. Phys. J. **C76** (2016) no. 1, 13, arXiv:1508.07819 [hep-ex].
- [51] CMS Collaboration, V. Khachatryan et al., *Measurement of differential and integrated fiducial cross sections for Higgs boson production in the four-lepton decay channel in pp collisions at $\sqrt{s} = 7$ and 8 TeV*, JHEP **04** (2016) 005, arXiv:1512.08377 [hep-ex].
- [52] CMS Collaboration, V. Khachatryan et al., *Measurement of the transverse momentum spectrum of the Higgs boson produced in pp collisions at $\sqrt{s} = 8$ TeV using $H \rightarrow WW$ decays*, JHEP **03** (2017) 032, arXiv:1606.01522 [hep-ex].
- [53] CMS Collaboration, A. M. Sirunyan et al., *Measurement of inclusive and differential Higgs boson production cross sections in the diphoton decay channel in proton-proton collisions at $\sqrt{s} = 13$ TeV*, arXiv:1807.03825 [hep-ex].
- [54] ATLAS Collaboration, M. Aaboud et al., *Observation of Higgs boson production in association with a top quark pair at the LHC with the ATLAS detector*, 2018.
- [55] CMS Collaboration, A. M. Sirunyan et al., *Observation of $t\bar{t}H$ production*, Phys. Rev. Lett. **120** (2018) 231801, arXiv:1804.02610 [hep-ex].
- [56] ATLAS Collaboration, M. Aaboud et al., *Search for the standard model Higgs boson produced in association with top quarks and decaying into a $b\bar{b}$ pair in pp collisions at $\sqrt{s} = 13$ TeV with the ATLAS detector*, Phys. Rev. **D97** (2018) no. 7, 072016, arXiv:1712.08895 [hep-ex].
- [57] CMS Collaboration, A. M. Sirunyan et al., *Search for $t\bar{t}H$ production in the $H \rightarrow b\bar{b}$ decay channel with leptonic $t\bar{t}$ decays in proton-proton collisions at $\sqrt{s} = 13$ TeV*, arXiv:1804.03682 [hep-ex]. Submitted to JHEP.
- [58] ATLAS Collaboration, M. Aaboud et al., *Evidence for the associated production of the Higgs boson and a top quark pair with the ATLAS detector*, Phys. Rev. **D97** (2018) 072003, arXiv:1712.08891 [hep-ex].
- [59] ATLAS Collaboration, *to be published*, ATLAS-PHYS-PUB-2018-XY, CERN, Geneva, 2018.
- [60] CMS Collaboration, *PAS in preparation*, CMS-PAS-FTR-2018-011.
- [61] CMS Collaboration, *Search for the associated production of a Higgs boson and a single top quark in pp collisions at $\sqrt{s} = 13$ TeV*, CMS Physics Analysis Summary CMS-PAS-HIG-18-009, CERN, Geneva, 2018. <http://cds.cern.ch/record/2628662>.
- [62] CMS Collaboration, *Search for production of a Higgs boson and a single top quark in multilepton final states in proton collisions at $\sqrt{s} = 13$ TeV*, CMS Physics Analysis Summary CMS-PAS-HIG-17-005, CERN, Geneva, 2017. <https://cds.cern.ch/record/2264553>.
- [63] CMS Collaboration, CMS Collaboration, *Search for the $tH(H \rightarrow b\bar{b})$ process at $\sqrt{s} = 13$ TeV and study of Higgs boson couplings*, CMS Physics Analysis Summary CMS-PAS-HIG-17-016, 2017. <http://cms.cern.ch/iCMS/analysisadmin/cadilines?line=HIG-17-016>.
- [64] CMS Collaboration, A. M. Sirunyan et al., *Measurements of Higgs boson properties in the diphoton decay channel in proton-proton collisions at $\sqrt{s} = 13$ TeV*, arXiv:1804.02716 [hep-ex].
- [65] F. Bishara, U. Haisch, P. F. Monni, and E. Re, *Constraining Light-Quark Yukawa Couplings from Higgs Distributions*, Phys. Rev. Lett. **118** (2017) no. 12, 121801, arXiv:1606.09253

[hep-ph].

- [66] M. Grazzini, A. Ilnicka, M. Spira, and M. Wiesemann, *Effective Field Theory for Higgs properties parametrisation: the transverse momentum spectrum case*, in *Proceedings, 52nd Rencontres de Moriond on QCD and High Energy Interactions: La Thuile, Italy, March 25-April 1, 2017*, pp. 23–27. 2017. arXiv:1705.05143 [hep-ph].
- [67] M. Grazzini, A. Ilnicka, M. Spira, and M. Wiesemann, *Modeling BSM effects on the Higgs transverse-momentum spectrum in an EFT approach*, JHEP **03** (2017) 115, arXiv:1612.00283 [hep-ph].
- [68] ATLAS Collaboration, G. Aad et al., *Measurements of the Total and Differential Higgs Boson Production Cross Sections Combining the $H \rightarrow \tau^+ \tau^-$ and $H \rightarrow Z Z^*$ Decay Channels at $\sqrt{s} = 8\text{TeV}$ with the ATLAS Detector*, Phys. Rev. Lett. **115** (2015) no. 9, 091801, arXiv:1504.05833 [hep-ex].
- [69] CMS Collaboration, *Measurements of properties of the Higgs boson decaying into the four-lepton final state in pp collisions at $\sqrt{s} = 13\text{ TeV}$* , JHEP **11** (2017) 47, arXiv:1706.09936 [hep-ex].
- [70] CMS Collaboration, *Measurements of Higgs boson production and couplings using decays to a W boson pair in pp collisions at 13 TeV*, CMS Physics Analysis Summary CMS-PAS-HIG-16-042, 2018. Submitted to *Phys. Lett. B*.
- [71] CMS Collaboration, *Observation of the Higgs boson decay to a pair of τ leptons with the CMS detector*, Phys. Lett. B **779** (2018) 283, arXiv:1708.00373 [hep-ex].
- [72] CMS Collaboration, *Inclusive search for a highly boosted Higgs boson decaying to a bottom quark-antiquark pair*, Phys. Rev. Lett. **120** (2018) 071802, arXiv:1709.05543 [hep-ex].
- [73] CMS Collaboration, A. M. Sirunyan et al., *Evidence for associated production of a Higgs boson with a top quark pair in final states with electrons, muons, and hadronically decaying τ leptons at $\sqrt{s} = 13\text{ TeV}$* , JHEP **08** (2018) 066, arXiv:1803.05485 [hep-ex].
- [74] CMS Collaboration, A. M. Sirunyan et al., *Search for $t\bar{t}H$ production in the $H \rightarrow b\bar{b}$ decay channel with leptonic $t\bar{t}$ decays in proton-proton collisions at $\sqrt{s} = 13\text{ TeV}$* , Submitted to *JHEP*, 2018.
- [75] CMS Collaboration, *Search for $t\bar{t}H$ production in the all-jet final state in proton-proton collisions at $\sqrt{s} = 13\text{ TeV}$* , JHEP **06** (2018) 101, arXiv:1803.06986 [hep-ex].
- [76] CMS Collaboration, *Search for the standard model Higgs boson decaying to two muons in pp collisions at $\sqrt{s} = 13\text{ TeV}$* , CMS Physics Analysis Summary CMS-PAS-HIG-17-019, 2017. Submitted to *Phys. Rev. Lett.*
- [77] CMS Collaboration, *Combined measurements of Higgs boson couplings in proton-proton collisions at $\sqrt{s} = 13\text{ TeV}$* , Submitted to *Eur. Phys. J. C*, 2018.
- [78] K. Klein, *The Phase-2 Upgrade of the CMS Tracker*, .
- [79] G. Buchalla, O. Catà, A. Celis, and C. Krause, *Fitting Higgs Data with Nonlinear Effective Theory*, Eur. Phys. J. **C76** (2016) no. 5, 233, arXiv:1511.00988 [hep-ph]. LMU-ASC-69-15.
- [80] G. Buchalla, O. Cata, A. Celis, and C. Krause, *Note on Anomalous Higgs-Boson Couplings in Effective Field Theory*, Phys. Lett. **B750** (2015) 298–301, arXiv:1504.01707 [hep-ph].
- [81] J. de Blas, O. Eberhardt, and C. Krause, *Current and Future Constraints on Higgs Couplings in the Nonlinear Effective Theory*, arXiv:1803.00939 [hep-ph].
- [82] A. Dobado and M. J. Herrero, *Phenomenological Lagrangian Approach to the Symmetry Breaking Sector of the Standard Model*, Phys. Lett. **B228** (1989) 495–502.
- [83] A. Dobado and M. J. Herrero, *Testing the Hypothesis of Strongly Interacting Longitudinal Weak Bosons in Electron - Positron Collisions at TeV Energies*, Phys. Lett. **B233** (1989) 505–511.
- [84] A. Dobado, D. Espriu, and M. J. Herrero, *Chiral Lagrangians as a tool to probe the symmetry breaking sector of the SM at LEP*, Phys. Lett. **B255** (1991) 405–414.

- [85] A. Dobado, M. J. Herrero, and J. Terron, *The Role of Chiral Lagrangians in Strongly Interacting $W(l)$ $W(l)$ Signals at pp Supercolliders*, Z. Phys. **C50** (1991) 205–220.
- [86] D. Espriu and M. J. Herrero, *Chiral Lagrangians and precision tests of the symmetry breaking sector of the Standard Model*, Nucl. Phys. **B373** (1992) 117–168.
- [87] M. J. Herrero and E. Ruiz Morales, *The Electroweak chiral Lagrangian for the Standard Model with a heavy Higgs*, Nucl. Phys. **B418** (1994) 431–455, arXiv:hep-ph/9308276 [hep-ph].
- [88] M. J. Herrero and E. Ruiz Morales, *Nondecoupling effects of the SM higgs boson to one loop*, Nucl. Phys. **B437** (1995) 319–355, arXiv:hep-ph/9411207 [hep-ph].
- [89] F. Feruglio, *The Chiral approach to the electroweak interactions*, Int. J. Mod. Phys. **A8** (1993) 4937–4972, arXiv:hep-ph/9301281 [hep-ph].
- [90] J. Bagger, V. D. Barger, K.-m. Cheung, J. F. Gunion, T. Han, G. A. Ladinsky, R. Rosenfeld, and C. P. Yuan, *The Strongly interacting WW system: Gold plated modes*, Phys. Rev. **D49** (1994) 1246–1264, arXiv:hep-ph/9306256 [hep-ph].
- [91] V. Koulovassilopoulos and R. S. Chivukula, *The Phenomenology of a nonstandard Higgs boson in $W(L)$ $W(L)$ scattering*, Phys. Rev. **D50** (1994) 3218–3234, arXiv:hep-ph/9312317 [hep-ph].
- [92] C. P. Burgess, J. Matias, and M. Pospelov, *A Higgs or not a Higgs? What to do if you discover a new scalar particle*, Int. J. Mod. Phys. **A17** (2002) 1841–1918, arXiv:hep-ph/9912459 [hep-ph].
- [93] L.-M. Wang and Q. Wang, *Electroweak chiral Lagrangian for neutral Higgs boson*, Chin. Phys. Lett. **25** (2008) 1984, arXiv:hep-ph/0605104 [hep-ph].
- [94] B. Grinstein and M. Trott, *A Higgs-Higgs bound state due to new physics at a TeV*, Phys. Rev. **D76** (2007) 073002, arXiv:0704.1505 [hep-ph].
- [95] A. Azatov, R. Contino, and J. Galloway, *Model-Independent Bounds on a Light Higgs*, JHEP **04** (2012) 127, arXiv:1202.3415 [hep-ph]. [Erratum: JHEP04,140(2013)].
- [96] R. Alonso, M. B. Gavela, L. Merlo, S. Rigolin, and J. Yepes, *The Effective Chiral Lagrangian for a Light Dynamical "Higgs Particle"*, Phys. Lett. **B722** (2013) 330–335, arXiv:1212.3305 [hep-ph]. [Erratum: Phys. Lett.B726,926(2013)].
- [97] G. Buchalla and O. Cata, *Effective Theory of a Dynamically Broken Electroweak Standard Model at NLO*, JHEP **07** (2012) 101, arXiv:1203.6510 [hep-ph].
- [98] G. Buchalla, O. Catà, and C. Krause, *Complete Electroweak Chiral Lagrangian with a Light Higgs at NLO*, Nucl. Phys. **B880** (2014) 552–573, arXiv:1307.5017 [hep-ph]. [Erratum: Nucl. Phys.B913,475(2016)].
- [99] G. Buchalla, O. Catà, and C. Krause, *On the Power Counting in Effective Field Theories*, Phys. Lett. **B731** (2014) 80–86, arXiv:1312.5624 [hep-ph].
- [100] F.-K. Guo, P. Ruiz-Femenia, and J. J. Sanz-Cillero, *One loop renormalization of the electroweak chiral Lagrangian with a light Higgs boson*, Phys. Rev. **D92** (2015) 074005, arXiv:1506.04204 [hep-ph].
- [101] G. Buchalla, O. Cata, A. Celis, M. Knecht, and C. Krause, *Complete One-Loop Renormalization of the Higgs-Electroweak Chiral Lagrangian*, Nucl. Phys. **B928** (2018) 93–106, arXiv:1710.06412 [hep-ph].
- [102] R. Alonso, K. Kanshin, and S. Saa, *Renormalization group evolution of Higgs effective field theory*, Phys. Rev. **D97** (2018) no. 3, 035010, arXiv:1710.06848 [hep-ph].
- [103] G. Buchalla, O. Cata, A. Celis, and C. Krause, *Comment on "Analysis of General Power Counting Rules in Effective Field Theory"*, arXiv:1603.03062 [hep-ph].
- [104] R. Grober, M. Muhlleitner, M. Spira, and J. Streicher, *NLO QCD Corrections to Higgs Pair Production including Dimension-6 Operators*, JHEP **09** (2015) 092, arXiv:1504.06577

[hep-ph].

- [105] J. H. Kim, Y. Sakaki, and M. Son, *Combined analysis of double Higgs production via gluon fusion at the HL-LHC in the effective field theory approach*, arXiv:1801.06093 [hep-ph].
- [106] G. Buchalla, M. Capozi, A. Celis, G. Heinrich, and L. Scyboz, *Higgs boson pair production in non-linear Effective Field Theory with full m_t -dependence at NLO QCD*, arXiv:1806.05162 [hep-ph].
- [107] M. Ghezzi, R. Gomez-Ambrosio, G. Passarino, and S. Uccirati, *NLO Higgs effective field theory and $\hat{I}\ddot{z}$ -framework*, JHEP **07** (2015) 175, arXiv:1505.03706 [hep-ph].
- [108] I. Brivio and M. Trott, *The Standard Model as an Effective Field Theory*, arXiv:1706.08945 [hep-ph].
- [109] G. Buchalla, O. Catà, and C. Krause, *A Systematic Approach to the SILH Lagrangian*, Nucl. Phys. **B894** (2015) 602–620, arXiv:1412.6356 [hep-ph].
- [110] G. F. Giudice, C. Grojean, A. Pomarol, and R. Rattazzi, *The Strongly-Interacting Light Higgs*, JHEP **06** (2007) 045, arXiv:hep-ph/0703164 [hep-ph].
- [111] HEPfit Collaboration, *HEPfit: a Code for the Combination of Indirect and Direct Constraints on High Energy Physics Models*, . in preparation.
- [112] HEPfit Collaboration, <http://hepfit.roma1.infn.it>.
- [113] ATLAS Collaboration, G. Aad et al., *Measurement of Higgs boson production in the diphoton decay channel in pp collisions at center-of-mass energies of 7 and 8 TeV with the ATLAS detector*, Phys. Rev. **D90** (2014) no. 11, 112015, arXiv:1408.7084 [hep-ex].
- [114] CMS Collaboration, V. Khachatryan et al., *Observation of the diphoton decay of the Higgs boson and measurement of its properties*, Eur. Phys. J. **C74** (2014) no. 10, 3076, arXiv:1407.0558 [hep-ex].
- [115] CMS Collaboration, C. Collaboration, *Measurements of properties of the Higgs boson in the diphoton decay channel with the full 2016 data set*, .
- [116] ATLAS Collaboration, G. Aad et al., *Measurements of Higgs boson production and couplings in the four-lepton channel in pp collisions at center-of-mass energies of 7 and 8 TeV with the ATLAS detector*, Phys. Rev. **D91** (2015) no. 1, 012006, arXiv:1408.5191 [hep-ex].
- [117] ATLAS Collaboration, M. Aaboud et al., *Measurement of the Higgs boson coupling properties in the $H \rightarrow ZZ^* \rightarrow 4\ell$ decay channel at $\sqrt{s} = 13$ TeV with the ATLAS detector*, JHEP **03** (2018) 095, arXiv:1712.02304 [hep-ex].
- [118] CMS Collaboration, V. Khachatryan et al., *Precise determination of the mass of the Higgs boson and tests of compatibility of its couplings with the standard model predictions using proton collisions at 7 and 8 TeV*, Eur. Phys. J. **C75** (2015) no. 5, 212, arXiv:1412.8662 [hep-ex].
- [119] CMS Collaboration, A. M. Sirunyan et al., *Measurements of properties of the Higgs boson decaying into the four-lepton final state in pp collisions at $\sqrt{s} = 13$ TeV*, JHEP **11** (2017) 047, arXiv:1706.09936 [hep-ex].
- [120] ATLAS Collaboration, G. Aad et al., *Observation and measurement of Higgs boson decays to WW^* with the ATLAS detector*, Phys. Rev. **D92** (2015) no. 1, 012006, arXiv:1412.2641 [hep-ex].
- [121] ATLAS Collaboration, G. Aad et al., *Study of $(W/Z)H$ production and Higgs boson couplings using $H \rightarrow WW^*$ decays with the ATLAS detector*, JHEP **08** (2015) 137, arXiv:1506.06641 [hep-ex].
- [122] ATLAS Collaboration, T. A. collaboration, *Measurements of the Higgs boson production cross section via Vector Boson Fusion and associated WH production in the $WW^* \rightarrow \ell\nu\ell\nu$ decay mode with the ATLAS detector at $\sqrt{s} = 13$ TeV*, .
- [123] CMS Collaboration, S. Chatrchyan et al., *Measurement of Higgs boson production and*

- properties in the WW decay channel with leptonic final states*, JHEP **01** (2014) 096, arXiv:1312.1129 [hep-ex].
- [124] CMS Collaboration, A. M. Sirunyan et al., *Measurements of properties of the Higgs boson decaying to a W boson pair in pp collisions at $\sqrt{s} = 13$ TeV*, Submitted to: Phys. Lett. (2018), arXiv:1806.05246 [hep-ex].
- [125] ATLAS Collaboration, G. Aad et al., *Search for the $b\bar{b}$ decay of the Standard Model Higgs boson in associated (W/Z) H production with the ATLAS detector*, JHEP **01** (2015) 069, arXiv:1409.6212 [hep-ex].
- [126] CMS Collaboration, S. Chatrchyan et al., *Search for the standard model Higgs boson produced in association with a W or a Z boson and decaying to bottom quarks*, Phys. Rev. **D89** (2014) no. 1, 012003, arXiv:1310.3687 [hep-ex].
- [127] CMS Collaboration, C. Collaboration, *VBF H to bb using the 2015 data sample*, .
- [128] ATLAS Collaboration, G. Aad et al., *Search for the Standard Model Higgs boson produced in association with top quarks and decaying into $b\bar{b}$ in pp collisions at $\sqrt{s} = 8$ TeV with the ATLAS detector*, Eur. Phys. J. **C75** (2015) no. 7, 349, arXiv:1503.05066 [hep-ex].
- [129] ATLAS Collaboration, M. Aaboud et al., *Evidence for the $H \rightarrow b\bar{b}$ decay with the ATLAS detector*, JHEP **12** (2017) 024, arXiv:1708.03299 [hep-ex].
- [130] CMS Collaboration, V. Khachatryan et al., *Search for the associated production of the Higgs boson with a top-quark pair*, JHEP **09** (2014) 087, arXiv:1408.1682 [hep-ex]. [Erratum: JHEP10,106(2014)].
- [131] CMS Collaboration, A. M. Sirunyan et al., *Evidence for the Higgs boson decay to a bottom quark-antiquark pair*, Phys. Lett. **B780** (2018) 501–532, arXiv:1709.07497 [hep-ex].
- [132] ATLAS Collaboration, G. Aad et al., *Evidence for the Higgs-boson Yukawa coupling to tau leptons with the ATLAS detector*, JHEP **04** (2015) 117, arXiv:1501.04943 [hep-ex].
- [133] CMS Collaboration, S. Chatrchyan et al., *Evidence for the 125 GeV Higgs boson decaying to a pair of τ leptons*, JHEP **05** (2014) 104, arXiv:1401.5041 [hep-ex].
- [134] CMS Collaboration, A. M. Sirunyan et al., *Observation of the Higgs boson decay to a pair of τ leptons with the CMS detector*, Phys. Lett. **B779** (2018) 283–316, arXiv:1708.00373 [hep-ex].
- [135] ATLAS Collaboration, M. Aaboud et al., *Search for the dimuon decay of the Higgs boson in pp collisions at $\sqrt{s} = 13$ TeV with the ATLAS detector*, Phys. Rev. Lett. **119** (2017) no. 5, 051802, arXiv:1705.04582 [hep-ex].
- [136] ATLAS Collaboration, G. Aad et al., *Measurements of the Higgs boson production and decay rates and coupling strengths using pp collision data at $\sqrt{s} = 7$ and 8 TeV in the ATLAS experiment*, Eur. Phys. J. **C76** (2016) no. 1, 6, arXiv:1507.04548 [hep-ex].
- [137] ATLAS Collaboration, M. Aaboud et al., *Searches for the $Z\gamma$ decay mode of the Higgs boson and for new high-mass resonances in pp collisions at $\sqrt{s} = 13$ TeV with the ATLAS detector*, JHEP **10** (2017) 112, arXiv:1708.00212 [hep-ex].
- [138] CMS Collaboration, S. Chatrchyan et al., *Search for a Higgs boson decaying into a Z and a photon in pp collisions at $\sqrt{s} = 7$ and 8 TeV*, Phys. Lett. **B726** (2013) 587–609, arXiv:1307.5515 [hep-ex].
- [139] CDF Collaboration, T. Aaltonen et al., *Combination fo Searches for the Higgs Boson Using the Full CDF Data Set*, Phys. Rev. **D88** (2013) no. 5, 052013, arXiv:1301.6668 [hep-ex].
- [140] D0 Collaboration, V. M. Abazov et al., *Combined search for the Higgs boson with the D0 experiment*, Phys. Rev. **D88** (2013) no. 5, 052011, arXiv:1303.0823 [hep-ex].
- [141] S. Boselli, C. M. Carloni Calame, G. Montagna, O. Nicrosini, F. Piccinini, and A. Shivaji, *Higgs decay into four charged leptons in the presence of dimension-six operators*, JHEP **01** (2018) 096,

[arXiv:1703.06667](#) [hep-ph].

- [142] G. R. Bower, T. Pierzchala, Z. Was, and M. Worek, *Measuring the Higgs boson's parity using tau —> rho nu*, Phys. Lett. **B543** (2002) 227–234, [arXiv:hep-ph/0204292](#) [hep-ph].
- [143] K. Desch, Z. Was, and M. Worek, *Measuring the Higgs boson parity at a linear collider using the tau impact parameter and tau —> rho nu decay*, Eur. Phys. J. **C29** (2003) 491–496, [arXiv:hep-ph/0302046](#) [hep-ph].
- [144] K. Desch, A. Imhof, Z. Was, and M. Worek, *Probing the CP nature of the Higgs boson at linear colliders with tau spin correlations: The Case of mixed scalar - pseudoscalar couplings*, Phys. Lett. **B579** (2004) 157–164, [arXiv:hep-ph/0307331](#) [hep-ph].
- [145] R. Harnik, A. Martin, T. Okui, R. Primulando, and F. Yu, *Measuring CP violation in $h \rightarrow \tau^+ \tau^-$ at colliders*, Phys. Rev. **D88** (2013) no. 7, 076009, [arXiv:1308.1094](#) [hep-ph].
- [146] A. Askew, P. Jaiswal, T. Okui, H. B. Prosper, and N. Sato, *Prospect for measuring the CP phase in the $h\tau\tau$ coupling at the LHC*, Phys. Rev. **D91** (2015) no. 7, 075014, [arXiv:1501.03156](#) [hep-ph].
- [147] R. JÃšszefowicz, E. Richter-Was, and Z. Was, *Potential for optimizing the Higgs boson CP measurement in $H \rightarrow \tau\tau$ decays at the LHC including machine learning techniques*, Phys. Rev. **D94** (2016) no. 9, 093001, [arXiv:1608.02609](#) [hep-ph].
- [148] S. Berge, W. Bernreuther, and J. Ziethe, *Determining the CP parity of Higgs bosons at the LHC in their tau decay channels*, Phys. Rev. Lett. **100** (2008) 171605, [arXiv:0801.2297](#) [hep-ph].
- [149] S. Berge and W. Bernreuther, *Determining the CP parity of Higgs bosons at the LHC in the tau to 1-prong decay channels*, Phys. Lett. **B671** (2009) 470–476, [arXiv:0812.1910](#) [hep-ph].
- [150] S. Berge, W. Bernreuther, B. Niepelt, and H. Spiesberger, *How to pin down the CP quantum numbers of a Higgs boson in its tau decays at the LHC*, Phys. Rev. **D84** (2011) 116003, [arXiv:1108.0670](#) [hep-ph].
- [151] J. Brod, U. Haisch, and J. Zupan, *Constraints on CP-violating Higgs couplings to the third generation*, JHEP **11** (2013) 180, [arXiv:1310.1385](#) [hep-ph].
- [152] M. R. Buckley and D. Goncalves, *Boosting the Direct CP Measurement of the Higgs-Top Coupling*, Phys. Rev. Lett. **116** (2016) no. 9, 091801, [arXiv:1507.07926](#) [hep-ph].
- [153] F. Boudjema, R. M. Godbole, D. Guadagnoli, and K. A. Mohan, *Lab-frame observables for probing the top-Higgs interaction*, Phys. Rev. **D92** (2015) no. 1, 015019, [arXiv:1501.03157](#) [hep-ph].
- [154] G. Mahlon and S. J. Parke, *Angular correlations in top quark pair production and decay at hadron colliders*, Phys. Rev. **D53** (1996) 4886–4896, [arXiv:hep-ph/9512264](#) [hep-ph].
- [155] J. Alwall, R. Frederix, S. Frixione, V. Hirschi, F. Maltoni, O. Mattelaer, H. S. Shao, T. Stelzer, P. Torrielli, and M. Zaro, *The automated computation of tree-level and next-to-leading order differential cross sections, and their matching to parton shower simulations*, JHEP **07** (2014) 079, [arXiv:1405.0301](#) [hep-ph].
- [156] R. Frederix, S. Frixione, V. Hirschi, F. Maltoni, O. Mattelaer, P. Torrielli, E. Vryonidou, and M. Zaro, *Higgs pair production at the LHC with NLO and parton-shower effects*, Phys. Lett. **B732** (2014) 142–149, [arXiv:1401.7340](#) [hep-ph].
- [157] S. Borowka, N. Greiner, G. Heinrich, S. P. Jones, M. Kerner, J. Schlenk, and T. Zirke, *Full top quark mass dependence in Higgs boson pair production at NLO*, JHEP **10** (2016) 107, [arXiv:1608.04798](#) [hep-ph].
- [158] G. Heinrich, S. P. Jones, M. Kerner, G. Luisoni, and E. Vryonidou, *NLO predictions for Higgs boson pair production with full top quark mass dependence matched to parton showers*, JHEP **08** (2017) 088, [arXiv:1703.09252](#) [hep-ph].
- [159] S. Borowka, N. Greiner, G. Heinrich, S. Jones, M. Kerner, J. Schlenk, U. Schubert, and T. Zirke,

- Higgs Boson Pair Production in Gluon Fusion at Next-to-Leading Order with Full Top-Quark Mass Dependence*, Phys. Rev. Lett. **117** (2016) no. 1, 012001, arXiv:1604.06447 [hep-ph]. [Erratum: Phys. Rev. Lett.117,no.7,079901(2016)].
- [160] S. Alioli, P. Nason, C. Oleari, and E. Re, *A general framework for implementing NLO calculations in shower Monte Carlo programs: the POWHEG BOX*, JHEP **06** (2010) 043, arXiv:1002.2581 [hep-ph].
- [161] S. Dulat, T.-J. Hou, J. Gao, M. Guzzi, J. Huston, P. Nadolsky, J. Pumplin, C. Schmidt, D. Stump, and C. P. Yuan, *New parton distribution functions from a global analysis of quantum chromodynamics*, Phys. Rev. **D93** (2016) no. 3, 033006, arXiv:1506.07443 [hep-ph].
- [162] L. A. Harland-Lang, A. D. Martin, P. Motylinski, and R. S. Thorne, *Parton distributions in the LHC era: MMHT 2014 PDFs*, Eur. Phys. J. **C75** (2015) no. 5, 204, arXiv:1412.3989 [hep-ph].
- [163] A. Carvalho, M. Dall’Osso, T. Dorigo, F. Goertz, C. A. Gottardo, and M. Tosi, *Higgs Pair Production: Choosing Benchmarks With Cluster Analysis*, JHEP **04** (2016) 126, arXiv:1507.02245 [hep-ph].
- [164] A. Carvalho, M. Dall’Osso, P. De Castro Manzano, T. Dorigo, F. Goertz, M. Gouzevich, and M. Tosi, *Analytical parametrization and shape classification of anomalous HH production in the EFT approach*, arXiv:1608.06578 [hep-ph].
- [165] CMS Collaboration, *Combined measurements of the Higgs boson’s couplings at $\sqrt{s} = 13$ TeV*, , CERN, Geneva, 2018. <https://cds.cern.ch/record/2308127>.
- [166] CMS Collaboration, *Combination of searches for Higgs boson pair production in proton-proton collisions at $\sqrt{s} = 13$ TeV*, CMS-PAS-HIG-17-030, CERN, Geneva, 2018. <https://cds.cern.ch/record/2628486>.
- [167] ATLAS Collaboration, *Combination of searches for Higgs boson pairs in pp collisions at 13 TeV with the ATLAS experiment.*, ATLAS-CONF-2018-043, CERN, Geneva, Sep, 2018. <https://cds.cern.ch/record/2638212>.
- [168] A. Azatov, R. Contino, G. Panico, and M. Son, *Effective field theory analysis of double Higgs boson production via gluon fusion*, Phys. Rev. **D92** (2015) no. 3, 035001, arXiv:1502.00539 [hep-ph].
- [169] D. de Florian, I. Fabre, and J. Mazzitelli, *Higgs boson pair production at NNLO in QCD including dimension 6 operators*, JHEP **10** (2017) 215, arXiv:1704.05700 [hep-ph].
- [170] A. Collaboration, *Technical Design Report for the ATLAS Inner Tracker Pixel Detector*, . <https://cds.cern.ch/record/2285585>.
- [171] *PUB note in preparation*, .
- [172] *Run 2 paper in preparation*, CERN-EP-2018-164.
- [173] CMS Collaboration, *Higgs pair production at the High Luminosity LHC*, .
- [174] CMS Collaboration, *Projected performance of Higgs analyses at the HL-LHC for ECFA 2016*, .
- [175] A. Adhikary, S. Banerjee, R. K. Barman, B. Bhattacherjee, and S. Niyogi, *Revisiting the non-resonant Higgs pair production at the HL-LHC*, Physics **2018** (2018) 116, arXiv:1712.05346 [hep-ph].
- [176] J. H. Kim, K. Kong, K. T. Matchev, and M. Park, *Measuring the Triple Higgs Self-Interaction at the Large Hadron Collider*, arXiv:1807.11498 [hep-ph].
- [177] C. G. Lester and D. J. Summers, *Measuring masses of semiinvisibly decaying particles pair produced at hadron colliders*, Phys. Lett. **B463** (1999) 99–103, arXiv:hep-ph/9906349 [hep-ph].
- [178] M. Burns, K. Kong, K. T. Matchev, and M. Park, *Using Subsystem MT2 for Complete Mass Determinations in Decay Chains with Missing Energy at Hadron Colliders*, JHEP **03** (2009) 143,

[arXiv:0810.5576 \[hep-ph\]](#).

- [179] A. J. Barr, T. J. Khoo, P. Konar, K. Kong, C. G. Lester, K. T. Matchev, and M. Park, *Guide to transverse projections and mass-constraining variables*, Phys. Rev. **D84** (2011) 095031, [arXiv:1105.2977 \[hep-ph\]](#).
- [180] P. Konar, K. Kong, and K. T. Matchev, $\sqrt{\hat{s}}_{min}$: A Global inclusive variable for determining the mass scale of new physics in events with missing energy at hadron colliders, JHEP **03** (2009) 085, [arXiv:0812.1042 \[hep-ph\]](#).
- [181] P. Konar, K. Kong, K. T. Matchev, and M. Park, RECO level \sqrt{s}_{min} and subsystem \sqrt{s}_{min} : Improved global inclusive variables for measuring the new physics mass scale in E_T events at hadron colliders, JHEP **06** (2011) 041, [arXiv:1006.0653 \[hep-ph\]](#).
- [182] M. L. Graesser and J. Shelton, Hunting Mixed Top Squark Decays, Phys. Rev. Lett. **111** (2013) no. 12, 121802, [arXiv:1212.4495 \[hep-ph\]](#).
- [183] W. S. Cho, D. Kim, K. T. Matchev, and M. Park, Probing Resonance Decays to Two Visible and Multiple Invisible Particles, Phys. Rev. Lett. **112** (2014) no. 21, 211801, [arXiv:1206.1546 \[hep-ph\]](#).
- [184] D. Debnath, D. Kim, J. H. Kim, K. Kong, and K. T. Matchev, Resolving Combinatorial Ambiguities in Dilepton $t\bar{t}$ Event Topologies with Constrained M_2 Variables, Phys. Rev. **D96** (2017) no. 7, 076005, [arXiv:1706.04995 \[hep-ph\]](#).
- [185] P. Konar, K. Kong, K. T. Matchev, and M. Park, Superpartner Mass Measurement Technique using 1D Orthogonal Decompositions of the Cambridge Transverse Mass Variable M_{T2} , Phys. Rev. Lett. **105** (2010) 051802, [arXiv:0910.3679 \[hep-ph\]](#).
- [186] P. Konar, K. Kong, K. T. Matchev, and M. Park, Dark Matter Particle Spectroscopy at the LHC: Generalizing $M(T2)$ to Asymmetric Event Topologies, JHEP **04** (2010) 086, [arXiv:0911.4126 \[hep-ph\]](#).
- [187] W. S. Cho, K. Choi, Y. G. Kim, and C. B. Park, Gluino Stransverse Mass, Phys. Rev. Lett. **100** (2008) 171801, [arXiv:0709.0288 \[hep-ph\]](#).
- [188] CMS Collaboration, A. M. Sirunyan et al., Identification of heavy-flavour jets with the CMS detector in pp collisions at 13 TeV, JINST **13** (2018) no. 05, P05011, [arXiv:1712.07158 \[physics.ins-det\]](#).
- [189] ATLAS Collaboration, Projected sensitivity to non-resonant Higgs boson pair production in the $b\bar{b}b\bar{b}$ final state using proton-proton collisions at HL-LHC with the ATLAS detector, .
- [190] F. Kling, T. Plehn, and P. Schichtel, Maximizing the significance in Higgs boson pair analyses, Phys. Rev. **D95** (2017) no. 3, 035026, [arXiv:1607.07441 \[hep-ph\]](#).
- [191] ATLAS Collaboration, Study of the double Higgs production channel $H(\rightarrow b\bar{b})H(\rightarrow \gamma\gamma)$ with the ATLAS experiment at the HL-LHC, , CERN, Geneva, Jan, 2017.
<https://cds.cern.ch/record/2243387>.
- [192] M. Grazzini, G. Heinrich, S. Jones, S. Kallweit, M. Kerner, J. M. Lindert, and J. Mazzitelli, Higgs boson pair production at NNLO with top quark mass effects, JHEP **05** (2018) 059, [arXiv:1803.02463 \[hep-ph\]](#).
- [193] A. Mitov, Top pair production at a future 27 TeV HE-LHC, HE/HL-LHC Workshop, CERN.
- [194] F. Demartin, F. Maltoni, K. Mawatari, B. Page, and M. Zaro, Higgs characterisation at NLO in QCD: CP properties of the top-quark Yukawa interaction, Eur. Phys. J. **C74** (2014) no. 9, 3065, [arXiv:1407.5089 \[hep-ph\]](#).
- [195] D. Gonçalves, T. Han, F. Kling, T. Plehn, and M. Takeuchi, Higgs Pair Production at Future Hadron Colliders: From Kinematics to Dynamics, [arXiv:1802.04319 \[hep-ph\]](#).
- [196] A. Alves, T. Ghosh, and K. Sinha, Can We Discover Double Higgs Production at the LHC?, Phys. Rev. **D96** (2017) no. 3, 035022, [arXiv:1704.07395 \[hep-ph\]](#).

- [197] D. de Florian and J. Mazzitelli, *Two-loop virtual corrections to Higgs pair production*, Phys. Lett. **B724** (2013) 306–309, arXiv:1305.5206 [hep-ph].
- [198] S. Bergstra, R. Bardenet, Y. Bengio, and B. Kégl, *Algorithms for hyper-parameter optimization.*, Advances in Neural Information Processing Systems (2011) 2546.
- [199] S. Bergstra, D. Yamins, and D. Cox, *Hyperopt: A Python Library for Optimizing the Hyperparameters of Machine Learning Algorithms.*, Proceedings of the 12th PYTHON in Science Conference, SciPy 2013 (2013) .
- [200] HyperOpt software package: <https://github.com/jberg/hyperopt> .
- [201] ATLAS Collaboration, G. Aad et al., *Search For Higgs Boson Pair Production in the $\gamma\gamma b\bar{b}$ Final State using pp Collision Data at $\sqrt{s} = 8$ TeV from the ATLAS Detector*, Phys. Rev. Lett. **114** (2015) no. 8, 081802, arXiv:1406.5053 [hep-ex].
- [202] CMS Collaboration, C. Collaboration, *First results on Higgs to gammagamma at 13 TeV*, .
- [203] *Prospects for measuring Higgs pair production in the channel $H(\rightarrow \gamma\gamma)H(\rightarrow b\bar{b})$ using the ATLAS detector at the HL-LHC*, , CERN, Geneva, Oct, 2014.
<http://cds.cern.ch/record/1956733>.
- [204] R. Contino et al., *Physics at a 100 TeV pp collider: Higgs and EW symmetry breaking studies*, CERN Yellow Report (2017) no. 3, 255–440, arXiv:1606.09408 [hep-ph].
- [205] S. Homiller and P. Meade, *Measurement of the Triple Higgs Coupling at a HE-LHC*, to appear (2018) .
- [206] V. Hirschi and O. Mattelaer, *Automated event generation for loop-induced processes*, JHEP **10** (2015) 146, arXiv:1507.00020 [hep-ph].
- [207] NNPDF Collaboration, R. D. Ball et al., *Parton distributions for the LHC Run II*, JHEP **04** (2015) 040, arXiv:1410.8849 [hep-ph].
- [208] P. Artoisenet, R. Frederix, O. Mattelaer, and R. Rietkerk, *Automatic spin-entangled decays of heavy resonances in Monte Carlo simulations*, JHEP **03** (2013) 015, arXiv:1212.3460 [hep-ph].
- [209] T. Sjöstrand, S. Ask, J. R. Christiansen, R. Corke, N. Desai, P. Ilten, S. Mrenna, S. Prestel, C. O. Rasmussen, and P. Z. Skands, *An Introduction to PYTHIA 8.2*, Comput. Phys. Commun. **191** (2015) 159–177, arXiv:1410.3012 [hep-ph].
- [210] M. L. Mangano, M. Moretti, F. Piccinini, and M. Treccani, *Matching matrix elements and shower evolution for top-quark production in hadronic collisions*, JHEP **01** (2007) 013, arXiv:hep-ph/0611129 [hep-ph].
- [211] J. Alwall et al., *Comparative study of various algorithms for the merging of parton showers and matrix elements in hadronic collisions*, Eur. Phys. J. **C53** (2008) 473–500, arXiv:0706.2569 [hep-ph].
- [212] M. McCullough, *An Indirect Model-Dependent Probe of the Higgs Self-Coupling*, Phys. Rev. **D90** (2014) no. 1, 015001, arXiv:1312.3322 [hep-ph]. [Erratum: Phys. Rev.D92,no.3,039903(2015)].
- [213] M. Gorbahn and U. Haisch, *Indirect probes of the trilinear Higgs coupling: $gg \rightarrow h$ and $h \rightarrow \gamma\gamma$* , arXiv:1607.03773 [hep-ph].
- [214] G. Degrassi, P. P. Giardino, F. Maltoni, and D. Pagani, *Probing the Higgs self coupling via single Higgs production at the LHC*, arXiv:1607.04251 [hep-ph].
- [215] W. Bizon, M. Gorbahn, U. Haisch, and G. Zanderighi, *Constraints on the trilinear Higgs coupling from vector boson fusion and associated Higgs production at the LHC*, JHEP **07** (2017) 083, arXiv:1610.05771 [hep-ph].
- [216] S. Di Vita, C. Grojean, G. Panico, M. Riembau, and T. Vantalon, *A global view on the Higgs self-coupling*, JHEP **09** (2017) 069, arXiv:1704.01953 [hep-ph].

- [217] T. Barklow, K. Fujii, S. Jung, M. E. Peskin, and J. Tian, *Model-Independent Determination of the Triple Higgs Coupling at $e+e-$ Colliders*, Phys. Rev. **D97** (2018) no. 5, 053004, arXiv:1708.09079 [hep-ph].
- [218] F. Maltoni, D. Pagani, A. Shivaji, and X. Zhao, *Trilinear Higgs coupling determination via single-Higgs differential measurements at the LHC*, Eur. Phys. J. **C77** (2017) no. 12, 887, arXiv:1709.08649 [hep-ph].
- [219] S. Di Vita, G. Durieux, C. Grojean, J. Gu, Z. Liu, G. Panico, M. Riembau, and T. Vantalon, *A global view on the Higgs self-coupling at lepton colliders*, JHEP **02** (2018) 178, arXiv:1711.03978 [hep-ph].
- [220] F. Maltoni, D. Pagani, and X. Zhao, *Constraining the Higgs self-couplings at e^+e^- colliders*, JHEP **07** (2018) 087, arXiv:1802.07616 [hep-ph].
- [221] G. Degrassi, M. Fedele, and P. P. Giardino, *Constraints on the trilinear Higgs self coupling from precision observables*, JHEP **04** (2017) 155, arXiv:1702.01737 [hep-ph].
- [222] G. D. Kribs, A. Maier, H. Rzehak, M. Spannowsky, and P. Waite, *Electroweak oblique parameters as a probe of the trilinear Higgs boson self-interaction*, Phys. Rev. **D95** (2017) no. 9, 093004, arXiv:1702.07678 [hep-ph].
- [223] L. Di Luzio, R. Gröber, and M. Spannowsky, *Maxi-sizing the trilinear Higgs self-coupling: how large could it be?*, Eur. Phys. J. **C77** (2017) no. 11, 788, arXiv:1704.02311 [hep-ph].
- [224] M. Bauer, M. Carena, and A. Carmona, *Higgs Pair Production as a Signal of Enhanced Yukawa Couplings*, Phys. Rev. Lett. **121** (2018) no. 2, 021801, arXiv:1801.00363 [hep-ph].
- [225] F. Boudjema and A. Semenov, *Measurements of the SUSY Higgs selfcouplings and the reconstruction of the Higgs potential*, Phys. Rev. **D66** (2002) 095007, arXiv:hep-ph/0201219 [hep-ph].
- [226] J. F. Gunion and H. E. Haber, *The CP conserving two Higgs doublet model: The Approach to the decoupling limit*, Phys. Rev. **D67** (2003) 075019, arXiv:hep-ph/0207010 [hep-ph].
- [227] D. Eriksson, J. Rathsman, and O. Stal, *2HDMC: Two-Higgs-Doublet Model Calculator Physics and Manual*, Comput. Phys. Commun. **181** (2010) 189–205, arXiv:0902.0851 [hep-ph].
- [228] R. Franceschini, G. Panico, A. Pomarol, F. Riva, and A. Wulzer, *Electroweak Precision Tests in High-Energy Diboson Processes*, JHEP **02** (2018) 111, arXiv:1712.01310 [hep-ph].
- [229] R. S. Gupta, A. Pomarol, and F. Riva, *BSM Primary Effects*, Phys. Rev. **D91** (2015) no. 3, 035001, arXiv:1405.0181 [hep-ph].
- [230] A. Pomarol, *Higgs Physics*, in *Proceedings, 2014 European School of High-Energy Physics (ESHEP 2014): Garderen, The Netherlands, June 18 - July 01 2014*, pp. 59–77. 2016. arXiv:1412.4410 [hep-ph].
<http://inspirehep.net/record/1334375/files/arXiv:1412.4410.pdf>.
- [231] B. Grzadkowski, M. Iskrzynski, M. Misiak, and J. Rosiek, *Dimension-Six Terms in the Standard Model Lagrangian*, JHEP **10** (2010) 085, arXiv:1008.4884 [hep-ph].
- [232] J. M. Butterworth, A. R. Davison, M. Rubin, and G. P. Salam, *Jet substructure as a new Higgs search channel at the LHC*, Phys. Rev. Lett. **100** (2008) 242001, arXiv:0802.2470 [hep-ph].
- [233] S. Banerjee, C. Englert, R. S. Gupta, and M. Spannowsky, *Probing Electroweak Precision Physics via boosted Higgs-strahlung at the LHC*, arXiv:1807.01796 [hep-ph].
- [234] ALEPH Collaboration, DELPHI Collaboration, L3 Collaboration, OPAL Collaboration, LEP TGC Working Group, *A Combination of Preliminary Results on Gauge Boson Couplings Measured by the LEP experiments*, LEPEWWG-TGC-2003-01. DELPHI-2003-068-PHYS-936. L3-Note-2826. LEPEWWG-2006-01. OPAL-TN-739. ALEPH-2006-016-CONF-2003-012, CERN, Geneva, Jan, 2003. <https://cds.cern.ch/record/2285934>. 2003 Summer Conferences.

- [235] A. Falkowski and F. Riva, *Model-independent precision constraints on dimension-6 operators*, JHEP **02** (2015) 039, arXiv:1411.0669 [hep-ph].
- [236] M. Baak, M. Goebel, J. Haller, A. Hoecker, D. Kennedy, R. Kogler, K. Moenig, M. Schott, and J. Stelzer, *The Electroweak Fit of the Standard Model after the Discovery of a New Boson at the LHC*, Eur. Phys. J. **C72** (2012) 2205, arXiv:1209.2716 [hep-ph].
- [237] R. Barbieri, A. Pomarol, R. Rattazzi, and A. Strumia, *Electroweak symmetry breaking after LEP-1 and LEP-2*, Nucl. Phys. **B703** (2004) 127–146, arXiv:hep-ph/0405040 [hep-ph].
- [238] R. Franceschini, G. Panico, A. Pomarol, F. Riva, and A. Wulzer, *Electroweak Precision Tests in High-Energy Diboson Processes*, JHEP **02** (2018) 111, arXiv:1712.01310 [hep-ph].
- [239] G. Panico, F. Riva, and A. Wulzer, *Diboson Interference Resurrection*, Phys. Lett. **B776** (2018) 473–480, arXiv:1708.07823 [hep-ph].
- [240] A. Azatov, J. Elias-Miro, Y. Reyimuaji, and E. Venturini, *Novel measurements of anomalous triple gauge couplings for the LHC*, JHEP **10** (2017) 027, arXiv:1707.08060 [hep-ph].
- [241] M. S. Chanowitz and M. K. Gaillard, *The TeV Physics of Strongly Interacting W's and Z's*, Nucl. Phys. **B261** (1985) 379–431.
- [242] A. Wulzer, *An Equivalent Gauge and the Equivalence Theorem*, Nucl. Phys. **B885** (2014) 97–126, arXiv:1309.6055 [hep-ph].
- [243] ATLAS Collaboration, G. Aad et al., *Measurements of $W^\pm Z$ production cross sections in pp collisions at $\sqrt{s} = 8$ TeV with the ATLAS detector and limits on anomalous gauge boson self-couplings*, Phys. Rev. **D93** (2016) no. 9, 092004, arXiv:1603.02151 [hep-ex].
- [244] ATLAS Collaboration, G. Aad et al., *Measurement of the double-differential high-mass Drell-Yan cross section in pp collisions at $\sqrt{s} = 8$ TeV with the ATLAS detector*, JHEP **08** (2016) 009, arXiv:1606.01736 [hep-ex].
- [245] ATLAS Collaboration, T. A. collaboration, *Electron efficiency measurements with the ATLAS detector using the 2015 LHC proton-proton collision data*.
- [246] F. Campanario, R. Roth, and D. Zeppenfeld, *QCD radiation in WH and WZ production and anomalous coupling measurements*, Phys. Rev. **D91** (2015) 054039, arXiv:1410.4840 [hep-ph].
- [247] J. Ellis, P. Roloff, V. Sanz, and T. You, *Dimension-6 Operator Analysis of the CLIC Sensitivity to New Physics*, JHEP **05** (2017) 096, arXiv:1701.04804 [hep-ph].
- [248] D. Racco, A. Wulzer, and F. Zwirner, *Robust collider limits on heavy-mediator Dark Matter*, JHEP **05** (2015) 009, arXiv:1502.04701 [hep-ph].
- [249] F. Pobbe, A. Wulzer, and M. Zanetti, *Setting limits on Effective Field Theories: the case of Dark Matter*, JHEP **08** (2017) 074, arXiv:1704.00736 [hep-ph].
- [250] A. Biekăćtter, A. Knochel, M. Krădmer, D. Liu, and F. Riva, *Vices and virtues of Higgs effective field theories at large energy*, Phys. Rev. **D91** (2015) 055029, arXiv:1406.7320 [hep-ph].
- [251] CMS Collaboration, A. M. Sirunyan et al., *Search for anomalous couplings in boosted WW/WZ $\rightarrow \ell\nu q\bar{q}$ production in proton-proton collisions at $\sqrt{s} = 8$ TeV*, Phys. Lett. **B772** (2017) 21–42, arXiv:1703.06095 [hep-ex].
- [252] L. J. Dixon and Y. Shadmi, *Testing gluon selfinteractions in three jet events at hadron colliders*, Nucl. Phys. **B423** (1994) 3–32, arXiv:hep-ph/9312363 [hep-ph]. [Erratum: Nucl. Phys.B452,724(1995)].
- [253] A. Azatov, R. Contino, C. S. Machado, and F. Riva, *Helicity selection rules and noninterference for BSM amplitudes*, Phys. Rev. **D95** (2017) no. 6, 065014, arXiv:1607.05236 [hep-ph].
- [254] U. Baur, T. Han, and J. Ohnemus, *Amplitude zeros in $W^+ - Z$ production*, Phys. Rev. Lett. **72** (1994) 3941–3944, arXiv:hep-ph/9403248 [hep-ph].

- [255] DELPHES 3 Collaboration, J. de Favereau, C. Delaere, P. Demin, A. Giannanco, V. LemaÃČÂtre, A. Mertens, and M. Selvaggi, *DELPHES 3, A modular framework for fast simulation of a generic collider experiment*, JHEP **02** (2014) 057, arXiv:1307.6346 [hep-ex].
- [256] F. Bishara, R. Contino, and J. Rojo, *Higgs pair production in vector-boson fusion at the LHC and beyond*, Eur. Phys. J. **C77** (2017) no. 7, 481, arXiv:1611.03860 [hep-ph].
- [257] R. Contino, C. Grojean, M. Moretti, F. Piccinini, and R. Rattazzi, *Strong Double Higgs Production at the LHC*, JHEP **05** (2010) 089, arXiv:1002.1011 [hep-ph].
- [258] R. Contino, C. Grojean, D. Pappadopulo, R. Rattazzi, and A. Thamm, *Strong Higgs Interactions at a Linear Collider*, JHEP **02** (2014) 006, arXiv:1309.7038 [hep-ph].
- [259] M. J. Dolan, C. Englert, N. Greiner, and M. Spannowsky, *Further on up the road: $hhjj$ production at the LHC*, Phys. Rev. Lett. **112** (2014) 101802, arXiv:1310.1084 [hep-ph].
- [260] G. Brooijmans et al., *Les Houches 2013: Physics at TeV Colliders: New Physics Working Group Report*, arXiv:1405.1617 [hep-ph].
- [261] L.-S. Ling, R.-Y. Zhang, W.-G. Ma, L. Guo, W.-H. Li, and X.-Z. Li, *NNLO QCD corrections to Higgs pair production via vector boson fusion at hadron colliders*, Phys. Rev. **D89** (2014) no. 7, 073001, arXiv:1401.7754 [hep-ph].
- [262] M. J. Dolan, C. Englert, N. Greiner, K. Nordstrom, and M. Spannowsky, *$hhjj$ production at the LHC*, Eur. Phys. J. **C75** (2015) no. 8, 387, arXiv:1506.08008 [hep-ph].
- [263] D. B. Kaplan and H. Georgi, *$SU(2) \times U(1)$ Breaking by Vacuum Misalignment*, Phys. Lett. **136B** (1984) 183–186.
- [264] G. P. Salam, *Towards Jetography*, Eur. Phys. J. **C67** (2010) 637–686, arXiv:0906.1833 [hep-ph].
- [265] M. Gouzevitch, A. Oliveira, J. Rojo, R. Rosenfeld, G. P. Salam, and V. Sanz, *Scale-invariant resonance tagging in multijet events and new physics in Higgs pair production*, JHEP **07** (2013) 148, arXiv:1303.6636 [hep-ph].
- [266] J. K. Behr, D. Bortoletto, J. A. Frost, N. P. Hartland, C. Issever, and J. Rojo, *Boosting Higgs pair production in the $b\bar{b}b\bar{b}$ final state with multivariate techniques*, Eur. Phys. J. **C76** (2016) no. 7, 386, arXiv:1512.08928 [hep-ph].
- [267] M. Cacciari, G. P. Salam, and G. Soyez, *FastJet User Manual*, Eur. Phys. J. **C72** (2012) 1896, arXiv:1111.6097 [hep-ph].
- [268] M. Cacciari, G. P. Salam, and G. Soyez, *The anti- k_t jet clustering algorithm*, JHEP **04** (2008) 063, arXiv:0802.1189 [hep-ph].
- [269] R. Contino, A. Falkowski, F. Goertz, C. Grojean, and F. Riva, *On the Validity of the Effective Field Theory Approach to SM Precision Tests*, JHEP **07** (2016) 144, arXiv:1604.06444 [hep-ph].
- [270] J. Kalinowski, P. Kozow, S. Pokorski, J. Rosiek, M. Szleper, and S. Tkaczyk, *Same-sign WW scattering at the LHC: can we discover BSM effects before discovering new states?*, Eur. Phys. J. **C78** (2018) no. 5, 403, arXiv:1802.02366 [hep-ph].
- [271] CMS Collaboration, A. M. Sirunyan et al., *Measurement of vector boson scattering and constraints on anomalous quartic couplings from events with four leptons and two jets in protonâŠproton collisions at $\sqrt{s} = 13$ TeV*, Phys. Lett. **B774** (2017) 682–705, arXiv:1708.02812 [hep-ex].
- [272] R. Gomez-Ambrosio, *Studies of Dimension-Six EFT effects in Vector Boson Scattering*, arXiv:1809.04189 [hep-ph].
- [273] E. E. Jenkins, A. V. Manohar, and M. Trott, *Renormalization Group Evolution of the Standard Model Dimension Six Operators I: Formalism and lambda Dependence*, JHEP **10** (2013) 087,

- arXiv:1308.2627 [hep-ph].
- [274] CMS Collaboration, A. M. Sirunyan et al., *Measurement of differential cross sections for Z boson pair production in association with jets at $\sqrt{s} = 8$ and 13 TeV*, arXiv:1806.11073 [hep-ex].
- [275] L. J. Dixon and M. S. Siu, *Resonance continuum interference in the diphoton Higgs signal at the LHC*, Phys. Rev. Lett. **90** (2003) 252001, arXiv:hep-ph/0302233 [hep-ph].
- [276] S. P. Martin, *Shift in the LHC Higgs diphoton mass peak from interference with background*, Phys. Rev. **D86** (2012) 073016, arXiv:1208.1533 [hep-ph].
- [277] L. J. Dixon and Y. Li, *Bounding the Higgs Boson Width Through Interferometry*, Phys. Rev. Lett. **111** (2013) 111802, arXiv:1305.3854 [hep-ph].
- [278] J. Campbell, M. Carena, R. Harnik, and Z. Liu, *Interference in the $gg \rightarrow h \rightarrow \gamma\gamma$ On-Shell Rate and the Higgs Boson Total Width*, Phys. Rev. Lett. **119** (2017) no. 18, 181801, arXiv:1704.08259 [hep-ph]. [Addendum: Phys. Rev. Lett.119,no.19,199901(2017)].
- [279] F. Coradeschi, D. de Florian, L. J. Dixon, N. Fidanza, S. Hoeche, H. Ita, Y. Li, and J. Mazzitelli, *Interference effects in the $H(\rightarrow \gamma\gamma) + 2$ jets channel at the LHC*, Phys. Rev. **D92** (2015) no. 1, 013004, arXiv:1504.05215 [hep-ph].
- [280] D. de Florian, N. Fidanza, R. J. Hernandez-Pinto, J. Mazzitelli, Y. Rotstein Habarnau, and G. F. R. Sborlini, *A complete $O(\alpha_S^2)$ calculation of the signal-background interference for the Higgs diphoton decay channel*, Eur. Phys. J. **C73** (2013) no. 4, 2387, arXiv:1303.1397 [hep-ph].
- [281] S. P. Martin, *Interference of Higgs diphoton signal and background in production with a jet at the LHC*, Phys. Rev. **D88** (2013) no. 1, 013004, arXiv:1303.3342 [hep-ph].
- [282] T. Gleisberg, S. Hoeche, F. Krauss, M. Schonherr, S. Schumann, F. Siegert, and J. Winter, *Event generation with SHERPA 1.1*, JHEP **02** (2009) 007, arXiv:0811.4622 [hep-ph].
- [283] S. Hoeche and S. Prestel, *The midpoint between dipole and parton showers*, Eur. Phys. J. **C75** (2015) no. 9, 461, arXiv:1506.05057 [hep-ph].
- [284] F. Caola, J. M. Lindert, K. Melnikov, P. F. Monni, L. Tancredi, and C. Wever, *Bottom-quark effects in Higgs production at intermediate transverse momentum*, JHEP **09** (2018) 035, arXiv:1804.07632 [hep-ph].
- [285] N. Kauer and G. Passarino, *Inadequacy of zero-width approximation for a light Higgs boson signal*, JHEP **08** (2012) 116, arXiv:1206.4803 [hep-ph].
- [286] F. Caola and K. Melnikov, *Constraining the Higgs boson width with ZZ production at the LHC*, Phys. Rev. **D88** (2013) 054024, arXiv:1307.4935 [hep-ph].
- [287] J. M. Campbell, R. K. Ellis, and C. Williams, *Bounding the Higgs width at the LHC using full analytic results for $gg \rightarrow e^-e^+\mu^-\mu^+$* , JHEP **04** (2014) 060, arXiv:1311.3589 [hep-ph].
- [288] J. M. Campbell, R. K. Ellis, and C. Williams, *Bounding the Higgs width at the LHC: Complementary results from $H \rightarrow WW$* , Phys. Rev. **D89** (2014) no. 5, 053011, arXiv:1312.1628 [hep-ph].
- [289] C. Englert and M. Spannowsky, *Limitations and Opportunities of Off-Shell Coupling Measurements*, Phys. Rev. **D90** (2014) 053003, arXiv:1405.0285 [hep-ph].
- [290] H. E. Logan, *Hiding a Higgs width enhancement from off-shell $gg(\rightarrow h*) \rightarrow ZZ$ measurements*, Phys. Rev. **D92** (2015) no. 7, 075038, arXiv:1412.7577 [hep-ph].
- [291] C. Englert, Y. Soreq, and M. Spannowsky, *Off-Shell Higgs Coupling Measurements in BSM scenarios*, JHEP **05** (2015) 145, arXiv:1410.5440 [hep-ph].
- [292] I. Anderson et al., *Constraining anomalous HVV interactions at proton and lepton colliders*, Phys. Rev. **D89** (2014) no. 3, 035007, arXiv:1309.4819 [hep-ph].
- [293] A. Azatov, C. Grojean, A. Paul, and E. Salvioni, *Taming the off-shell Higgs boson*, Zh. Eksp. Teor. Fiz. **147** (2015) 410–425, arXiv:1406.6338 [hep-ph]. [J. Exp. Theor.

Phys.120,354(2015)].

- [294] J. M. Campbell and R. K. Ellis, *Higgs Constraints from Vector Boson Fusion and Scattering*, JHEP **04** (2015) 030, arXiv:1502.02990 [hep-ph].
- [295] F. Caola, M. Dowling, K. Melnikov, R. Roentsch, and L. Tancredi, *QCD corrections to vector boson pair production in gluon fusion including interference effects with off-shell Higgs at the LHC*, JHEP **07** (2016) 087, arXiv:1605.04610 [hep-ph].
- [296] J. M. Campbell, R. K. Ellis, M. Czakon, and S. Kirchner, *Two loop correction to interference in $gg \rightarrow ZZ$* , JHEP **08** (2016) 011, arXiv:1605.01380 [hep-ph].
- [297] J. M. Campbell, R. K. Ellis, E. Furlan, and R. Roentsch, *Interference effects for Higgs boson mediated Z-pair plus jet production*, Phys. Rev. **D90** (2014) no. 9, 093008, arXiv:1409.1897 [hep-ph].
- [298] F. Caola, K. Melnikov, R. Roentsch, and L. Tancredi, *QCD corrections to ZZ production in gluon fusion at the LHC*, Phys. Rev. **D92** (2015) no. 9, 094028, arXiv:1509.06734 [hep-ph].
- [299] F. Caola, K. Melnikov, R. Roentsch, and L. Tancredi, *QCD corrections to W^+W^- production through gluon fusion*, Phys. Lett. **B754** (2016) 275–280, arXiv:1511.08617 [hep-ph].
- [300] M. Bonvini, F. Caola, S. Forte, K. Melnikov, and G. Ridolfi, *Signal-background interference effects for $gg \rightarrow H \rightarrow W^+W^-$ beyond leading order*, Phys. Rev. **D88** (2013) no. 3, 034032, arXiv:1304.3053 [hep-ph].
- [301] S. Alioli, F. Caola, G. Luisoni, and R. RÃºntschi, *ZZ production in gluon fusion at NLO matched to parton-shower*, Phys. Rev. **D95** (2017) no. 3, 034042, arXiv:1609.09719 [hep-ph].
- [302] M. Duhrssen, S. Heinemeyer, H. Logan, D. Rainwater, G. Weiglein, and D. Zeppenfeld, *Extracting Higgs boson couplings from CERN LHC data*, Phys. Rev. **D70** (2004) 113009, arXiv:hep-ph/0406323 [hep-ph].
- [303] B. A. Dobrescu and J. D. Lykken, *Coupling spans of the Higgs-like boson*, JHEP **02** (2013) 073, arXiv:1210.3342 [hep-ph].
- [304] D. A. Dicus and S. S. D. Willenbrock, *Photon Pair Production and the Intermediate Mass Higgs Boson*, Phys. Rev. **D37** (1988) 1801.
- [305] Z. Bern and D. A. Kosower, *The Computation of loop amplitudes in gauge theories*, Nucl. Phys. **B379** (1992) 451–561.
- [306] Z. Bern, A. De Freitas, and L. J. Dixon, *Two loop amplitudes for gluon fusion into two photons*, JHEP **09** (2001) 037, arXiv:hep-ph/0109078 [hep-ph].
- [307] Z. Bern and A. G. Morgan, *Massive loop amplitudes from unitarity*, Nucl. Phys. **B467** (1996) 479–509, arXiv:hep-ph/9511336 [hep-ph].
- [308] Z. Bern, L. J. Dixon, and D. A. Kosower, *One loop corrections to five gluon amplitudes*, Phys. Rev. Lett. **70** (1993) 2677–2680, arXiv:hep-ph/9302280 [hep-ph].
- [309] Z. Bern, L. J. Dixon, and C. Schmidt, *Isolating a light Higgs boson from the diphoton background at the CERN LHC*, Phys. Rev. **D66** (2002) 074018, arXiv:hep-ph/0206194 [hep-ph].
- [310] S. Catani and M. H. Seymour, *A General algorithm for calculating jet cross-sections in NLO QCD*, Nucl. Phys. **B485** (1997) 291–419, arXiv:hep-ph/9605323 [hep-ph]. [Erratum: Nucl. Phys.B510,503(1998)].
- [311] J. M. Campbell, R. K. Ellis, and C. Williams, *Vector boson pair production at the LHC*, JHEP **07** (2011) 018, arXiv:1105.0020 [hep-ph].
- [312] A. Djouadi, P. Gambino, and B. A. Kniehl, *Two loop electroweak heavy fermion corrections to Higgs boson production and decay*, Nucl. Phys. **B523** (1998) 17–39, arXiv:hep-ph/9712330 [hep-ph].
- [313] G. Degrassi and F. Maltoni, *Two-loop electroweak corrections to the Higgs-boson decay $H \rightarrow$*

- gamma gamma*, Nucl. Phys. **B724** (2005) 183–196, arXiv:hep-ph/0504137 [hep-ph].
- [314] G. Passarino, C. Sturm, and S. Uccirati, *Complete Two-Loop Corrections to $H \rightarrow \gamma\gamma$* , Phys. Lett. **B655** (2007) 298–306, arXiv:0707.1401 [hep-ph].
- [315] LHC Higgs Cross Section Working Group Collaboration, S. Dittmaier et al., *Handbook of LHC Higgs Cross Sections: 1. Inclusive Observables*, arXiv:1101.0593 [hep-ph].
- [316] *Projections for measurements of Higgs boson signal strengths and coupling parameters with the ATLAS detector at a HL-LHC*, ATL-PHYS-PUB-2014-016, CERN, Geneva, Oct, 2014.
<http://cds.cern.ch/record/1956710>.